THERMOELASTOHYDRODYNAMIC ANALYSIS OF LARGE THRUST PAD BEARINGS

by

YAHYA MAHMOUD HASSAN ALI EL-SAIE

A thesis submitted for the degree of

DOCTOR OF PHILOSOPHY

OF THE UNIVERSITY OF LONDON

and also for the

DIPLOMA OF IMPERIAL COLLEGE

June, 1982

Mechanical Engineering Department

Imperial College,

London SW7.

ABSTRACT

A comprehensive numerical model is developed for tilting pad thrust bearings. The solutions are generated by simultaneously solving the Reynolds and energy equation in the oil film, the elastic and thermal deformations as well as the energy equation in the pad, the energy equation in the runner, and the mixing conditions in the oil groove.

The energy model in the pad is fully three-dimentional. A quasi-three-dimentional model is used for the energy equation in the oil film. A 'Polynomial Difference' technique is employed for the solution of pad deflections to deal more efficiently with the lengthy equations involved.

A comparison between results for the model and previous experimental investigations shows good agreement over the thrust pad size range.

Size effects on large thrust bearing design are highlighted. The effects of various modifications to existing large bearing designs are predicted.

ACKNOWLEDGEMENTS

I would like to express my gratitude to Dr. C. Ettles for conceiving this research project, and for his supervision, help, and advice.

I also express my gratitude to Dr. R. Fenner for his help and advice, and for accepting to supervise me whilst Dr. Ettles was on leave.

I offer my thanks to Professor A. Cameron for the oppurtunity to work in the lubrication group.

Finally, I thank the Science Research Council for providing contract GR/A/8105.8 for a three year period.

CONTENTS

List of Figures

List of Tables

NOMENCLATURE

A	area
$\bar{A}$	geometry matrix
AC	angle subtended by cavity
AP	pad angle
B	breadth
$\underline{b}$	stress vector
c	specific heat capacity
c_r	crown height
D	plate rigidity $=h^3/12(1-\nu^2)$
D	down face
$\delta\theta$	angle subtended by control volume
E	Young's modulus
E	east face
$\bar{F}$	condition matrix
h	film thickness
h_i	inlet film thickness
h^2	square of mesh length
I	node position in radial direction
I	second moment of area
J	node position in tangential direction
K	node position in z-direction (oil film)
k	conductivity

k	spring stiffness
k_h	hot oil carryover factor
L	node position in z-direction (pad)
l	length
LL	node position in z-direction (runner)
M	bending moment
MAWR	mean absolute weighted residual
m	number of nodes in radial direction
N	number of deflection molecules
N	north face
n	order of deflection polynomial
n	number of nodes in tangential direction
p	pressure
Q	heat flux
q	flow rate
r	radial position
Re	Reynolds number (ρ rΩh/μ)
S	south face
SHTC	surface heat transfer coefficient
T	temperature
T_{amb}	ambient temperature
T_r	rotor temperature
T_{bath}	bath temperature
U	top face
U	runner velocity
u	fluid velocity in radial direction

V	shear force at edge
v	fluid velocity in tangential direction
W	load
W	west face
w	deflection
z	direction across film thickness
θ	circumferential position from leading edge
μ	viscosity
τ	shear stress in fluid
Δ	change (or increment)
ρ	density
Ω	angular velocity
α	surface heat transfer coefficient
ν	Poisson's ratio
α, Φ	angles of pad inclination

SUBSCRIPTS

piv	pivot
min	minimum
o	outer
i	inner

SUPERSCRIPTS

-1	inverse of matrix
T	transpose of matrix

CHAPTER 1

1.1 INTRODUCTION

The capacity of modern hydroelectric power plants continues to increase. Consequently the thrust bearings carrying the turbogenerators are required to sustain heavier loads.

In order to maintain safe bearing operation, a hydrodynamic oil film must be maintained between the runner and bearing pads. The pressure generation within the oil film is governed by several interrelated mechanisms; all of which should be accounted for in a successful design. These include the stresses within the fluid, the effect of temperature on the rate of shear in the fluid (viscosity), the deflection of the solid components (pad and runner) due to the pressure generated in the fluid and due to thermal stresses within the solids, the effect of shear stresses within the fluid in generating heat energy, and the effect of the oil flow in the grooves between successive pads.

Rapid design aids {R1} require assumptions and approximations in order to simplify the design process. For heavily loaded large bearings, very few assumptions can be made without sacrificing the safety of bearing operation. On the other hand, prototypes and test rigs are very expensive.

Researchers have devoted a considerable effort in analysing the mechanisms of hydrodynamic thrust bearing operation. Three

broad areas can be identified at present: the mechanism of pressure generation; the energy effects; and the distortion mechanism. The recent historical background to each of the three mechanisms is outlined in the introductions to chapters 2,3 and 4 respectively.

The work described in this thesis was undertaken to set up a comprehensive model for tilting thrust pad bearings and to correlate the model predictions with existing experimental results for different bearing sizes.

1.2 Outlime of Thesis

The literature review for the present work has been presented in the introduction to chapters 2,3 and 4.

In chapter 2, a mathematical model for the solution of the Reynolds equation is presented including a pivoting model to allow pad tilting. In chapter 3, an energy model is developed for the oil film, pad and runner. This includes a three-dimensional solution of conduction in the pad. For the runner, only a two-dimensional solution is necessary as the temperature field is assumed axisymmetrical. The temperature variations along, across and through the oil film are accounted for in a quasi three-dimensional model - restricting the temperature profile through the oil film to a parabola.

In chapter 4, the 'polynomial differece method' is described in detail as applied to beam deflection. The method is then applied to plates with various boundary conditions and compared with

previous published results.

In chapter 5, the assembly of the mathematical models into a co-ordinated overall model is presented.

In chapter 6, comparisons between the model presented and previous experimental results are given for three bearing sizes: large button supported pads; medium pad size; and small line pivoted pads.

In chapter 7, excessive pad distortion for large pads is shown to be due to a size effect. Various modifications are proposed to curb the excessive pad distortion. The bearing characteristics are predicted numerically for a number of modifications. Finally, in chapter 8, overall conclusions are presented.

CHAPTER 2

FLUID MECHANICS

Introduction

2.1 Main Assumptions

2.2 Thrust Bearing Geometry and co-ordinate System

2.3 The Reynolds Equation

2.4 The Numerical Solution

2.5 Boundary Conditions

2.6 Pivoting

2.7 Tests for the Equations

2.8 Drawbacks

INTRODUCTION

Pressure generation in thrust pad bearings depends on several factors.. The sliding velocity, the shape of the oil film and the viscosity distribution in the film are three main factors. In practice, several other factors can influence pressure generation, such as surface roughness, oil supply conditions, the design of the mixing grooves between thrust pads, inertia forces and turbulence. In this chapter, a suitable form of the Reynolds equation is developed to model the pressure generation. The solution, using a numerical finite difference technique, is outlined. The shortcomings of the model and the numerical technique are also discussed.

2.1 Main Assumptions

The assumptions chosen render a numerically soluble form of the Reynolds equation. In addition to simplifying the complexity of the problem, they are designed to give quantitative as well as qualitative results. Many assumptions are standard {R2,R3} :

a) The height of the film h is very small compared to other dimensions.

b) The pressure does not vary across the film thickness.

c) No slip is allowed at the bearing/oil interfaces.

d) The lubricant is Newtonian.

e) Body forces arising from magnetic, gravitational and

inertia are neglected.

f) The lubricant is of constant density.

Since the temperature is a variable in the cross film direction (z), the viscosity is also expected to vary. In this analysis, the viscosity used in the z-direction has a parabolic profile, as well as the usual radial and circumferential variations, (this will be detailed in the energy chapter 3.)

For large thrust bearings, turbulence plays a significant role. The deviations from the laminar characteristics have been shown experimentally for 10 1/2 to 12 inch diameter bearings at high operating speeds {R4}. Three main theories have been presented {R5}. The theory based on that of Ng, Pan and Elrod is used to modify the Reynolds equation. This can account for the turbulence including turbulent inertia effects (without inertia no turbulence is possible). Thus a laminar flow regime (comprising Couette and Poiseille flow) is used to derive the equations, which are subsequently modified to include turbulence effects.

2.2 Thrust Bearing Geometry and Co-ordinate System

The sector shaped pads (Fig 2F-1) are most easily described in polar cylindrical co-ordinates. In practice the centre of revolution of the pads does not always coincide with that of the runner or support collar. The model presented does not allow for this. One major disadvantage is that the Reynolds equations become significantly more complex. On the other hand, it does not

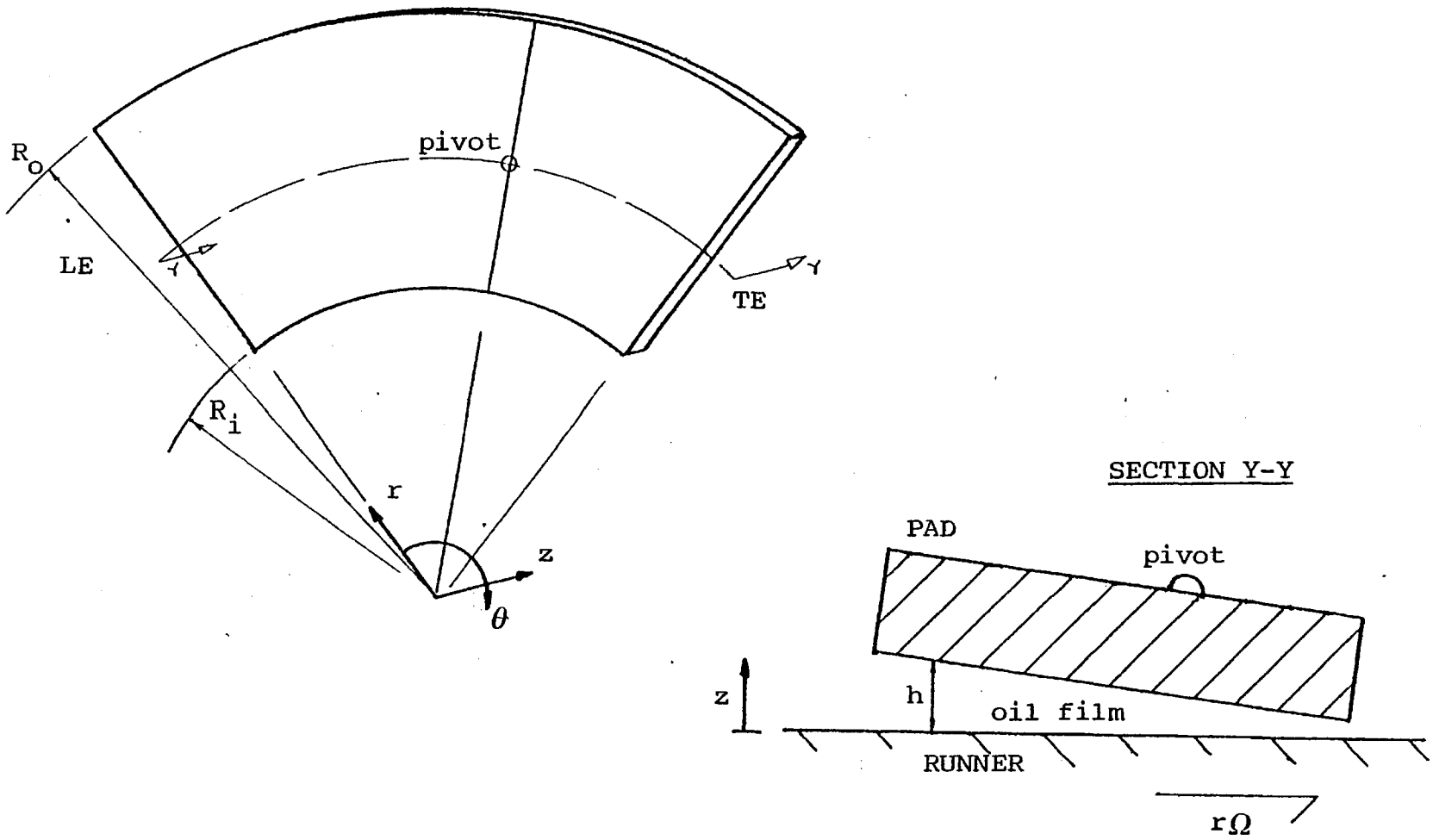

Figure 2F-1 Pad Co-ordinates

represent the general case and is therefore omitted.

Since the angles of inclination are small, the working area which the pad covers is assumed to be the plan area of the pad.

2.3 The Reynolds Equation

$$\frac{1}{r}\frac{\partial}{\partial\theta}\left(\frac{\partial p}{\partial\theta}\,\Gamma_1\right) + \frac{\partial}{\partial r}\left(r\,\frac{\partial p}{\partial r}\,\Gamma_1\right) = -r\,\frac{\partial}{\partial\theta}\left(\Gamma_2\right) \qquad \text{E2-1}$$

where $$\Gamma_2 = \int_0^h F_2\,dz \qquad \text{E2-2}$$

$$\Gamma_1 = \int_0^h F_1\,dz \qquad \text{E2-3}$$

and $$F_1 = \int_0^h \frac{z}{\mu}\,dz - \frac{I_2}{I_1}\int_0^z \frac{1}{\mu}\,dz \qquad \text{E2-4}$$

$$F_2 = z\frac{\int_0^h \frac{1}{\mu}\,dz}{I_1} \qquad \text{E2-5}$$

and $$I_1 = \int_0^h \frac{1}{\mu}\,dz \qquad \text{E2-6}$$

$$I_2 = \int_0^h \frac{z}{\mu}\,dz \qquad \text{E2-7}$$

The derivation may be found in Appendix A.

Several investigators have solved variations of the above equation. Pinkus and Sternlicht {R2} as well as Cameron {R3} give standard numerical solutions for pivoted pad thrust bearings using isoviscous theory. The solution of the Reynolds equation alone is, however, of academic interest. It is a good check for a more involved solution when heat generation and deflection are relatively small.

2.4 The Numerical Solution

The Reynolds equation E2-1 is an elliptic partial differential equation. A finite difference technique is employed for the solution. An irregular finite difference system is used for generality. A typical grid system is shown on Figure 2F-2.

The transformation of the Reynolds equation into a finite difference set of linear equations is given in Appendix B. It involves expressing the pressure at a node in terms of the pressures at its closest neighbours. An iterative process across the whole field is used to successively update pressure values until convergence. Where pressure values are known (or assumed) at particular nodes, they are excluded from the iterative process. A field of 'steady' values is eventually reached. The tolerance defining 'steady' is to be chosen so that a converged solution of the required accuracy is obtained for the whole field.

An optimised successive over relaxation factor is used - based on a technique developed by Brazier {R6}.The technique allows for a field of relaxation factors, one for each node, in order to minimise the number of iterations required for a converged solution.

The iterative method presented has certain advantages over a direct method of solution. A direct method does not allow for cavitation - nor any other floating boundary condition. The iterative method can allow for jacking nodes with relative simplicity, whereas the direct method requires the set up of a new

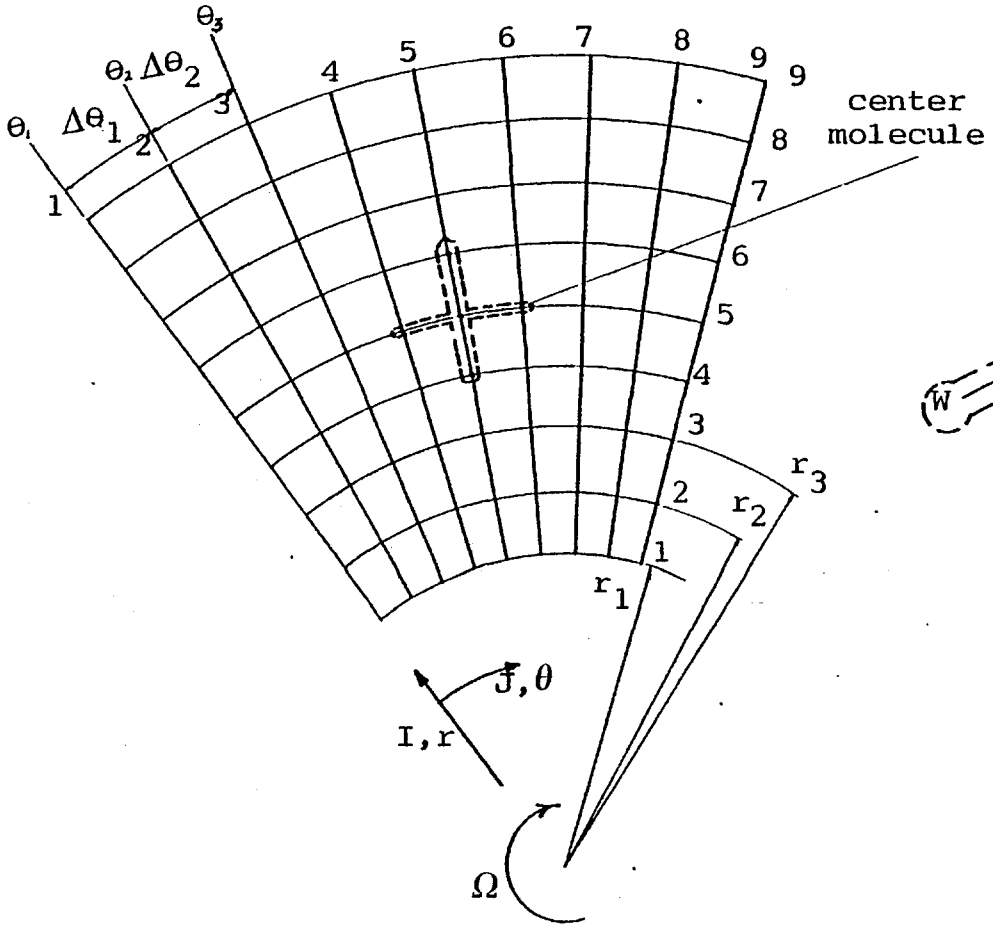

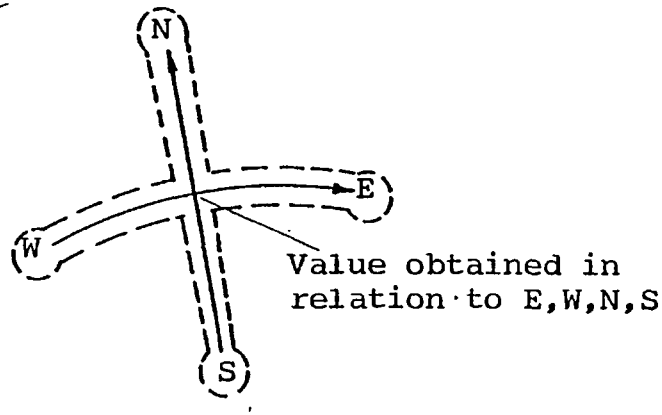

CENTER MOLECULE

Figure 2F-2 The Grid System

matrix of finite difference linear equations and its inversion,(see next section.)

2.5 Boundary Conditions

At the pad edges, zero pressure (gauge) is assumed. This is not strictly the case. Sternlicht {R2} describes several boundary effects, the most important of which is the ram effect at the entry region to the pad leading edge. The oil flow between pads has to be accurately modelled in order to solve the latter point. This is not part of the present analysis.

If jacking is included, the pressure at nodes where jacking is required is maintained at the relevant pressure throughout the numerical procedure.

Even though thrust bearings do not cavitate in general, they are liable to do so under high load due to deformation of the pads. A converging diverging wedge resulting from deformation can cause cavitation as is the case with journal bearings. The Reynolds boundary condition is adopted in this analysis, which proposes that both the pressure and its gradient equal zero at the cavitation boundary. This is close to what happens in reality. Pinkus and Sternlicht show experimental pressure curves for a cavitated bearing {R2}. A small negative pressure loop follows the main positive region. The Reynolds boundary condition represents a good approximation for computing purposes. It negelects the negative loop but determines the position where the pressure falls to zero.

The point at which cavitation occurs in bearings is important since this determines the extent of the positive pressure region.

2.6 Pivoting

The solution of the Reynolds equation alone is insufficient for tilting pad bearings. A hardened steel button is designed to support the pad, allowing it to tilt to any required angle. The moments generated by the oil pressure and shear stresses about the pivot must be zero in order for the pad to balance. This involves an iterative procedure where the pad inclination is varied - varying the film shape - until the generated pressure has zero moment about the pivot. Some thrust bearings are able to incline freely, whereas others are line pivoted (where inclination is allowed about only one axis.) Thus the generalised case is for inclination about two axes. The amount by which the inclination is varied is non-linear and depends on the size, geometry and loading condition of the bearing. A technique has been developed to take account of the non-linearity. For a certain initial inclination, the centre of pressure (where the moments are zero) does not coincide with the actual pivot position. The normalised errors in the X and Y axes (Fig 2F-3) are δx_i and δy_i respectively. If the normalised errors are plotted ($\delta x_i, \delta y_i$), it may be deduced that the inclination should vary so as to position ($\delta x_i, \delta y_i$) close to the curve $|\delta y| = |\delta x|$ .This allows the use of differing increments of inclination in X and Y. The ratio is decided in the X direction by

$$X_{inc\ new} = X_{inc\ old} \left(1 - R_f \left(\delta x^{pow} \right) \right) \qquad E2\text{-}8$$

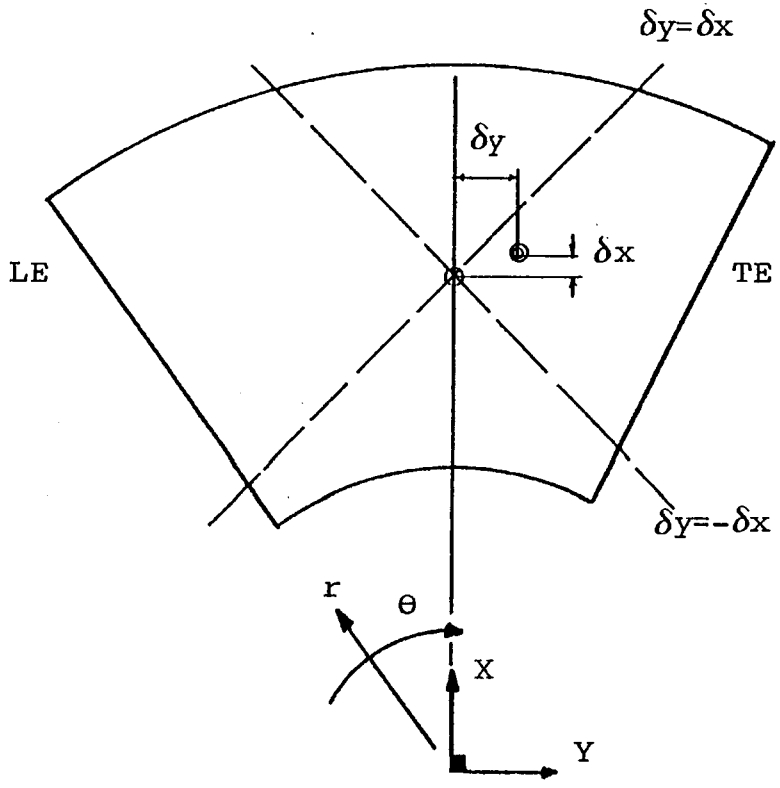

◎ center of pressure

○ pivot position

Figure 2F-3 Cartesian Co-ordinates

where

R_f is an additional relaxation factor for fine tuning

$$pow = (\delta x^2 + \delta y^2)/\delta x \qquad \text{E2-9}$$

X_{inc} is a measure of inclination eg angle of inlet to outlet film thickness

Equations E2-8 and E2-9 result in balancing the normalised errors, along the $|\delta y| = |\delta x|$ line.

2.7 Tests for the Equations

Results for the solution of the Reynolds equation are quoted by Cameron {R3} for rectangular plane pads. The rectangular pad can be simulated using a very small pad angle and large radii. The non-dimensional solutions are presented in Figure 2F-4. The results are in good agreement with Cameron {R3}. The values are quoted for a 16x16 mesh system (equally spaced).

The results of further tests to show the accuracy of the solution are presented (Fig 2F-5). The solution of the 8x8 mesh system has a maximum of 5% differnce from that of 32x32 mesh. The difference between the 4x4 and 32x32 mesh is about 30%. The square of the normalised mesh length (either in r or in θ , as specified) is plotted against non-dimesional load (Fig 2F-6). The

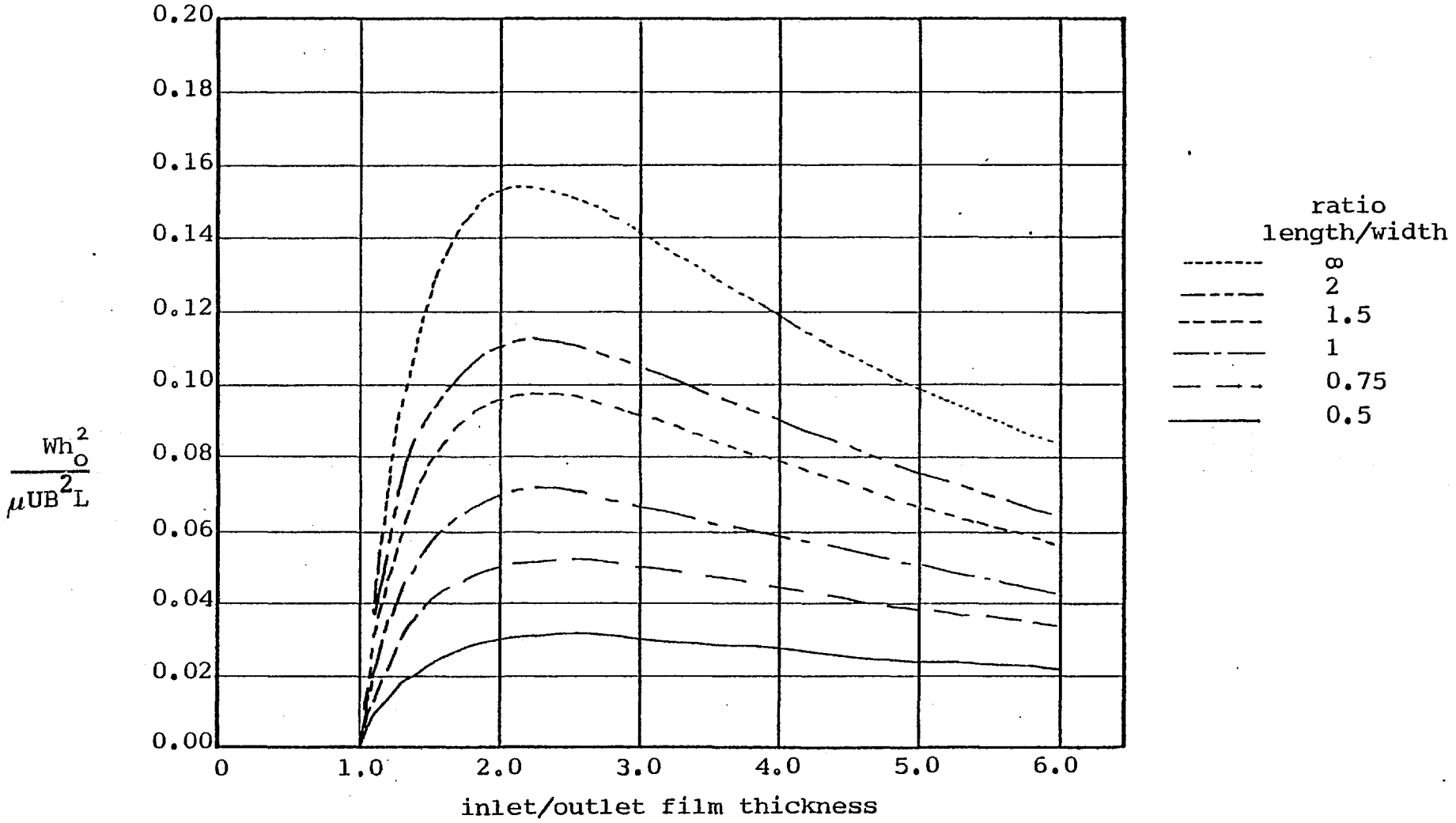

Figure 2F-4 Non-dimensional Load Capacity Versus Inlet/Outlet Film Thickness for Isoviscous Plane Rectangular Thrust Bearings

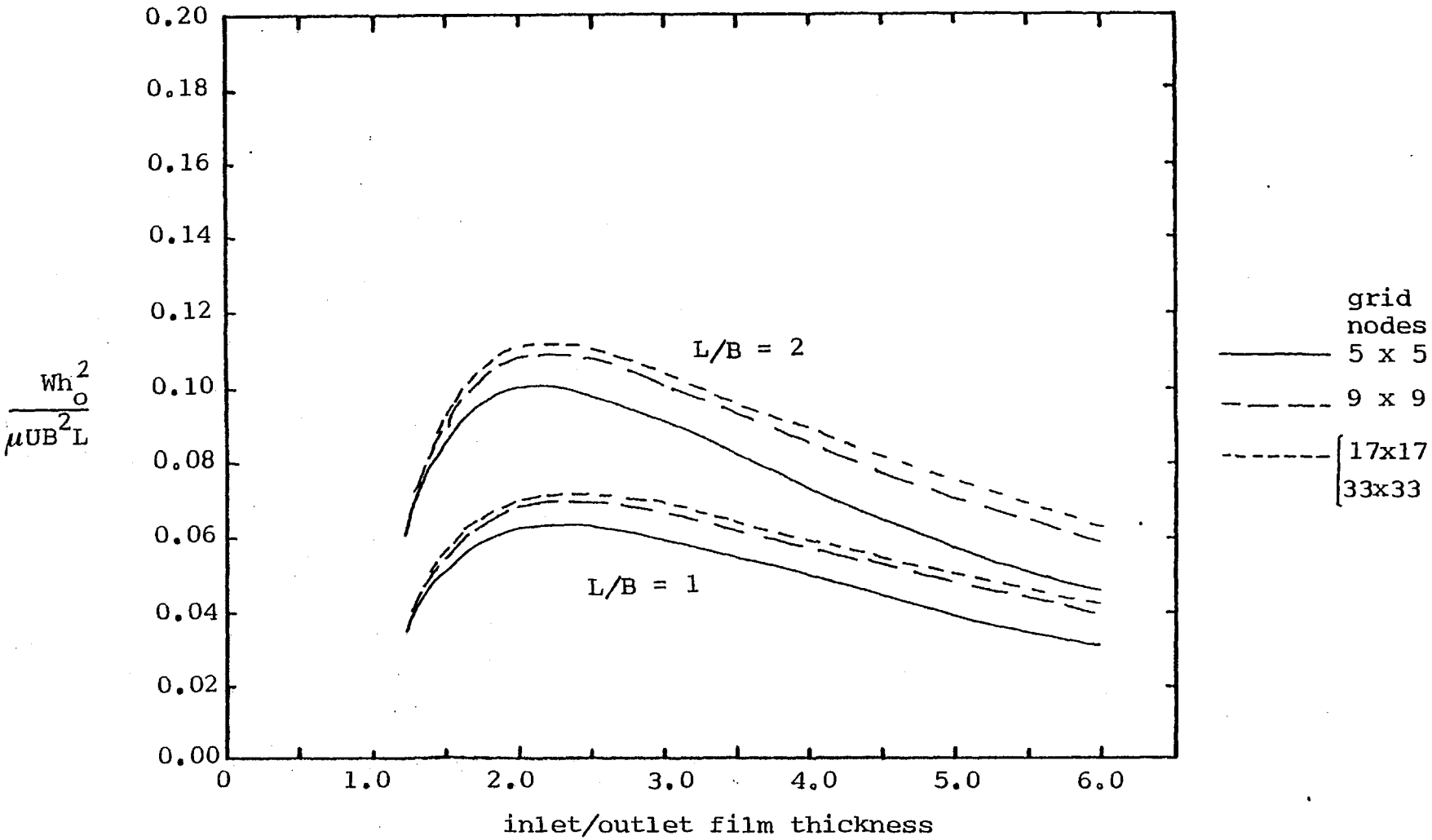

Figure 2F-5 Non-dimensional Load Capacity Versus Inlet/Outlet Film Thickness for Plane Rectangular Thrust Bearings

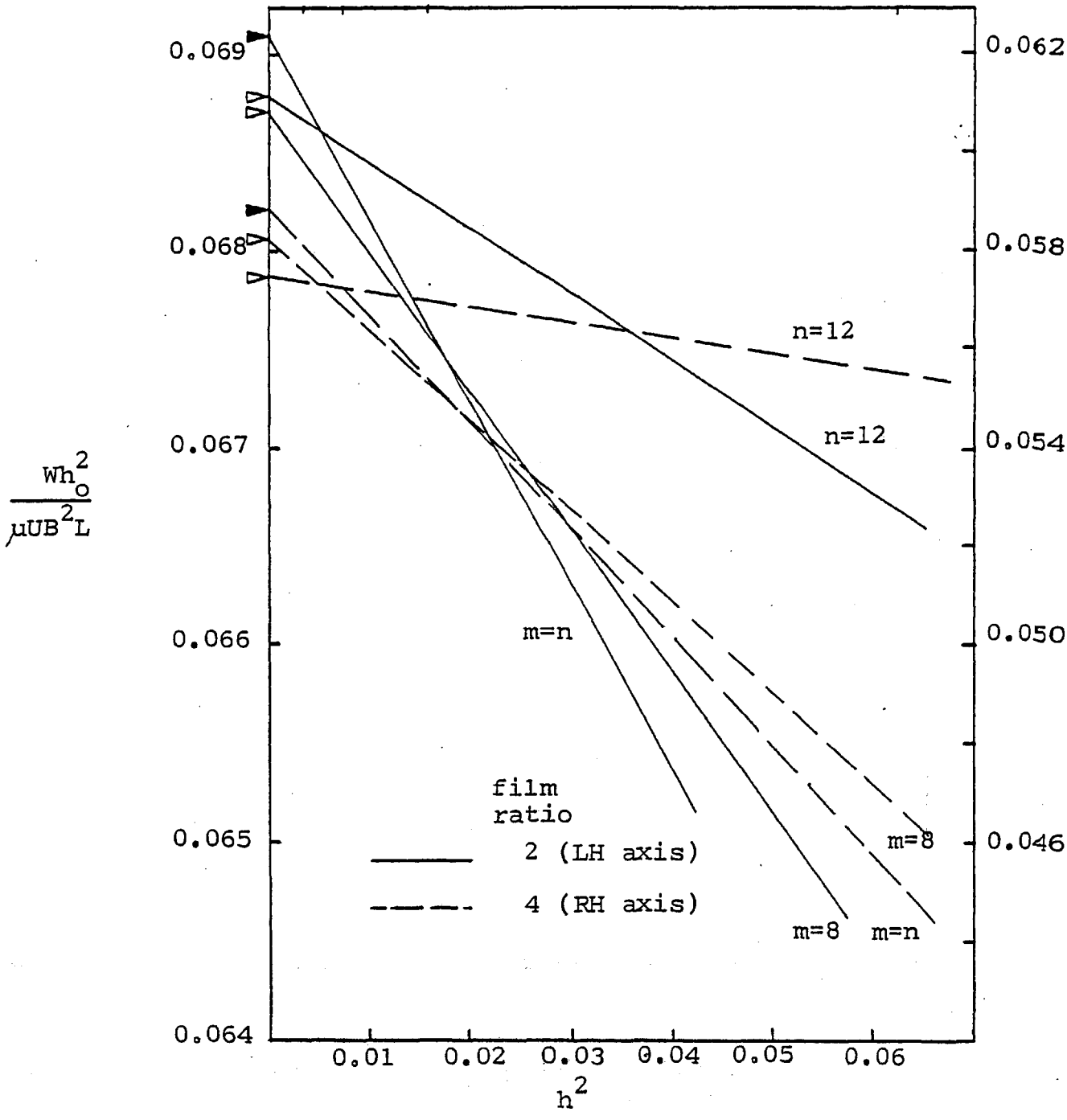

Figure 2F-6 Non-dimensional Load Versus h^2 (the square of the mesh length)

number of mesh lengths is varied systematically (in the radial direction alone keeping a fixed number (n=12) in the circumferential direction, vice versa (m=8), or both together: m=n). Straight line curves are obtained. This indicates the consistency of the numerical technique. Where $h^2=0$, a value is extrapolated for the infinite mesh size. It is noted that the extrapolated value for the load is different for the three cases. This is expected, since if a grid is infinite in one direction but not in the other an error results. It is also significant to note that the variation of the mesh size in the circumferential direction (m=8 curves) has a more pronounced effect than in the radial direction (n=12 curves). This results in steeper gradients for the circumferential variation in the number of nodes.

In order to verify the Brazier technique {R6} a convergence test has been applied. The variation of the middle node pressure for successive iterations was observed for one test case using the Brazier successive overrelaxation. A multiplying factor ranging from 0.6 to 1.2 has then been multiplied by the Brazier factor and used for other runs. The rate of convergence is found to be optimum with a factor of one multiplying Brazier's factor (Fig 2F-7).

2.8 Drawbacks

2.8.1 Model

The main drawback is considered to be the inlet boundary condition. Experimental streamlines of the lubricant flow at the

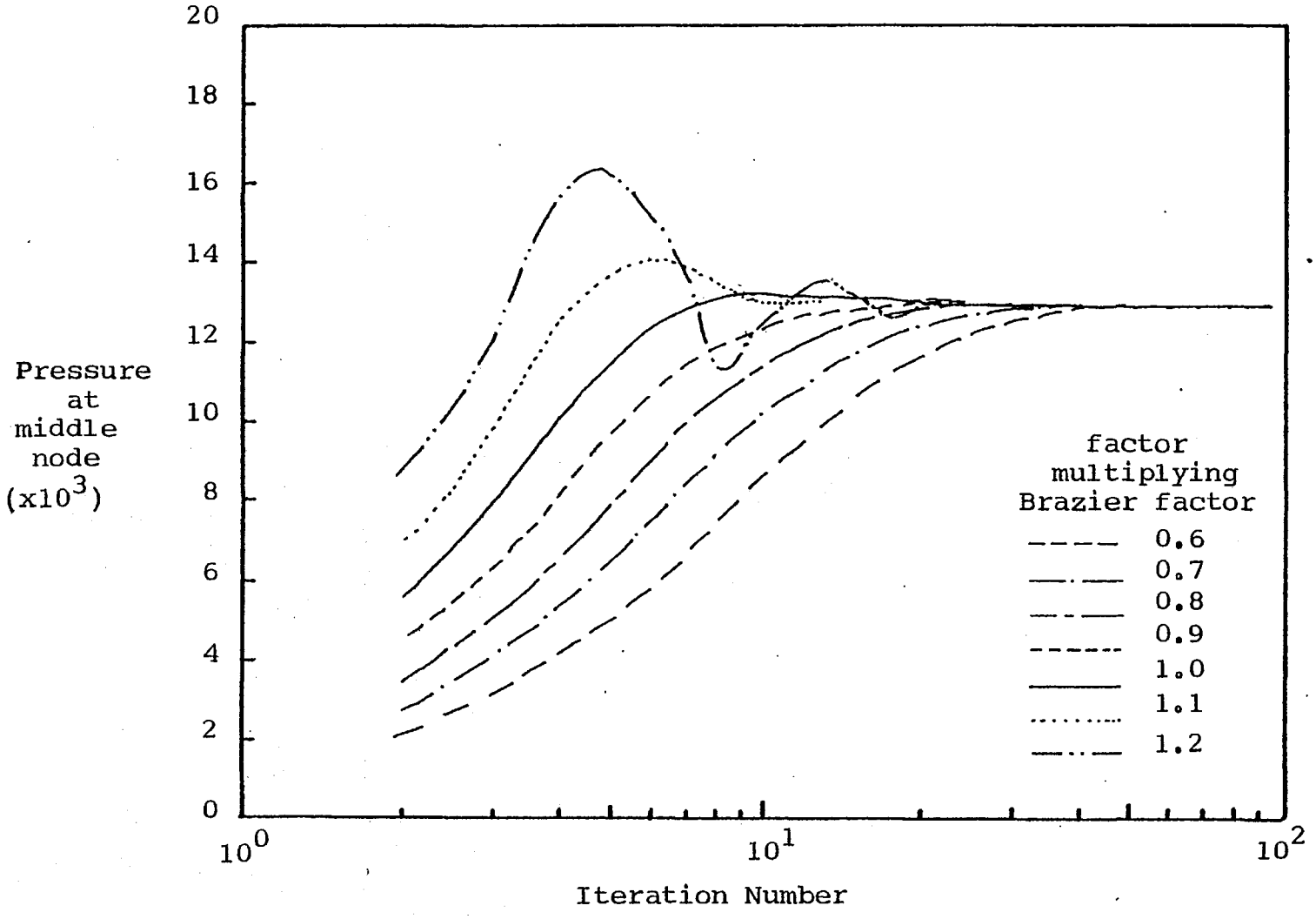

Figure 2F-7 Middle Node Pressure Versus Number of Iterations for the Brazier SOR Factor Multiplied by Different Factors

pad leading edge indicate that the pads may support a load and tilt to form a converging wedge due to the moment exerted by the lubricant ram effect, once a load has been applied {R2}.

The method cannot predict details of striation in the cavitated film region. These depend on phenomena such as surface tension which are not included in the analysis.

2.8.2 Numerical Technique

The present technique assumes a film shape and evaluates the pressure field, hence the bearing load. In practice it is the load rather than the film thickness that is specified. Thus more iterations are required since the pivot film thickness has to be varied until a suitable load is obtained. This will be further discussed in chapter 5.

CHAPTER 3

ENERGY CONSIDERATIONS

Introdouction

3.1 Heat Transfer in The Oil Film

3.1.1 Model

3.1.2 Assumptions

3.1.3 Boundary Conditions

3.1.4 Tests

3.2 Flow of Heat in The Pad

3.2.1 Model

3.2.2 Assumptions

3.2.3 Boundary Conditions

3.2.4 Tests

3.3 Flow of Heat in The Runner

3.3.1 Model

3.3.2 Assumptions

3.3.3 Boundary Conditions

3.4 The Total Energy Equation Solution

3.4.1 Surface Heat Transfer Coefficients

3.4.2 Hot Oil Carry Over and Runner Temperature

3.4.3 Bearing Oil Temperature

3.5 Numerical Considerations

Introduction

Observations concerning the ability of parallel surface sliders to sustain a load {R7} have prompted reasearch into thermodynamics of hydrodynamic thrust bearings. In 1941, Christopherson {R8} attempted a thermohydrodynamic analysis of journal bearings solving for both pressure and temperature using the 'relaxation' technique. This was followed by several investigations concerning thermal effects on hydrodynamic lubrication {R9,R10,R11,R12,R13,R14}. The oil film was viewed either in plan or in elevation as a three-dimensional model was too compilcated to solve at the time (nevertheless, a three-dimensional model was put forward in 1969 by Hahn and Kettleborough {R9}.) When viewed in elevation, an infinite bearing width was assumed {R14,R13,R10,R9}. When viewed in plan, a constant temperature through the lubricant film thickness was assumed {R15,R16,R17}. In 1957, Sternlicht {R18} showed that isoviscous theory is not a bad approximation, provided the lubricant film thicknesses are large. For small thicknesses the bearing characteristics are markedly altered by the inclusion of thermal effects.

In 1965, Ettles {R19} compared the influence of various factors on the load capacity of thrust bearings. For a typical 'parallel' surface thrust bearing the ratios of distortion to viscosity variation to density variation effects were given as 400:-20:1. At higher film thicknesses, the variation of viscosity

becomes dominant. In 1968, Castelli and Malanoski {R16} developed a solution proceedure for thrust bearings which included a comprehensive energy model. The effects of heat conduction via pad and rotor were included. The main drawback was that the temperature was assumed constant through the lubricant film thickness. An 'up-wind' finite difference scheme was employed to solve the energy equation. This scheme provided greater stability and hence better convergence for the iterative solution. In addition, the flows in and out of a particular computing cell (control volume) were balanced (see section 3.1.1). This prevented the formation of heat sources or sinks in the iterative process. In 1969, Advani {R20} confirmed the importance of viscosity variations from a design point of view. He also added the hot oil carryover in his analysis (prediction of oil film inlet temperature based on oil exit temperature from previous pad). He obtained accurate temperature rise predictions compared to experiment. The prediction of absolute temperature at inlet remained unsatisfactory.

Neal {1970-R21} showed that an isoviscous theory is weak at determining an effective viscosity if applied to compute the oil temperature rise. The idea of effective viscosity is very useful from a rapid design point of view, and many have attempted to evaluate it {R22}.

Stokes {1972-R23} attempted a comprehensive journal bearing analysis assuming the temperature has a parabolic-(quadratic) temperature profile through the oil film thickness. In fact, only

the mean temperature through the oil film was used to determine the heat convected in the other two-directions (heat convected$_x$=$m_x c T_{mean}$). This is, nevertheless, invaluable because a good estimate of the heat fluxes conducted to the upper and lower surfaces is obtained. The problem of how to determine a surface heat transfer coefficient at the solid outer surfaces is highlighted.

In 1973, Ezzat and Rohde {R24} presented a fully three-dimensional energy equation. Conduction in the stationery surface was also included. It was concluded that bearing performance - ignoring pad deflection - is dominated by cross-film temperature. In 1975, Rohde and Kong Ping Oh {R25} excluded the conduction terms in the direction of flow within the lubricant. Comparing results with Ezzat and Rohde, it was concluded that these terms have a negligible effect on the solution. In 1974, Heubner {R26} developed a three-dimensional model, including conduction to the stationery as well as the moving surfaces. The load capacity results were very similar to the case where the solid surfaces were assumed adiabatic. Thus, a much faster, yet accurate, routine can be used provided deflection is negligible. It was also concluded that bearing performance is strongly dominated by the type of lubricant, its inlet temperature, bearing speed, and the inlet to outlet film thickness ratio.

A major area of uncertainty is the heat transfer effects between pads. Ettles and Cameron {1968,R27} studied hot oil

carryover for a parallel surface bearing. They concluded that 60 - 95% of oil entering the leading edge of the pad oil film comes from the previous pad oil film. They also concluded that the thermal boundary layer developing in the inter pad cavity was an order of magnitude thinner than the velocity boundary layer. The hot oil carryover factor was coined to represent the film entry temperature in relation to the film exit temperature and the supply temperature (see section 3.1.3). The inlet oil film temperature was found to be largely dependent on the rotor temperature. Ettles {1968,R28} attempted a two-dimensional theorectical analysis of flow in a bearing groove - typical of the gap between successive pads. He found that recirculation - a vortex flow - in the groove is an order of magnitude higher than in the oil film. The heat transfer to the moving surface was found to be greater than to the stationery surfaces. The analysis did not include turbulence. It predicted hot oil carryover factors similar to those obtained experimentally {R27}. A comparison between different sizes, geometries and oil conditions was summarised by Ettles {1970,R29}, and hot oil carryover curves obtained for design purposes. Speed and film wedge ratio were taken into account. In 1979, Ettles {R30} gave a modified form of the oil carryover factor versus sliding speed, in which pad spacing was also taken into account.

In this chapter, a solution method is proposed for the total energy balance. It involves a three-dimensional treatment of conduction in the pad and runner. It also stipulates a three-dimensional variation of temperature in the oil film. The

cross-film temperature profile is limited to a parabola. Hot oil carryover theory is used to determine the 'shape' of the leading edge temperature profile. The method requires the oil bath temperature and heat transfer coefficients for the back faces of the pad and runner, but allows the runner temperature distribution to be determined. It also allows for the ratio of heat conducted to heat convected, as well as the proportion of heat conducted to runner relative to that conducted to pad to be determined.

3.1 Heat Transfer in The Oil Film

3.1.1 Model

Since heat transfer in the oil film is only one part of a comprehensive analysis to model thrust pad bearings, almost all previous such studies have neglected temperature variation through the lubricant film thickness. There is no justification for this simplification, but it does allow a solution for the whole problem and, in numerical terms, it permits an order of magnitude saving in computer time - besides other peripheral benefits in storage and analysis. A serious drawback to neglecting temperature variations through the film is that the effects of the heat conducted away to bearing solids on the performance of the oil film have to be estimated. A three-dimensional solution, however, yields the temperature gradients normal to the bearing solids. Hence, an accurate estimate of the temperature distribution in the solids can be obtained. The distribution of viscosity is in turn obtained in

three dimensions.

Since the oil film varies in thickness, a fully three-dimensional representation presents certain complexities in the cross-film direction. Ettles {1981,R31} presented a two dimensional solution, viewing the film in elevation. A distorted grid was used. The treatment of shear forces and flow into a control volume is more complicated than with a polar or cartesian mesh. If the same method is to be applied considering the breadth of the film, a large number of nodes may be necessary (at a vast expense in computer time).

In order to avoid a trapezoidal mesh system as used by Ettles {R31} a parabolic temperature profile may be assumed through the film thickness. A parabola will allow different temperature gradients normal to the upper and lower film surfaces. Previous solutions {R25,R31} show that temperature profiles are largely parabolic in nature (that is containing one turning point).

A typical grid system is shown, Fig 3F-1 (Note that grid spacing is irregular in the r and θ directions). Only three surfaces are required through the film to represent a quadratic temperature distribution. The temperature at the upper and lower surfaces for the grid system are assumed known (or may be determined subsequently). Thus, only the middle node value (K=2) remains unknown. At every node position (I,J), a control volume is set up to encompass three nodes across the film. A typical volume is shown in Fig 3F-2.

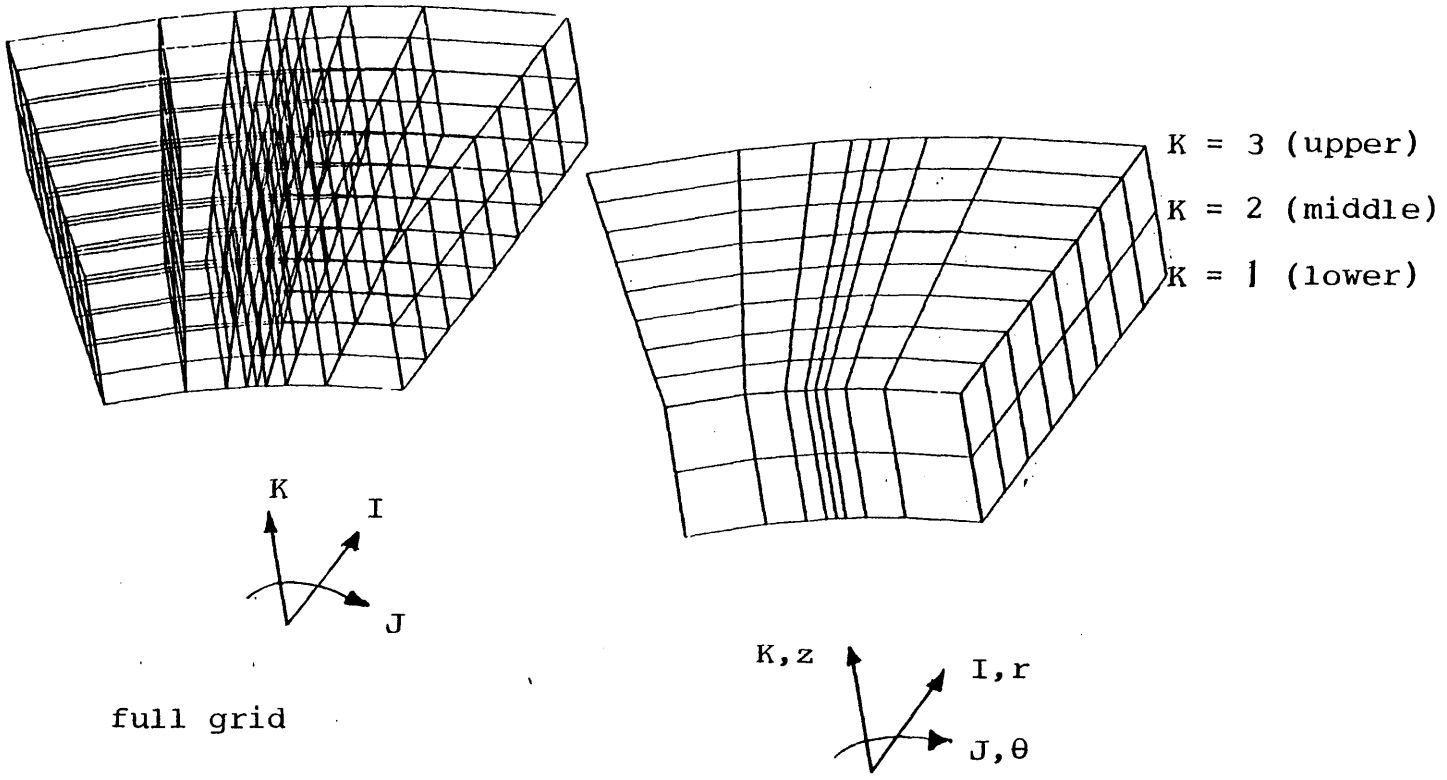

Figure 3F-1 Grid System for Oil Film

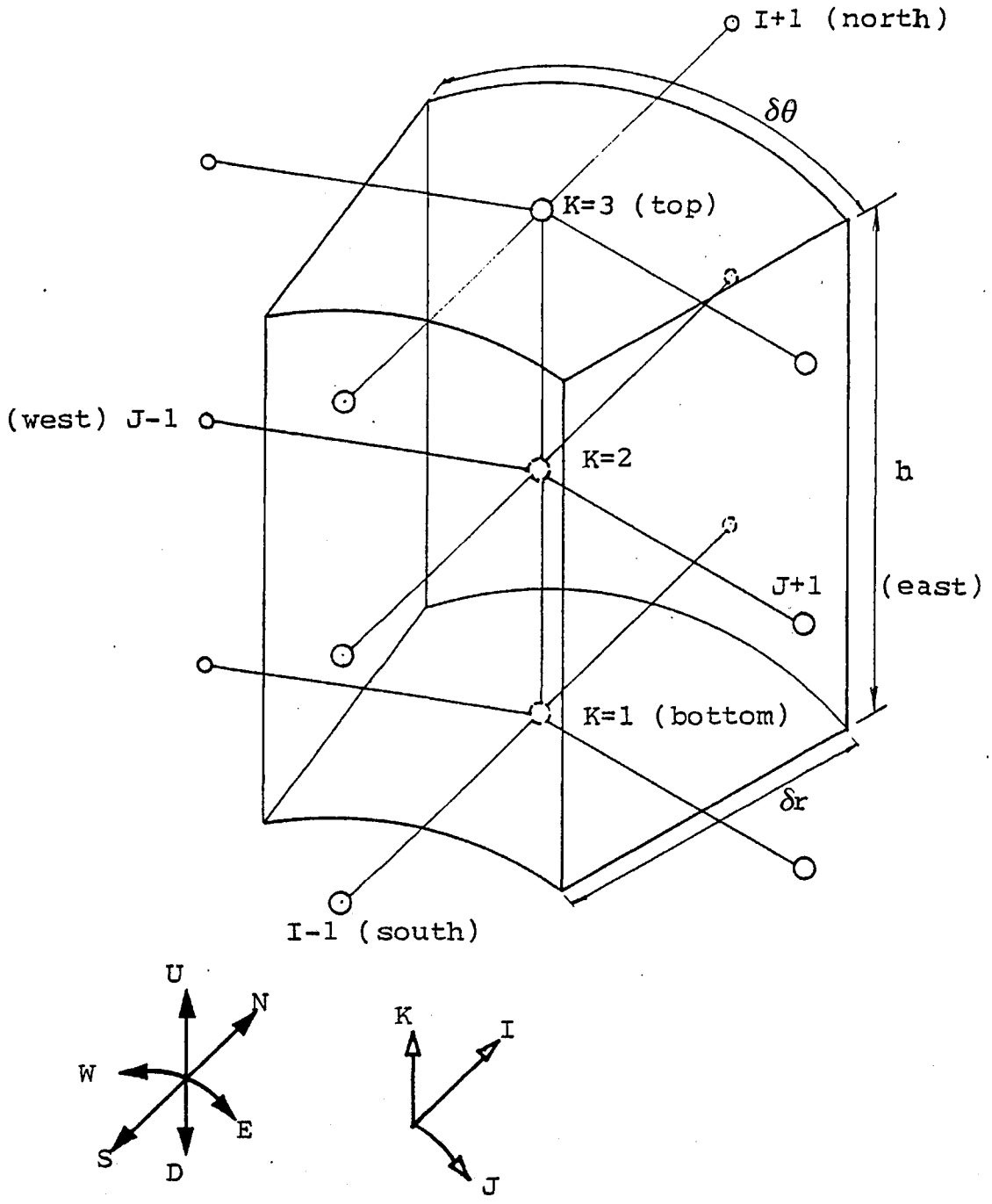

Figure 3F-2 A typical Oil Film Control Volume

The energy equation (first law of thermodynamics) applied to the control volume is: Sum of the heat flux into the control volume (conduction and convection) + flow work done on the control volume + work done within the control volume by internal stresses = rate of increase of energy of the contents of the control volume + heat flow out of the control volume.

a) The convected heat into and out of the control volume is calculated in an up-wind difference scheme {R16}. In such a scheme, the temperature assigned to a flow crossing a control volume boundary is the temperature at nodes upstream or 'up-wind'. For example the flux crossing the West face of the control volume (Fig 3F-2) can have two possible directions. If the flow is in the positive coordinate direction, the temperature profile assigned is the parabola between the stations at J-1, that is (I,J-1,1), (I,J-1,2) and (I,J-1,3). If the flow is negative, then the upwind profile is assumed, which is the parabola determined by (I,J,1), (I,J,2) and (I,J,3). The velocity profiles are obtained from the solution of the Reynolds equation as discussed in Chapter 2.

b) The stresses at top and bottom faces of the control volume can be evaluated from the velocity profiles

$$\tau_\theta = \mu \frac{\partial u}{\partial z} \qquad ; \qquad \tau_r = \mu \frac{\partial v}{\partial z}$$

c) Since the pressure is assumed constant in the cross-film direction, the flow work is the product of the pressure on a certain face (E,W,N,S) and the relevant flow across that face.

The convected heat flux to or from the control volume across

any face is evaluated as $\rho c \int_0^h v T \delta z \delta l$. v represents the velocity in the required direction (r or Θ). The viscosity inverse ($1/\mu$) has been assumed to have a parabolic profile,

$$1/\mu_{ij} = a_{ij} z^2 + b_{ij} z + c_{ij} \qquad \text{E3-1}$$

and the temperature another parabolic profile,

$$T_{ij} = d_{ij} z^2 + e_{ij} z + f_{ij} \qquad \text{E3-2}$$

Hence, the convected flux across the south face can be given as

$$\begin{aligned} Q_s = \rho c \delta \theta r \frac{\partial p}{\partial r} \Bigg\{ & d\left[\frac{ah^7}{28} + \frac{bh^6}{18} + \frac{ch^5}{10} - \frac{I_2}{I_1}\left(\frac{ah^6}{18} + \frac{bh^5}{10} + \frac{ch^4}{4}\right)\right] \\ & + e\left[\frac{ah^6}{24} + \frac{bh^5}{15} + \frac{ch^4}{8} - \frac{I_2}{I_1}\left(\frac{ah^5}{15} + \frac{bh^4}{8} + \frac{ch^3}{3}\right)\right] \\ & + f\left[\frac{ah^5}{20} + \frac{bh^4}{12} + \frac{ch^3}{6} - \frac{I_2}{I_1}\left(\frac{ah^4}{12} + \frac{bh^3}{6} + \frac{ch^2}{2}\right)\right] \Bigg\} \end{aligned} \qquad \text{E3-3}$$

$$I_1 = \int_0^h \frac{1}{\mu} dz = \frac{ah^3}{3} + \frac{bh^2}{2} + ch \qquad \text{E3-4}$$

$$I_2 = \int_0^h \frac{z}{\mu} dz = \frac{ah^4}{4} + \frac{bh^3}{3} + \frac{ch^2}{2} \qquad \text{E3-5}$$

Details of the integration for the convected flows on all faces as well as the summation of all terms in the energy equation are given in Appendix C.

As far as the flow of heat due to conduction is concerned, only cross-film conduction is allowed for (for reasons given in the introduction). The middle node temperature previously obtained (or

guessed) is used to determine the conduction fluxes at the top and bottom surfaces of the control volume, that is, using the parabolic profile obtained during the previous iterative sweep. Thus, at every control volume the middle node temperature only is updated. The process is iterative.

Consideration of convection in the z-direction is not required as this happens within the control volume (top and bottom surfaces being impermeable). Jacking grooves are an exception and will be discussed later. (The number of nodes involved in the iteration process is the same as for the case of uniform temperature in the z - direction).

Castelli and Malanoski {R16} have shown that the net flow of oil into a control volume must be zero, or else a heat source/sink is created due to the excess flow which continually accumulates flux within the control volume on each pass of an iterative scheme. The flows crossing each boundary are subject to truncation error and will not sum to zero. The net flow, nominally zero, is typically 2% of total flow into the control volume. To obtain flow balance, the flows may be multiplied by a correction factor

$$q_{in,new} = (1 + \lambda) \, q_{in,old} \qquad \text{E3-6}$$

$$q_{out,new} = (1 - \lambda) \, q_{out,old} \qquad \text{E3-7}$$

$$\text{where} \quad \lambda = (\varphi - 1)/(\varphi + 1) \qquad \text{E3-8}$$

$$\varphi = q_{out,old}/q_{in,old} \qquad \text{E3-9}$$

Thus ensuring $q_{in,new} = q_{out,new}$ E3-10

The factor λ is calculated for each control volume, and subsequently applied for incoming and outgoing flows.

3.1.2 Assumptions

In addition to assumptions made for the Reynolds equation in Chapter 2, the main assumptions for the energy equation are:

a) Temperature varies parabolically across the oil film,

b) Viscosity varies with temperature only,

c) Conduction is significant across the oil film thickness only,

d) Specific heat capacity is constant for the oil,

e) Thermal conductivity of the oil is constant,

f) Steady state effects only are considered.

3.1.3 Boundary Conditions

In determining the mid-plane temperature, the lubricant temperature at the upper and lower boundaries (K=1 and K=3 in Fig 3F-2) are assumed to be known values. The direction of individual flows into and out of each control volume is determined from the solutions of the Reynolds equation. Each control volume is bounded by six faces which will be denoted as E(east); W(west); N(north); S(south); U(up); D(down). Except where jacking takes place, flow across the U and D faces is zero since the surfaces are impermeable.

A switching array is used to indicate the direction of flow for every face for all the control volumes. Appendix C details the calculation of flows.

In the pad leading edge control volumes, some or all of the flows at the leading edge face are incoming flows. For both incoming and outgoing flows (in the θ direction), the temperatures at K=1 and K=3 are taken to be those of the solid faces (U and D) at that control volume. The middle node temperature (K=2) is determined using the temperature gradient ($\partial T/\partial z$) from hot oil carryover theory. Ettles {R31} gave the assumed general form of temperature profile of the oil approaching the leading edge - see Fig 3F-3. He concluded that the mean entry temperature within the entry stream tube is close to the rotor surface temperature. The approach temperature profile is taken to

be linear and the temperature drop ΔT (see Fig 3F-3) is taken as

$$\Delta T=(T_r-T_{amb})(1-k_h)h_1/h_{min} \qquad \text{E3-11}$$

where k_h = hot oil carryover factor {R27,R28}

T_r = rotor temperature

T_{amb} = Oil bath tempreature

h_1/h_{min} = Inlet/minimum film thickness ratio

Ettles {R31} emphasized that it is the rotor surface temperature calculation which is important, as pointed out by Vohr {R32}. Thus, the middle node temperature is defined in this work as

$$T_{K=2,entry} = T_{K=1} + \Delta T/2 \qquad \text{E3-12}$$

where $T_{K=1}$ is the rotor surface temperature.

At the upper surface (K=3) there are two possibilities:

a) That $T_{K=3}$ is defined

$$T_{K=3,entry} = T_{K=1} + \Delta T \qquad \text{E3-13}$$

or

b) That $T_{K=3,entry} = T_{K=3}$ at (I,J) E3-14

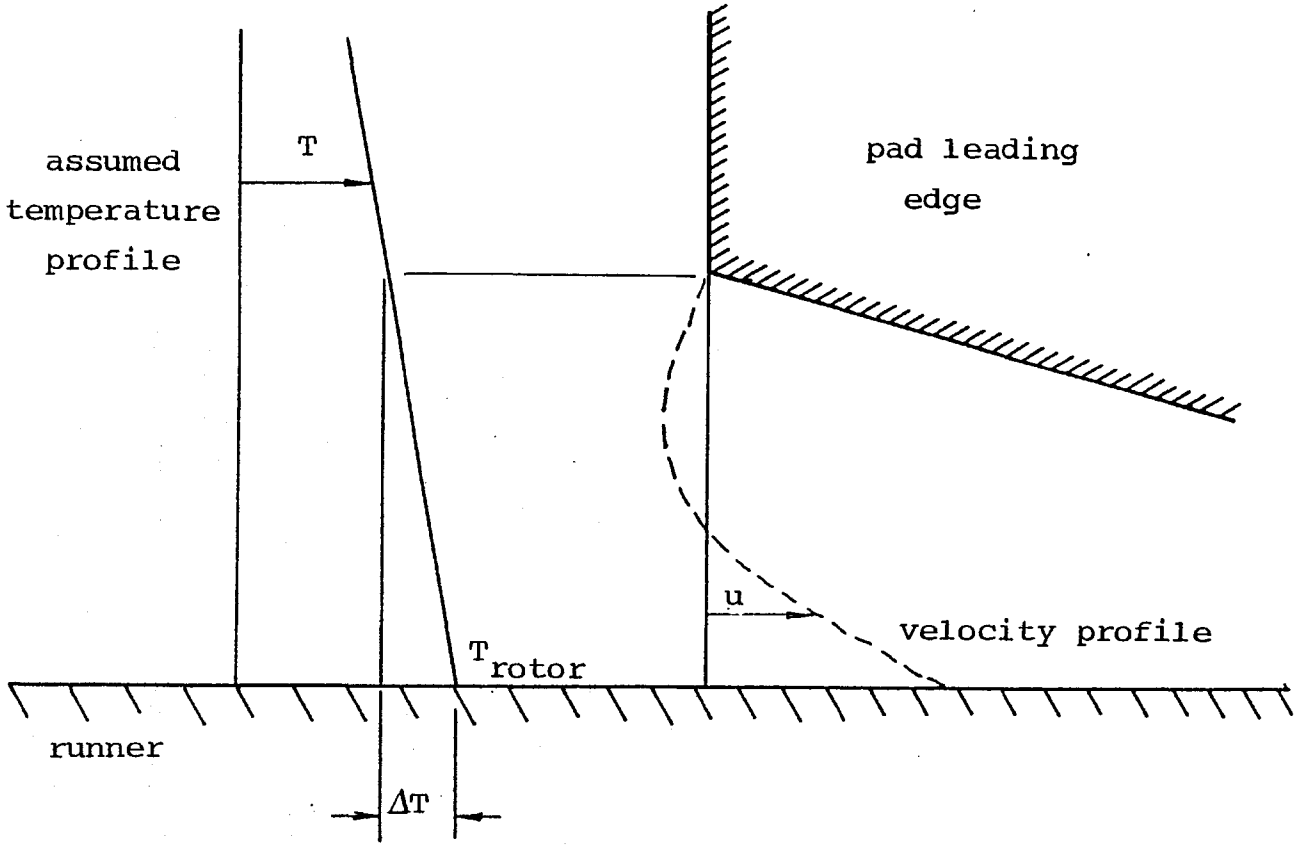

Figure 3F-3 The Approach Temperature Profile

The second is adopted. It is thought that since recirculation takes place at the inlet as well as conduction to the upper face, the temperature of the solid face is more representative of the back flow region - Fig 3F-4. It is noted that this definition of inlet temperature profile does not depend directly on the exit temperature. This allows considerable flexibility for solutions, in that the varying hot oil carryover factor does not cause a major boundary condition variation at the film inlet. The determinations of the rotor and pad surface temperatures will be discussed later in the relevant sections.

For incoming flows, at faces at the sides or edges of the flow field, a similar procedure is adopted. The difference is that at other faces the uniform temperature profile of $T = T_{amb}$ is assumed. This is an oversimplification of the real condition. The design of the bearing assembly will influence this choice. It is thought unlikely that oil will enter at faces other than the leading edge - especially for the self lubricating thrust pad bearing arrangements.

For outgoing flows no difficulty is presented. The up-wind difference scheme dictates that the characteristics of an outgoing flow are those from which it orignates. Thus, the temperature profile of an outgoing flow is taken to be that of the control volume from which it originates.

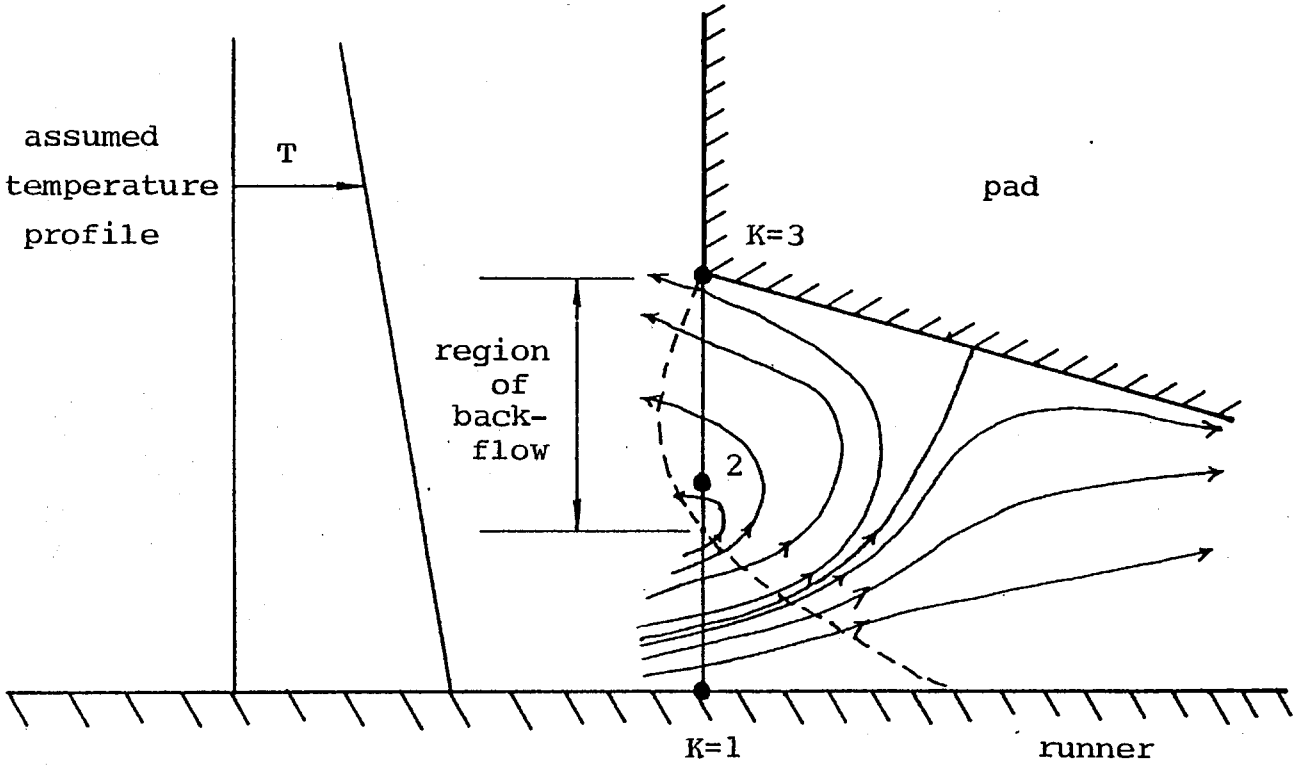

Figure 3F-4 Flow Pattern at the Leading Edge

Jacking is treated as a flow through a port in the control volume (the port being U). The amount of flow through the port can be determined as the net flow resulting from summing all other flows (E, W, N, S) into the control volume, designating outgoing flows as negative incoming flows. If the jacking flow is incoming, it is considered to have a constant temperature - that of the supply. If the jacking flow is outgoing (that is the pressure in the oil film is higher than the supply pressure) a choice is available. It is difficult to postulate what the temperature profile for the temperature is, but it will be in the range of the temperature profile for the jacking control volume. In this study, an outflow to the jacking port is given the middle node temperature value, (for simplicity). Experimentation and further analysis are necessary to determine such a temperature, perhaps requiring a fully three-dimensional analysis for the energy in the oil film.

Special 'floating' boundary conditions (the Reynolds boundary conditions) are required where cavitation takes place. Cavitation is allowed for where the fluid film pressure falls below zero gauge, inside the pad boundaries, by setting the pressure to zero gauge during the solution of the Reynolds equation (see Chapter 2). The flow rate of lubricant, beyond the cavitation boundary, remains constant with negligible side leakage. Streamers develop to make up the extra volume in the cavitation region. Account must be taken of all the above factors in order to correctly predict the temperature field beyond the cavitation boundary.

An infinite number of streamers are used to model the two phase flow. No attempt is made to include surface tension effects or to determine the actual development of streamers. Thus, it is the ratio of, gas to liquid for each control volume that is determined.

A switching array is set up to store the position of nodes 'at' the cavitation boundary (during Reynolds calculations). The circumferential flow rates are evaluated. These are then taken as the effective flow rates for nodes beyond the cavitation boundary at the same radii. The volume ratio for control volumes beyond the cavitation boundary is taken as the ratio of flow at the cavitation boundary to local Couette flow in absence of cavitation. This ratio is used to scale down the conduction heat transfer across the thickness of the oil film, as well as the shear work done by the runner face. The convection and flow work terms are also modified to use the cavitation boundary flow at the same radius.

3.1.4 Tests

a) The omission of the flow work term gives a useful simplification in analytical work. The temperature variation in the transverse direction (Fig 3F-5) for a thin (width<<length) rectangular pad is small. Using the assumption of constant temperature across the oil film thickness, the heat balance equation reduces to (in cartesian co-ordinates)

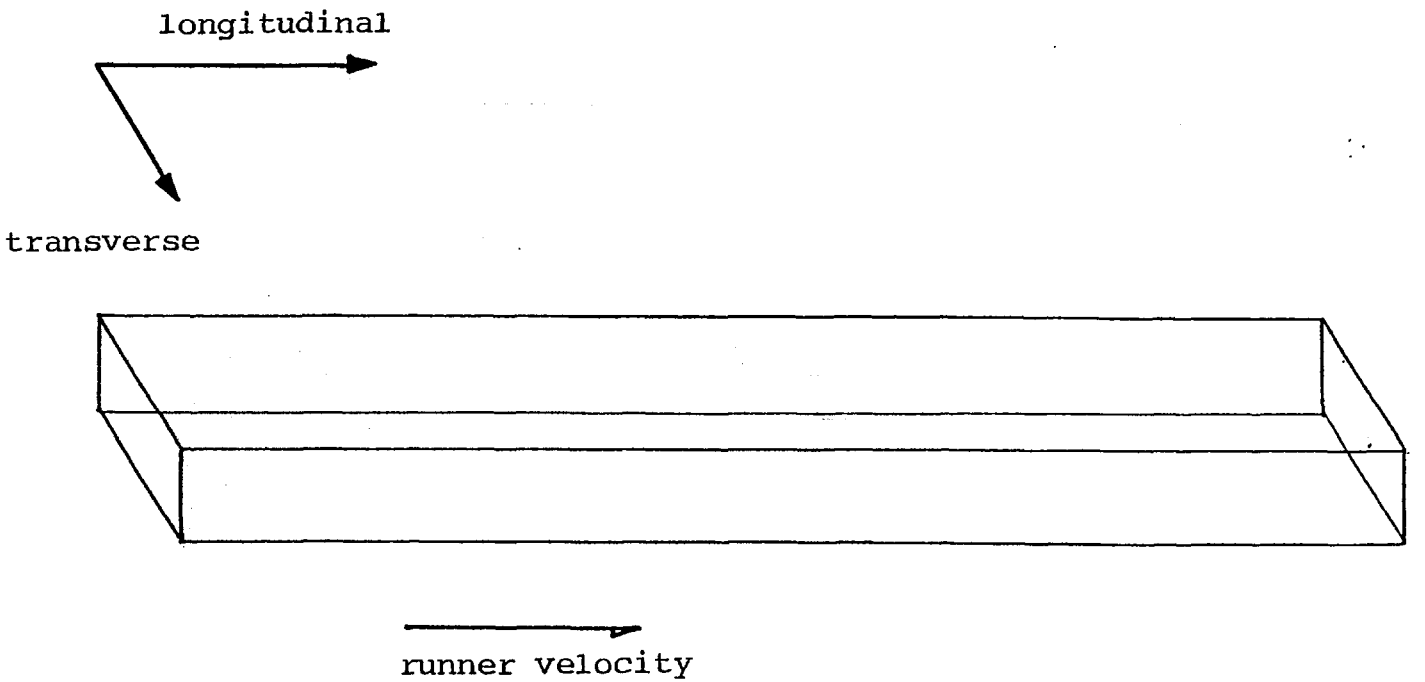

Figure 3F-5 Thin Rectangular Pad

$$U\tau = \rho c q_x \, dT/dx \qquad \text{E3-15}$$

where q_x is the flow along the pad

U is the surface velocity

τ is the shear stress at the sliding surface boundary

For a parallel surface slider, the flow work term, pq, becomes zero, since no pressure is generated. A pure Couette flow results. The definition of the shear stress for a linear velocity profile (Couette flow) is given by

$$\tau = \mu U/h \qquad \text{E3-16}$$

The flow is given in the x direction as

$$q_x = Uh/2 \qquad \text{E3-17}$$

and

$$dT/dx = 2U\mu/\rho c h^2 \qquad \text{E3-18}$$

For a slider of length B, the temperature difference between inlet and outlet is therefore given by

$$\Delta T = 2UB\mu/\rho c h^2 \qquad \text{E3-19}$$

where the viscosity is assumed uniform. In order to solve numerically for a rectangular pad, a small pad angle has been chosen (0.02 rads) with R_i=999m and R_o=1000m. This renders a good approximation to a cartesian system. The effective length B is

$$B = (R_o + R_i)AP/2 = 20m \qquad \text{E3-20}$$

For $\Omega = 8.38 \times 10^{-2}$ rads/sec , $h = 1 \times 10^{-3} m$

$\mu_o = 3.02 \times 10^{-2}$ kg/m s , $\rho = 866$ kg/m^3

U = 83.8 m/s , c = 1880 J/kg deg C

then from E3-19

$\Delta T = 62.2$ deg C

The energy program may be tested in conjuction with the Reynolds program for the above case. The inlet temperature is fixed at 50 deg C. A boundary condition is imposed such that the node temperatures in the upper and lower (K=1,K=3) faces are set equal to the middle node (K=2) temperature, for every control volume. The tilt is set to zero. This results in a zero pressure field, as expected. The program gave a result of ΔT=62.0 deg C (that is, at exit, T=112 deg C). It is also found that the temperature gradient in the transverse direction is zero. This result is obtained for a mesh of 7,7 and 3 nodes in I, J and K directions. The pad angle 0.01 rads produces a temperature rise of 31.1 deg C - again consistent with E3-20.

b) Since test (a) is grid independent (because a constant temperature gradient only exists) another test is performed for a sector shaped pad (table 3T-1).

3T-1 Specifications for Test b

Pad Angle	1 rad
R_i	1m
R_o	2m
T_{inlet}	50 deg C
Ω	41.9 rad/sec
ρ	866 kg/m^3
c	1880 J/kg deg C
h_{max}/h_{min}	2:1
h_{middle}	1×10^{-3}m

Again a uniform temperature distribution across the film thickness is imposed. Fig 3F-6'A' shows the variation of load for successive temperature modifications to the initial temperature setting. The Reynolds equation is solved repeatedly until convergence is achieved. The convergence is said to have occurred when the mean absolute weighted residual (defined in Appendix D) is smaller than a specified convergence criterion - in this case 1×10^{-7} (choice of tolerances will be discussed in Chapter 5). Oil number 1 is used (details in table 3T-2).

Table 3T-2

Oil No.1 Details

T(deg C)	μ(centistokes)
22	150
46.5	40
72.8	15

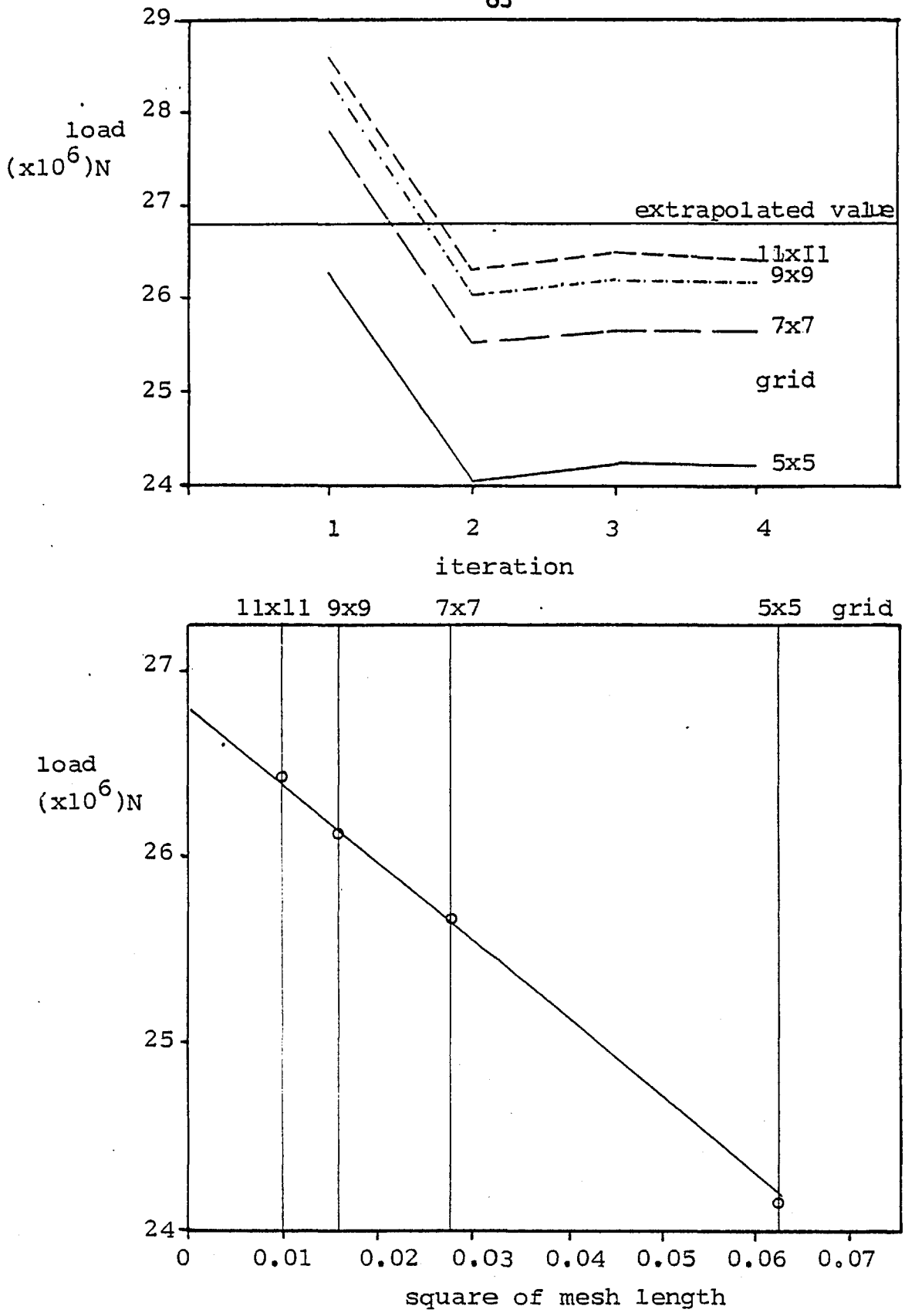

Figure 3F-6 Results for Solution of Temperature Field in a Fixed Thrust Pad

Once the pressures and flows are found, a solution for the temperature field follows. Again an iterative process is carried out to update the temperature values until a convergence criterion is satisfied - in this case $1x10^{-3}$ for the temperature field. The new temperature field is used to update the viscosity values. The updated viscosity values are used to obtain new pressure and flow fields. The process is repeated until convergence is obtained for successive fields. In Fig 3F-6'A', the uniform viscosity field is found to overestimate the load capacity compared to the converged solution. This confirms the work of previous analyses on the effect of varying the viscosity field compared to an isoviscous solution {R21}. On the same graph, the solution for different grid sizes is shown. For all grid sizes, the second energy modification causes an underestimation of the load capacity. This indicates that underrelaxation is required for the temperature field between successive applications of the energy equation.

Fig 3F-6'B' shows results of h^2 extrapolation of load capacities (square of mesh length versus load capacity - finally converged solution). The percentage error of the 5x5 grid compared to the extrapolated value is about 10%. This improves by an order of magnitude for an 11x11 grid.

Fig 3F-7 shows how the choice of a suitable relaxation factor can enhance the convergence of the iterative energy model. A minimum number of sweeps is obtainable at a relaxation factor of 0.71. The energy solution is found to be highly stable

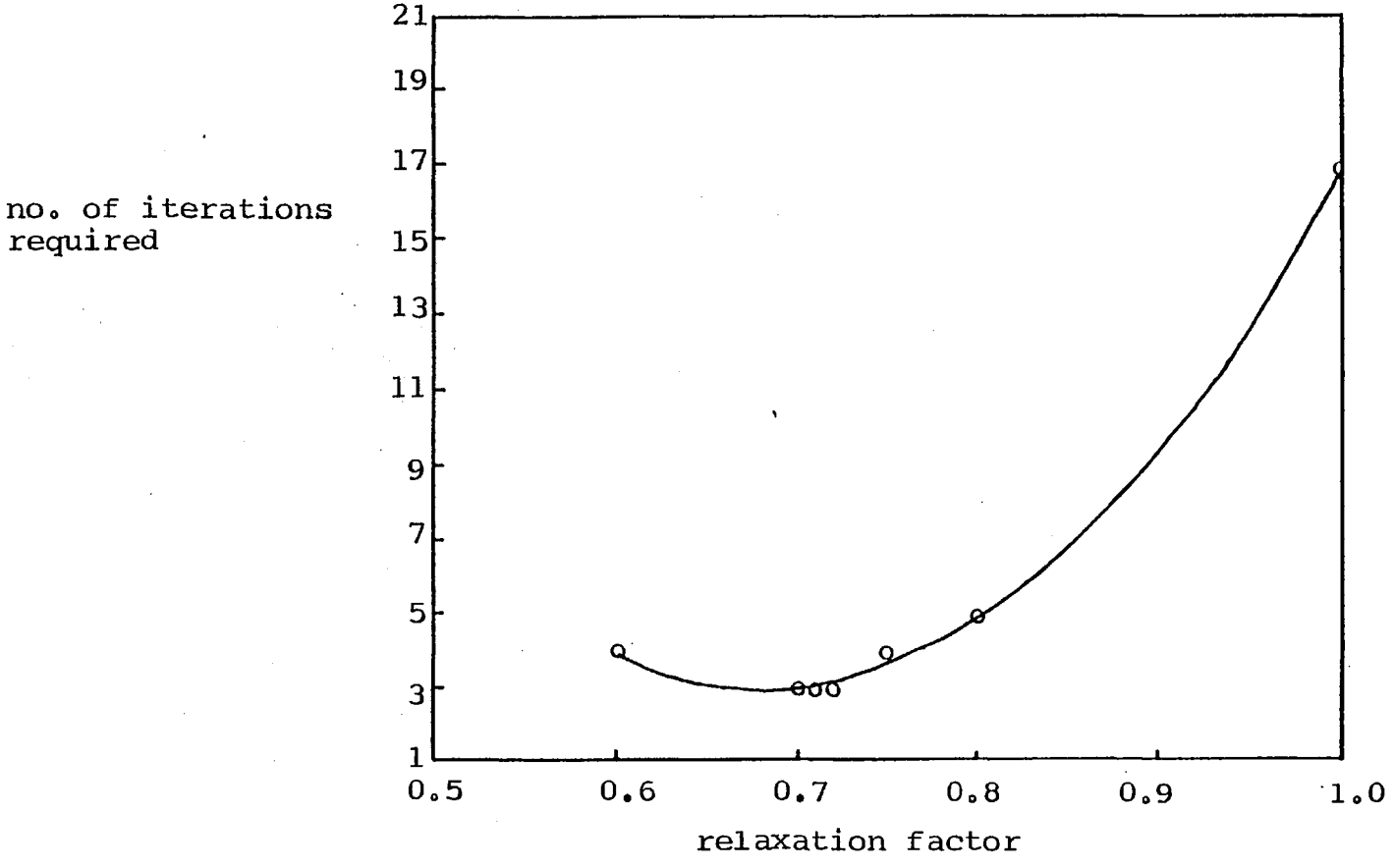

Figure 3F-7 Choice of Relaxation Factor - Oil Film

- requiring only three sweeps with a suitable choice of relaxation factor.

3.2 Flow of Heat im The Pad

3.2.1 Model

A three-dimensional model of a sector shaped pad is presented, allowing conduction within the pad, and convection on the surfaces. The model is fully three-dimensional, a minimum of 3 nodes being required in each co-ordinate direction (r, θ, z).

Figure 3F-8 shows a typical grid system. The grid spacing in the radial and tangential directions is the same as that for the oil film grid for any one case. In fact, an interface exists between the two mesh systems at the pad/oil film face. The pad plane L=1 corresponds to the oil film plane K=3, where they physically meet.

The heat flow in the pad is governed by the Laplace equation (in the abscence of sources and sinks.)

$$\frac{k}{r^2}\frac{\partial^2 T}{\partial \theta^2} + \frac{k}{r}\frac{\partial}{\partial r}\left(r\frac{\partial T}{\partial r}\right) + k\frac{\partial^2 T}{\partial z^2} = 0 \qquad \text{E3-21}$$

The finite difference method is again employed, and details of the application may be found in Appendix F. The solution is iterative, requiring several sweeps before convergence can be obtained.

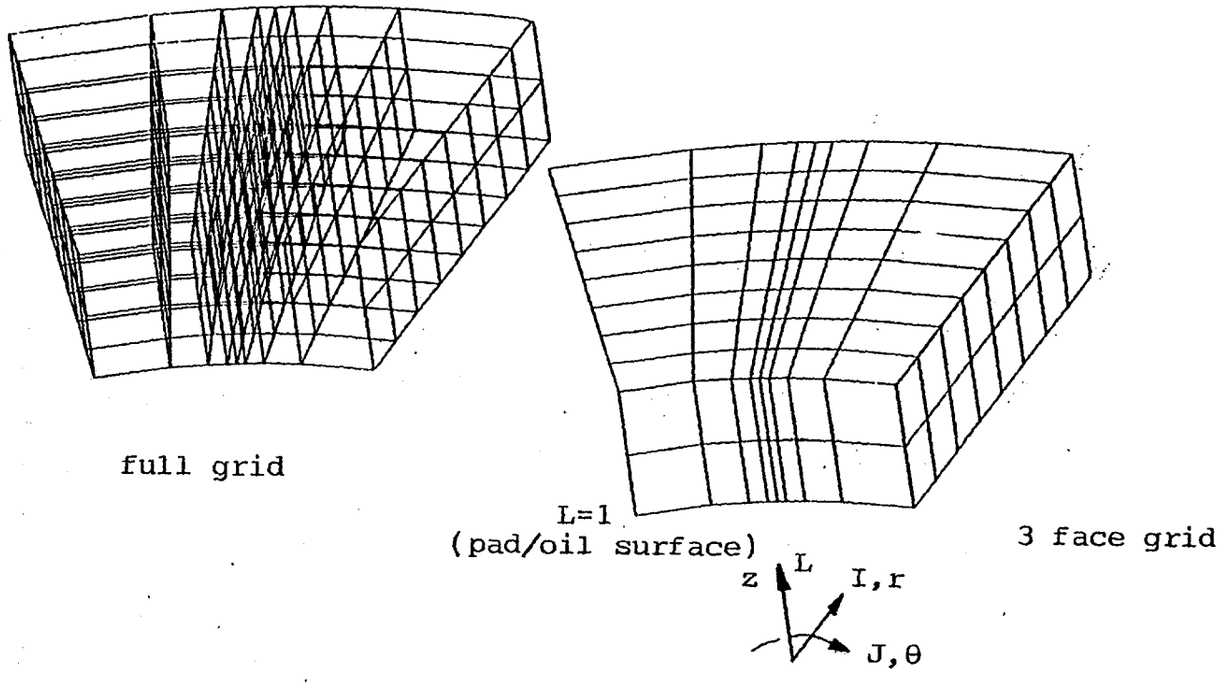

Figure 3F-8 Grid System for Pad - fully three dimensional

A fully three-dimensional system such as the present model is amenable to many useful modifications. A heat source can be included in any region. A cavity can be handled - for example a groove. On the other hand, because a three-dimensional system is involved, the sheer amount of work necessary for each modification will limit its use to particular cases.

Convection at the pad back faces is treated using surface heat transfer coefficients. Each face can have a different coefficient depending on the flow condition - if known - on that particular face. Computer storage prohibits the use of local surface heat transfer coefficients (SHTCS) at every surface node, although it is viable in principle. The determination of SHTC depends on the bearing configuration. This will be detailed in a special section.

The solutions for temperature in the pad and oil film are coupled. Previously (section 3.1.3), temperatures at the pad/oil interface have been assumed. A certain temperature profile results for each oil film control volume. The temperature gradient at the interface can be evaluated, resulting in a heat flux, to which the pad is subjected. This 'heat flux' is one aspect of the coupling (Since the heat flux must be continuous at the interface, the same heat flux is assumed to enter the pad). The other aspect of the coupling is that the interface temperature field is the same for both oil film and pad.

An oil bath temperature is required to evaluate fluxes at the remaining pad faces - (using the SHTCS - see section 3.2.3).

3.2.2 Assumptions

(a) Steady state conduction

(b) Uniform thermal conductivity

(c) All SHTCs are constant

(d) No heat sources or sinks exist within the pad .

3.2.3 Boundary Conditions

For a typical control volume (Fig 3F-9) one of four boundary conditions exists at each control volume face:

i) A conduction boundary within the pad,

ii) A convection boundary at the pad surface,

iii) A fixed temperature at the pad surface,

iv) A specified heat flux at the pad surface.

For condition (ii) the oil bath temperature is required at the free stream temperature. Thus the flux entering the pad surface at this plane is

$$Q_s = \alpha_s A_s (T_{BATH} - T_s) \qquad \text{E3-22}$$

where s refers to the surface considered

A area at s

α surface heat transfer coefficient at s (SHTC)

T_{BATH} oil bath temperature

T_s temperature at surface

Q_s heat flux into control volume at surface s

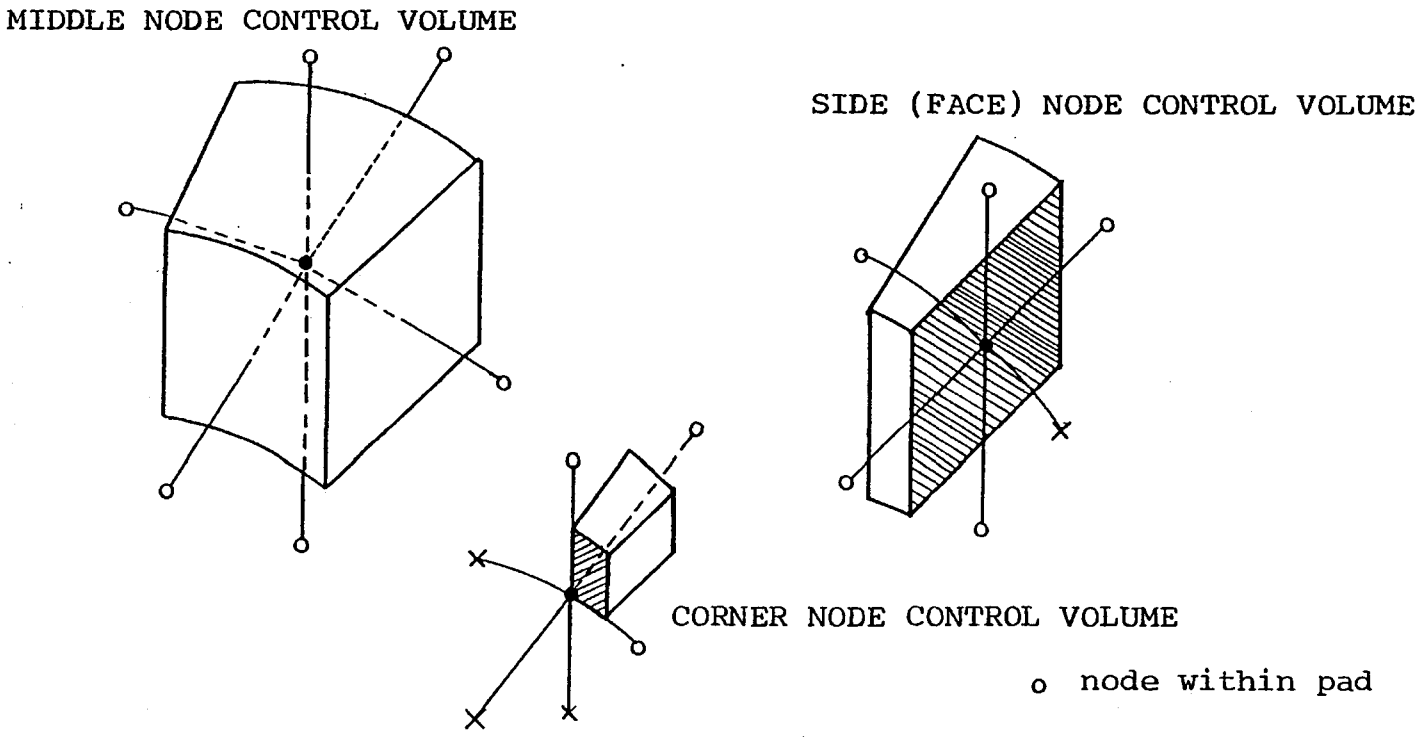

Figure 3F-9 Conduction Model - Typical Control Volumes

In an iterative finite difference scheme a fixed temperature boundary condition requires the omission of the particular fixed temperature node during the iterative solution process.

A specified heat flux (iv) is treated as a source or sink of energy in the energy equation. This condition is applied at the pad/oil interface, where the heat flux is calculated from the energy equation in the oil film (see 3.1).

In some bearing configurations, the temperature of the oil flowing around the back surfaces of the pad may not be the bath oil temperature. This may be due to other heat sources present, or due to more effective cooling in this region of the bearing. Thus, for each pad face, an extra layer of nodes has been added (for example, K=0, K=4 for the upper and lower faces). This simplifies computation of the finite difference coefficients because every node is then surrounded by six others, even at the surfaces or at corners. Hence, the iteration process is continuous for each node with respect to its nearest 6 neighbouring nodes. The boundary conditions are therefore included in the computing coefficients. This automatically takes into account the variation of oil bath temperature if required. The extra grid surfaces (for example, K=0, I=0, J=0 etc) are assigned temperature values as required - usually the oil bath temperature.

3.2.4 Tests

Two tests have been devised to test the conduction heat transfer technique. The first involves insulation of the pad sides ($\alpha_E=\alpha_W=\alpha_N=\alpha_S=0$). A uniform heat flux is applied at the pad/oil interface. On the pad upper surface a SHTC is specified. The configuration thus reduces to a one-dimensional system for which an analytical solution is available

$$Q = k_{oil} \left.\frac{dT}{dz}\right|_{oil} = k_{pad} \left.\frac{dT}{dz}\right|_{pad} = \alpha (T_{pad\ surface} - T_{oil}) \qquad \text{E3-23}$$

where the temperature is uniform for any particular value of z.

Table 3T-3 gives details of the values chosen for the first case.

Table 3T-3

T_{oil} = 53 deg C , R_i = 0.209m , R_o = 0.3937m

K_{oil} = 0.15 J/m s deg C , AP = 0.668 rads

K_{pad} = 100 J/m s deg C , pad thickness = 0.0381m

α_U = 1000 J/m^{2}s deg C

(i) $\left.\frac{dT}{dz}\right|_{oil} = 10^5$ that is T across pad = 5.715 deg C

(ii) $\left.\frac{dT}{dz}\right|_{oil} = 10^6$ that is T across pad = 57.15 deg C

A numerical field convergence criterion of $1x10^{-3}$ has been chosen (see Appendix D). For trial (i), ΔT from the model is 5.5 deg C, and for trial (ii), ΔT=56 deg C is obtained. In general, a local variation of about 1 deg C is obtained (it can be reduced by applying a more stringent convergence criterion). Fig 3F-10 shows the bottom and top pad surfaces (for L=3). The temperature variation follows the direction of scan in the iteration, that is starting from the bottom left hand corner and scanning circumferentially until the top right hand corner is reached (at (9,9) in this case).

The second case is the same as the first , but without insulation. A SHTC = 1000 J/m^2s deg C is given to E, W, N, and S faces. The temperature pattern in the pad becomes circular, accompanied by a general drop in temperatures. Fig 3F-11 shows the contours for case (i) (see table 3T-3).

The above cases satisfy quantitative as well as qualitative expectations required from the conduction model.

Temperature in degrees C

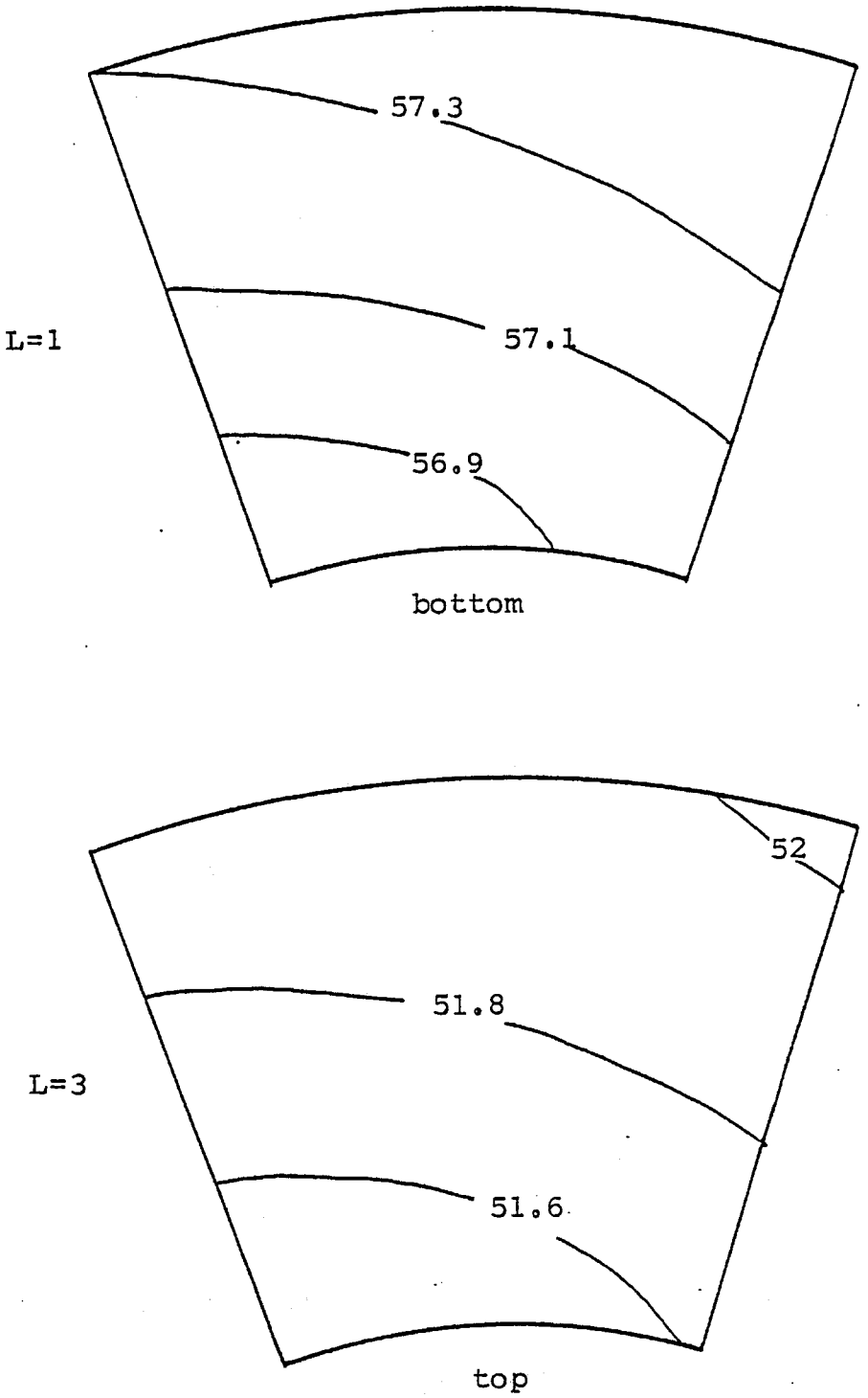

Figure 3F-10(i) Insulated Pad Contours

$\frac{\delta T}{\delta z} = 10^5$

Temperature in degrees C

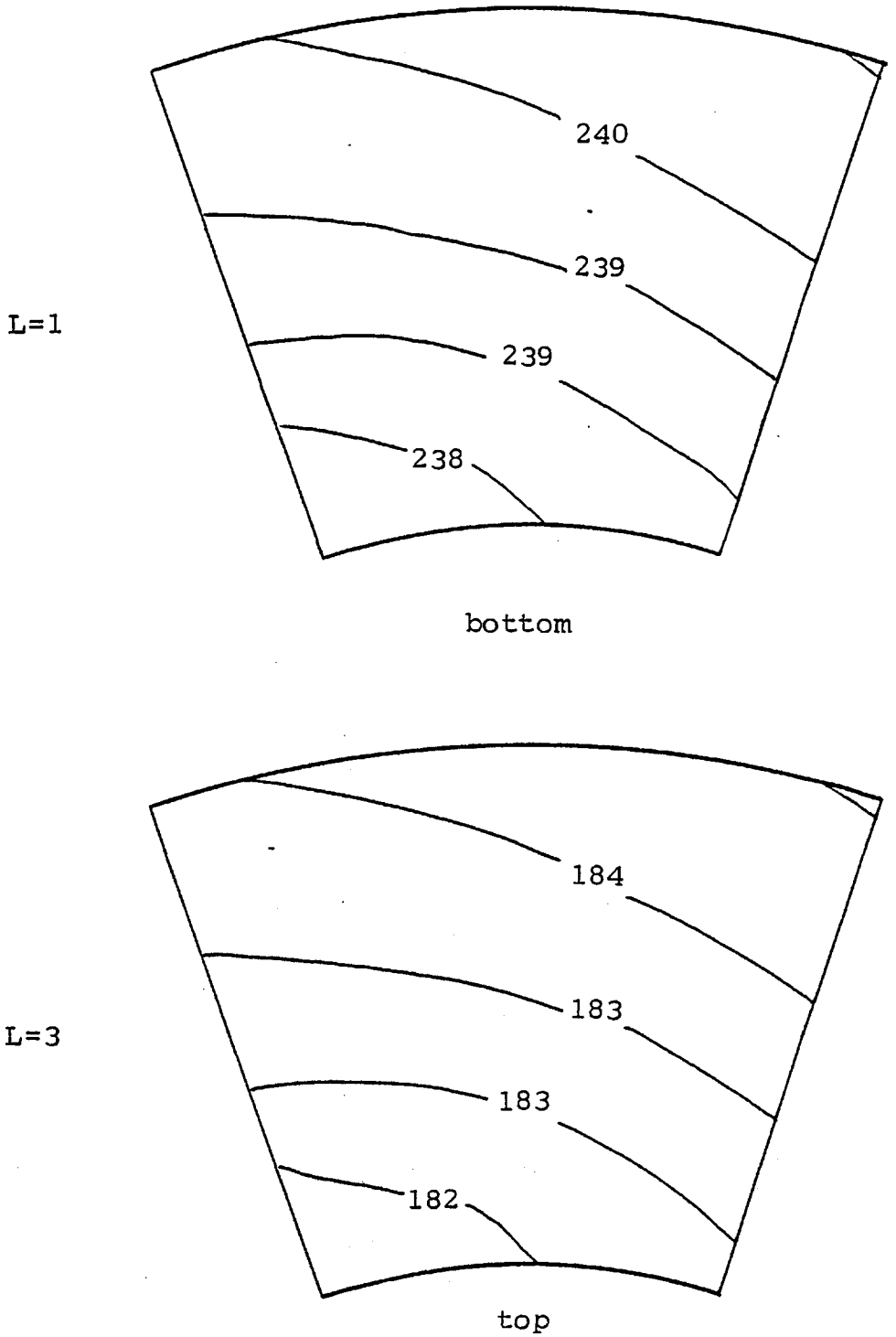

Figure 3F-10(ii) Insulated Pad Contours

$\frac{\partial T}{\partial z} = 10^6$

Temperature in degrees C

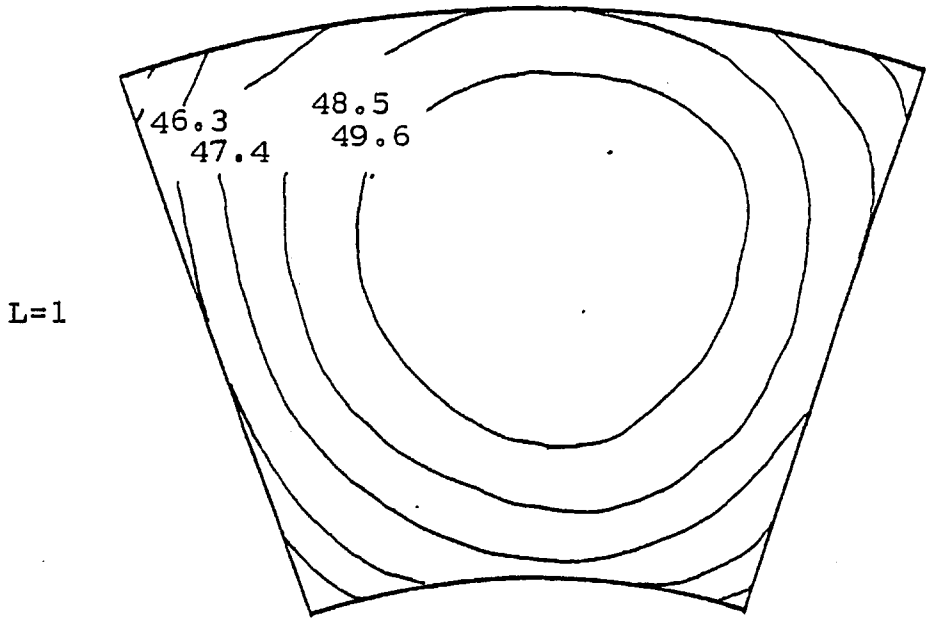

L=1

bottom

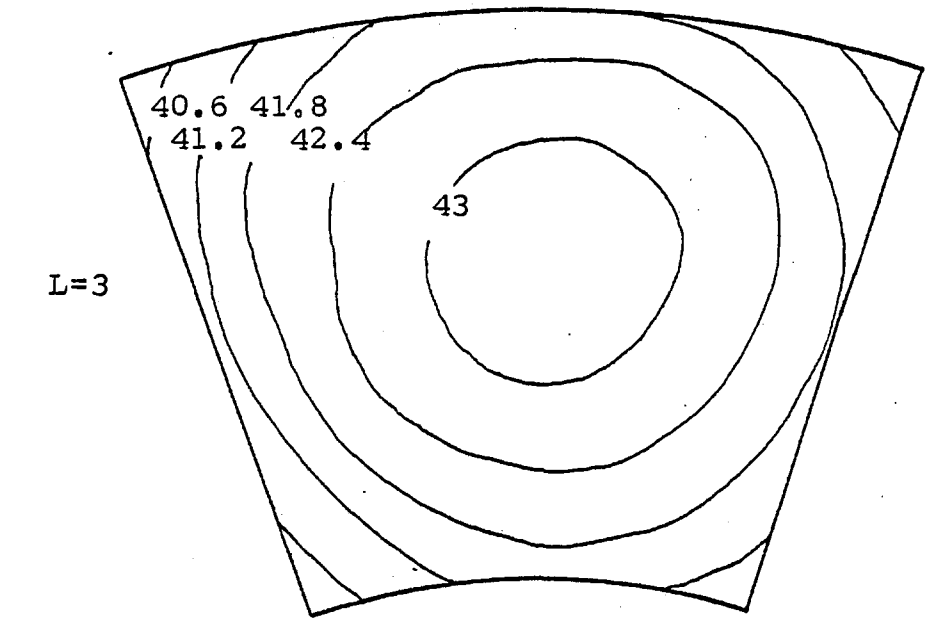

L=3

top

Figure 3F-11 Pad Temperature Contours - Insulation Removed

3.3 Flow of Heat in the Runner

3.3.1 Model

The runner is thought to play an important role in heat exchange to and from the oil film and to the bulk oil in cavities between successive pads {R16, R27, R28, R31, R32, R33}. In a recent publication by Neal {R33}, results of an experimental investigation confirmed the basis of a theoretical model also proposed by Ettles {R31}. A control volume featuring the runner as a major heat recipient as well as a heat donor is shown in Fig 3F-12. The arrows indicate directions of heat transfer: F_{4g}, the heat transfer from rotor to cavity, as well as F_{4s}, the heat transfer from oil film to rotor.

The rotor temperature contours are circular following a two-dimensional temperature distribution in (r,z) directions {R16}. This is a result of the negligible "flash" temperature variations (dynamic heating and cooling due to runner rotation). A quantitative analysis of the depth of heat penetration is presented by Neal {R33}. The maximum flash temperature rise is shown to be very small. Hence, a quasi three-dimensional system is used where circumferential heat transfer is neglected.

Fig 3F-13 shows F_1 ($= F_{11}+F_{12}$) and F_2 as fluxes similar to those considered by Ettles {R31}. In addition, F_3 and F_4 are included as a part of a quasi three-dimensional model. The grid system for the conduction equation is similar to that in the pad

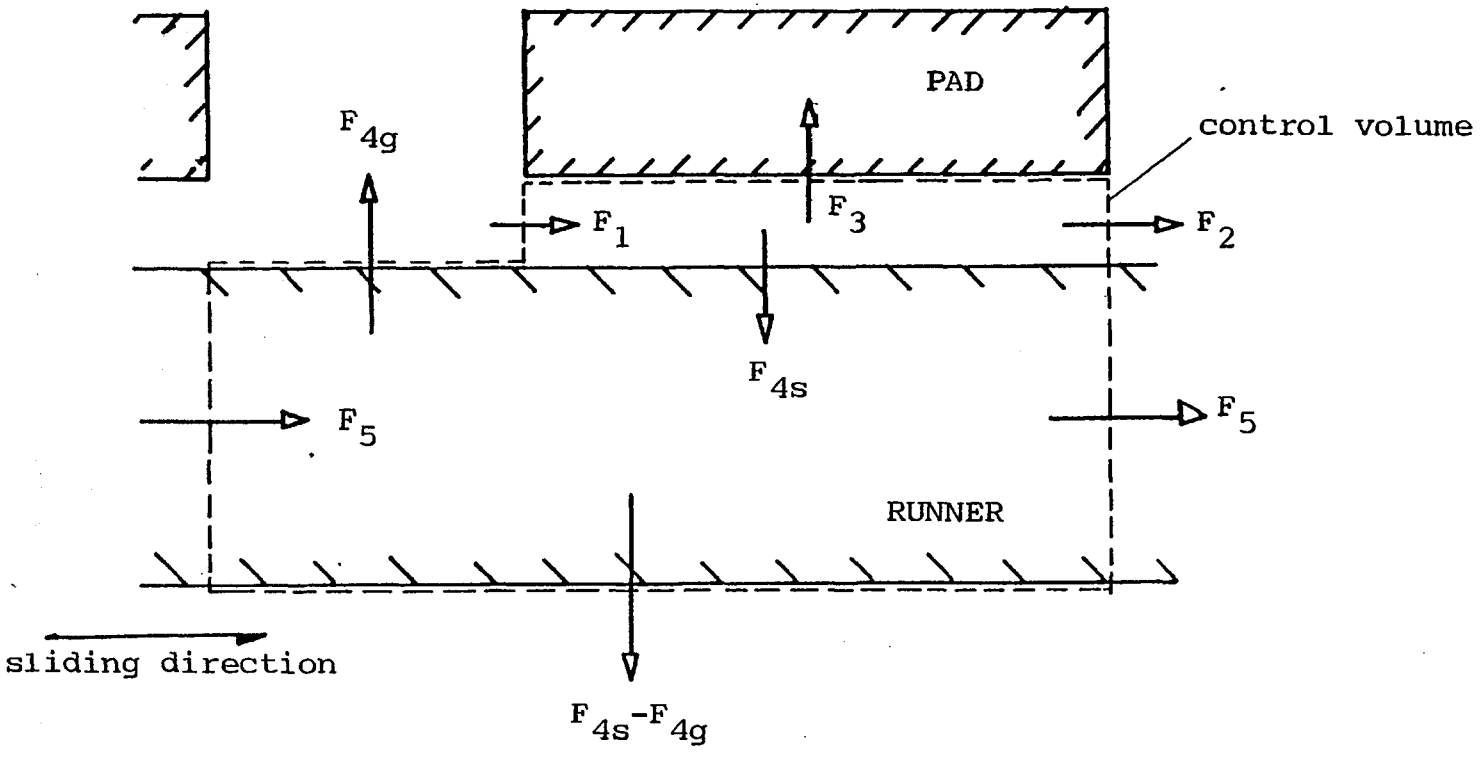

Figure 3F- 12 Rotor Heat Transfer and Control Volume

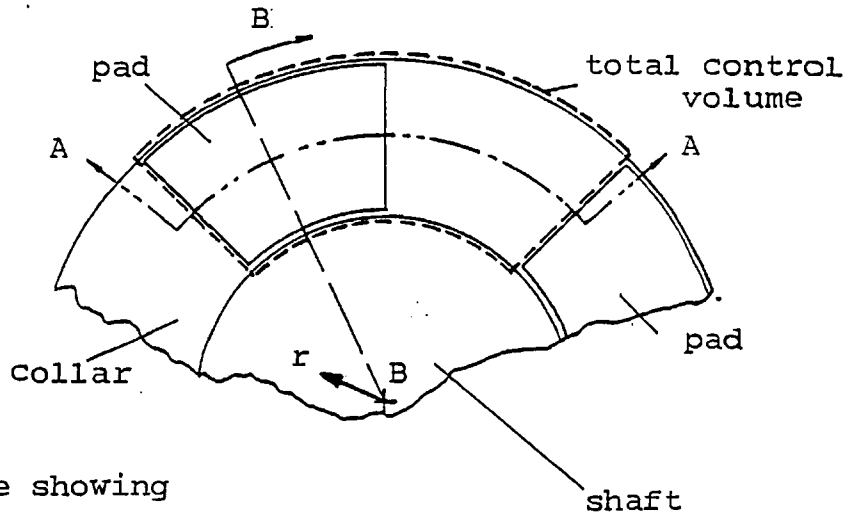

total control volume showing pad position

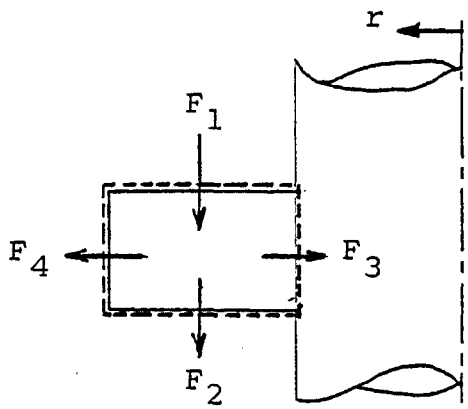

SECTION B-B

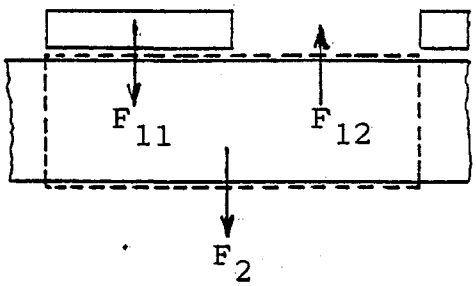

SECTION A-A

Figure 3F- 13 Runner Model (Showing Various Fluxes)

(see section 3.2). Two differences exist. Firstly a factor is applied to the depth of the grid in order to obtain the correct runner geometry (allowing different pad and collar thicknesses). Secondly, for a particular (z_i, r_i) position, only one node is used. This represents the temperature at all other circumferential node positions on the runner at (z_i, r_i). This is a useful economizer on computer storage.

Thus, for a control volume at the runner surface, both F_{11} and F_{12} are to be considered. An integral of the heat flux at the radial position represented by this control volume is formed. Thus F_{11} is added to F_{12} and used as a single flux to the control volume. Circumferentially the length of the control volume is

$$L_{cv} = (AP + AC) \; r_i$$

where

AP is the pad angle

r_i is the rotor radius

AC is the cavity angle

as shown in Fig 3F-14.

3.3.2 Assumptions

All assumptions applying to the pad conduction model apply to the runner model. In addition,

(a) Circumferential heat flow is negligible

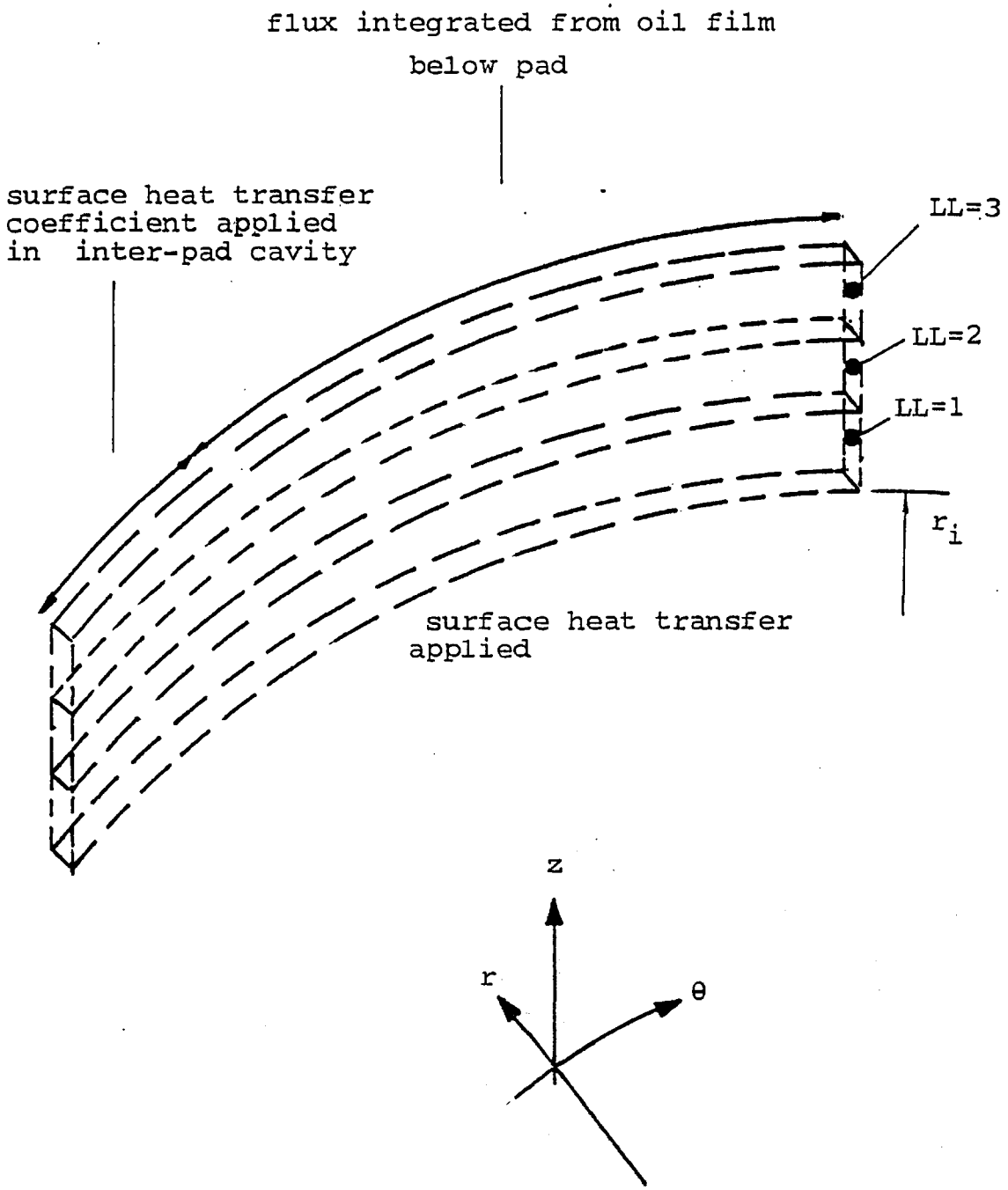

Figure 3F-14 Runner Control Volumes

(b) flash (dynamic) temperature changes are neglected

3.3.3 Boundary Conditions

Again, boundary conditions established for pad conduction apply (see section 3.2.3).

One extra problem arises when considering the shaft. This concerns the flow of heat to the shaft body outside the bearing. The true condition varies according to the overall installation of the bearing. The shaft may be hollow. The heat flux concerned is F_3 in Fig 3F-13. It is thought that the temperature in the shaft to which the collar is fitted will be close to that of the oil bath temperature - for a flooded bearing. A uniform temperature boundary condition is used at the collar/shaft interface for most cases. In some particular cases, this is dispensed with and replaced with a SHTC and will be specifically discussed in later chapters.

Fig 3F-15 shows a section of the runner, with the finite difference grid nodes superimposed. Now the LL=3 plane on the runner is the plane K=1 for the oil film. For the runner grid nodes (each having one control volume) at LL=3, a heat flux boundary condition is imposed at the upper face. At I=1 - the inner radial face - the oil bath temperature is fixed as a boundary temperature value. In the iteration process the I=1 nodes are bypassed.

At other runner faces the convection boundary condition applies (see E3-22). Again, fictitious temperature nodes are assigned at each runner outer surface (LL=0, LL=1+2, I=0,

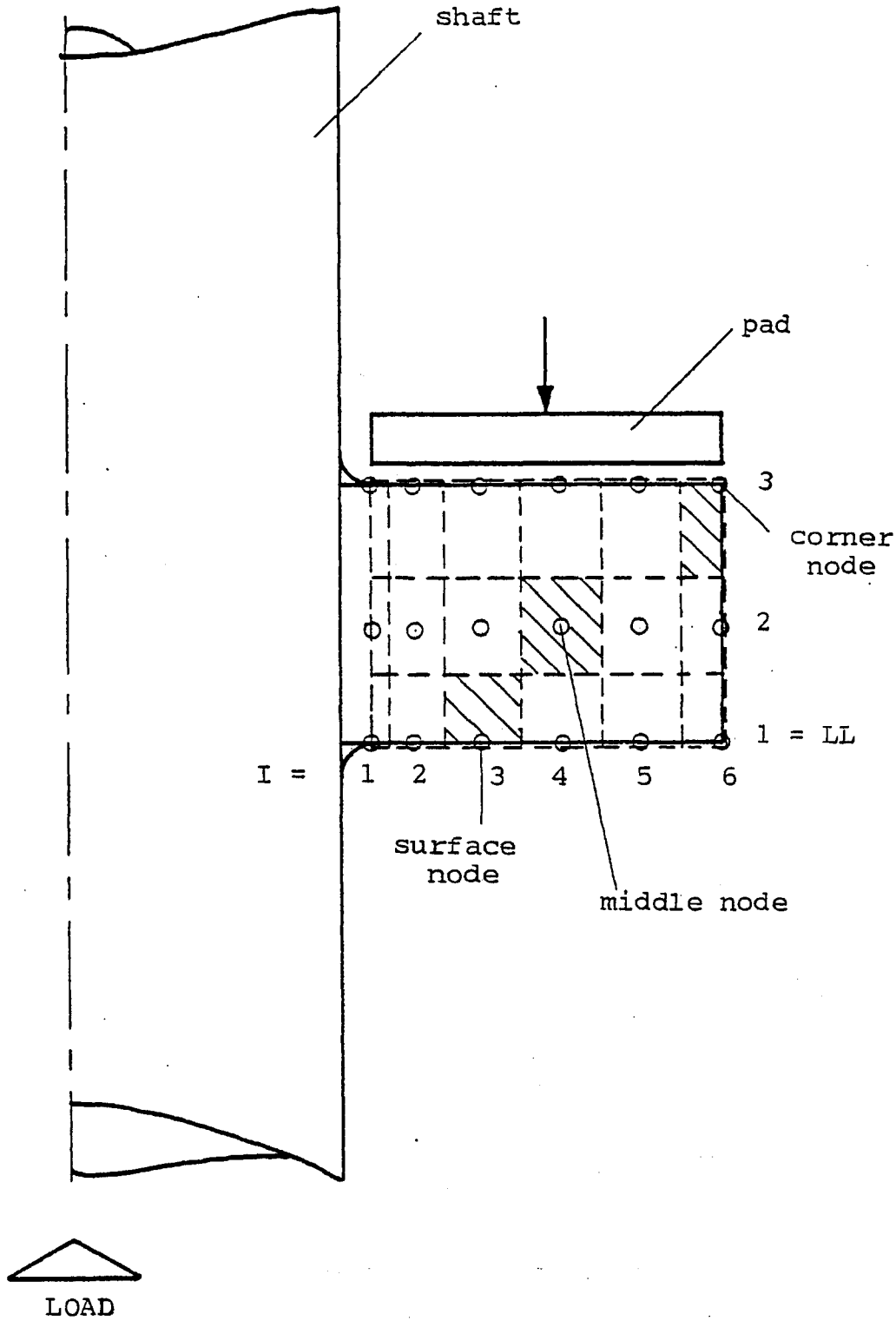

Figure 3F-15 Grid Distribution in Rotor

I=M+2)(see section 3.2.3)

3.4 The Total Energy Equation Solution

3.4.1 Surface Heat Transfer Coefficients(SHTCs)

The surface heat transfer coefficients represent a major simplification in the heat transfer analysis. This is, nevertheless, a necessary step. Firstly, an involved analysis of heat and mass transfer at the back faces of the pad and runner is as complicated a problem as that of the oil film itself, if not more so. Secondly, for each pad configuration and design major modifications will be required. Thirdly, an approximate estimate of the surface heat transfer coefficients can be obtained from simpler models - for example, flow of heat between parallel plates {R34}. Another alternative is to estimate surface heat transfer coefficients from available experimental data. These are scarce, and may not apply in the design of new configurations; but are useful in verifying the model presented. Previous techniques involved in prediction of oil film temperatures as part of a comprehensive analysis have involved less realistic assumptions. In one analysis, {R17}, a fixed percentage is allowed for heat conduction from the bearing oil film. In others {R18,R25,R16} an adiabatic runner temperature is assumed. Thus, it is hoped that the choice of surface heat transfer coefficient will minimize the errors involved in a comprehensive analysis. On the other hand, the method is versatile in being able to accept variations of SHTC with speed,

material and design considerations.

The use of SHTCs is useful in determining the effect of a flooded runner compared to a runner with the back face (LL=1, Fig 3F-13) exposed to the atmosphere (that is, a gas). It is also useful to show the effect of insulation - by setting $\alpha_{face}=0$, or the effect of forced cooling - by setting $\alpha > \alpha_{usual}$.

3.4.2 Hot Oil Carryover and Runner Temperature

From analyses of the pad, rotor and oil film; it can be established that the oil inlet temperature directly depends on all three. Moreover, the inlet temperature profiles can vary radially as well as through the film thickness (z-direction). In the present model, the film exit temperature has a marginal role compared to the rotor surface temperature. At any particular radial position, the rotor temperature is obtained considering the oil film as well as the inter-pad cavity. The effect of rotor temperature is thus enhanced.

The role played by film exit temperature serves to decide the middle node inlet temperature (at any radial position). Its effect is limited to the particular entry control volume, and not directly to the whole field. The top node (K=3) temperature (at entry) is fixed as that of the pad. Hence, the average film inlet temperature is more influenced by the heat flow equations rather than pure hot oil carryover theory.

For a particular test case, all temperatures are initially set to the oil bath temperature. The Reynolds equation is solved. Assuming the pad and rotor temperature are fixed; the oil film middle node temperatures (K=2) are evaluated. The new oil film temperature profiles supply the necessary flux to the upper and lower faces, that is to the pad and runner respectively. The pad temperatures are evaluated using the conduction model. This involves a new temperature distribution at the pad/oil film interface. A similar procedure follows for the runner, resulting in a new temperature distribution for runner/oil interface. At this point, the whole temperature distribution field has been updated. Using the upper (K=3) and lower (K=1) temperature distributions, the middle node temperature distribution is again evaluated. This provides new oil film temperature profiles. Thus, a new flux distribution is available at the upper and lower faces. The process is repeated until two conditions are satisfied. The first relates to the pad/oil interface temperature distribution: When the predicted distribution compared to the previous distribution has a mean absolute weighted residual less than a specified value (usually $1x10^{-2}$). The second condition relates to the runner/oil interface temperature distribution. Again, a mean absolute weighted residual is required to be satisfied ($1x10^{-2}$). The oil entry temperature (at middle node, K=2) is updated at every iteration that involves film middle node temperatures.

Initially, the fluxes induced after calculating the oil middle node temperatures are very high. This is because the actual pad and

runner temperatures are higher than their initial values (set at T_{bath}). The temperature gradients in the oil film are very large because of its relatively small thickness compared to pad or runner thickness. The oil film resistivity is higher than for the solid components, causing amplified initial temperature gradients.

The high temperature gradients result in very high fluxes to pad and rotor. This in turn may yield very high temperatures in the pad and runner. These are then used to predict middle oil film temperatures. The values predicted may be very low - or even negative. Thus the process is highly unstable. An underrelaxation factor is applied to the heat fluxes to help eliminate the problem at its roots. Fig 3F-16 shows three underrelaxation factors used. At a value of 0.3 a negative temperature is reached before a solution is reached. A value of 0.1 seems to be optimum, whilst a value of 0.05, although giving convergence, requires more iterations than 0.1. A value of 0.05 has been chosen as some cases produced instability at a value of 0.1.

Once a converged solution for the temperature field is obtained the Reynolds equation is adjusted to match the new viscosity distribution and a new pressure field is obtained. The subsequent converged solutions of the energy equation require fewer iterations than in the first case.

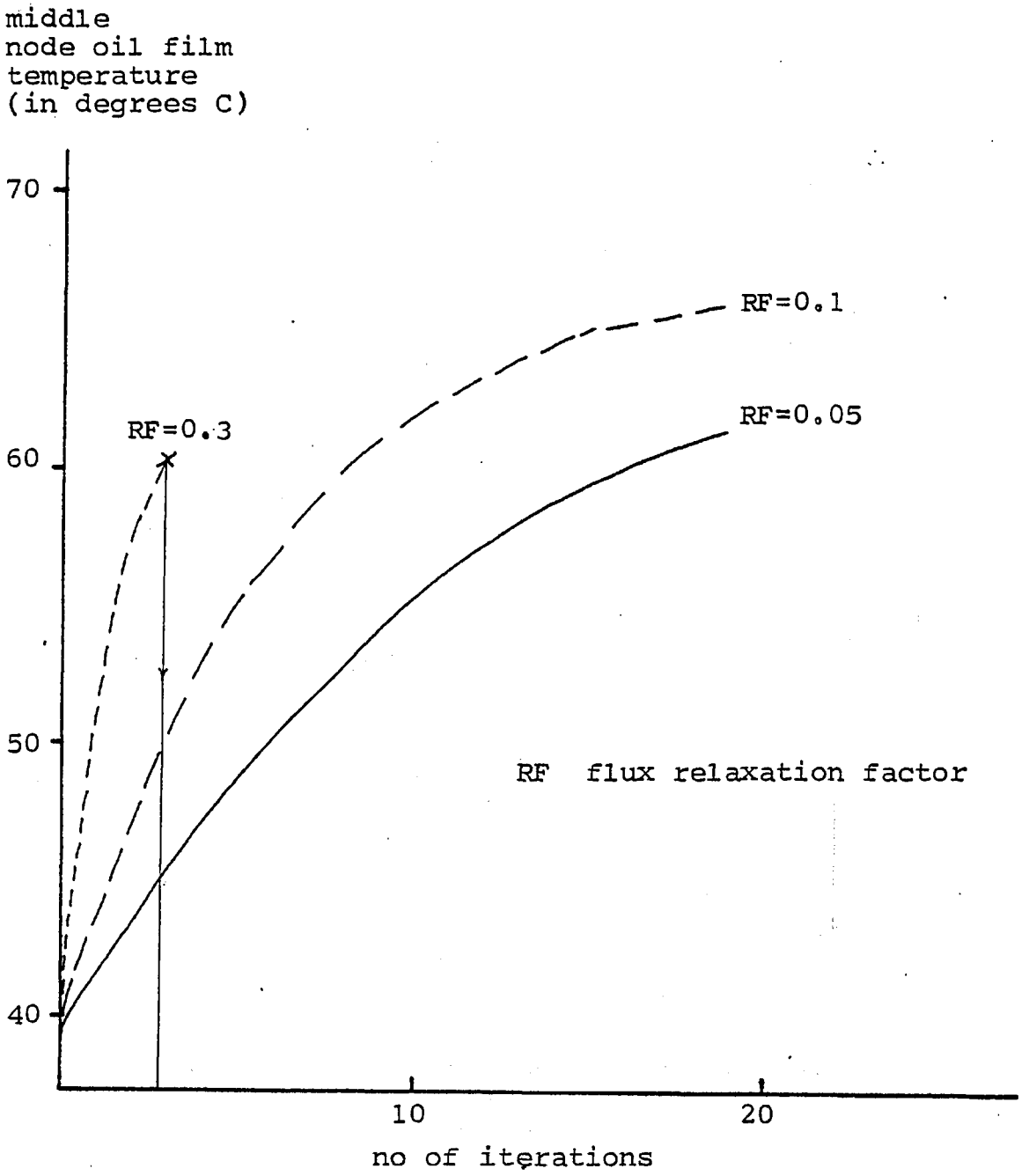

Figure 3F-16 Choice of Flux Relaxation Factor

3.4.3 Bearing Oil Temperature

In the foregoing analysis, the bath oil temperature has been assumed fixed. This is not the case in practice. Factors that affect the oil bath temperature (T_{bath}) include the heat generated in the oil film, the heat generated by oil churning in the bearing cavities, the bearing materials and casing design, which in turn regulate the amount of heat given to the bearing surroundings.

Neal {R33} described T_{bath} as a link between the 'pad level' analysis and the 'bearing level' analysis. The present analysis requires T_{bath} as an input value. The temperature distribution in pad, oil film, and runner are then determined. In order to proceed to the 'bearing level', knowledge (or analysis) of the factors affecting churning and heat loss through the casing etc. is required.

For design purposes, an order of magnitude analysis of the various heat loss components can be carried out. A certain T_{bath} is chosen. Cooling of the chamber oil can then be used as a means of controlling T_{bath}. (for example a water cooled jacket with thermostatic control of flow). This method is suitable for large bearings where the problem is severe.

3.5 Numerical Considerations

Various numerical parameters influence the speed and accuracy of the heat transfer analysis combined with the fluid flow. The

various convergence criteria, the number of nodes, as well as the coupling of the equations can all influence the computer time taken to reach a converged result.

A description of the nodal successive overrelaxation (Chapter 2) for the pressure generation has been given. The choice of a uniform relaxation factor for the oil film temperature solution has already been given. A special two-dimensional tilting routine has also been given (Chapter 2). The tilting proceedure allows for non-linear characteristics and works for all the cases encountered.

Initially, the conduction routines (pad and collar) are found to require a large number of iterations. This very quickly drops to 2-3 iterations for every pass through the conduction sections of the program. Thus, no attempt has been made to insert a relaxation factor. In fact, the computer time required to calculate one (as is done for the pressure solution) may exceed the benefits gained in saving. Typically, the equivalent of six iterations are required to calculate local relaxation coefficients {R6}.

The error due to mesh size variation is given in Fig 3F-6. For an 8x8 grid an error of 2.2% compared to the extrapolated value (for an infinite number of nodes) is typical. Beyond a 10x10 grid size, the computer time rises sharply. At Imperial College, computer central memory (CM) also severely limits the mesh sizes that can be used iteratively (that is, using a computer terminal for both

feeding data and obtaining results as they are produced). A 10x10 grid has been found to be the maximum usable mesh size (11x11 nodes), but to conserve computer time, an 8x8 mesh size (9x9 nodes) has been used throughout. In the z-direction, the oil film is fixed at 3 nodes; only one layer participating in the iteration solution. The remaining two layers are used to set up the coefficients necessary for the quasi three-dimensional solution, as well as in the calculation of the heat fluxes to rotor and pad.

The conduction equations are three-dimensional. The number of nodes in the z-direction has been fixed at the minimum value of three. This applies to both rotor and pad. It has been thought that a saving on storage is better made here (conduction modelling) than in any other. The total model is likely to be less sensitive to the number of nodes used in the z-direction compared to the r and θ directions. All nodes are considered free nodes (9x3 in rotor; 9x9x3 in pad). Including the fictitious boundary condition nodes, an 11x11x5 storage is required for the pad as well as 11x5 for the runner temperature. This excludes all storage required for the coefficients for each node.

Thus, all the features of a three-dimensional system have been maintained at the lowest cost in storage and computer time. At the same time, the accuracy of the solution is maintained at an acceptable level for quantitative analysis (see section 3.2.4).

The choice of convergence criteria will be discussed in relation to the total solution, including deflection, in later

chapters. This is again closely linked with the overall system coupling. The relationship between the conduction solution (in the pad and runner) to the oil film has already been mentioned. It is important to note that the convergence criterion for solving the conduction in the pad alone is more stringent (an order of magnitude smaller) than the convergence criterion applied to the coupling phase. This latter phase compares the interface temperature between the pad and oil.

CHAPTER 4

DEFLECTION ANALYSIS

Introduction

4.1 Development of the Polynomial Difference method as Applied to Beams

4.2 Application of The Method to Beams

4.3 Handling of Singular Boundary Conditions

4.4 The Polynomial Method Difference for Variable Rigidity Sector Shaped Thin Plates

4.5 Test Cases for Plates

4.6 Conclusions From Test Cases

4.7 Numerical Considerations

4.8 Drawbacks

4.9 Other Modes of Distortion

Introduction

The initial development of hydrodynamic lubrication theory witnessed a conflict between the various factors thought to influence it. This is exemplified by the variety of thrust bearing designs, such as the parallel surface bearing, the inclined slider bearing and the pivoted pad bearing.

In attempting to explain the action of the parallel surface bearings, Swift {1946,R35} proposed that thermal distortion was responsible. Charnes et al {R36,1953} showed analytically that transverse curvature was detrimental to bearing capacity. In the discussion that followed, Raimondi {R37} pointed out that deformation of centrally pivoted pads was responsible for their load capacity. Raimondi and Boyd {R38,1955} later showed that a positive (convex) crown is benefical to the load capacity of pivoted pad bearings, and that it accounts for the load carrying action of the centrally pivoted pads. In the discussion, Baudry {R39} commented that thermal crowning may have an important role to play in the action of such bearings.

An experimental investigation was undertaken by Kettleborough et al {R40} to obtain data for a pivoted pad bearing. Contours of film thickness showed crowning. An important factor - the pivot position - was varied and its effect on determining the film shape highlighted. In 1957, Ettles and Cameron {R41} carried out a detailed analysis of the various modes of deformation for a uniform

thickness pad. Thermal distortion was shown to be of critical importance. Other factors included elastic distortion due to bending shear, fibre crushing and direct thermal expansion.

Baudry, Kuhn and Wise {R42} in 1957 considered thrust pad distortion in large bearing installations, as used in high capacity waterwheel generators. Two problems were discussed. Firstly, the method of pad support may cause locally high contact pressures before the formation of the oil film - during start up. the use of a multiple support system was suggested as a means of lowering such local pressures to an acceptable level. Secondly, the method of pad support must allow convex distortion during operation. The optimum position of supports for both problems is not coincident. hence a compromise should be carefully chosen.

Sternlicht et al {R43} showed that neglect of thermal deformation leads to an optimistic design. Raimondi {R44} in 1960 showed that the optimum crown for a square centrally pivoted pad is about one half the minimum film thickness. He also showed that concavity is very detrimental to load capacity. Sternlicht et al {R45,1961} carried out a comprehensive analysis of centrally pivoted sector thrust pads. An optimum pad thickness was suggested, while thermal deflection was not accounted for.

Neal et al {R46,1961}, in reference to an experimental investigation, emphasized the importance of thermal distortion. Hemingway {R47,1965} carried out an experimental investigation of a 'parallel-surface' thrust bearing. He agreed with Pinkus and

Sternlicht {R2} that the film shape between the inlet and minimum film thickness values was not of significance.

Ettles {R19} confirmed experimentally the importance of distortion in the action of parallel surface thrust bearings. Bennet {R48,1967} designed a 'parallel' surface self acting thrust bearing, where the 'pads' are fixed sector-shaped cantilevers. Allowance was made in the design for elastic and thermal deflection to give favourable load capacity characteristics, and this was verified experimentally. Hemingway reported a similar investigation {R49,1968} for an elastically stepped and shrouded thrust bearing.

Hahn and Kettleborough {R9,1969} considered thermal effects in slider bearings. They concluded that the distortion effects were important and amenable to an accurate analysis using modern computers. In a later paper {R10} a simplified theoretical analysis of thermal distortion was presented. Castelli and Malanoski {R16} employed the Ritz method to analyse deformation as part of a comprehensive solution procedure for tilting thrust pads.

In 1971, Shawcross and Dudley {R50} showed that runner curvature results in a marked reduction in load capacity for line pivoted thrust pads. In 1972, Dayson {R51} proposed a flexible stepped thrust bearing similar to the Rayleigh stepped bearing. Distortion of the step allows an extended range of performance over the conventional fixed step design. Rohde and Oh {R25,1975} solved for the deflection of a finite slider using two methods. The first

treats the pad as a semi-infinite solid and results in a closed form solution for deflection. The second is iterative and solves the biharmonic equation for a simply supported plate.

In 1975, Robinson and Cameron {R52} carried out a careful analysis of the various components of pad distortion. In addition to the solution of the biharmonic equation, direct elastic and thermal compression were incorporated. Good agreement was obtained between experimental results for line pivoted pads and a comprehensive theoretical model including distortion. In the same year, Ettles {R17} described a generalised computer analysis for sector shaped tilting pad thrust bearings including distortion. Comparison with published experimental work was sufficiently satisfactory to justify the model used for deflection. The model used the circular plate approximation to the sector. It also assumed a symmetrical pressure distribution about the centre of the plate.

Gardner {R53,1975} experimentally investigated the effect of varying the support position as well as choosing different materials such as copper and aluminium for tilting pads.

The solution for the bending of sectorial plates has recieved considerable attention outside the field of lubrication. The analysis of steam turbine diaphragms prompted Robinsin {R54} in 1923 to consider the deflection of a semicircular plate. Later, Wahl {R55} developed an approximate solution for the bending of a semicircular plate with a central cutout by considering an initially

curved bar, bent out of its plane of initial curvature. His results were used by Taylor {R56} in conjuction with an experimental study and agree well for maximum deflection. Carrier and Ithaca {R57} tabulated deflections of a clamped sectorial plate. Deverall and Thorne {R58} provided several results for sector-shaped plates and rings of varying geometries. The sine transform method was used to obtain the solutions but no indication of errors was given. In 1951, Conway et al {R59} published further results for semicircular and quadrant plates. The magnitude of error was well documented by comparisons with other methods. The analyses used two types of series solutions.

In 1956 Muster and Sadowsky {R60} solved for a semicircular plate, free along the diameter and simply supported along the remaining edge. Chen and Picket {R61} reported results of a numerical method coupled with a series solution for improved accuracy. They report errors of 'considerable' magnitude in a number of previously published results. They also give results for various shapes of plate; for example elliptical and triangular.

Bhattacharya {R62} reviewed some variational techniques based on Galerkin's method, and proceeded to give the maximum deflection for a clamped semicircular plate. Rubin {R63}, in a more recent paper (1975), applied the theorem of minimum potential energy. Depending on the choice of function, accurate results could be obtained. On the other hand an unsuitable function yields large errors.

Lo et al {R64}, in 1977, gave details of a higher order version of the plate equations in a non-clasical form. These equations incorporated shear deflection as well as bending deflection. It appears that the solution of these new equations is unobtainable for sector shaped plates. They give an important estimation of errors involved due to neglecting the shear deflection. For 'thin' plates with a thickness to minimum length ratio of about 1:4, the error is in the range of 4 to 10%.

Thermal deformation of plates was treated by Goodier {R65}. Equations for the solution of thermal deformation have been set out in detail by Szilard {R66}.

In 1980, Ettles {R67} showed that thermal distortion undergoes a size effect; increasing exponentially as the pad size is increased. This emphasizes the increasingly dominant role of deflection in large thrust bearings and the need to account for it in a comprehensive bearing model. In this chapter, a method termed 'the polynomial difference method' is developed for the solution of beam deflection. The method is then applied to plates. The deflection equations of variable rigidity sector shaped thin plates are also given. Comparisons are made with other known solutions. The advantages of the present technique as well as its disadvantages are also given. Finally, other modes of distortion are discussed.

4.1 Development of The Polynomial Difference Method As Applied to Beams

Consider a simply supported , uniformly loaded, beam, where five discrete points (or nodes) are considered along the length (Fig 4F-1). For small deflections:

$$M = - EI \frac{d^2 w}{dx^2} \qquad E4\text{-}1$$

and $$\frac{d^4 w}{dx^4} = - \frac{p}{EI} \qquad E4\text{-}2$$

Assume that the deflection at any node j can be writen as a polynomial:

$$w_j = a_1 + a_2 x_j + a_3 x_j^2 + a_4 x_j^3 + a_5 x_j^4 \qquad E4\text{-}3$$

or

$$w_j = \sum_{i=1}^{5} a_i x_j^{i-1} \qquad E4\text{-}4$$

The coefficients a_i are unknown and are to be determined. For each independent node on the beam an equation of geometry in the form of E4-3 is obtained. Thus five equations are obtained for the five nodal positions. These may be written in matrix form:

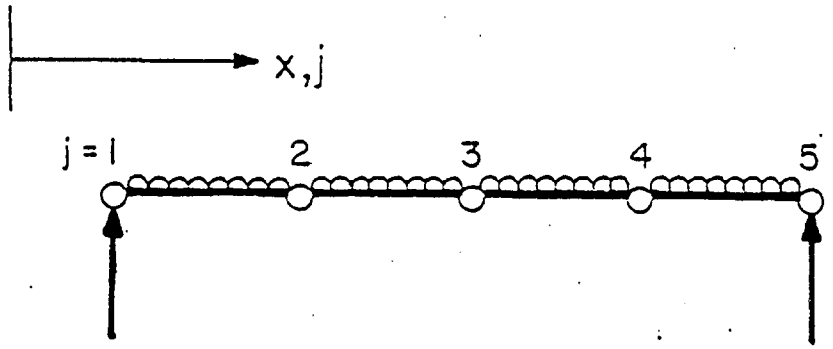

Figure 4F-1 Representation of a Simply Supported Beam

$$\begin{bmatrix} W_1 \\ W_2 \\ W_3 \\ W_4 \\ W_5 \end{bmatrix} = \begin{bmatrix} 1 & x_1 & x_1^2 & x_1^3 & x_1^4 \\ 1 & x_2 & x_2^2 & x_2^3 & x_2^4 \\ 1 & x_3 & x_3^2 & x_3^3 & x_3^4 \\ 1 & x_4 & x_4^2 & x_4^3 & x_4^4 \\ 1 & x_5 & x_5^2 & x_5^3 & x_5^4 \end{bmatrix} \begin{bmatrix} a_1 \\ a_2 \\ a_3 \\ a_4 \\ a_5 \end{bmatrix} \qquad \text{E4-5}$$

$$\text{or} \quad \underline{w} = \bar{A}\underline{a} \qquad \text{E4-6}$$

where $\underline{w}$ is the deflection vector

$\bar{A}$ is the geometry matrix

$\underline{a}$ is the coefficient vector

Differentiating equation E4-3 results in

$$\left(\frac{dw}{dx}\right)_j = 0 + a_2 + 2a_3 x_j + 3a_4 x_j^2 + 4a_5 x_j^3 \qquad \text{E4-7}$$

$$\text{or} \quad \left(\frac{dw}{dx}\right)_j = \sum_{i=1}^{5} a_i (i-1) x_j^{i-2} \qquad \text{E4-8}$$

and differentiating again yields

$$\left(\frac{d^2w}{dx^2}\right)_j = 0 + 0 + 2a_3 + 6a_4 x_j + 12a_5 x_j^2 \qquad \text{E4-9}$$

$$\text{or} \quad \left(\frac{d^2w}{dx^2}\right)_j = \sum_{i=1}^{5} a_i (i-1)(i-2) x_j^{i-3} \qquad \text{E4-10}$$

and $$\left(\frac{d^3w}{dx^3}\right)_j = \sum_{i=1}^{5} a_i\,(i-1)\,(i-2)\,(i-3)\,x_j^{i-4} \qquad \text{E4-11}$$

and $$\left(\frac{d^4w}{dx^4}\right)_j = \sum_{i=1}^{5} a_i\,(i-1)\,(i-2)\,(i-3)\,(i-4)\,x_j^{i-5} \qquad \text{E4-12}$$

For the case in Figure 4F-1, The boundary conditions may be applied as follows,

$w_1=0$ fixed node E4-13

$M_1=0$ moment zero E4-14

$M_5=0$ moment zero E4-15

$w_5=0$ fixed node E4-16

in addition to the beam equation E4-2.

This results in the equation set:

$$\begin{array}{lll}
W_1=0 & 0 = a_1 + a_2 x_1 + a_3 x_1^2 + a_4 x_1^3 + a_5 x_1^4 & \\
M_1=0 & 0 = 2a_3 + 6a_4 x_1 + 12a_5 x_1^2 & \\
M_5=0 & 0 = 2a_3 + 6a_4 x_5 + 12a_5 x_5^2 & \\
W_5=0 & 0 = a_1 + a_2 x_5 + a_3 x_5^2 + a_4 x_5^3 + a_5 x_5^4 & \\
\frac{d^4w}{dx^4} = -\frac{p}{EI} & -\frac{p}{EI} = 24a_5 & \text{E4-17}
\end{array}$$

Or in matrix form

$$\begin{bmatrix} 0 \\ 0 \\ -\frac{p}{EI} \\ 0 \\ 0 \end{bmatrix} = \begin{bmatrix} 1 & x_1 & x_1^2 & x_1^3 & x_1^4 \\ 0 & 0 & 2 & 6x_1 & 12x_1^2 \\ 0 & 0 & 0 & 0 & 24 \\ 0 & 0 & 2 & 6x_5 & 12x_5^2 \\ 1 & x_5 & x_5^2 & x_5^3 & x_5^4 \end{bmatrix} \begin{bmatrix} a_1 \\ a_2 \\ a_3 \\ a_4 \\ a_5 \end{bmatrix} \qquad \text{E4-18}$$

or

$$\underline{b}=\bar{F}.\underline{a} \qquad \text{E4-19}$$

$\bar{F}$ will be termed the condition matrix

$\underline{b}$ will be termed the stress vector

From equation E4-6 an inversion yields

$$\underline{a}=\bar{A}^{-1}\underline{w} \qquad \text{E4-20}$$

where $\bar{A}^{-1}$ is the inverse matrix of $\bar{A}$

Substituting E4-20 in E4-19 yields

$$\underline{b}=\bar{F}\bar{A}^{-1}\,\underline{w} \qquad \text{E4-21}$$

By further inversion E4-21 yields

$$\underline{w} = \bar{A}\bar{F}^{-1}\underline{b} \qquad \text{E4-22}$$

or $$\underline{w} = \bar{X}\,\underline{b} \qquad \text{E4-23}$$

where $$\bar{X} = \bar{A}\bar{F}^{-1} = (\bar{F}\bar{A}^{-1})^{-1} \qquad \text{E4-24}$$

Thus the solution for deflections is obtained in equation E4-23.

Equation E4-21 can be written in the form

$$b_k = \sum_{i=1}^{5}\left[C_{ki}\left(\sum_{j=1}^{5} m_{ij}\, w_j\right)\right] \qquad \text{E4-25}$$

where k refers to the row position in the vector,

m_{ij} represents an element in the matrix $\bar{A}^{-1}$
(Convention: first subscript indicates row
second subscript indicates column)

C_{ki} represents an element in the matrix $\bar{F}$. It represents a factor dependent on the

derivative (whether first, second, third or fourth order) for example (i-1)(i-2) x^{i-3} in equation E4-10 for a second order derivative.

Equation E4-25 effectively describes an algebraic method of obtaining the elements of the matrix $\bar{X}^{-1}$ since from E4-23,

$$\underline{b} = \bar{X}^{-1}.\underline{w} \qquad \text{E4-26}$$

Thus an inversion of matrix $\bar{X}^{-1}$ yields $\bar{X}$. The solution is then obtained as in E4-23.

Consider now the example in figure 4F-2a where a beam is simply supported at two points and has one free end. The beam is uniformly loaded with pressure p_o and the system is divided into twelve nodes (N=12).The boundary conditions are

$$w_1 = 0 \qquad \text{E4-27}$$

$$M_1 = 0 \qquad \text{E4-28}$$

$$w_7 = 0 \qquad \text{E4-29}$$

$$M_{12} = 0 \qquad \text{E4-30}$$

$$V_{12} = 0 \qquad \text{E4-31}$$

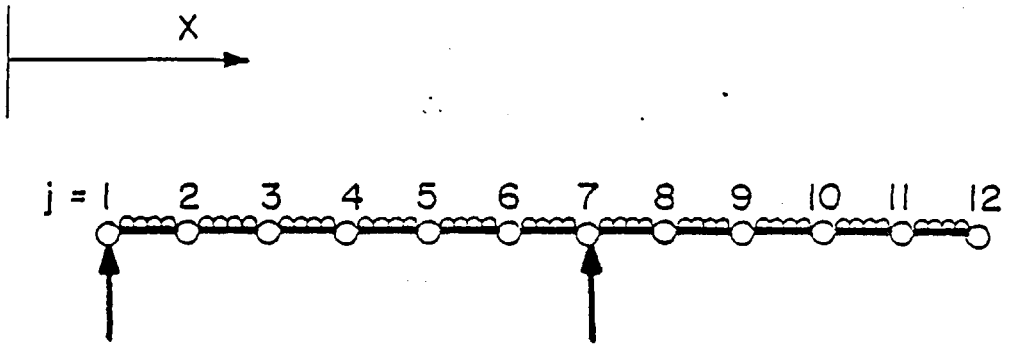

(a)

Beam simply supported at two points and a free end

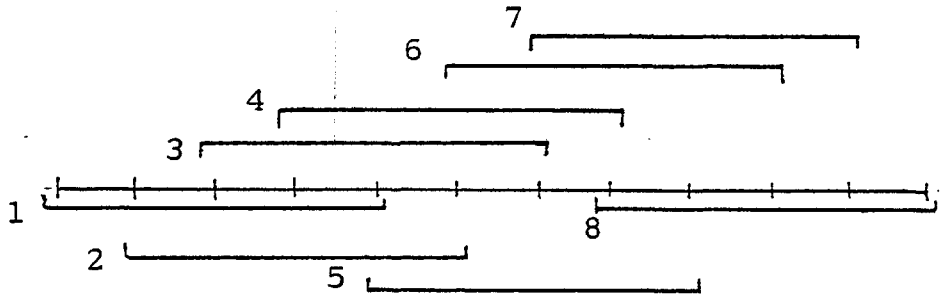

(b)

Positions of Computing Molecules (closely packed)

Figure 4F-2 Beam with Various Boundary Conditions

Suppose it is desired to solve this system using a polynomial for the deflection of the same order n=4 (equation E4-3). The nodes may be grouped together in overlapping molecules of five. For example, nodes 1 to 5 form the first molecule with an associated set of constants a_{11}, a_{12}, a_{13}, a_{14}, a_{15}. Nodes 2 to 6 form the second molecule with constants a_{21}, a_{22}, a_{23}, a_{24}, a_{25}, and so on. In this example N-n=8 molecules are formed, each with its set of constants and geometry matrix $\bar{A}$. Figure 4F-2b shows the position along the beam of the molecules. It appears initially that there are 8x5=40 unknowns but the overlapping of nodes can be used in a simple and systematic way to reduce the system to 12 unknowns. For example, considering the first three molecules only, the geometric relationships can be written

$$\begin{bmatrix} \underline{w}_1 \\ \underline{w}_2 \\ \underline{w}_3 \end{bmatrix} = \begin{bmatrix} \bar{A}_1 & 0 & 0 \\ 0 & \bar{A}_2 & 0 \\ 0 & 0 & \bar{A}_3 \end{bmatrix} \begin{bmatrix} \underline{a}_1 \\ \underline{a}_2 \\ \underline{a}_3 \end{bmatrix} \qquad \text{E4-32}$$

or $$\underline{w}_L = \bar{A}_L \, \underline{a}_1 \qquad \text{E4-33}$$

Here

$$\left[\underline{W}_1\right]^T=\left[W_1,\ w_2,\ w_3,\ w_4\ \ w_5\right] \qquad \text{E4-34}$$

$$\left[\underline{W}_2\right]^T=\left[W_2,\ w_3,\ w_4,\ w_5\ \ w_6\right] \qquad \text{E4-35}$$

$$\left[\underline{W}_3\right]^T=\left[W_3,\ w_4,\ w_5,\ w_6\ \ w_7\right] \qquad \text{E4-36}$$

The geometry matrices $\overline{A}$ are defined by equation E4-5 and E4-6 and involve only the node co-ordinate x. The origin of x can be arbitrary and non-uniform spacing of the nodes can be easily accommadated. The partitioned system E4-32 can be inverted to give:

$$\begin{bmatrix} \underline{a}_1 \\ \underline{a}_2 \\ \underline{a}_3 \end{bmatrix} \quad \begin{bmatrix} \overline{A}_1^{-1} & 0 & 0 \\ 0 & \overline{A}_2^{-1} & 0 \\ 0 & 0 & \overline{A}_3^{-1} \end{bmatrix} \begin{bmatrix} \underline{W}_1 \\ \underline{W}_2 \\ \underline{W}_3 \end{bmatrix} \qquad \text{E4-37}$$

$$\text{or} \qquad \underline{a}_L = \overline{A}_L^{-1}\, \underline{W}_L \qquad \text{E4-38}$$

Each molecule has a condition matrix $\overline{F}$ which can be used to express the governing equation and also the boundary conditions where appropriate. For example for the case in Fig 4F-2. The first

few condition matrices are:

For molecule 1:

$$\begin{matrix} w_1 = 0 \\ M_1 = 0 \\ \text{at (3)} \end{matrix} \quad \begin{bmatrix} 0 \\ 0 \\ -\frac{p}{EI}o \end{bmatrix} = \begin{bmatrix} 1 & x_1 & x_1^2 & x_1^3 & x_1^4 \\ 0 & 0 & 2 & 6x_1 & 12x_1^2 \\ 0 & 0 & 0 & 0 & 24 \end{bmatrix} \begin{bmatrix} a_1 \\ a_2 \\ a_3 \\ a_4 \\ a_5 \end{bmatrix}_1 \qquad \text{E4-39}$$

For molecule 2:

$$\text{at (4)} \quad \left[-\frac{p}{EI}o\right] = \begin{bmatrix} 0 & 0 & 0 & 0 & 24 \end{bmatrix} \begin{bmatrix} a_1 \\ a_2 \\ a_3 \\ a_4 \\ a_5 \end{bmatrix}_2 \qquad \text{E4-40}$$

For molecule 3:

$$\text{at (5)} \quad \left[-\frac{p}{EI}o\right] = \begin{bmatrix} 0 & 0 & 0 & 0 & 24 \end{bmatrix} \begin{bmatrix} a_1 \\ a_2 \\ a_3 \\ a_4 \\ a_5 \end{bmatrix}_3 \qquad \text{E4-41}$$

etc., for molecules 4, 6 and 7.

For molecule 5:

$$\text{at (7)} \quad \begin{bmatrix} 0 \end{bmatrix} = \begin{bmatrix} 1 & x_7 & x_7^2 & x_7^3 & x_7^4 \end{bmatrix} \begin{bmatrix} a_1 \\ a_2 \\ a_3 \\ a_4 \\ a_5 \end{bmatrix}_5 \qquad \text{E4-42}$$

Finally for molecule 8:

$$\begin{matrix} \text{at (10)} \\ M_{12} = 0 \\ V_{12} = 0 \end{matrix} \quad \begin{bmatrix} -\frac{p_o}{EI} \\ 0 \\ 0 \end{bmatrix} = \begin{bmatrix} 0 & 0 & 0 & 0 & 24 \\ 0 & 0 & 2 & 6x_{12} & 12x_{12}^2 \\ 0 & 0 & 0 & 6 & 24x_{12} \end{bmatrix} \begin{bmatrix} a_1 \\ a_2 \\ a_3 \\ a_4 \\ a_5 \end{bmatrix}_8 \qquad \text{E4-43}$$

The above constitute 12 equations. The overlapping nodes give

28 further equations. For example node 2 is present in molecules 1 and 2, thus:

$$w_{2,1} - w_{2,2} = 0 \qquad \text{E4-44}$$

$$\text{or} \quad [0] = \left[1 \; x_2 \; x_2^2 \; x_2^3 \; x_2^4 \; -1 \; -x_2 \; -x_2^2 \; -x_2^3 \; -x_2^4\right] \left[a_{11} \; a_{12} \; a_{13} \; a_{14} \; a_{15} \; a_{21} \; a_{22} \; a_{23} \; a_{24} \; a_{25}\right]^T \qquad \text{E4-45}$$

The system of 40 equations can be set up as

$$\underline{b}_L = \overline{F}_L \cdot \underline{a}_L \qquad \text{E4-46}$$

The corresponding geometry system has already been derived (equation E4-38) and is

$$\underline{a}_L = \overline{A}_1^{-1} \, \underline{w}_L \qquad \text{E4-38}$$

Using E4-38 in E4-46 gives

$$\underline{b}_L = \overline{F}_L \overline{A}_L^{-1} \cdot \underline{w}_L \qquad \text{E4-47}$$

$$\text{or} \qquad \underline{b}_L = \overline{C}_L \cdot \underline{w}_L \qquad \text{E4-48}$$

Although E4-48 represents a system of 40 equations, it should be remembered that the solution matrix $\underline{w}_L$ contains repeats of the

deflections at individual nodes. Furthermore $\bar{A}_L^{-1}$ has a simple partitioned structure as shown in E4-37. Equation E4-48 may be restructured to order 12, prior to inverting $\bar{C}_L$ to obtain the solution. It is never actually necessary to form the full equation set. Instead, the reduced form (of order 12) can be assembled directly (doing away with overlapping and placing elements in the matrix in relation to their respective deflections directly .)

The solution for deflection follows as previously:

$$\underline{w}_L = \bar{X}_L . \underline{b}_L \qquad \text{E4-49}$$

The choice of order n of the molecule depends on the equation to be solved. To complete the deflection of beams at least a fourth-order polynomial is necessary to accomadate the governing equation. Higher orders can also be used. The maximum order is limited by the total number of nodes in the grid.

4.2 Application of the Method to Beams

For the case of the simply supported beam Fig 4F-1, the deflection may be given,

$$w = p_o \left(-\frac{x^4}{24} + \frac{lx^3}{12} - \frac{l^3 x}{24} \right) \qquad \text{E4-50}$$

where l is the length of the beam

x is the distance along the beam

(beginning at the left support)

p_o the constant pressure

EI is assumed equal to unity

Hence the central deflection is $5p_o l^3/384$.

Using the technique outlined in section 4.1, the numerical method was able to reproduce the central deflection with n=5. Thus only 5 nodes are required to give the exact analytical solution. This is not surprising since an examination of equation E4-50 reveals a fourth order polynomial. The method was applied to a uniformly loaded cantilever beam. Five nodes are again used. Node 5 was designated the free edge and consequently the boundary condition

$$\left(\frac{d^3w}{dx^3}\right)_5 = 0 \qquad \text{(or shear force at edge=0)} \qquad \text{E4-51}$$

replaced the condition w=0 for the simply supported case. Again the exact analytical solution ($p_o l^4/8$) was reproduced.

A beam with varying load may be treated in two ways. Higher order molecules may be used. Thus for a parabolic load profile n=6 is required. Another method is to use n=4 molecules but increase the number of nodes. This latter method can handle any type of load distribution provided enough nodes are used. It also has the

advantage of smaller geometry matrices (which require inversion). Its disadvantage is that the solution is only approximate.

Consider the cantilever shown in Fig 4F-3 where the pressure varies arbitrarily. At the free end the boundary conditions of zero bending moment and zero shear force give at node 1:

$$\left(\frac{d^2w}{dx^2}\right)_1 = 0 \qquad \text{E4-52}$$

$$\left(\frac{d^3w}{dx^3}\right)_1 = 0 \qquad \text{E4-53}$$

For any arrangement of nodes, the geometry matrices (which are solely dependent on node position) can be easily derived. To illustrate the effect on accuracy of considering a varying load, the test case shown in the inset of Figure 4F-4 was evaluated using the polynomial difference method outlined. To accentuate errors due to non-uniform loading, particularly near the free end, the loading is assumed to increase parabolically to a maximum value at the tip. Figure 4F-4 shows the error for uniformly distributed nodes (line 'a') and for the cases where the first mesh length $\beta.\Delta x$ (at free end, see Figure 4F-3) was $0.1\Delta x$ and $0.01\,\Delta x$ respectively,as shown by lines 'b' and 'c'. It can be seen that non-uniform loading can be accurately computed given a sufficient number of nodes and that the accuracy can be improved by grouping nodes at the free end.

In the above cases, only two support positions were chosen. A

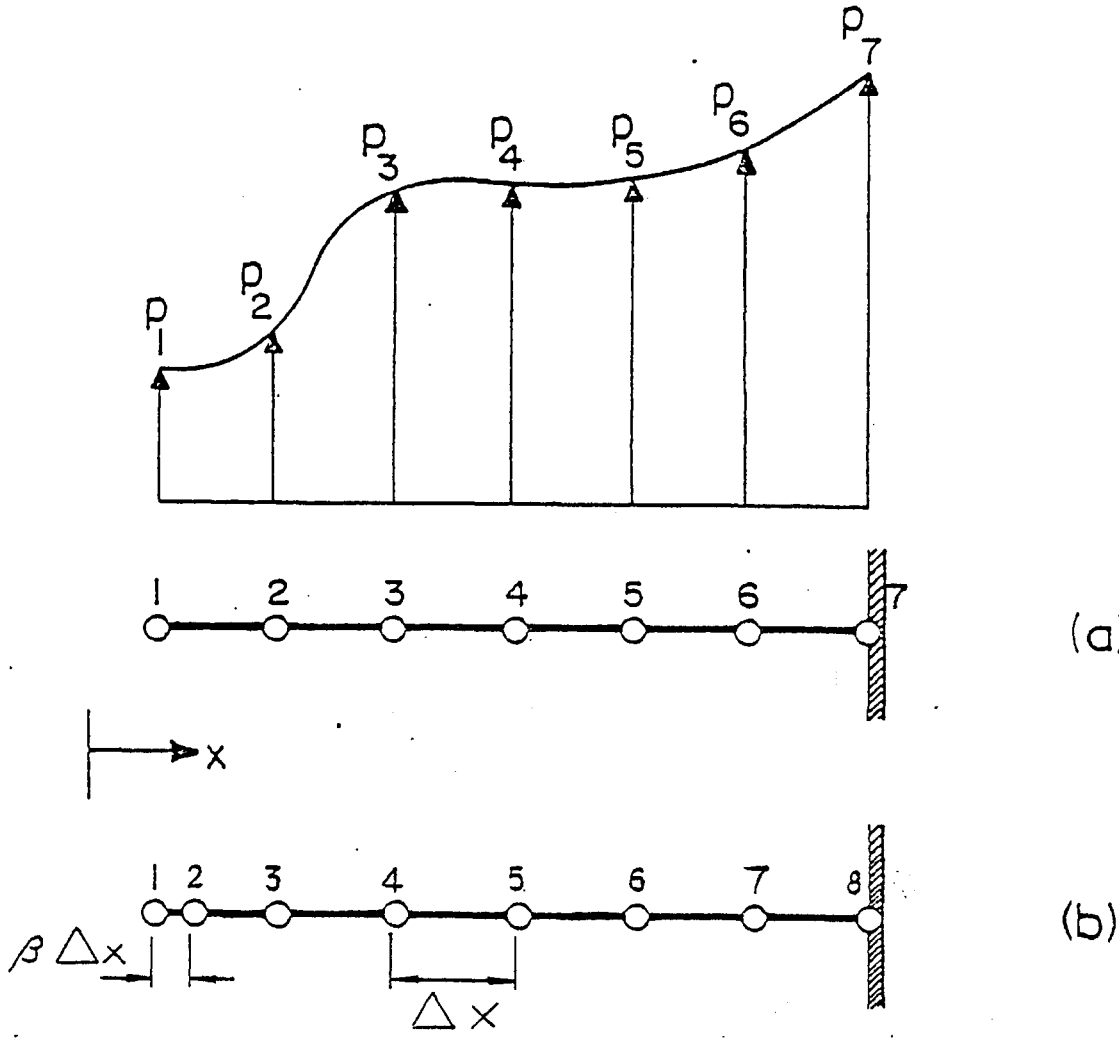

Figure 4F-3 Cantilever Beam Grids

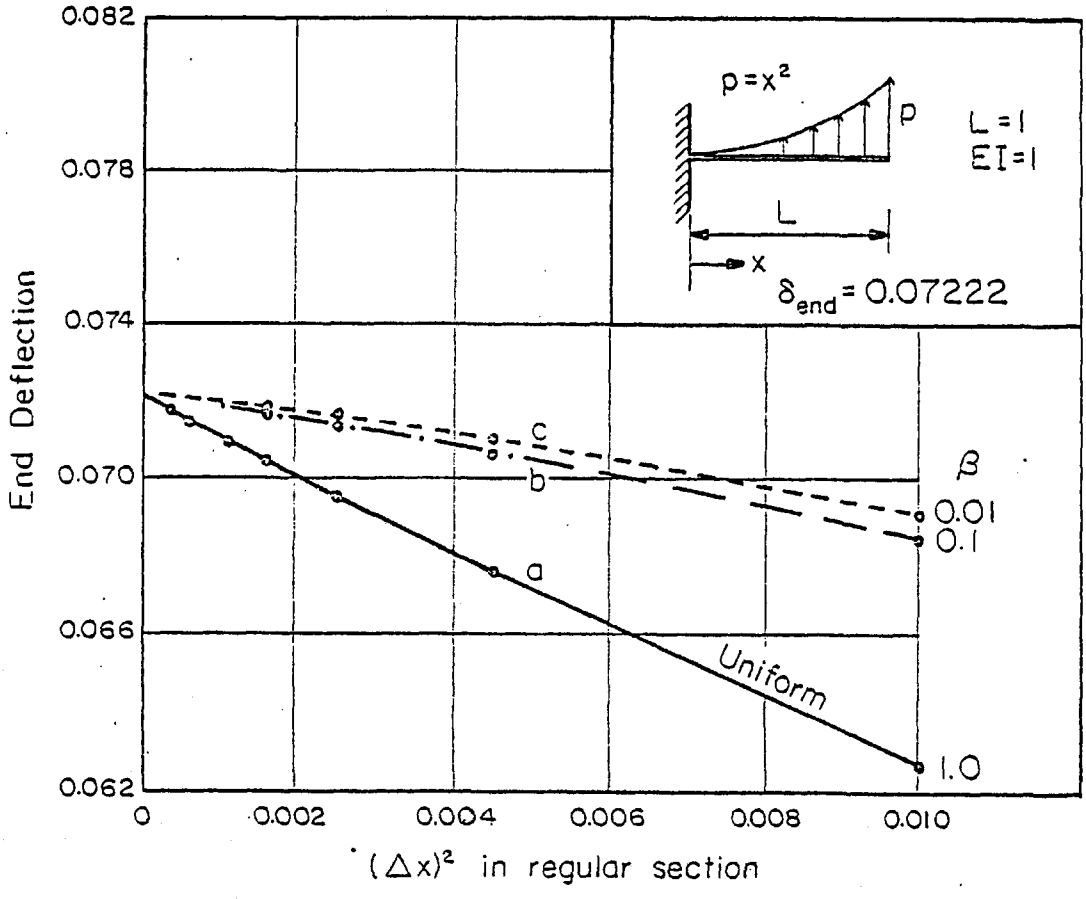

Figure 4F-4 End Deflection Versus the Square of the Mesh Length for a Cantilever with a Non-uniform Load Distribution

beam simply supported at five points is a far more complex case, and requires even more nodes for a correct and accurate solution. Figure 4F-5 shows the deflection of a beam supported at evenly spaced intervals with a uniform load. The effect of varying the number of nodes (number of intervals +1) is also shown. If five nodes are chosen - themselves the support points - then no deflection is possible. For nine nodes (that is , inserting one node between every two supports) the pattern shows a large negative deflection near the beam edges. Using 17 nodes and successively increasing the number, a clear patern emerges for deflection as shown for the 65 node solution.

The effect of a load distribution is shown in Fig 4F-6 for a beam - simply supported at stations 1/4 and 3/4 length along the beam. The total load was equal to unity for both the linear and the parabolic distributions ,(the parabolic distribution is symmetrical and has a maximum at the beam centre). The position of maximum positive deflection is reversed for the different loadings. A large negative deflection is possible for the parabolic load distribution. The deflection patterns will depend on the support positions, too. If the beam is supported at the edges then the deflection pattern for both distributions will be closer to curve i - concave. On the other hand if the supports are positioned very close to each other, then the deflection pattern is similar to curve ii - convex.

For the case of a beam supported elastically,the boundary condition at the support is:

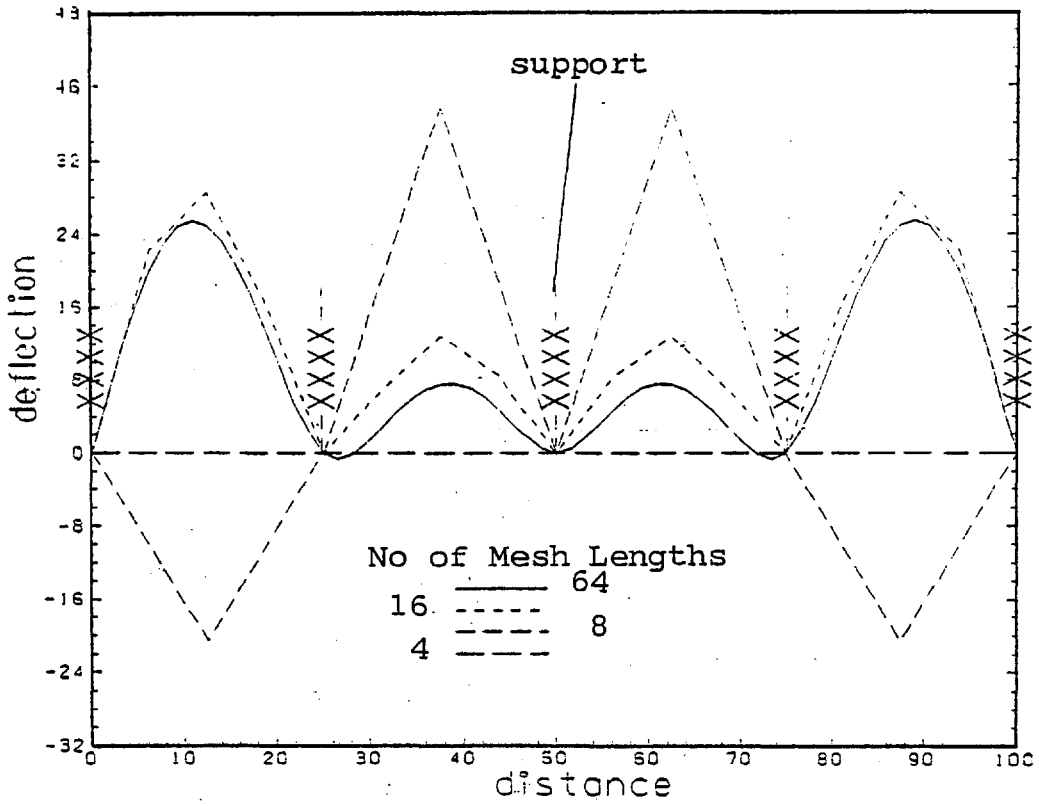

Figure 4F-5 Uniformly Loaded Beam Supported at Five Points

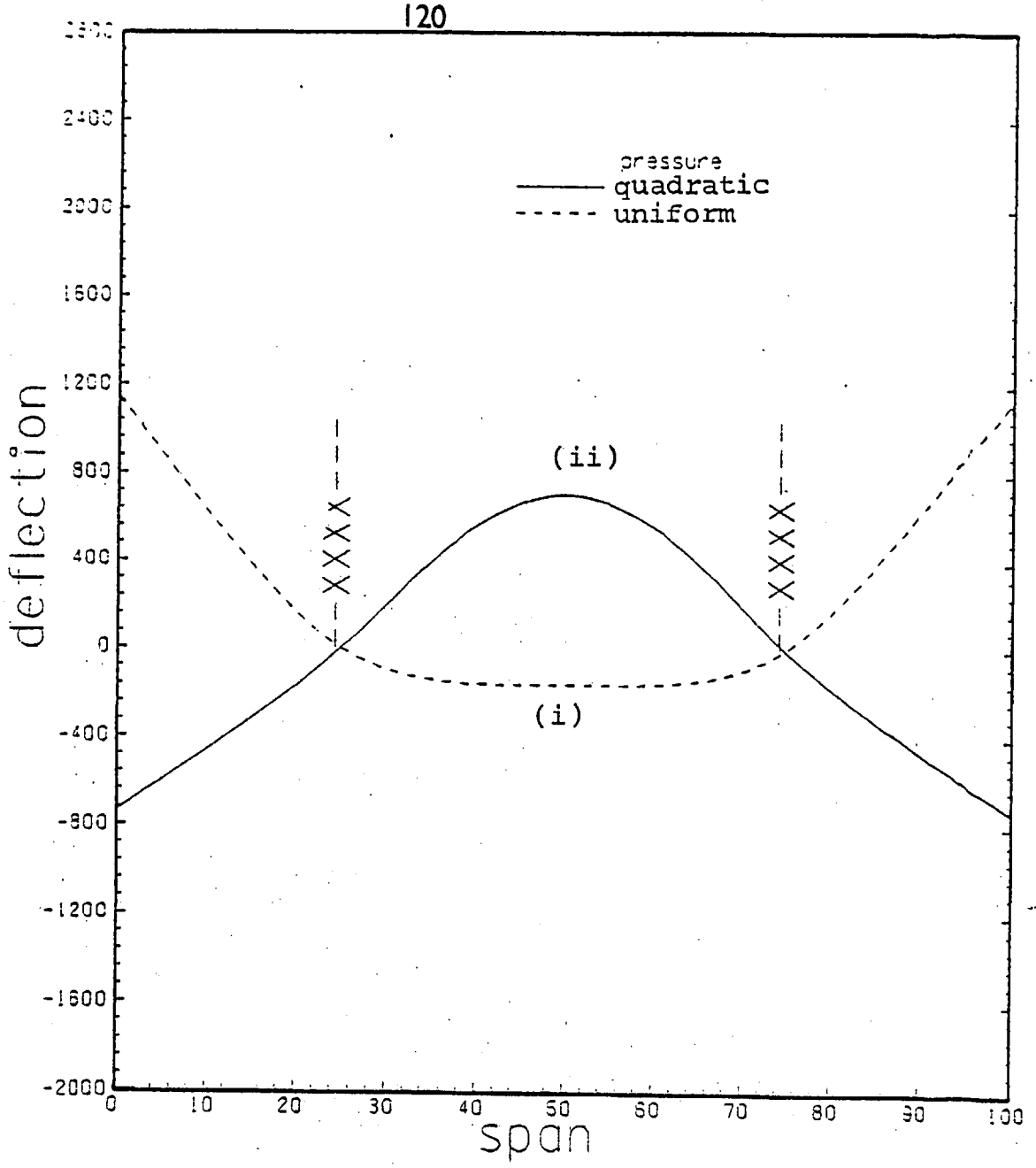

Figure 4F-6 Effect of Load Distribution in a Beam

$$\frac{d^4w}{dx^4} = - \frac{p}{EI} + \frac{kw}{\epsilon EI} \qquad \text{E4-54}$$

where ϵ is the length of the beam element associated with the support node.

k is the stiffness of the support

Thus the elastic support exerts a force modelled in a similar manner to the pressure (more on point forces follow in the next section). Three elastic supports (k=1) are used for the example presented in Fig 4F-6*B* The deflections for a constant load distribution as well as a parabolic one are shown. The total load - in both cases - is unity. Summing the deflections at the three support positions gives a total deflection of one for both cases, confirming the validity of the model.

4.3 Handling of Singular Boundary Conditions:

The representation of a point force at the centre of a simply supported beam can be modelled as a pressure over an appropriate length. This may be done as in case(a), Fig 4F-7, where for the central node the pressure p is set as $P=F/\Delta x$. The error is shown in Fig 4F-8 as a function of $(\Delta x)^2$, together with the central processor time for inversion of the system using a CDC 6500 machine. Since

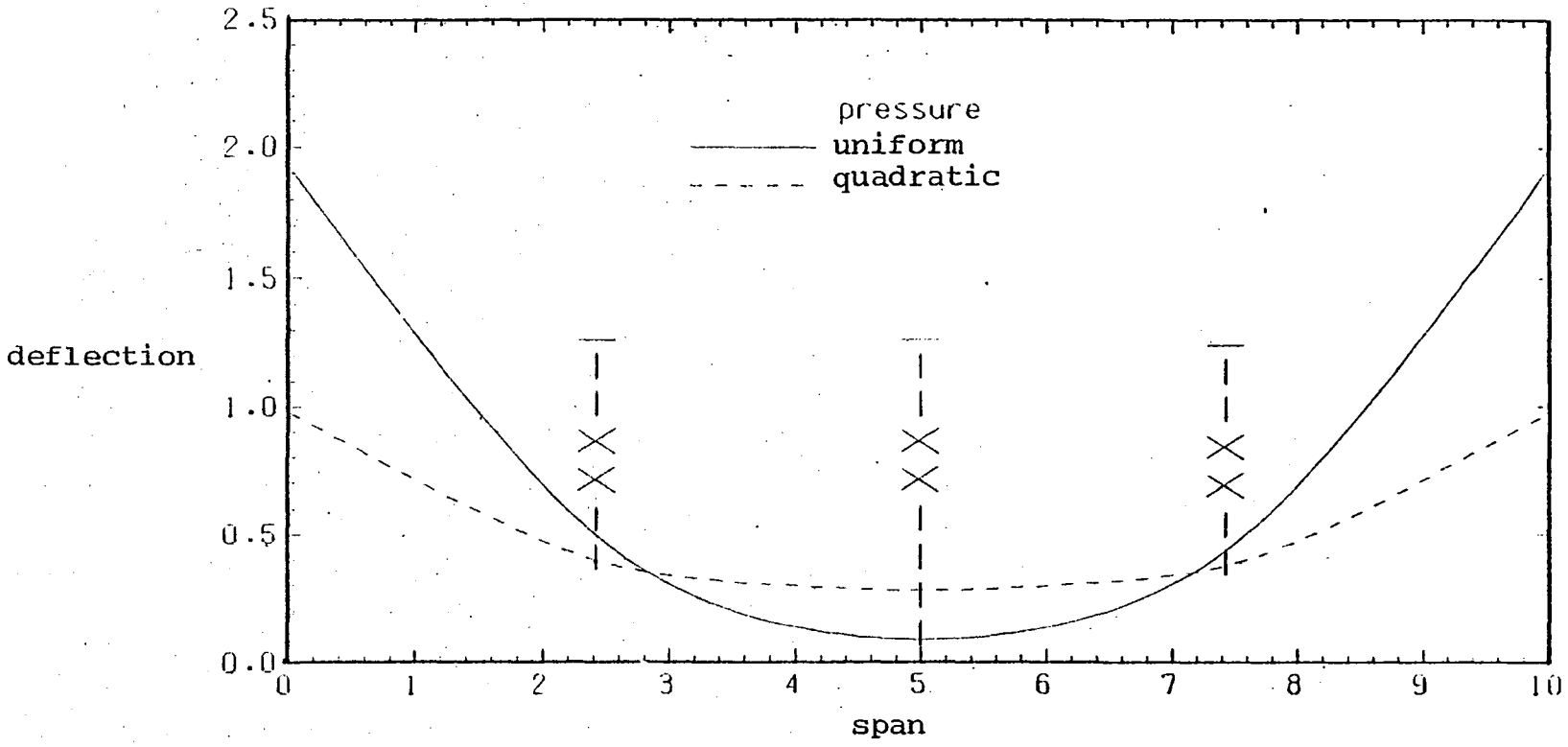

Figure 4F-6B Deflections for an Elastically Supported Beam

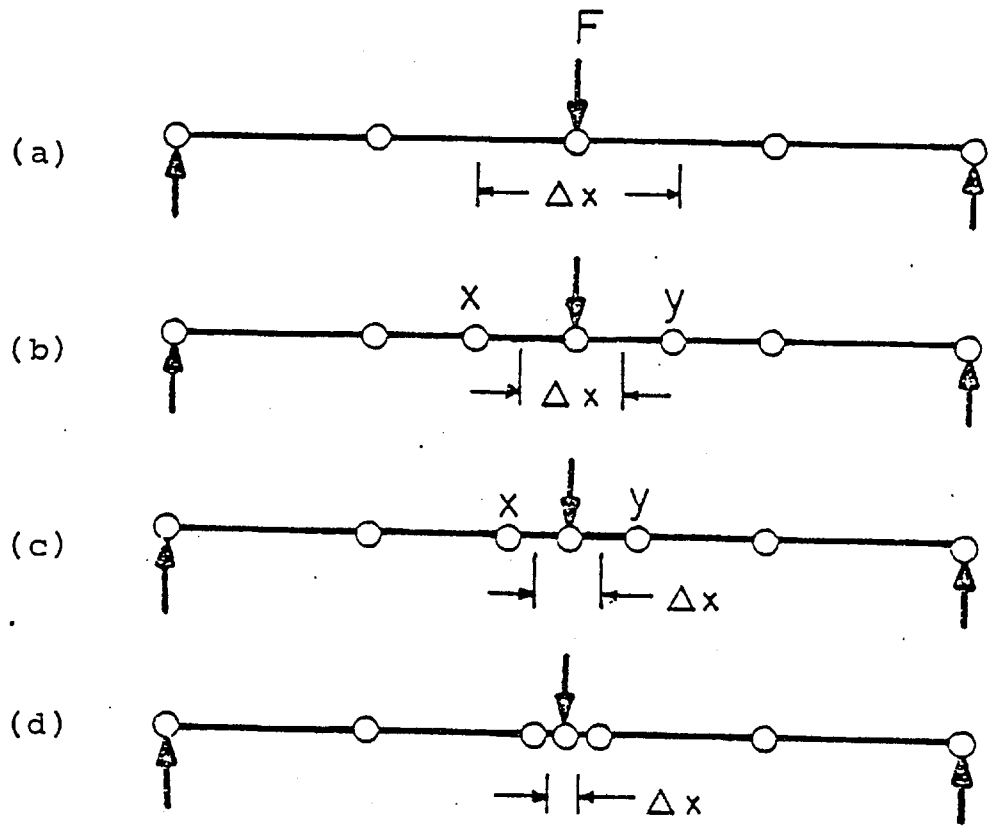

Figure 4F-7 Representation of a Point Force

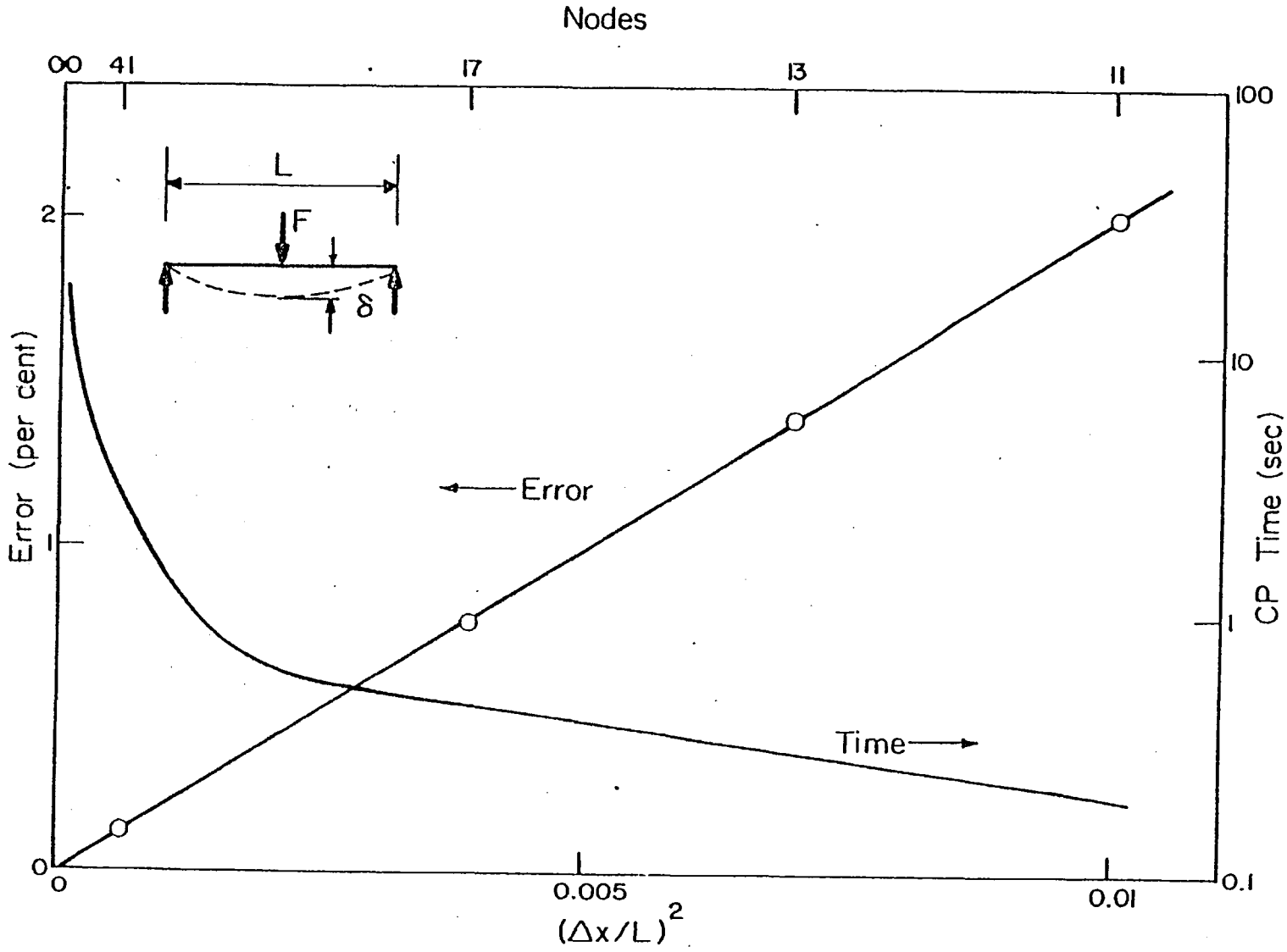

Figure 4F-8 Percentage Error Versus Square of Mesh Length

the method allows for a non-uniform mesh, the effect of modelling the point force as shown in Fig F4-7 cases b, c, and d was attempted. Extra nodes X, Y are added and the force distributed over the lengths shown. The solutions obtained for b, c,and d reflected more accurate modelling of the point force. When X and Y are brought closer together the accuracy of the solution continues to improve towards the analytical solution.

The method may be thought of as a combination of the finite difference and finite element methods at a value of n=5. The simplicity with which the nodes are arranged resembles the arrangement of nodes in a typical finite diference (FD) grid. As the number of nodes are increased the accuracy increases in proportion to the square of the mesh length - again as would be expected from a FD arrangement. On the other hand, nodes may be grouped (as discussed earlier in the section) to improve the accuracy - typical of finite element (FE) grids. This does not require a modification to the method. The boundary conditions are inserted in a similar manner as in a typical finite element scheme. This allows a greater flexibility than a pure FD arrangement - where fictitious nodes may be necessary and the computing molecules adjusted. At values of n greater than 5, the method possesses the ability to deal with higher order equations (greater than 4th order), again without any extra modifications. For both the FE and FD methods the 'molecules' or 'elements' used have to be changed (or extended) to handle the higher orders.

4.4 The Polynomial Difference Method for Variable Rigidity Sector Shaped Thin Plates

The equations for variable rigidity thin sector shaped plates have been derived and are given in Appendix G. Both thermal and elastic distortion are considered. The principal complication is that the governing equation is very lengthy, containing twelve differential terms of deflection. An advantage of the polynomial difference method is that these terms, and others for the boundary conditions, can be easily expressed. In principle any polynomial of sufficiently high order may be applied. A 5x5 grouping of nodes was taken as the basic molecule where:

$$
\begin{aligned}
w_{ij} = {} & a_1 + a_2\,\theta_j + a_3\,\theta_j^2 + a_4\,\theta_j^3 + a_5\,\theta_j^4 \\
& + (a_6 + a_7\,\theta_j + a_8\,\theta_j^2 + a_9\,\theta_j^3 + a_{10}\,\theta_j^4)\, r_i \\
& + (a_{11} + a_{12}\,\theta_j + a_{13}\,\theta_j^2 + a_{14}\,\theta_j^3 + a_{15}\,\theta_j^4)\, r_i^2 \\
& + (a_{16} + a_{17}\,\theta_j + a_{18}\,\theta_j^2 + a_{19}\,\theta_j^3 + a_{20}\,\theta_j^4)\, r_i^3 \\
& + (a_{21} + a_{22}\,\theta_j + a_{23}\,\theta_j^2 + a_{24}\,\theta_j^3 + a_{25}\,\theta_j^4)\, r_i^4
\end{aligned}
\qquad \text{E4-55}
$$

or

$$
w_{ij} = \sum_{l=1}^{5} \sum_{k=1}^{5} r_i^{l-1}\, \theta_j^{k-1}\, a_m \qquad \text{E4-56}
$$

where $m = 5\,(l-1) + k$ E4-57

(see Fig 4F-9)

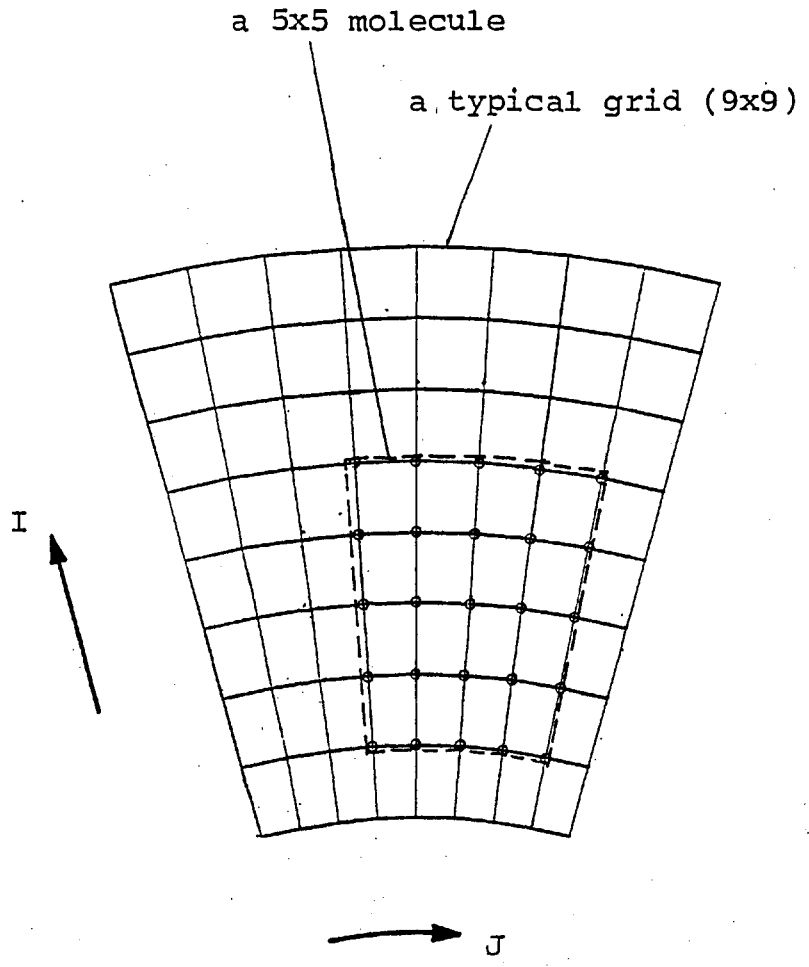

Figure 4F-9 Position of a Molecule in the Grid

The geometric relationships similar to equations E4-5 and E4-6 can be formed to give:

$$\underline{w} = \bar{A}.\underline{a} \qquad \text{E4-58}$$

where $\bar{A}$ is of the order 25x25. A condition matrix $\bar{F}_L$ may be derived by applying the governing equation or the boundary conditions in the same way as has been shown for beams

$$\underline{b}_L = \bar{F}_L.\underline{a}_L \qquad \text{E4-59}$$

In $\bar{F}_L$, each row may be composed of a summation of derivatives as required. It is not necessary to the method for the molecules to overlap closely, although close overlap has been assumed in the examples given on beams. For example if a 9x9 grid is used to define the plate, four 5x5 molecules may be used. This results in 100 coefficients and 81 nodes, of which 19 are overlapping (Fig 4F-10). As in equations E4-38 to E4-49 one finally obtains:

$$\underline{w}_L = \bar{X}_L.\underline{b}_L \qquad \text{E4-60}$$

where $$\bar{X}_L = \bar{C}_L^{-1} \qquad \text{E4-61}$$

molecule 1

molecule 2

molecule 3

molecule 4

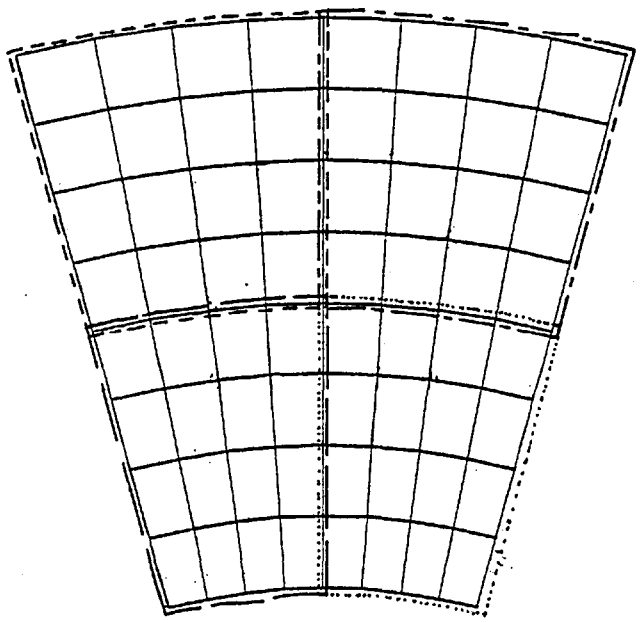

Figure 4F-10 Loosely Packed Molecules for a 9x9 Grid

It is possible to set up an iterative process to solve for a particular stress vector $\underline{b}_L$. Thus for the system described by E4-60 and E4-61:

$$\overline{C}_L \cdot \underline{w}_L = \underline{b}_L \qquad \text{E4-62}$$

Since the molecules are 5x5, each row in matrix $\overline{C}_L$ will contain 25 non trivial coefficients. The deflection at one node may be expressed:

$$\sum_{k=1}^{25} C_k \, w_k = b \qquad \text{E4-63}$$

or

$$w_1 = \frac{b - \sum_{k=2}^{25} C_k \, w_k}{C_1} \qquad \text{E4-64}$$

Equation E4-64 expresses deflection w_1 in terms of the deflections in the molecule. Thus once matrix $\overline{C}_L$ is set up it can be directly inverted to yield $\overline{X}_L$, or, the equations set in an iterative form as in E4-64; one equation for each row in matrix $\overline{C}_L$. The two methods can act as a check for each other. This was done

for several of the test cases (mentioned later in section 4.5). The solutions for both methods were identical for any one case. Typically, the iterative solution requires 500 to 4000 iterations for grid sizes of 9x9 to 19x19 respectively.

The direct matrix inversion method was used as the main solution technique. It has an important advantage over the iterative technique in that once $\bar{X}_L$ is obtained any stress vector can be handled by a simple matrix-vector multiplication (E4-60). The iterative technique, on the other hand, will require a large number of iterations for each different stress vector. It will be shown later that the solution for several different stress vectors is required (see Chapter 5). In addition storage problems in the assembled bearing program favour the direct matrix inversion method (see Chapter 5.) A typical direct matrix inversion for a 9x9 mesh requires less 100 CP seconds whereas the iterative solution may take up to 1000 CP seconds.

4.5 Test Cases for Plates

Case 1: The equations for deflection of thin rectangular plates are given by Szilard {R66}. For a rectangular plate of breadth a and length 2a the maximum deflection is given as {R66}:

$$w_{max} = 0.0101\ p_o a^4/D \qquad \text{E4-65}$$

where p_o is a uniform load (pressure) over the plate - simply supported at all edges.

The boundary conditions are shown in Fig 4F-11a. The nodes at which the governing equation is applied are shown in Fig 4F-11b. Here the deflection at the node is expressed in terms of the governing equation applied at that node. It is possible to express the application of the governing equation at the node (5,5)(see Fig 4F-11b) using any node within a 5x5 molecule containing node (5,5). This is shown in Fig 4F-11c. Nodes (1,3) or (9,9) can both be used. If it is decided to use node (1,3) then the geometry matrix for molecule 3 is used. If node (9,9) is chosen then molecule 2 is used. It should be remembered that each node in the grid is represented by one row in matrix $\overline{C}_L$, that is, one equation. Therefore, if (1,3) is used, the deflection at node (1,3) is expressed in terms of the governing equation applied at node (5,5). For simplicity, the deflection at node (5,5) is expressed by the governing equation applied at node (5,5).

Figure 4F-11a shows that two boundary conditions must be satisfied at each edge (M_x=0, M_y=0, w=0). At the corners three boundary conditions are required. For each edge location, only one node is available. Thus, the deflections at the row closest to the boundary are used to express the second boundary condition applied at the edge locations. This is shown in Fig 4F-11b. At the edge

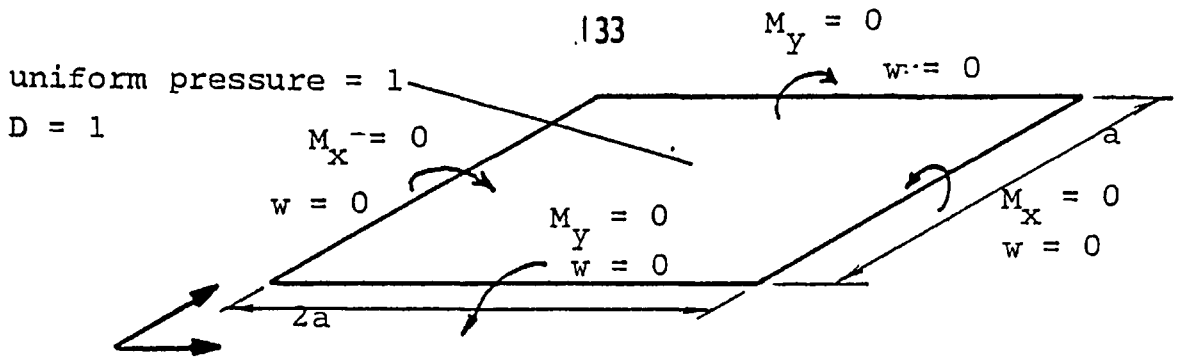

(a)

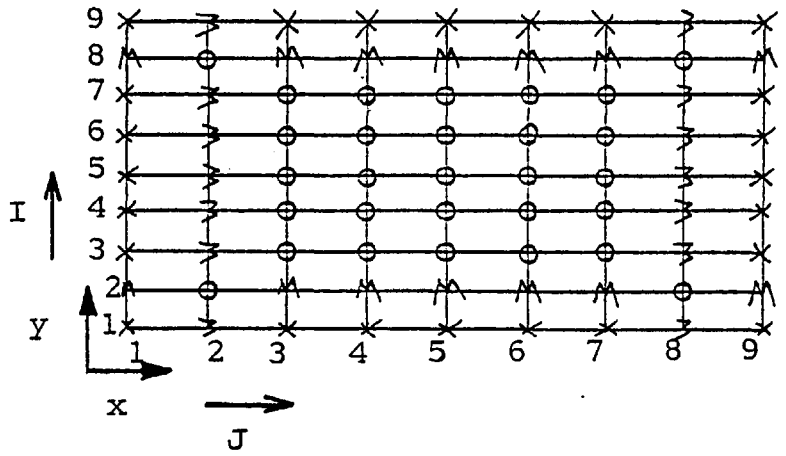

o pressure node

$M_y = 0$

$M_x = 0$

(b)

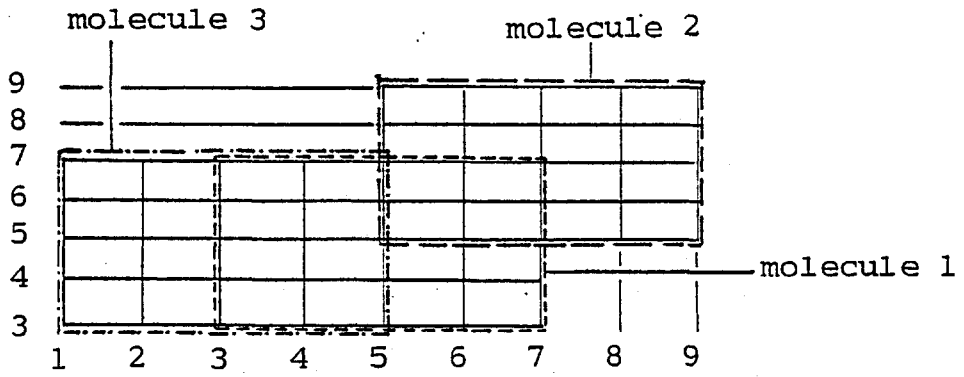

(c)

Figure 4F-11 Case (i) - Boundary Conditions

location, the three closest nodes are used (see Fig 4F-11b).

The results for maximum deflection versus the square of the mesh length for several grid sizes is shown in Fig 4F-12. The extrapolated value for an infinite mesh size is identical with the analytical solution in equation E4-65. The error for the 9x9 grid is less than 6%. For grids larger than 11x11 the iterative method is always used (see discussion of advantages '4.6' and drawbacks '4.8' for reasons).

Case ii: Figure 4F-13a shows a uniformly loaded clamped circular plate also supported at its centre. The boundary condition distribution is shown in Fig 4F-13b. Szilard [R66] gives the deflection as:

$$w = \frac{p_o}{64D} r_o^4 \left(\frac{r}{r_o}\right)^2 \left(\left(\frac{r}{r_o}\right)^2 - 1 - 2 \ln \frac{r}{r_o} \right) \qquad \text{E4-66}$$

Thus for D=1; p_o=1; r_o=1; r=0.5

$$w = 2.48552 \times 10^{-3} \qquad \text{E4-67}$$

Fig 4F-14 shows the deflections at r=0.5 plotted versus the square of the mesh length. For a 9x9 grid an error of about 6% results. For a 15x15 grid the error reduces to about 2%.

Case iii: Figure F4-15 shows a circular plate simply supported at

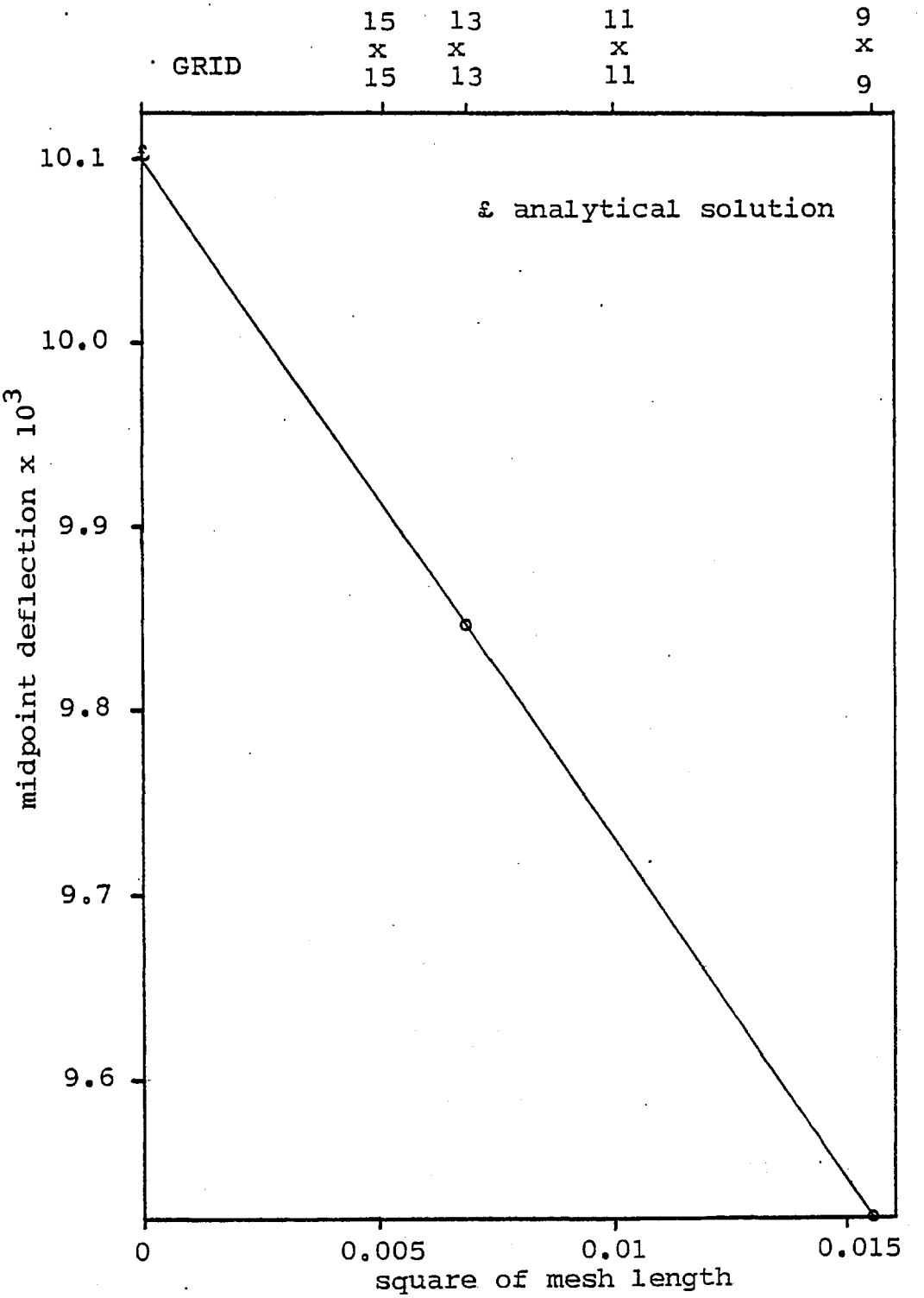

Figure 4F-12 Maximum Deflection Versus Square of Mesh Length - Case (i)

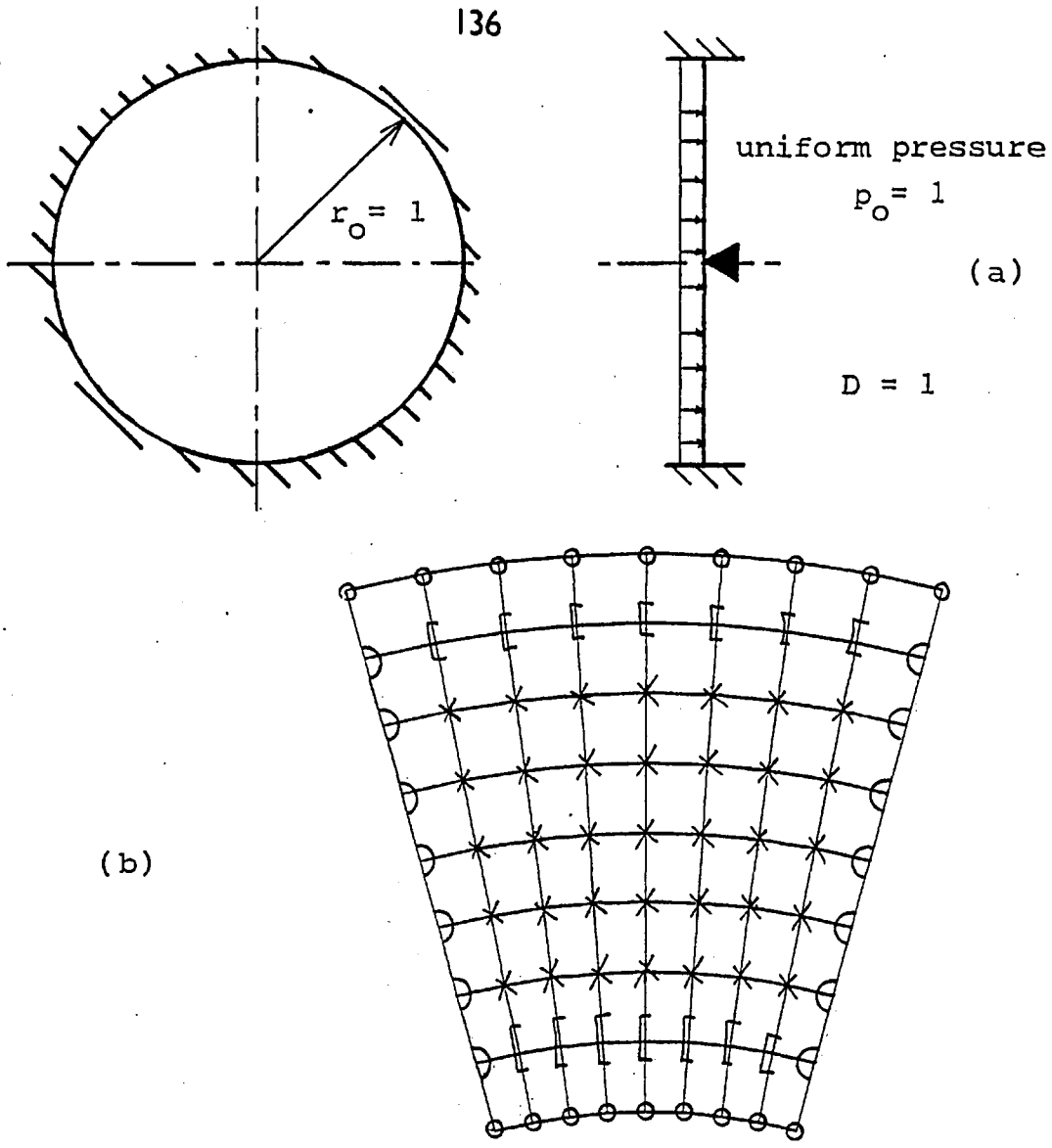

Figure 4F-13 Case (ii) - The Grid and Boundary Conditions

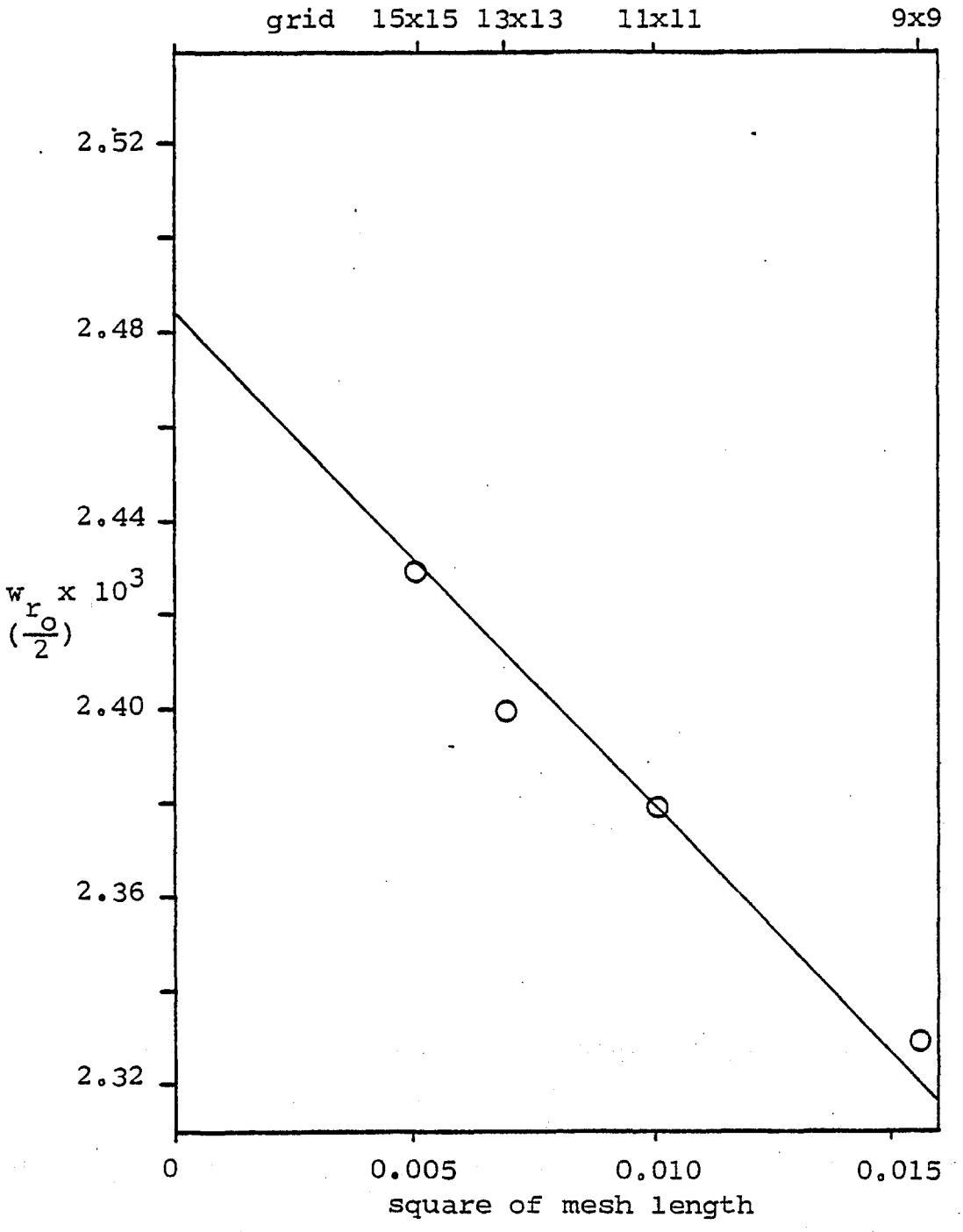

Figure 4F-14 Case (ii) - r_{mean} Deflection Versus Square of Mesh Length

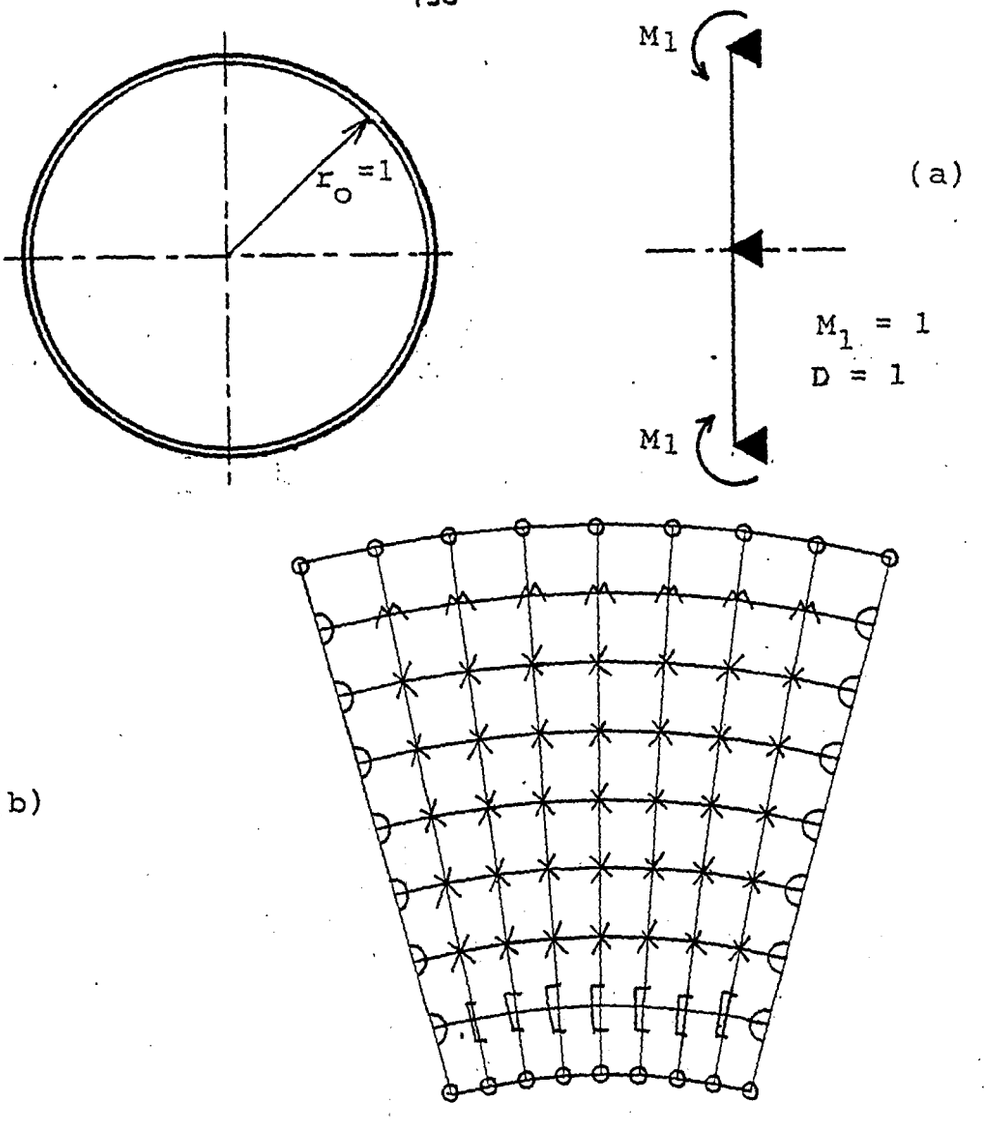

Figure 4F-15 Case (iii) - The Grid and Boundary Conditions

the outer edge and inner edge. In addition a moment M_1 is applied at the outer edge. Szilard gives the deflection as,

$$w = \frac{-M_1 r_o^2}{D(3+\nu)} \left(\frac{r}{r_o}\right)^2 \ln\left(\frac{r}{r_o}\right) \qquad \text{E4-68}$$

For $M_1 = r_o = D = 1$ and $\nu = 0.3$ $r = 0.5$

$$W = 0.0525112$$

The boundary conditions are shown in Fig 4F-15b. A plot of deflection at r=0.5 versus grid size is shown on Fig 4F-16. A 9x9 grid yields 4% error whereas a 15x15 grid yields 2% error. It should be noted that all deflections are due to the edge moment alone ($p_o = 0$).

Case iv: This case deals with a ring simply supported at its outer edge. A shear force at its inner edge is applied - as shown in Fig 4F-17. Szilard {R66} gives the deflection as:

$$w = \frac{F_1 r_o^2 r_1}{8D}\left[\left(\frac{3+\nu}{1+\nu} - 2K\right) C_1 + 4\frac{(1+\nu)}{(1-\nu)} K C_3 + 2C_2\right] \qquad \text{E4-69}$$

where

$$K = \frac{\beta^2}{1-\beta^2} \ln\beta \qquad \text{E4-70}$$

$$\beta = \frac{r_1}{r_o} \qquad \text{E4-71}$$

$$C_1 = 1 - \left(\frac{r}{r_o}\right)^2 \qquad \text{E4-72}$$

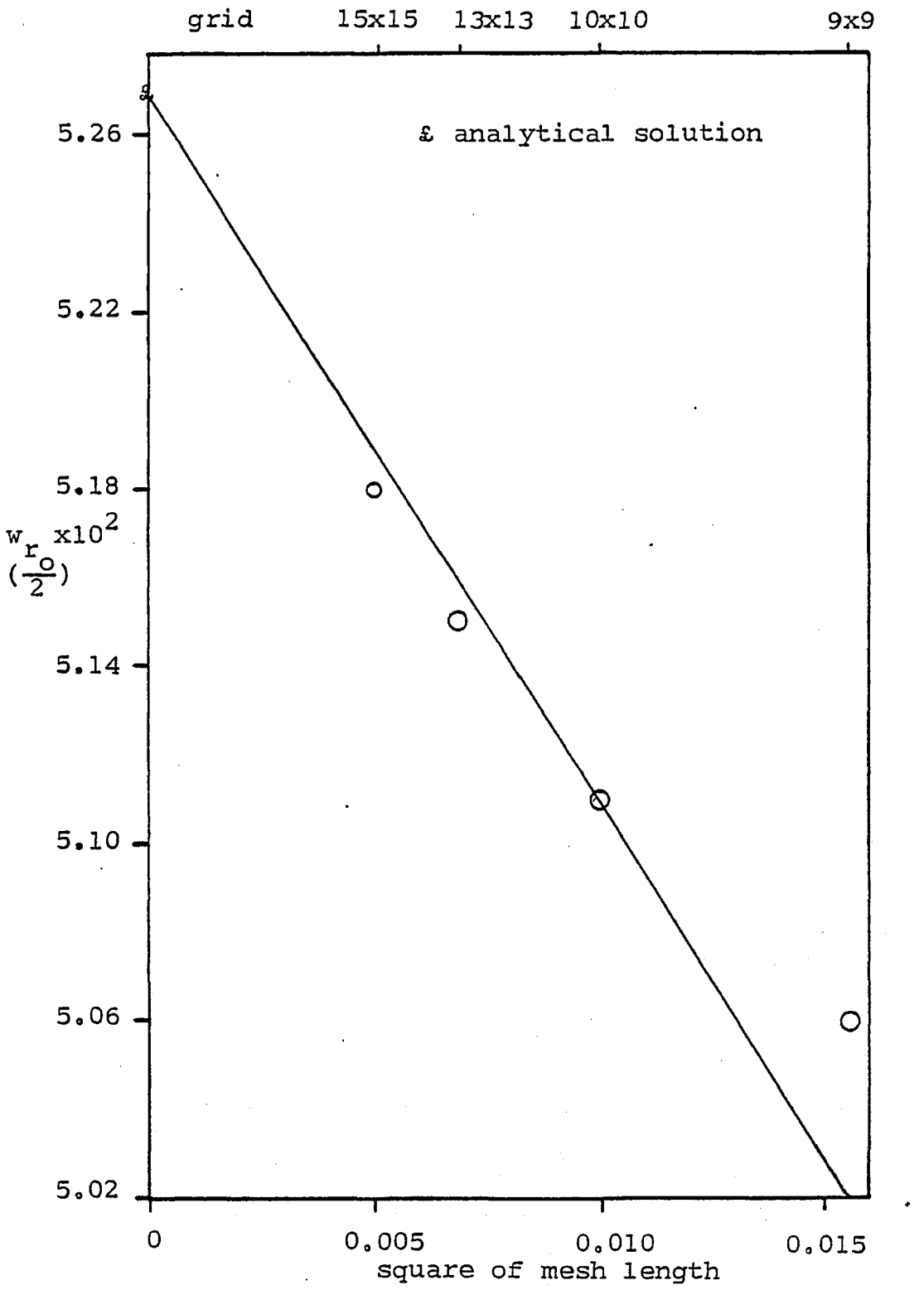

Figure 4F-16 Case (iii) - $r_o/2$ deflection Versus Square of Mesh Length

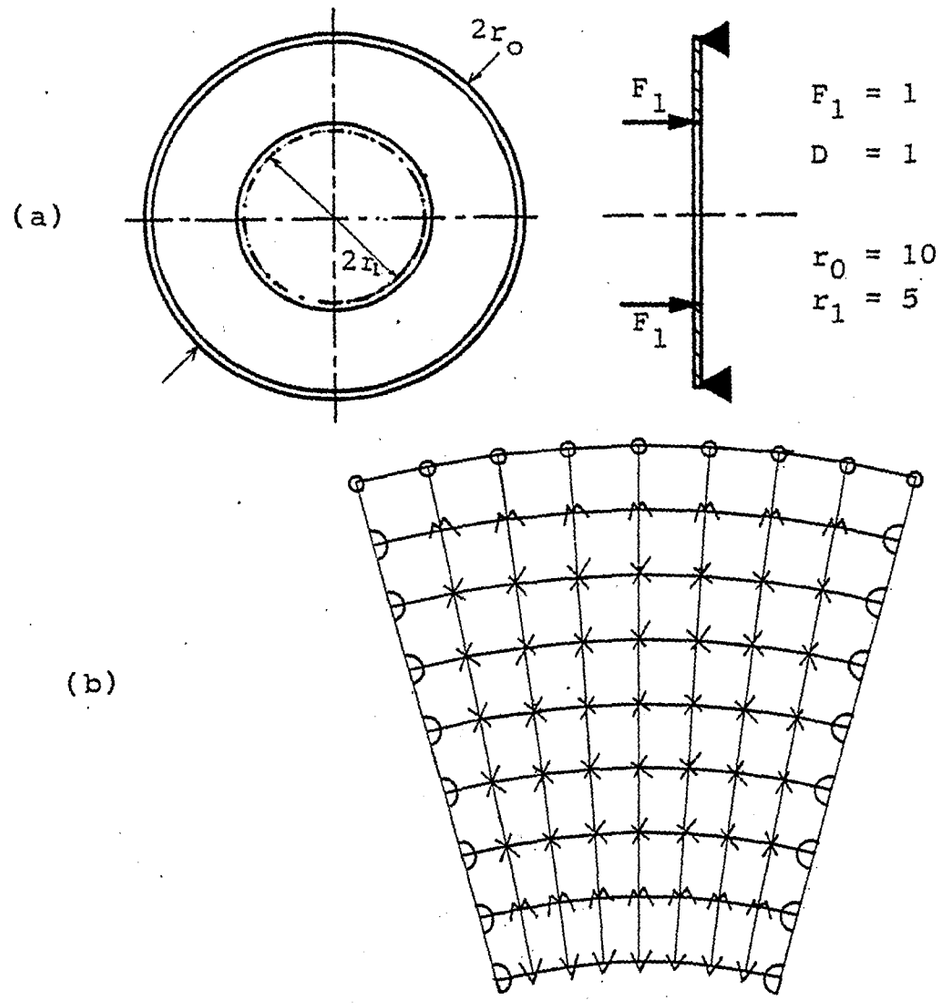

Figure 4F-17 Case (iv) - The Grid and Boundary Conditions

$$c_2 = \left(\frac{r}{r_o}\right)^2 \ln\left(\frac{r}{r_o}\right) \qquad \text{E4-73}$$

$$c_3 = \ln\left(\frac{r}{r_o}\right) . \qquad \text{E4-74}$$

for

$$r_o=10 \; ; \; D=F_1=1 \; ; \; r_1=5 \; ; \; r=7.5 \; ; \; \nu=0.3$$

$$w=92.679$$

A graph for deflection at r=7.5 versus square of the mesh length is shown in Fig 4F-18. An error of about 18% is found for the 9x9 grid. The error drops to about 10% for a 13x13 grid. The presence of a free boundary (as opposed to fixed boundaries) is reflected in the magnitude of error (errors are additive for a free boundary as errors propagate towards edge - fixed boundaries limit errors as errors are zero at edges.)

Case v: Cases for variable thickness thin plates for which analytical solutions are available are very few. An axisymmetric case found was that for a circular ring, clamped at the inner edge and free at the outer edge, subjected to a uniform load distribution. The geometry is presented in Fig 4F-19 as well as the boundary conditions. The solution for maximum deflection is given by Szilard {R66} as:

$$W_{max} = c_1 \frac{p_o r_o^4}{EH^3} \qquad \text{E4-75}$$

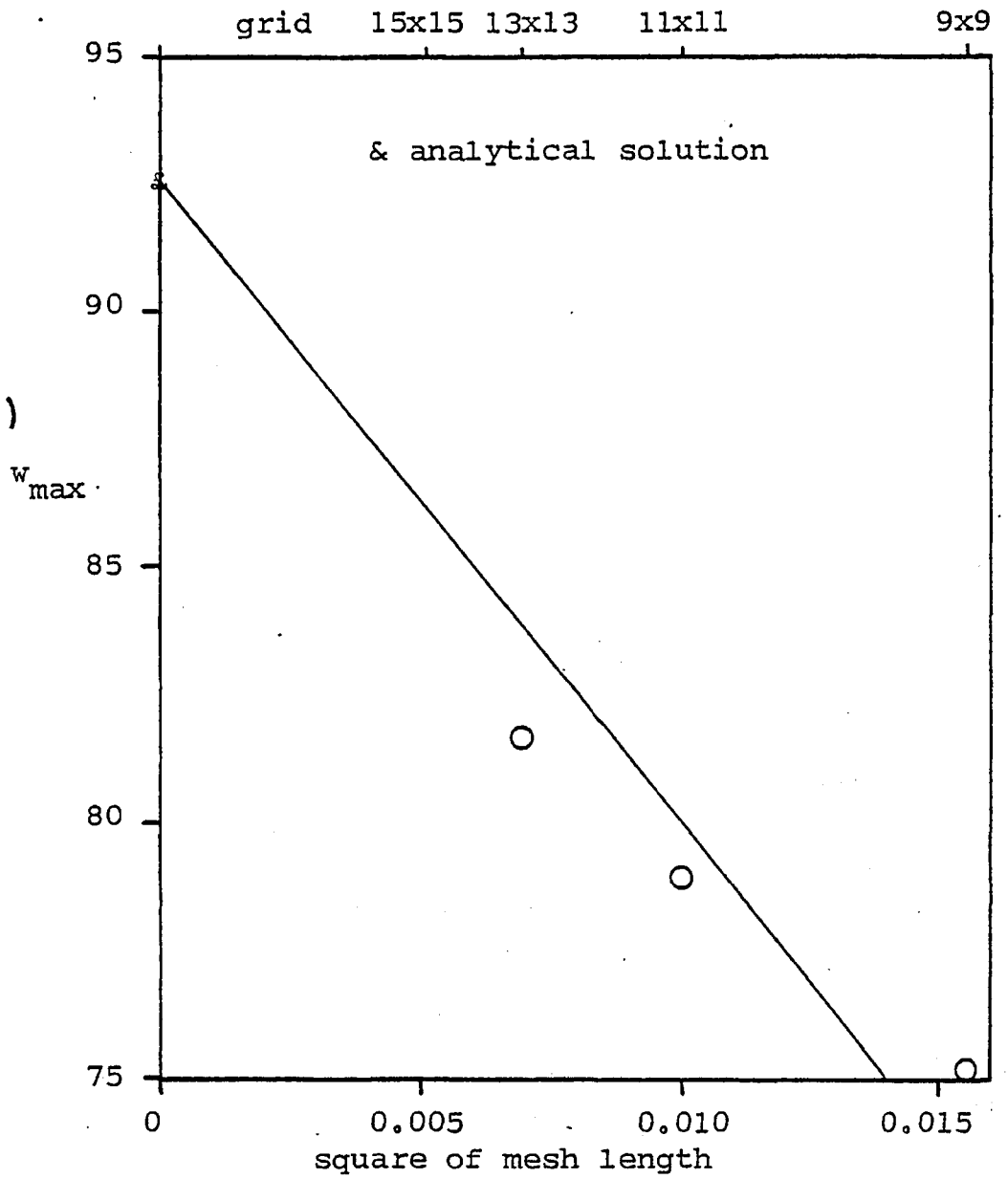

Figure 4F-18 Case (iv) - Maximum Deflection Versus Square of Mesh Length

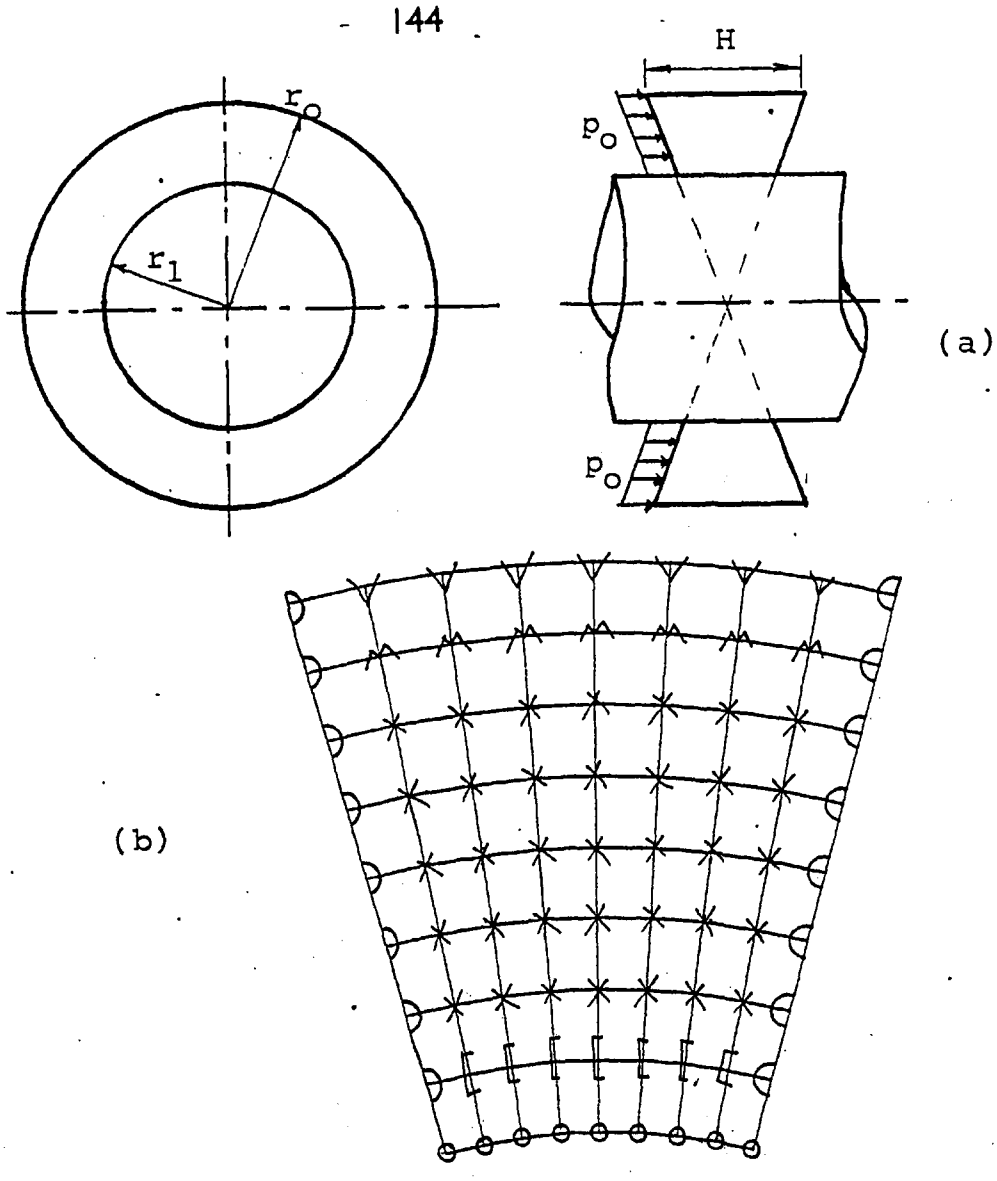

⊙ w = 0

◁ gradient $\frac{\partial w}{\partial \theta}$ and

▷ deflection equal at a particular radial position

X pressure node

[$\frac{\partial w}{\partial r} = 0$

⩙ $M_r = 0$

⩒ $V_r = 0$

Figure 4F-19 Case (v) - The Grid and Boundary Conditions

where $c_1 = 0.00372$ for $r_o/r_i = 1.25$ E4-76

or $c_1 = 6.283$ for $r_o/r_i = 5$ E4-77

H is the plate maximum thickness (at $r=r_o$)

For $p_o=E=1$; $r_o=10$; $r_o/r_i=1.25$

$$w_{max} = 37.2$$

Curve I on Fig 4F-20 shows the deflection versus square o f mesh length. An error of about 23% is found for a 9x9 grid and decreases to 9% for a 15x15 grid. Thus the presence of a variable rigidity plate suggests that more nodes are required to obtain a certain level of accuracy compared to the constant rigidity plate. For $p_o=E=1$; $r_o=10$; $r_o/r_i=5$ Szilard gives,

$$W_{max}=62830$$

Curve II shows about 80% error for a 9x9 grid, decreasing to about 27% error for a 15x15 grid. The extrapolated values for an infinitely small mesh size for both curves I and II correspond with the analytical solutions.

The above five cases have been modelled and compared with analytical solutions. Fig 4F-21 shows four configurations (cases vi to ix) for which previous solutions have been found. The results from the present method are compared in Table 4T-1. In general the agreement with published data is satisfactory although the data itself shows some scatter, for example case (a). Chen and Pickett {R61} report errors of 'considerable' magnitude in a

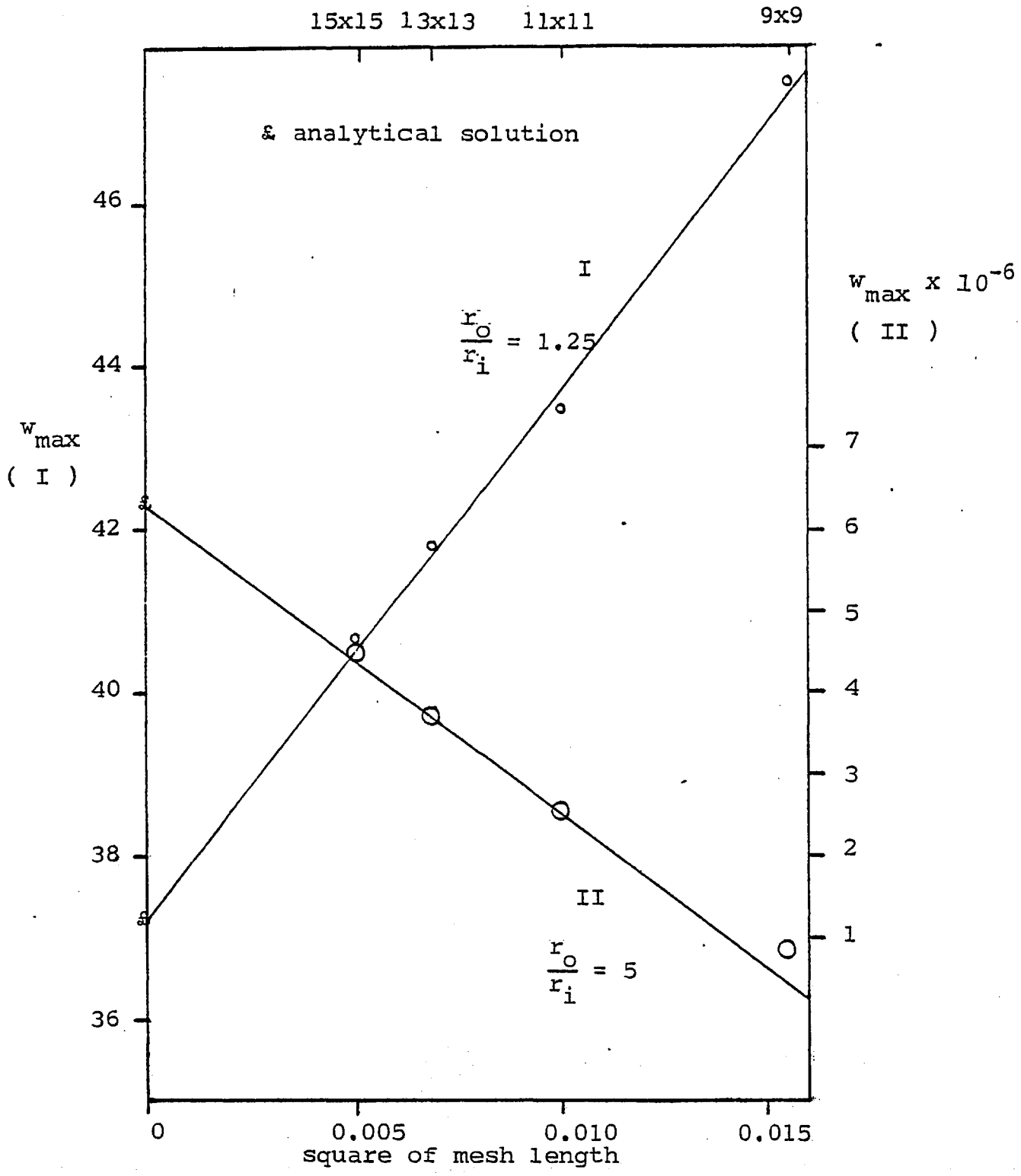

Figure 4F-20 Case (v) - Maximum Deflection Versus Square of Mesh Length

a) Clamped

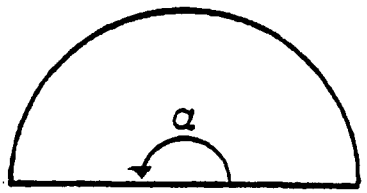

$\alpha = \pi$

b) Clamped

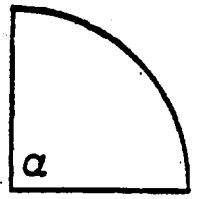

$\alpha = \pi/2$

c) Simply supported

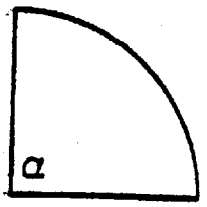

$\alpha = \pi/2$

d) Clamped

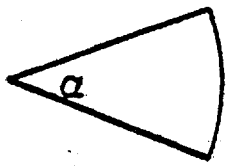

$\alpha = \pi/6$

Figure 4F-21 Four Plate Configurations

Table 4T-1

Comparison of Deflection Result for Cases (vi),(vii),(viii), and (ix)

$p_o = 1$, $D = 1$, $r_o = 1$, $\nu = 0.3$

Case	Deflection Result	Published Results
a	2.0144×10^{-3} at r=0.5 (Extrapolated Value)	Maximum Deflection 2.016×10^{-3} r=0.485 {92} 2.023×10^{-3} r=0.4859 {93} 2.020×10^{-3} r=0.486 {59} 2.07×10^{-3} r=0.4915 {62} 2.14×10^{-3} {63}
b	max=6.38×10^{-4} (r=0.57) (8x8) mesh	7.1655×10^{-4} r=0.594 {59}
c	2.14×10^{-3} at r=0.5 (8x8) mesh	2.26×10^{-3} r=0.5 {63} 2.25×10^{-3} r=0.5 {80}
d	1.40×10^{-5} at r=0.5 (8x8) mesh	1.45×10^{-5} r=0.5 {63}

number of previously published results.

Case x: A constant rigidity plate subjected to a uniform temperature gradient deflects to a spherical shape. Fig 4F-22 shows the geometry of a sector plate supported at three equally spaced points P, Q, S. It can be shown {R52} that,

$$\frac{1}{R} = \frac{\alpha \Delta T}{H} \qquad \text{E4-78}$$

where

H is the plate thickness

ΔT is the tempreature gradient

From geometry (Fig 4F-22)

$$R = \frac{r_2^2}{2w_c} \qquad \text{E4-79}$$

where w_c is the deflection at point C

at the center of PQS

or

$$W = \frac{\alpha \Delta T \; r_2^2}{2H} \qquad \text{E4-80}$$

or

From geometry $r_2 = 0.57735$ (in the example), and for

$H = 0.2$; $\alpha = 12 \times 10^{-4}$; $\Delta T = 40$

$$w_c = 0.04$$

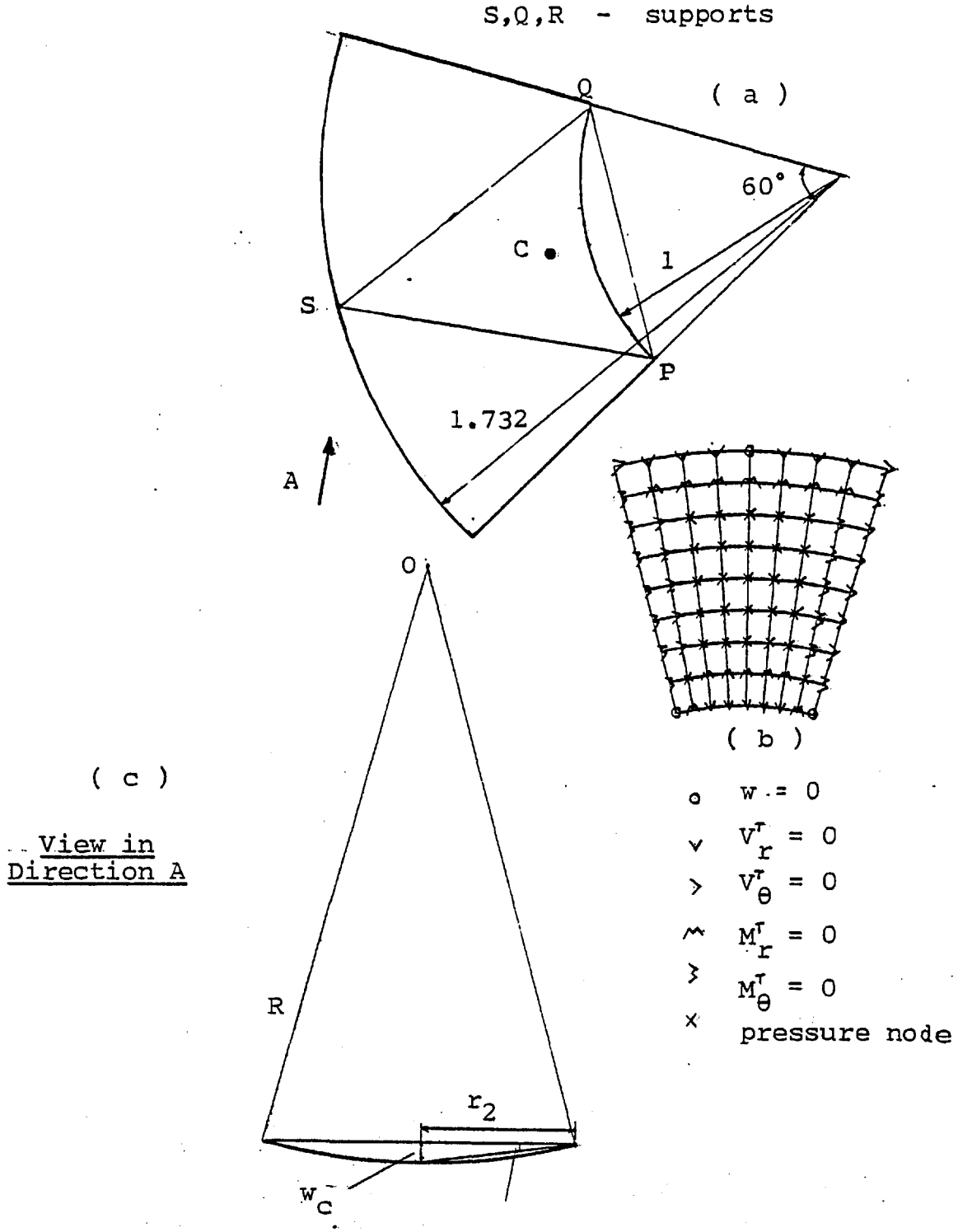

Figure 4F-22 Case (x) - The Geometry and Grid Boundary Conditions

The set up of the boundary conditions for the plate is shown in Fig 4F-22c. The plate has free edges except at the three support nodes. The support positions were chosen to allow the plate to bend into a spherical shape. The numerical solution for a 7x7 grid gives W=0.0398 at the node closest to the position C. A 9x9 grid gives W=0.0399 at the node closest to C, yielding an error of 0.25%. Circular contours for deflection were obtained indicating a spherical surface.

4.6 Conclusions From Test Cases

The polynomial difference technique has been applied to a variety of different cases and has been shown to give satisfactory quantitative and qualitative results for the thermal and elastic deflection of sector shaped plates. The method is easily adaptable to any co-ordinate system (cartesion and polar used in 4.6). The method can handle relatively lengthy equations with relative ease, since the various terms can be processed individually (see E4-25). Thus the possibility of an error in calculating a coefficient is vastly reduced and is limited to defining the particular term in the equation. The method can handle any type of boundary condition such as point supports, edge supports or multiple supports. Variable loading can also be handled. Since variable rigidity terms are incorporated into the plate equations, this can also be handled. Elastic supports are also easily incorporated. The flexibility of defining the boundary conditions renders the

method accessible to many other applications.

Applied to thrust pad bearings, the method can analyse the pad deflections due to pressure and temperature variations in the bearing (see Chapters 5 and 6). Thrust pads may be supported using a hardened steel button forming a 'ring' support. Others are 'line' supported . Some large configurations use an elastic foundation support for the pads. The deformation of the bearing components has been shown to be critical to bearing performance (see introduction). Comparison with finite difference and finite element techniques (section 4.3) shows that the method combines advantages of both.

4.7 Numerical Considerations.

Three main factors affect the success of a numerical solution. The length of the computer code, the computer storage requirements of the program and the time in central processor seconds required for a solution. The present technique offers huge savings in both time and effort in programming terms compared to the traditional finite difference technique. For in the finite difference technique, the molecule coefficients have to be manually set up in finite difference terms (as in the Reynolds equation - Chapter 2). Each boundary condition will require a different set up depending on the type of condition and its position of application in the grid system.

Computer storage requirements may be minimised by using the iterative procedure. The direct matrix inversion method requires $(nxm)^2$ words (where n is the number of grid positions in the circumferential direction, and m for the radial direction). For a 9x9 grid system 6561 words are required. For an 11x11, 14641 words are required. In order to invert the matrix a Nottingham Algorithm routine (NAGF04 AAF) was used. This requires double the storage of the matrix to be inverted. Hence for an 11x11 grid 29282 words are required. The present system available at Imperial College limits storage to 100,000 octal - or 32,768 (decimal) words for iterative use. For batch work (non iterative) a maximum of 100,000 (decimal) words is available. This allows a maximum grid size of 15x15 to be inverted. For larger grid sizes, the matrix may be partitioned into four matrices, that is

$$(\overline{C}_L) = \begin{pmatrix} \overline{C}_1 & \overline{C}_2 \\ \overline{C}_3 & \overline{C}_4 \end{pmatrix} \qquad \text{E4-81}$$

The inverse may be obtained from matrix algebra as {R68}:

$$(\overline{X}) = \begin{pmatrix} \overline{Y}_1 & \overline{Y}_2 \\ \overline{Y}_3 & \overline{Y}_4 \end{pmatrix} \qquad \text{E4-82}$$

where $$\bar{Y}_1 = (\bar{C}_1 - \bar{C}_2 \bar{C}_4^{-1} \bar{C}_3)^{-1} \qquad \text{E4-83}$$

$$\bar{Y}_2 = - \bar{C}_1^{-1} \bar{C}_2 (\bar{C}_4 - \bar{C}_3 \bar{C}_1^{-1} \bar{C}_2)^{-1} \qquad \text{E4-84}$$

$$\bar{Y}_3 = - \bar{C}_4^{-1} \bar{C}_3 (\bar{C}_1 - \bar{C}_2 \bar{C}_4^{-1} \bar{C}_3)^{-1} \qquad \text{E4-85}$$

$$\bar{Y}_4 = (\bar{C}_4 - \bar{C}_3 \bar{C}_1^{-1} \bar{C}_2)^{-1} \qquad \text{E4-86}$$

Thus, it is not actually neccessary to store the whole matrix at the same time. The process involves file manipulation in order to store the initial matrix, as well as its inverse (after the required inversions have been performed to the submatrices.) More efficient inversion routines are available for very large matrices such as Cholesley's decomposition method (not used). A 9x9 grid has been used for most test cases unless specified (using NAG - F04AAF). In general a seperate program is used to set up matrix $\bar{C}_L$. The program is capable of inverting $\bar{C}_L$ up to an 11x11 grid size. A special flag is used to indicate for larger grid sizes. This directs the program to save the $\bar{C}_L$ onto a local file. The matrix can then be read by another program at a later stage. A second program was set up to read and invert a matrix for grids 13x13 and 15x15 (in batch mode). The inverted matrix $\bar{X}$ is in all cases saved in permanent computer file (physically on a magnetic disc) along with a header identifying the plate geometry, grid size and boundary conditions. The file is ready to be read and directly multplied with any stress vector required, yielding the plate deflections.

For grid sizes larger than 15x15 a third program has been set up. It reads the matrix $\bar{C}_L$, partitions it and inverts it according to equations E4-82 to E4-86. It then writes the matrix $\bar{X}_L$ onto a permanent file with the required header as in other methods.

The iterative method requires 25xmxn real stores for the computing coefficients (using 5x5 molecules). Thus a 35x35 grid can be handled interactively. The main drawback is that the solution of only one stress vector can be handled, whereas the direct inversion method can handle any stress vector using one inversion only. In addition, the iterative technique is very slow to converge. As part of a larger program, this severely limits the use of an iterative routine to handle the deflection of thrust pads (see Chapter 5). Nevertheless, the iterative routine has been useful in confirming the direct method results (as in section 4.5) and in obtaining solutions for large grid sizes.

4.8 Drawbacks

The central processor time required for setting up matrix $\bar{C}_L$ is greater than for a finite difference scheme, as it involves inversion of the geometry matrices $\bar{A}$. The program required to set up $\bar{C}_L$ is necessarily a seperate unit - from a computer storage consideration. For multiple support systems, care has to be taken in choosing the number of nodes (refer to case of beam supported at five positions Fig 4F-5). A change in the size of a sector plate (of the same geometry) requires the set up of two different matrices $\bar{C}_L$. This is not the case for the method used by

Ettles {R17}.

More efficient methods can be developed to invert the large matrix $\bar{C}_L$. Cholesley's decomposition is very efficient numerically. This is necessary for grids of 21x21 nodes or larger to make savings on the enormous computer time required.

4.9 Other Modes of Distortion

So far, only bending deformation has been considered. Shear deformation, direct thermal and elastic compression, as well as fibre crushing constitute other modes investigated by Ettles and Cameron {R41}. These can be taken as thick plate effects. For an axisymmetric circular plate with a button support (button support radius/plate radius=1/3) and a conical pressure distribution, Ettles and Cameron {R41} show that shear deflection is the most influential thick plate factor (apart from bending deflection). Comparison of theory and experiment shows reasonable agreement. The thermal effects accounted for more than 90% of the total theoretical distortion (The bearing outer radius was 48 inches, the plate thickness 7.125 inches). Thus the effects of shear distortion, direct thermal and elastic compression and fibre crushing cannot account for more than 10% of the total distortion. The bearing size is typical of large thrust bearings used for waterwheel generators. In addition, the simplifications required to incorporate the thick plate effects into the quasi-three-dimensional variable thickness plate theory questions the validity of the approach. It may be better to solve for a fully three dimensional solid body. This

latter approach is outside the bounds of the present work, and may not be practicable for lubrication problems of this nature. Robinson and Cameron {R52} solved the bending deflection of constant thickness plates and included direct compresion and direct thermal expansion effects. The effects of direct compression and direct thermal expansion are different in sign, undermining both their effects. For a pad operating at $10MN/m^2$, an approximate temperature difference across the pad of 10 deg C is typical. For steel both the deformations are of the same order of magnitude. Lo et al {R64} proposed a high-order theory of plate deformation which acounts for the effects of transverse shear deformation, transverse normal strain, and a non-linear distribution of the in-plane displacements. It was found that when the ratio of the characteristic length ℓo the plate thickness is of the order of unity, lower order theories are inadequate. The error involved in neglecting thick plate effects increases rapidly beyond a ratio of 0.5 for plate thickness/characteristic length. A ratio of 0.25 yields errors of about 10%. Considering the accuracy of the numerical technique presented, it is thought that the bending analysis (both elastic and thermal) is on its own, sufficiently accurate - the neglect of shear deflection being the major simplification for large pivoted pads.

CHAPTER 5

OVERALL MODEL AND PROGRAM ASSEMBLY

Introduction

5.1 Interface of Deflection

5.2 Viscosity-Temperature Relation

5.3 Turbulence and Inertia

5.4 Pivoting

5.5 Load,Flow and Power Loss

5.6 Overall Assembly

5.7 Relaxation Factors and Residuals

Introduction

Chapters 2,3, and 4 described three basic components of an overall model for thrust pad bearings. For a given pad/collar geometry, a lubricant film shape is obtained. The shape is dependent on pad deflection, too. The pad deflection depends on elastic and thermal stresses in the pad which in turn depend on three factors: the lubricant pressure forces; the temperature distribution in the pad; and the support method. The pressure and temperature distributions depend on the oil flow in the film, which in turn depends on the oil film shape. Hence, the solutions for deflection, temperature and flow fields are coupled and must proceed simultaneously.

The flow pattern also determines the rate of shear, and hence the energy generation and the temperature distribution. In the oil film, the viscosity distribution will depend on the temperature distribution. The flow pattern is dependent on the viscosity and is therefore also dependent on the temperature distribution.

For tilting pad bearings a further condition must be satisfied. For a free tilting pad, the moments about the pivot are zero. Thus, the pad inclination has to be adjusted with respect to the collar - by changing the basic geometry - in order to satisfy this latter condition. The moments about the pivot are dependent on the pressure and shear forces exerted by the oil film.

In chapter 3, a detailed explanation of the solution for the

temperature distribution has been given. Local flow, viscosity, geometry and deflection are assumed input variables. The temperature distribution in the pad, oil film and collar can then be obtained. The dependence of viscosity on temperature forms the link between the solution for temperature and the subsequent flow pattern found by a fresh solution for pressure. As well as a new viscosity distribution, a new film shape can be obtained using the deflections in the pad due to the pad temperature variations. These can be used to determine the ensuing flow pattern. At higher velocities, turbulence becomes significant and is therefore included in the flow model (see section 5.3 .)

The path chosen to determine the overall converged solution is important, since the numerical technique can be unstable. A component part of the overall solution, the solution of the energy equation, uses an up-wind scheme {R16}. The solution stability is greatly enhanced in return for neglecting "down-wind" effects - in this case conduction within the oil film in the direction of flow. Even if all components of the overall solution show satisfactory stability individually, their combination can still be unstable.

In this chapter, the incorporation of deflection into the general model is presented. The viscosity-temperature relation and the turbulence model chosen are also given. The determination of film shape and subsequent adjustments (pivoting) are given. The method of obtaining useful bearing characteristics is detailed. Finally, a flow chart is given for the assemled model with

references to the convergence tests performed to check the final solution.

5.1 Interface of Deflection

In chapter 4, two numerical methods have been presented for the solution of pad deflection. The method of direct matrix inversion has been shown to be advantageous in an overall solution. For this method, a separate program (or programs) is to be used to set up matrix $\bar{C}_L$ (see chapter 4) and invert it, yielding matrix $\bar{X}_L$. $\bar{X}_L$ is then stored on a computer file for later use with a suitable header referencing the geometry and boundary conditions. Matrix $\bar{X}_L$ can be used in conjunction with any stress vector to yield the deflections as

$$\bar{X}_L \cdot \underline{b}_L = \underline{w}_L \qquad \text{E5-1}$$

This operation requires negligible computer time (CP time) compared to the time required to set up or invert $\bar{C}_L$. Thus, once $\bar{X}_L$ is obtained for a particular geometry, it can be read in the main bearing program and used (as above) as many times as is required. In practice a further advantage concerning the minimising of storage can be obtained. Only one row of matrix $\bar{X}_L$ need be read and stored at a time. This can be multiplied by $\underline{b}_L$ to yield one element in vector $\underline{w}_L$. This can be repeated until all $\underline{w}_L$ is obtained, that is, the vector of required deflections. Thus the computer memory available to the main bearing program can be more efficiently allocated.

The stress vector is composed of the right hand side of the governing equation (Appendix G) at the nodes where it applies (that is, other than edge related and support nodes). This is composed of a pressure and derivatives of the thermal moments. These are evaluated in the main program (using the finite difference technique - see Appendix B) from the pressure and temperature fields in core.

Once the deflections are obtained, they can be used to modify the film shape. The angles of inclination of the pad are sufficiently small to allow direct addition of deflections to the existing pad shape. Problems can arise in that a particular combination of inclinations and deflection may appear to yield negative film thicknesses. These will be dealt in section 5.4.

5.2 Viscosity-Temperature Relation

For each new temperature field in the oil film the associated viscosity field is updated according to the viscosity-temperature relationship for the oil. The new viscosity field can be used in the Reynolds equation to modify the flow equations. Several formulae exist to model the viscosity-temperature relation, and are obtained by curve fitting experimental data [R3]. Vogel's formula has been chosen as it is an accurate and suitable function for computing. This can be given as

$$\mu = K \exp (b/ (1 + \theta)) \qquad E5\text{-}2$$

where,

b, θ, K are oil characteristic constants.

Since E5-2 contains three unknowns, three values of viscosity at three different temperatures are required. Reynolds formula {R3} requires only two values of viscosity and is easier to compute but is less accurate and is only valid for small changes in temperature.

For cases where viscosities at only two temperatures are available, the points are plotted on an ASTM chart for viscosity versus temperature (Fig 5F-1). The third value is chosen as the midpoint of the line joining the other two. If only one value is available, a line is drawn through the point, parallel to lines for oils of similar behavior.

5.3 Turbulence and Inertia

In 1954, results of an experimental investigation {R69} showed a critical Reynolds number ($\rho Uh/\mu$) of 600 at which a laminar-turbulent transition took place. Several investigators analysed the turbulence theoretically and Taylor {R70} summarised the two most common theories. Both turbulence theories neglected mean fluid inertia and temperature effects. Constantinescu {R71} studied the contribution of thermal effects in the fluid film, and concluded

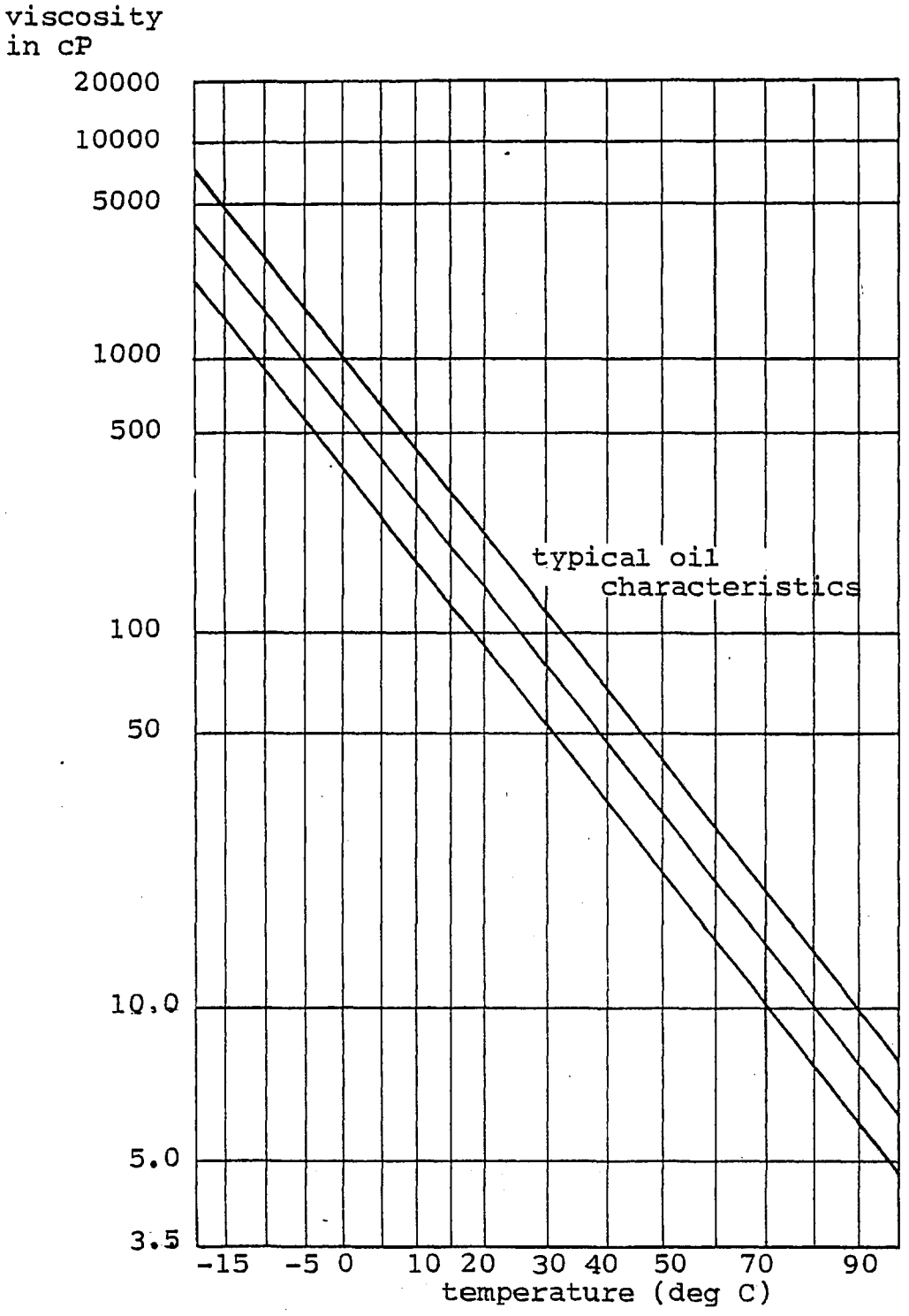

Figure 5F-1 ASTM chart

that their effect on the flow pattern is diminished in the turbulent regime compared to the laminar one. In 1973, Hirs {R72} introduced the bulk flow theory approach. Taylor and Dowson {R73} gave an excellent comparison of the three available methods. These were namely: Constantinescu's mixing length model; Ng, Pan and Elrod using the concept of eddy viscosity; and finally the bulk flow adopted by Hirs. All three depend on correlated experimental measurements to determine equation constants. The form of Reynolds equation used is that presented in App. A.. The values of k_x and k_z, the turbulence correction factors, are equal to 1 for the laminar regime. In the values correlated by Hirs, they are allowed to drop below 1 - which is physically not possible {R73}. Taylor and Dowson have argued that although Constantinescu's work is pioneering, the results of Ng, Pan and Elrod are accurate. Thus the formulae correlated by Ng, Pan and Elrod are used in the present work, namely

$$k_x = (12 + 0.0136\ Re^{0.9})/12$$

$$k_z = (12 + 0.0043\ Re^{0.96})/12$$

$$\tau_c = 1 + 0.00099\ Re^{0.96}$$

$$\text{for} \quad Re = < 10000$$

where τ_c is the factor multiplying the Couette component of the shear stress.

Ng, Pan and Elrod utilised the concept of eddy viscosity to represent the turbulent stresses in terms of the mean velocity gradient. In so doing Reichardt's formulation for eddy diffusivity

was employed {R73}. Venkateswarlu et al {R75} used the Van Driest damping parameter {R74} to analyse the turbulent film. This is backed by good agreement between theory and experiment. Inertia and viscous terms were included in the model (depending on their importance) forming different classes of solutions. This approach is not directly amenable to use in the modification of the Reynolds equation as presented in Chapter 2. For very large Reynolds numbers the errors in previous methods become of the order of magnitude of the characteristics required, especially the load capacity. In the present work, the Reynolds numbers remain well below this level and the theory proposed by Ng, Pan and Elrod is sufficiently accurate.

Burton et al {R76} carried out an experimental investigation of turbulent film tilting pad bearings, including the measurement of velocity profiles. Leading edge effects were shown to have a dominant role - but are still not properly understood. The pivot position had a marked effect on the turbulence regime. In general, little experimental evidence has been found to support a general turbulence model. This is a characteristic of the turbulence phenomenon rather than a specific problem related to bearings.

In a recent publication, Pinkus and Lund {R77} considered centrifugal effects in thrust bearing pads. Generally undesirable properities such as cavitation (scavenging) at the pad inner radius and hence a lower load capacity and higher temperatures result. This effect is significant near $Re^{*}=1$ (or above),

where $$Re^{*} = Re_i \, h_2/R_{out}$$

and $Re_i = \rho R_{out} \Omega h_2 / \mu_{inlet}$

h_2 = film thickness at midpoint of film trailing edge

The effect is enhanced by larger pad angles. For a pad angle of 40 degrees a 20% reduction in load capacity results at $Re^* = 1$. The reduction becomes 50% for a pad angle of 90 degrees. Radial taper ($\partial h / \partial r$ negative) is suggested as a possible cure for centrifugal effects.

5.4 Pivoting

Chapter 2, section 2.2 mentioned briefly one aspect of pivoting. In this section the relationship between inclination, deflection and film shape is discussed.

Fig 5F-2 shows the pivoting co-ordinates X, Y. X is the line through the bearing as well as the pivot point. Y is perpendicular to X, and passes through the pivot point, too. Two angles may be defined. α is the inclination of the Y axis with respect to the collar plane. It is positive if the trailing edge is above the leading edge along the Y axis. Similarly, angle Φ is the inclination of the X axis, and is positive if the outer edge is higher than the inner edge (at inner radius). For a plane pad the film thickness is defined as:

$$h_p = \sin\Phi(r \cos (\theta - \theta_{piv}) - r_{piv}) + \sin\alpha(r \sin (\theta - \theta_{piv})) + h_{piv}$$

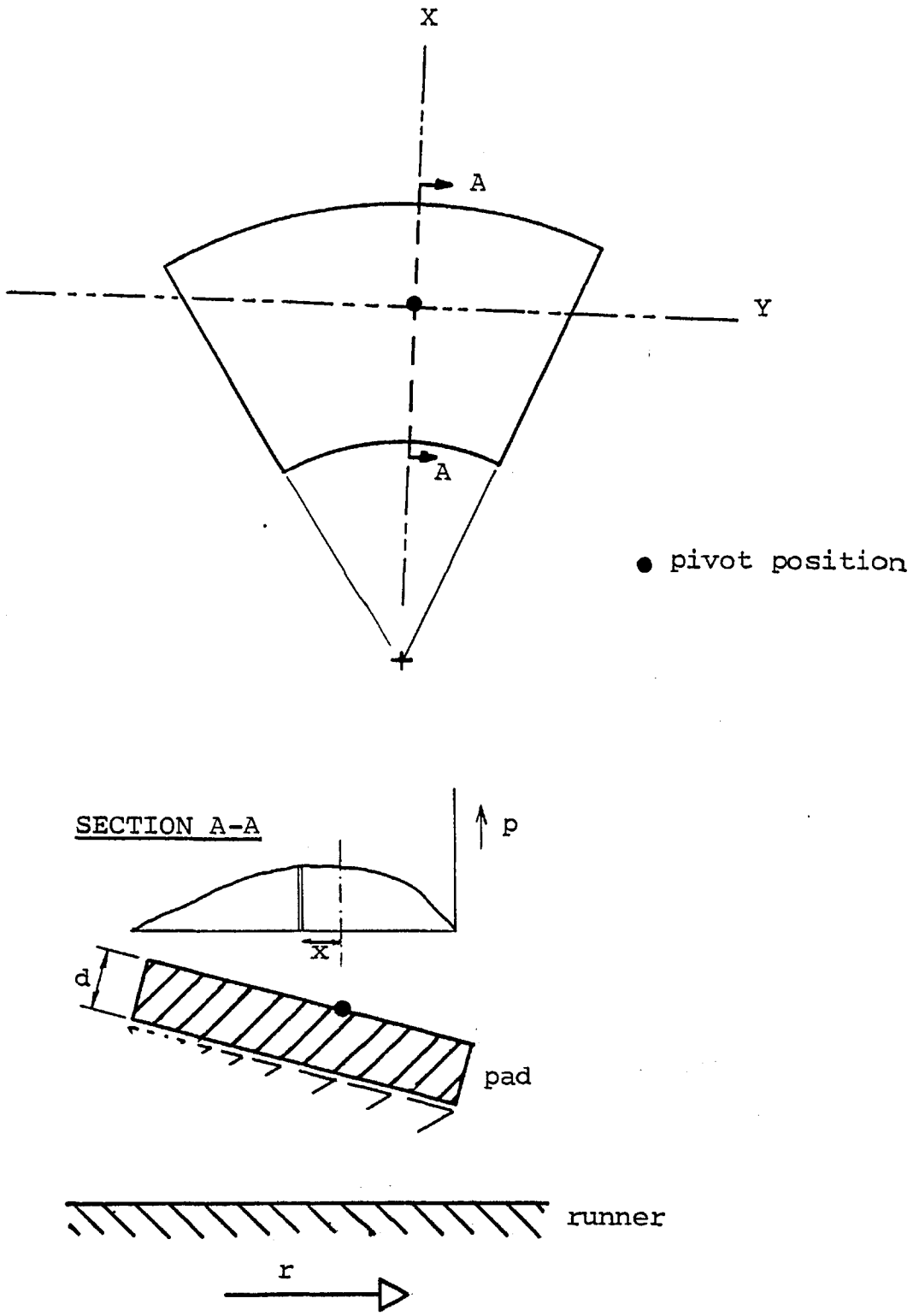

Figure 5F-2 Pivoting Co-ordinates

If positive pressures acting on the pad surface produce positive deflections, the film thickness is written,

$$h = h_p + w$$

This is justified since the deflections are small compared to the pad geometry. If the pad is crowned, a two-dimensional quadratic is used to represent the crown in the oil film shape (a close approximation for the small crowns involved {R44}):

$$h = h_p + w + \left(1 - \left(\frac{r - r_m}{r_m - r_i} \right)^2 \right) \left(1 - \left(\frac{\theta - \theta_{piv}}{\theta_{piv}} \right)^2 \right) C_r$$

or $h = h_p + w + f(C_r)$

where $r_m = \frac{r_o + r_i}{2}$

When used in the bearing program, h is evaluated from the above expression. The input values are the maximum crown height (C_r), the inclination angles and and the film thickness at the pivot point (excluding distortion at the pivot position; for example, for a button support the centre of the button may deflect although the moments about it are zero). If undefined, the

radial pivot position is chosen so as to produce zero moment about the Y axis - for a uniformly loaded pad:

$$r_{piv} = \frac{2}{3} \left(\frac{r_o^3 - r_i^3}{r_o^2 - r_i^2} \right) \left(\frac{\sin (AP - \theta_{piv}) \sin (\theta_{piv})}{AP} \right)$$

The film shape assumed at the start of the bearing program reflects the initial condition for the Reynolds equation. Φ is set to zero, whilst α is set to give a 2:1 film thickness ratio (inlet:outlet) along the X axis:

$$\alpha = \sin^{-1} \left(\frac{-h_{piv}}{r_{piv} (\sin (\theta_{piv}) + 2 \sin (AP - \theta_{piv}))} \right)$$

The pressure distribution is evaluated using the first film shape.

The moments about the pivot are evaluated for the X and Y axes. These consist of moments due to the pressure field as well as moments due to the oil shear force acting at the pad/oil interface (see Fig 5F-2). The changes in angles of inclination required depend on inlet/outlet film thickness ratios as well as the position of zero moments. The method of correcting inclinations (in an effort to bring the centre of presssure closer to the actual pivot position) has been described in Chapter 2 section 2.7. The measure of inclination (X_{inc}) is taken as the

inlet/outlet film thickness ratio. In the circumferential direction, the inlet film thickness is taken as the middle node A (see Fig 5F-3), whilst the outlet film thickness is taken at node B. Similarly in the radial direction, nodes C and D are used (Fig 5F-3). The advantage of applying changes in this manner is threefold. The film thickness ratio takes into account deflection and crowning. Secondly, it is easier to avoid negative film thicknesses, for if angles are used, it is possiblle that large angular changes result in negative film thickness, (Fig 5F-4). Thirdly, a more positive response is obtained at low inlet/outlet ratios - suitable at low loads. A more sensitive approach can involve the maximum and minimum film thicknesses to correct the tilt - especially when deflections are very large.

The technique described is further modified for 'fine tuning' of the centre of pressure. Once the distance of the centre of pressure from the actual pivot position is less than 1% of a typical pad dimension, pivoting is enhanced by a further stage of corrections (In the radial direction $R_{out}-R_{in}$ is used as the pad dimension, $R_m\theta_{pad}$ is used in the circumferential direction). The first stage is to use the technique already mentioned. The second is to use the changed angles α and Φ rather than film thickness ratios in the second correction. Both stages lead to a more rapid correction whilst the risk of a negative film thickness is vastly reduced as convergence to 1% of a typical pad dimension has already been obtained.

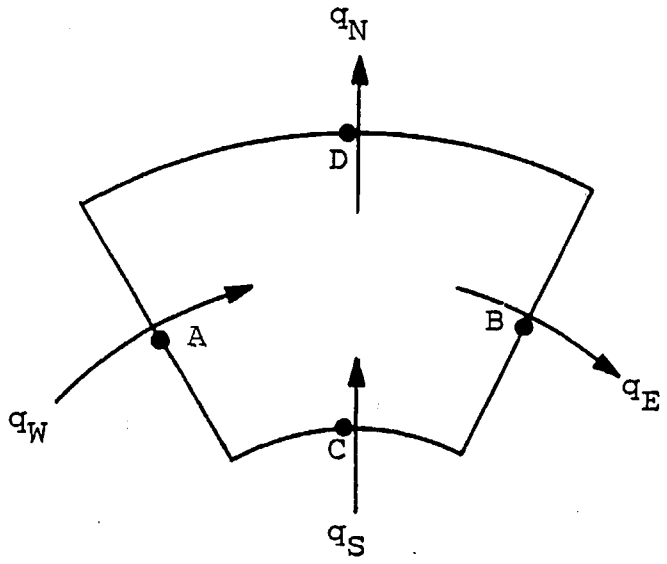

Figure 5F-3 Location Of Flows Calculated In a Pad

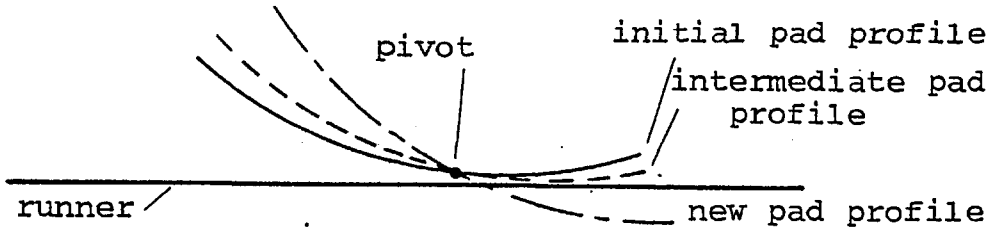

Figure 5F-4 Successive Film Shapes for Angular Pivoting Corrections

5.5 Load, Flow and Power Loss:

5.5.1 Load

The load is evaluated as follows:

$$W = \int_{r_i}^{r_o} \int_{0}^{AP} pr \; \delta\theta \; \delta r$$

Simpson's numerical integration technique is applied to solve the double integral. The average pressure is obtained by dividing the load over the pad area.

5.5.2 Flow

The radial and tangential flows are expressed:

$$q_r = \int_{0}^{AP} \int_{0}^{h} vr \; dz \; d\theta$$

$$q_\theta = \int_{r_i}^{r_o} \int_{0}^{h} u \; dz \; dr$$

or

$$q_r = \int_{0}^{AP} r \frac{\partial p}{\partial r} \Gamma_1 \; d\theta$$

$$q_\theta = \int_{r_i}^{r_o} \left(\frac{1}{r} \frac{\partial p}{\partial \theta} \Gamma_1 + r\Omega\Gamma_2\right) dr$$

See Appendix A for definition of Γ_1 and Γ_2.

Four flows are evaluated, namely q_W, q_E, q_N, q_S at the pad edges (see Fig 5F-3). q_W is the inlet oil flow to the pad. The calculated flows only represent quantities pertaining to the oil film (the total bearing flow can be regulated). Again Simpson's technique is used to numerically integrate the flows.

5.5.3 Power Loss:

Bearing power loss includes energy used in heating the oil, energy loss in churning between pads and energy loss due to conduction. The first is termed convective loss. Conduction from the oil film is mainly through the pad and collar.

The energy lost in conduction or the heat flux from oil to pad and collar is calculated for the purpose of the energy model (Chapter 3). A summation of the flux from oil to pad yields the heat lost due to conduction through the pad. Similarly a summation of heat flux from oil to collar yields the heat lost by conduction through the collar. The total rate of work done on the film is equal to the sum of the shear forces/unit length multiplied by the surface velocity of the rotor. This is converted to convective and conductive energy as well as flow work. The flow work terms are small. Thus the convection may be approximated as: 'Convection energy loss= Total energy due to shear stress at collar wall - Conduction Loss due to collar - Conduction Loss due to

pad'

The energy due to churning cannot be accurately evaluated unless a separate numerical model is used for the flow in the groove. Ettles [R28] has modelled flow in a typical groove, and a vortex flow is shown to be dominant.

5.6 Overall Assembly

A flow chart of program layout is given in Figs 5F-5 and 5F-6. The flow chart is mapped by five areas describing the main program functions. Area 1 is termed the Initialisation section. Area 2 shows the energy evaluation section. Area 3 is the deflection evaluation and final checks section. Area 4 shows the flow evaluation and balancing section. Area 5 represents the final printout section and the resetting of a new pivot film thickness value.

In the initialisation stage, a choice is available as to whether to start a fresh run or to read the last stage of a previous solution. In both cases the geometry is read from local file TAPE1. TAPE1 has to be produced by the deflection program (see Chapter 4 - section 4.7) and includes the mesh distribution, as well as the inverse matrix $\bar{X}_L$. At this stage the necessary data is read and TAPE1 rewound - ready for further reading later. For a fresh start, the input conditions include oil bath temperature, number of pads, crown, the pivot film thickness, the angular velocity and the ratio of collar/pad thickness. If a continuation is specified the new

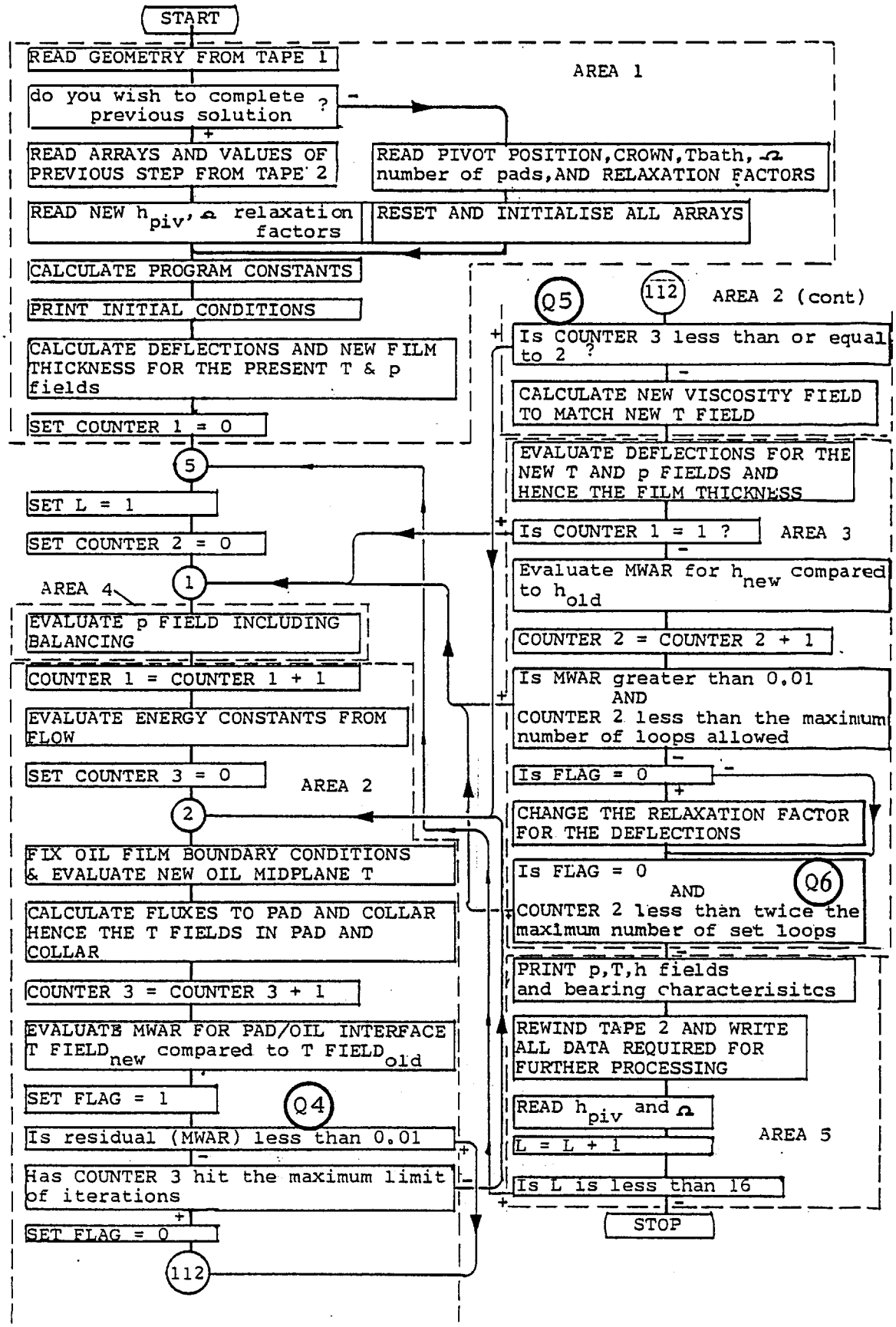

Figure 5F-5 Program Flowchart

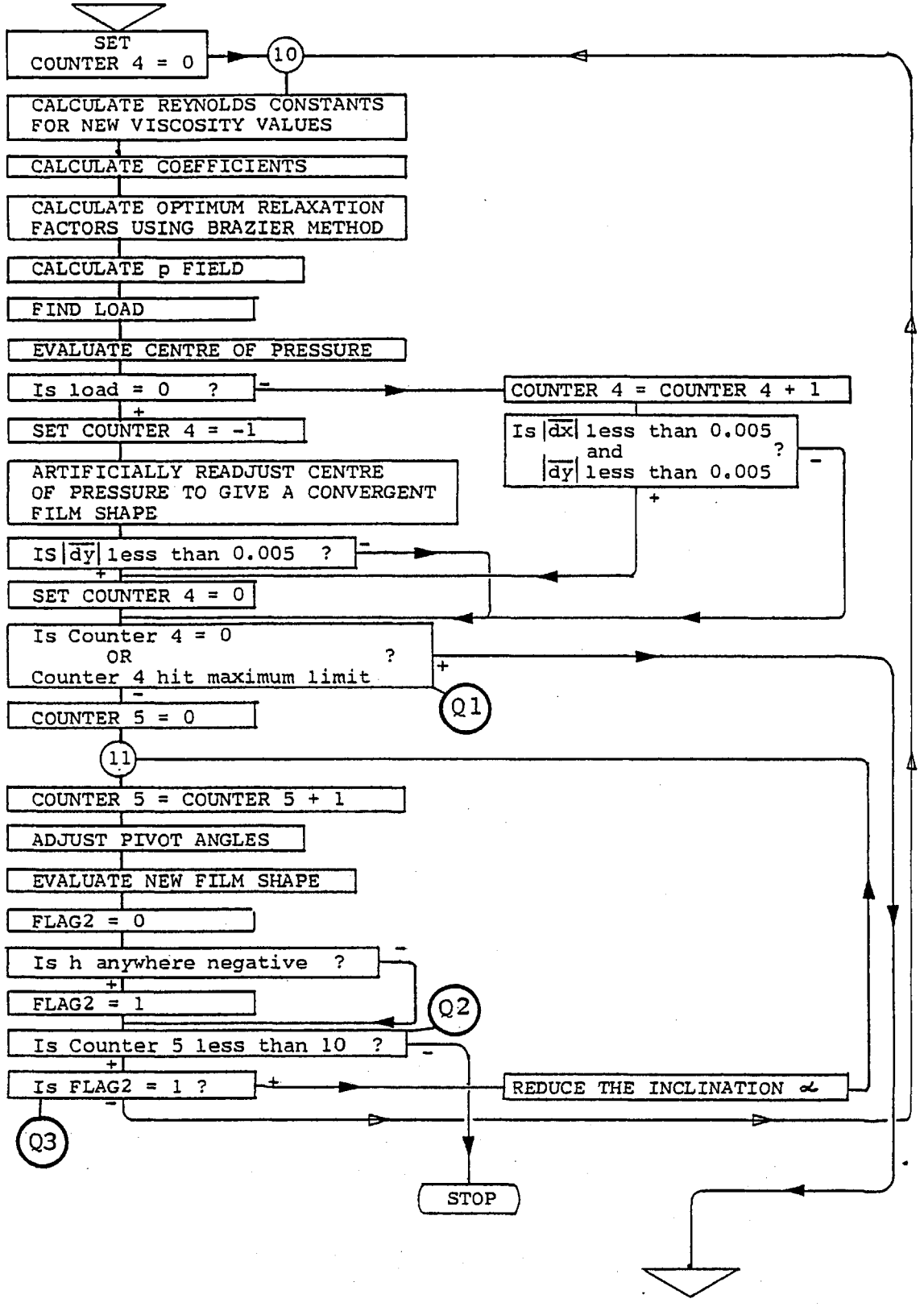

Figure 5F-6 Program Flowchart - Area 4

pivot film thickness and angular velocity are required. An allowance has also been made for varying the surface heat transfer coefficients as a function of input velocity if required. Parameters constant throughout the program run are evaluated at this stage. An output of the initial situation and input values is also given. The deflections due to the current temperature and pressure fields are evaluated. This requires reading the rows of matrix $\overline{X}_L$ from TAPE2, one by one, and multiplying by the stress vector. In setting up the stress vector, the information available on the header of TAPE2 is used to identify the various governing equation nodes. The film shape is then evaluated using the initial angles of inclination (see section 5.4).

Area 4 is detailed in Fig 5F-6. Counter 4 is initialised to zero on entry to this area. It is used to check for the convergence of the pivoting model. The pressures are evaluated as described in Chapter 2. A mean absolute weighted residual (MAWR) of $1x10^{-7}$ has been chosen to check convergence of succesive pressure fields (Convergence criteria will be discussed in a later section). The load is subsequently evaluated (see section 5.5). Next, the position of centre of pressure relative to the pivot position is found (see section 5.4). At this stage one problem may arise (not necessarily in the first loop round the system). If the load is found to be zero, then a hydrodynamic film has not been formed. This can be produced for a parallel or diverging wedge film shape especially at low loads. Counter 4 is set to -1 and the position of centre of pressure is artifically readjusted to cause a

converging wedge (when new film thickness is evaluated.) If the displacement of centre of pressure from the pivot position is less than 0.5% of a typical pad dimension (see section 5.4); counter 4 is reset to zero - showing that the pivoting routine has converged. If a positive load is found, counter 4 is incremented by +1, indicating a pivoting loop. A check for the displacement of centre of pressure from the pivot position is made as before. If convergence has been attained counter 4 is reset to zero. Table 5T-1 summarises the significance of counter 4.

Table 5T-1 Pivoting Counter 4

Counter 4= 0	convergence has been attained
Counter = -1	zero load and no convergence - set a converging film shape
Counter >= 1	No convergence - MP indicates number of pivoting loops

Question box Q1 (see Fig 5F-6) checks for pivoting convergence as well as the maximum number of allowed pivoting loops. A maximum of 20 loops is usually allowed. Either condition will cause an exit from the pivoting routine and the conditions of exit are printed in the output. If both are not satisfied, a counter '5' is set to zero. At point 11 in the flow chart it is incremented by +1. This counter records the number of loops required to obtain a positive film thickness at all nodes. Next, the pivot angles are adjusted as described in section 5.4. The new film thickness is

evaluated and FLAG2 set to zero. If the film thickness at any node is negative, FLAG2 is set to +1. At box Q2 a check is made for counter 5. If it exceeds 9, the whole program is stopped at this point indicating the film shape condition. This condition is encountered for large changes in the pivot film thickness, requiring very large changes in the angles of inclination. It can be avoided by limiting the step size in varying the pivot film thickness (and hence the load.) For the condition where counter 5 is less than 10 a check is made in question box Q3 as to whether the film thickness is all positive. If it is (FLAG2=0), the program returns to point 10, where another solution of the Reynolds equation is carried out, and so on. If the film shape includes negative film thicknesses, the magnitude of the angle of inclination circumferentially is multiplied by a factor of 0.8 - reducing the inclination and, therefore, reducing or eliminating the negative film thicknesses. The program returns to point 11, at which counter 5 is incremented by +1 and a new film shape evaluated. Thus, the only exit position for the pressure solution and balancing (Area 4) is question box Q1.

Area 2 concerns the solution of the energy equation in the pad, runner and oil film. The total energy equation solution has been dealt with in chapter 3. On entry, counter 1 is incremented by +1, indicating a further energy balance loop. The energy equation constants which depend on flow are evaluated. Counter 3 is set to zero, indicating a fresh energy loop. At point 2, the oil midplane temperature is evaluated. The fluxes at the oil/pad and oil/collar

interfaces are used to determine the new temperature fields in pad and collar. Counter 3 is incremented by +1 to indicate a full loop through the energy routines. An underrelaxation factor set at 0.7 initially is used in evaluating the oil mid plane temperatures (see Fig3-7,Chapter3). If the number of iterations exceeds a limit of 50 loops, the relaxation factor is modified by a factor of 0.8. The fluxes used for the conduction to pad and collar may initially produce large temperature gradients across the pad and collar. This has a destabilising effect on the total energy equation solution, since the oil film boundary conditions are fixed by the conduction routines (in pad and collar) - see Chapter 3. Thus, an underrelaxation factor of 0.05 has been found necessary to establish stability (Fig3F-16 Chapter 3) between successive temperature fields at the film upper and lower boundaries. The mean absolute weighted residual (MAWR) between successive temperature fields is calculated before the underrelaxation is applied. Question box Q4 checks for MAWR between successive interface (oil/solid) fields. If MAWR is greater than 0.01 , another loop is commenced at point 2 unless the maximum number of iterations for the total energy loop has been reached (set usually at 6 iterations). In the latter case the FLAG is set to zero to indicate incomplete convergence or outright divergence. If convergence is obtained a check is made for counter 3. Question box Q5 is used to have two compulsory loops for the total energy equation, for every entry into area 2. Next, the viscosity field is updated to match the new oil film temperatures (see section 5.2). Thus, on exit from Area 2, Flag determines

convergence (+1 for converged solution, 0 for non convergence).

In Area 3, the pad deflections are evaluated for the new pressure and temperature fields (see section 5.1). The new film thicknesses are evaluated using an underrelaxation factor initially set at 1. Next, a check is made for counter 1 (which is never reset). If it is the first loop through the program, another mandatory loop is required to ensure that deflection and energy play a full role in the convergence of the equations. The MAWR for successive film thicknesses is evaluated. Counter 2 is incremented by +1 to indicate a total loop through all equations. A check is then made for MAWR of film shape just calculated. If convergence has not been satisfied (residual less than 0.01) and the maximum number of iterations not reached (usually 10); another total program loop is restarted at point 1. If FLAG is zero, the deflection underrelaxation factor is multuplied by 0.9 to damp out divergence caused by large deflections. In question box 6, a check is made for the convergence of the energy equations. This is necessary since the successive film thickness values can appear to have converged before convergence for the total energy system is reached. If FLAG has a value of zero, the maximum number of iterations through all equations (that is for counter 2) is doubled to allow for the slower energy routine convergence - and another loop is commenced at point 1. Hence on exit from Area 3, either a totally converged solution, or a partially converged solution results. Special warnings are output to show whether the pivoting, energy and film thickness have converged.

In Area 5, the results of the previous program loop (for a particular film thickness and speed) are output. The pressure, temperature, and film thickness distribution are printed. The bearing load, flow and power loss are also printed. All program values necessary for a further program loop are written on TAPE 2 (a local file) after rewinding of the TAPE. Thus, only the last set of values are kept on TAPE 2 for reasons of economy.

At this stage, another pivot film thickness and angular velocity may be chosen. L is incremented by +1 to indicate a new input condition. A maximum of 15 values are set to limit the number of output lines.

5.7 Relaxtion Factors and Residuals

The choice of relaxation factors and residuals (MAWRs) affects the speed of execution of the total bearing program. The bearing program is composed of a series of iterative loops. Fig 5F-7 is a schematic diagram of the main program loops. Some loops may be in parallel - as for loops 2b and 2c. Some may be in series as for loops 1 and 2. A loop may be within another loop: - loop 2a within loop 2, and loop 1a within loop 1. Brazier's optimization method has been shown to be very efficient in determining relaxation factors - Chapter 2. A MAWR smaller than $1x10^{-4}$ is satisfactory for obtaining a stable pressure field. In order to have the accuracy required for the pivoting(outer) loop a value of $1x10^{-6}$ is required. A value of $1x10^{-7}$ is used as all other loops depend on the accuracy of the pressure field. The method of

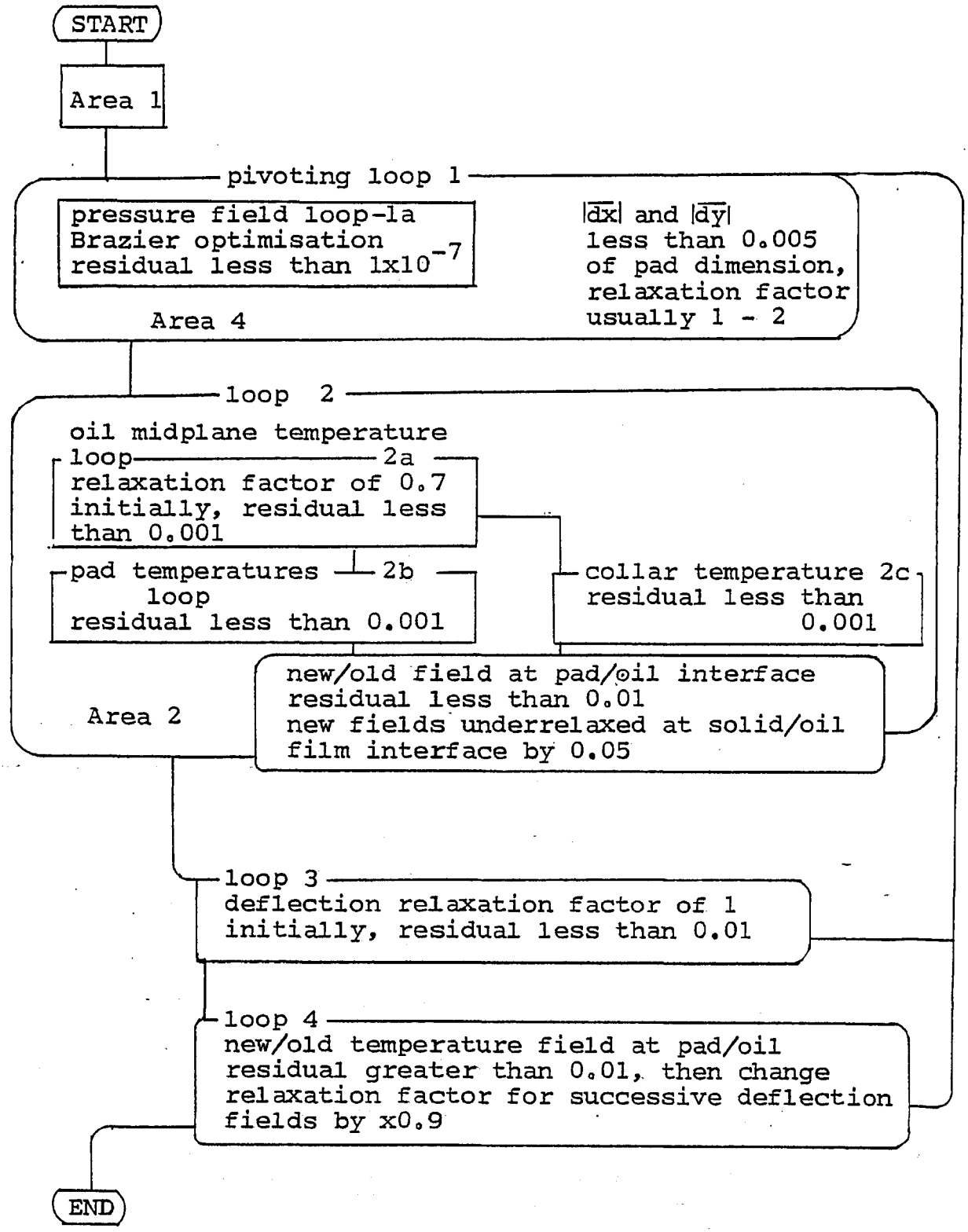

Figure 5F-7 Flow Chart for Relaxation Factors

pivoting has already been described (section 5.4). The accuracy of the position of the centre of pressure is required to be less than 0.005 of a typical pad dimension in both the X and Y co-ordinates (refer to 5F-2). This ensured an accuracy of better than 1% for the total load over the runs made.

Loops 2a, 2b and 2c have a maximum acceptable MAWR of $1x10^{-3}$ for the field changes. The outer loop 2 requires a MAWR of 0.01, an order of magnitude greater than for the inner loops. This setup makes a significant reduction in computer time compared to a constant value of $1x10^{-3}$ for loop 2. The overall accuracy is 0.01 or 1%, whilst truncation error effects are eliminated due to the more accurate inner loops. The new solid/oil film interface temperature fields are underrelaxed by a factor of 0.05. This is a source of delay in the initial program run loops, but nevertheless necessary (see Chapter 3).

In loop 3 the residual (MAWR) for sucessive deflection fields is set not to exceed 0.01. Thus two checks are performed concerning the oil film shape: the first in the pivoting loop 1 and the second in loop 3.

Loop 4 is conditional for the case where the energy equation has not converged. An underrelaxation factor of 0.9x old relaxation factor is used for loop 3. This is designed to combat the thermal ratcheting effect which occurs for heavily loaded bearings where a non-convergent oscillation of the temperature and deflection is set in motion. Since the temperature loops are already underrelaxed,

successive deflection fields are also subjected to underrelaxation to overcome this problem.

Fig 5F-8 shows the progress of a typical thrust pad bearing solution. The Y-axis scale represents $|\delta y|$ only. Curves for the temperature and pressure at the pad midpoint are superimposed (with different scales on the Y axis). It can be seen that the effect of a new temperature value is strongly reflected in both the pressure and pivot position solution. The peaks are seen to shrink rapidly, the pressure and centre of pressure both reinforcing each others convergence.

In Fig 5F-9 $|\delta y|$ is plotted versus $|\delta x|$ for the same case as in Fig 5F-8. It can be seen that the pivoting technique suceeds in drawing the centre of pressure towards the pivot position. For preliminary program runs, the same pivot film thickness and speed are input successively to ensure that the bearing characteristics are evaluated correctly and to the required accuracy. The difference for load capacity never exceeded 0.5%, whilst maximum bearing temperature was accurate to 0.1%. A typical bearing run requires 800 central processor (CP) seconds on a CDC-6500 machine. This is approximately equivalent to 200 CP seconds for a CDC-7600 machine. The run produces the bearing characteristics for 15 load conditions governed by the input angular velocity and pivot film thickness. The progam may be run iteratively at a terminal or sent as a batch job. The central memory storage required for compilation (using the MNFS ICCC compiler) is less than 24,500

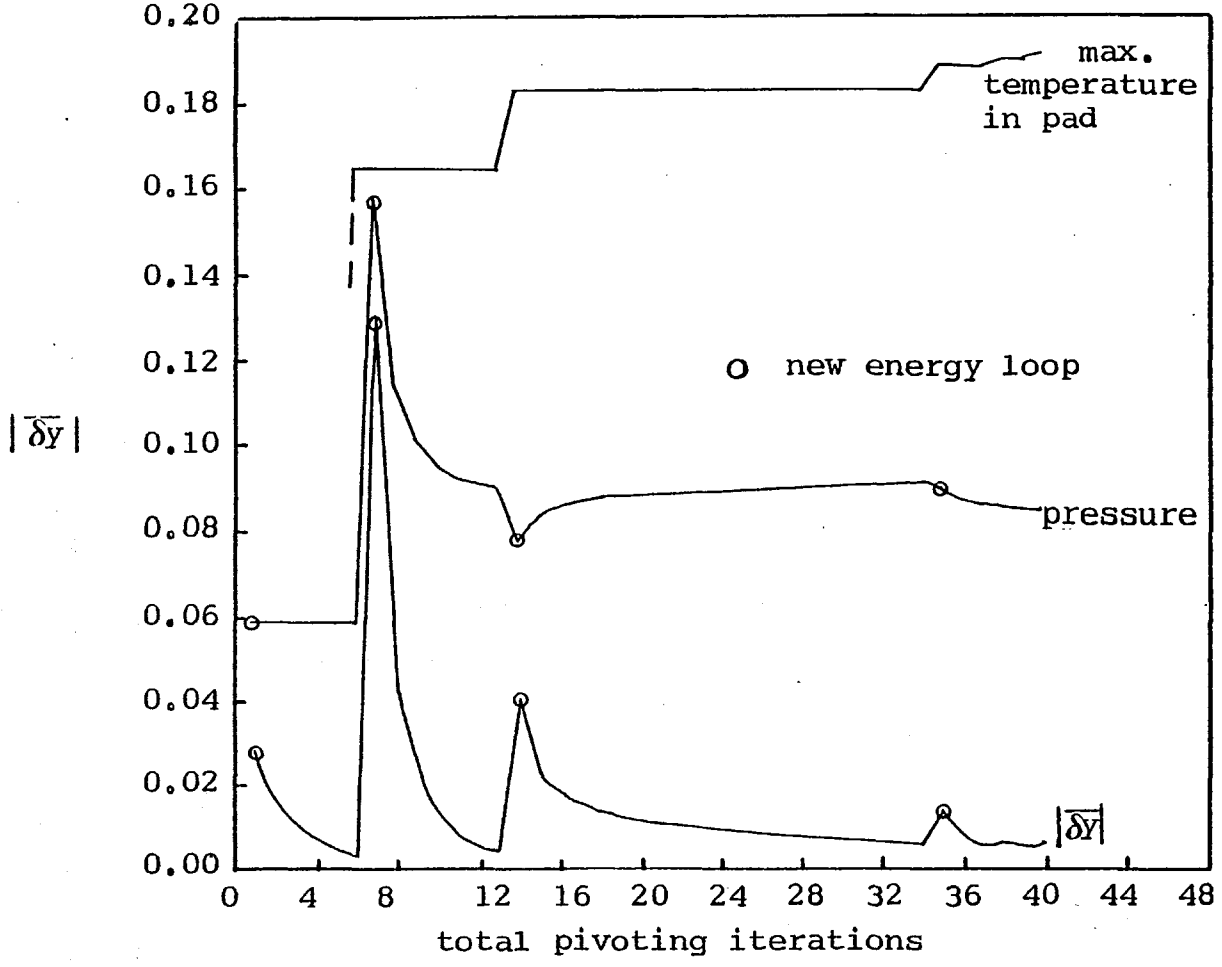

Figure 5F-8 Progress of a Typical Numerical Solution

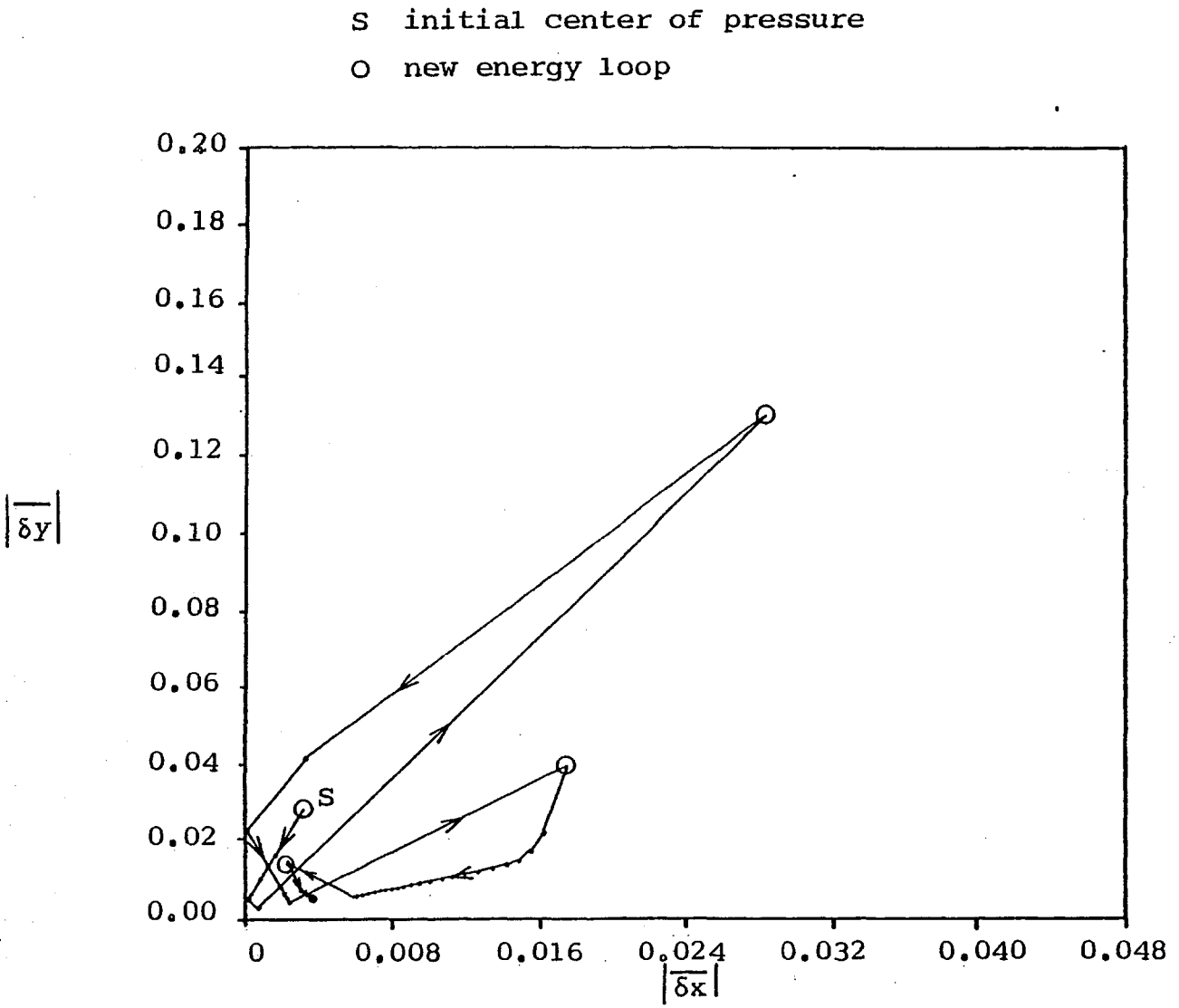

Figure 5F-9 Variation in position of center of pressure for Successive Pivoting Loops

words. To load and execute the program requires 30,000 words. A seperate program was written to process the results on TAPE 2 for contouring the temperatures, pressures and film thicknesses (see Chapter 6 for results).

CHAPTER 6

COMPARISON BETWEEN THEORY AND EXPERIMENT

Introduction

The previous four chapters have dealt with the numerical modelling of tilting thrust pad bearings. The validity of the present model as a whole can only be verified by comparison with experimental results. Tests have been performed for individual parts of the model (see chapters 2,3 and 4), but these are not sufficient to guarantee a good overall model.

Three test cases have been chosen. The first concerns a large tilting thrust bearing typical of the type used for large hydroelectric generators. The second is medium sized, typical of marine thrust bearings. The third is a small bearing size, typical of the high angular velocity small rotor applications. These three test cases span across the tilting thrust bearing size range and therefore present good check for the model used.

6.1.1 Case 1 - Large Thrust Bearing

The experimental results have been accessed through an internal company report {R79}. The basic bearing specifications are listed in Table 6T-1. The bearing is composed of ten equally spaced pads. The basic pad geometry is shown in Fig 6F-1. The pads are individually supported by centrally relieved buttons. They were designed to control the amount of pad deflection and to provide some flexibility in the bearing, thus equalising the individual loads on the pads. Extensive temperature measurements in the pads were carried out. The thermocouple installation and positions for all

Table 6T-1 (Case 1)

Pad Angle	29.5 degrees
Inner Radius (R_i)	0.7493 m
Outer Radius (R_o)	1.4732 m
Number of Pads	10
Pad Thickness - min	0.0762 m
- max	0.2032 m
Pivot Position	
radius	1.151 m
circumferential at 0	16.05 degrees
Angular velocity	85.7 rpm
Oil Viscosity	625 SSU at 100 deg F
	169 SSU at 150 deg F (interpolated)
	210 SSU at 210 deg F (interpolated)
Bath Temperature	48 deg C
Pad Material	STEEL

(Values Constant Throughout)

Oil Density	899 kg/m^3
Oil Conductivity	0.15 J/m s deg C
Oil Specific Heat	1880 J/kg s deg C
Steel Conductivity	45 J/kg s deg C
Steel Coefficient of Linear Expansion	1.1×10^{-5}
Poisson's Ratio	0.3

ten pads of the bearing are shown in Fig 6F-1. The thermocouples along the inlet edges of the pad were very close to the working surface whereas the remaining thermocouples were approximately 13 mm from the surface. At four positions on one of the pads, thermocouples were installed on the backface as well as 13 mm from the working surface. By assuming a parabolic law for the temperature profile across the pad thickness, it has been possible to obtain values for the surface temperatures.

During start up, the bearing is hydraulically jacked via a jacking oil groove in the pad face (see Fig 6F-1). During operation, the jacking oil supply is shut off and a pressure gauge installed to measure the oil film pressure immediately in front of the thrust pad in the jacking pipeline, with the jacking pump switched off. The oil bath temperature was kept constant at 48 deg C.

6.1.2 Numerical Model

Since the pads are not centrally pivoted, the grid spacings were varied to accomodate the support shape (a circular ring) as closely as possible. Fig 6F-2 shows a plan of the pad with the grid superimposed. Also shown are the support nodes chosen as the nodes closest to the ring support. The boundary conditions used for the pad deflection are also shown. These include free pad edges and corners. At the support positions, no allowance has been made for the pivot elasticity. At the corners, the shear forces produced by the torsional moments (M_{xy}, M_{yx}) are additive {R80}. A net force

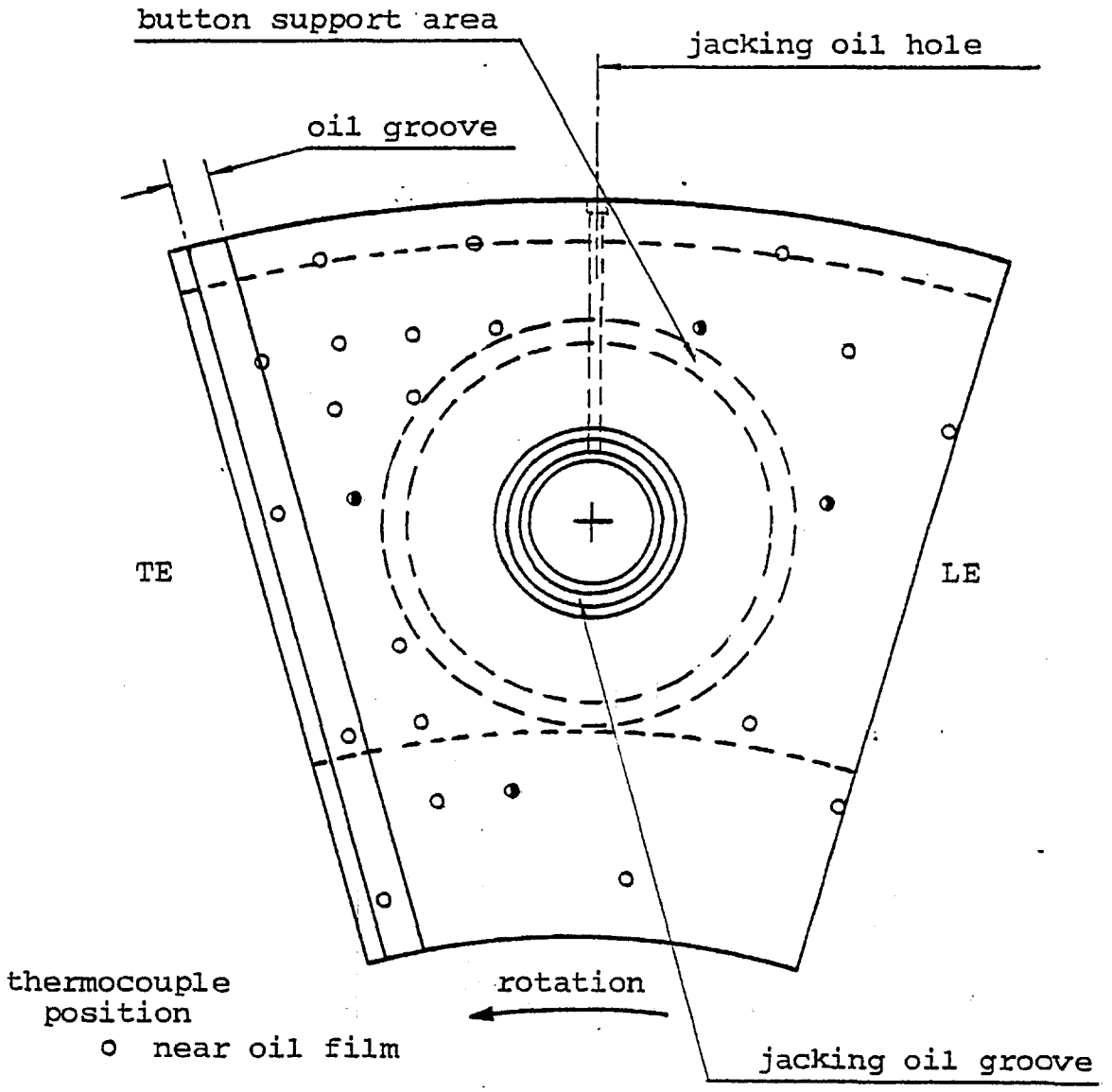

Figure 6F-1 Case 1 - Pad Geometry

$M_{r\theta} = 0$

$V_r = 0$ × pressure node

$M_r = 0$ $V_\theta = 0$

$w = 0$ $M_\theta = 0$

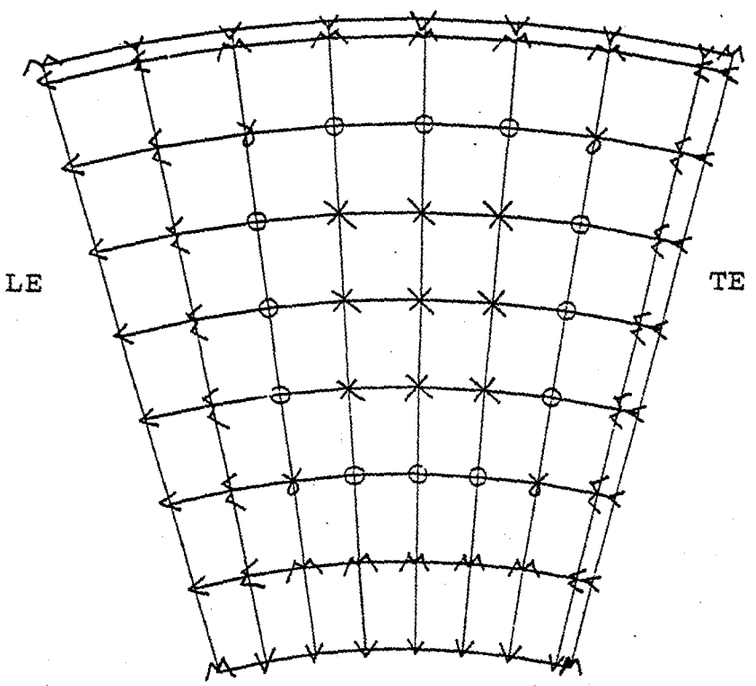

Figure 6F-2 Case 1 - The Grid and Boundary Conditions for Deflection

($= 2M_{xy}$) is thus produced at the corners and must be set to zero in a free corner case.

In order to estimate the surface heat transfer coefficient at the backface of the pads, the oil bath temperature has been used as the 'free' stream temperature. Thus,

$$\alpha \left(T_{bath} - T_{surface} \right) = k \left(\frac{T_{surface} - T_{pad}}{depth} \right)$$

where $T_{surface}$ is the backface temperature

T_{pad} is the temperature at a location near the pad working surface

depth is the distance from the backface to the location of T_{pad}

k is the conductivity of the pad

α is the surface heat transfer coefficient

From the temperature measurements, a surface heat transfer coefficient of between 200 to 450 J/m^2s deg C could be obtained depending on loading and location in the pad. Since the temperature profile is expected to be quadratic, the higher values are used, as the true surface gradients are likely to be steeper than in a linear profile (Fig 6F-3). A value of 450 J/m^2s deg C has been used in this case.

The pad thickness varies between a minimum of 0.0762 to a

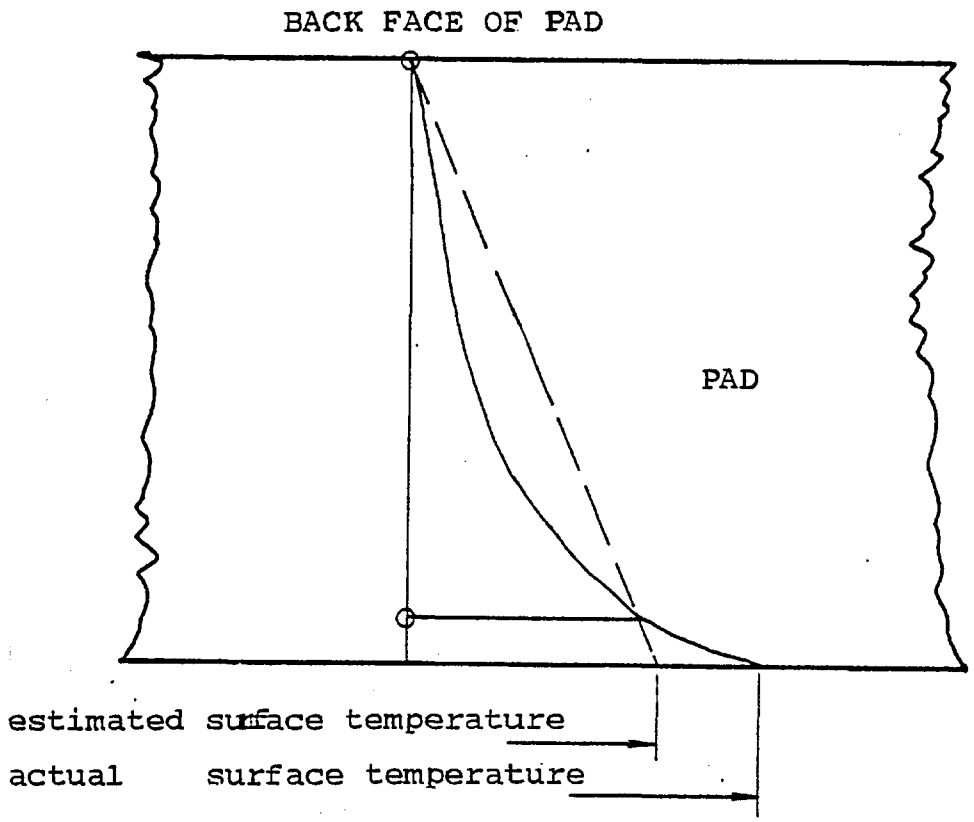

o thermocouple locations

actual temperature profile

temperature profile estimated from measurements

Figure 6F-3 Effect of Underestimating the Temperature Gradients at the Pad Surface for a Linear Interpolation

maximum of 0.2032m. A 9X9 grid cannot reflect the abrupt changes in pad thickness in detail. Thus an average value of 0.127 has been used. The collar thickness has been taken to be twice the pad thickness.

6.1.3 Analysis of Results

Fig 6F-4 shows a graph of maximum pad surface temperature versus load. Another curve is plotted for the leading edge temperature versus load. Since the bearing supports a turbo-generator, an initial load of 16.2 bars represents the weight of the moving parts. An additional thrust is exerted by the water flow in the turbine which can be regulated to produce the different loading conditions. Both curves show a discrepancy in the range 0 - 3 deg C between the model and experiment. In numerical terms, this is considered satisfactory. The agreement between the experimental results and the numerical model is improved at the higher loadings. A maximum test load of 40 bars produced a maximum pad temperature of 90 deg C, compared to a value of 88.5 deg C for the present model.

In Fig 6F-5 experimental and theoretical contour plots for temperature are presented at the pad/oil interface. It should be noted that the experimental contours for the pad surface have been interpolated and are likely to be lower than the true values (see Section 6.1.2). The shape of the temperature contours is very similar. The position of the maximum temperature is also approximately the same - a small distance from the trailing

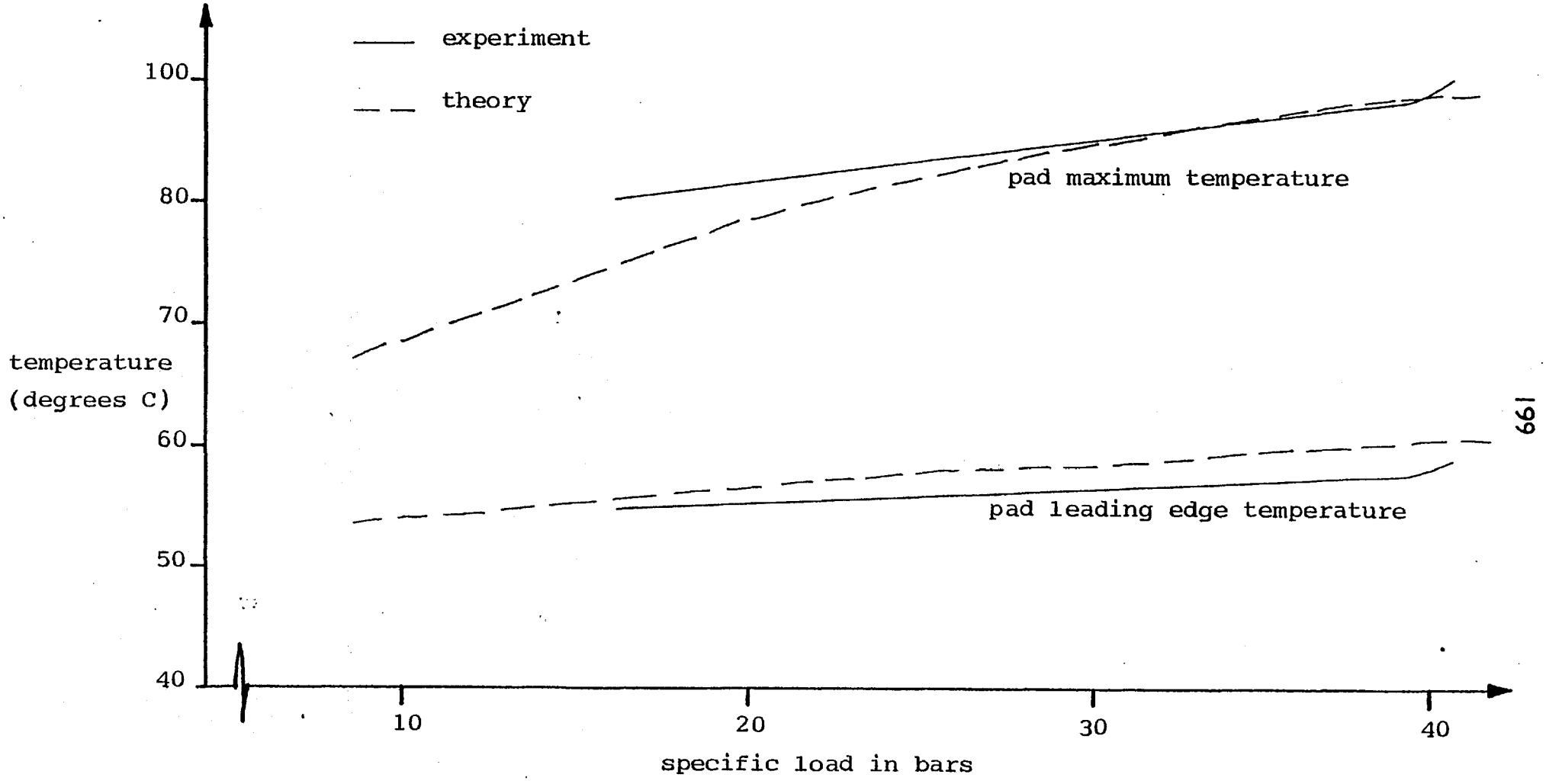

Figure 6F-4 Pad Temperature Versus Load - Case 1

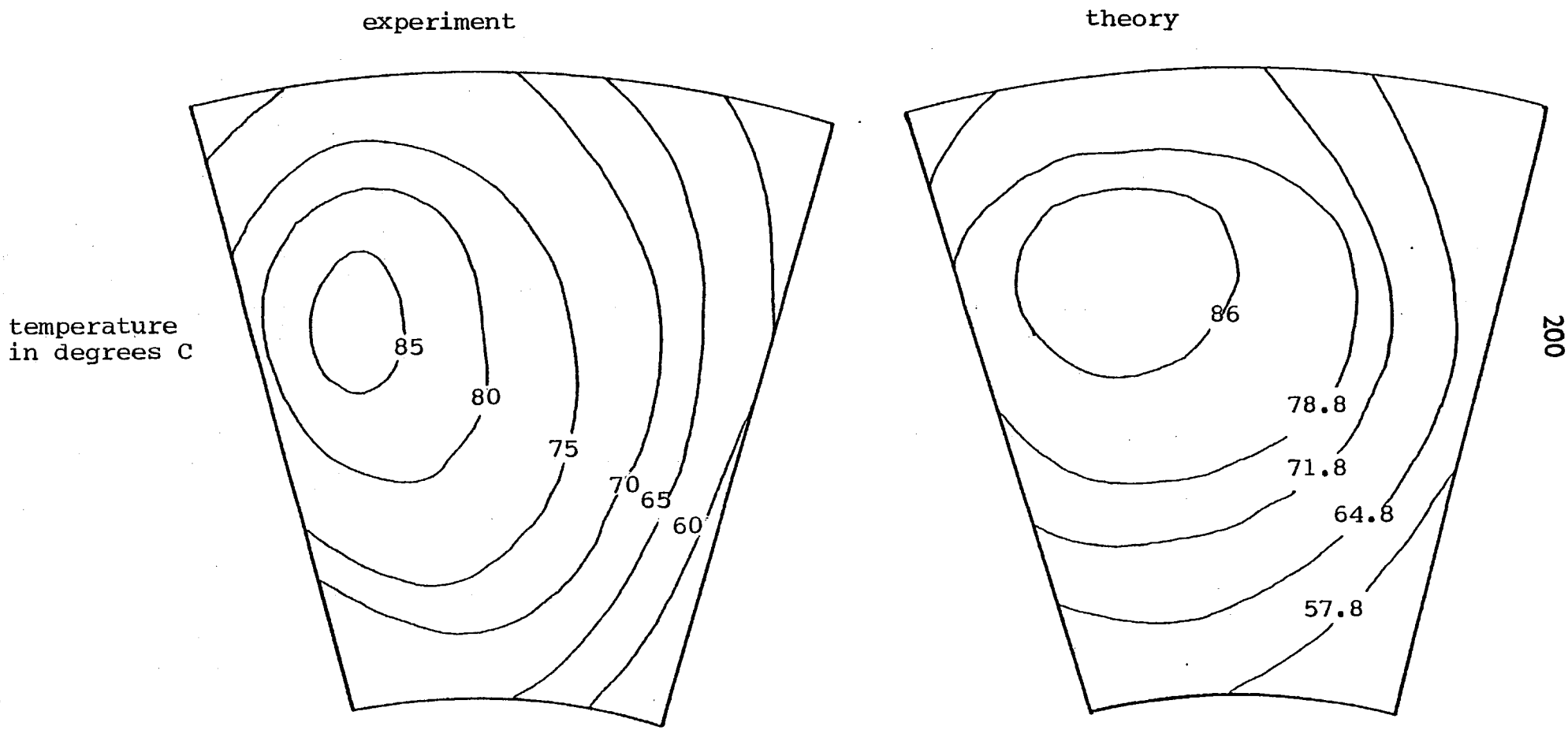

Figure 6F-5 Experimental and Theoretical Temperature Contours at Pad/Oil Interface

edge,(close to the "75-75" position). The inclusion of the conduction model for the pad is thought to be primarily responsible. If conduction is neglected, the position of the theoretical maximum temperature will be at the pad/trailing edge as there is no path for the heat generated to escape from the oil film.

Figs. 6F-6a, b, c, and d summarise the theoretical characteristics for the pads. At a total bearing load of 16 MN (approximately 40 bars), the minimum film thickness approaches (Fig 6F-6b) 30 microns. This necessitates an average surface roughness less than 2 microns {R81,R3}. The ratio of maximum to minimum film thickness increases from 2 at 10 bars to 4 at 40 bars. The total oil film energy loss increases as the load is increased. The energy loss in the oil film may be divided into four components: conduction to the pad; conduction to the runner; convection of the heat in the oil; and flow work.

The flow work term is very small (as mentioned in chapter 5 .) The ratio of heat conducted to heat convected increases from 1 to 3 over the range 10 - 40 bars. In fact the amount of heat convected decreases. This casts doubts over the previous methods that lack a conduction model to both the pad and runner {R16,R24,R26,R43,R17} and to their ability to correctly predict the oil film temperatures. Fig 6F-6d shows a sizeable decrease in the amount of oil entering the film leading edge as the load is increased. In contrast, the amount of heat convected shows only a small decrease (approx. 20%). This is reflected as an increase

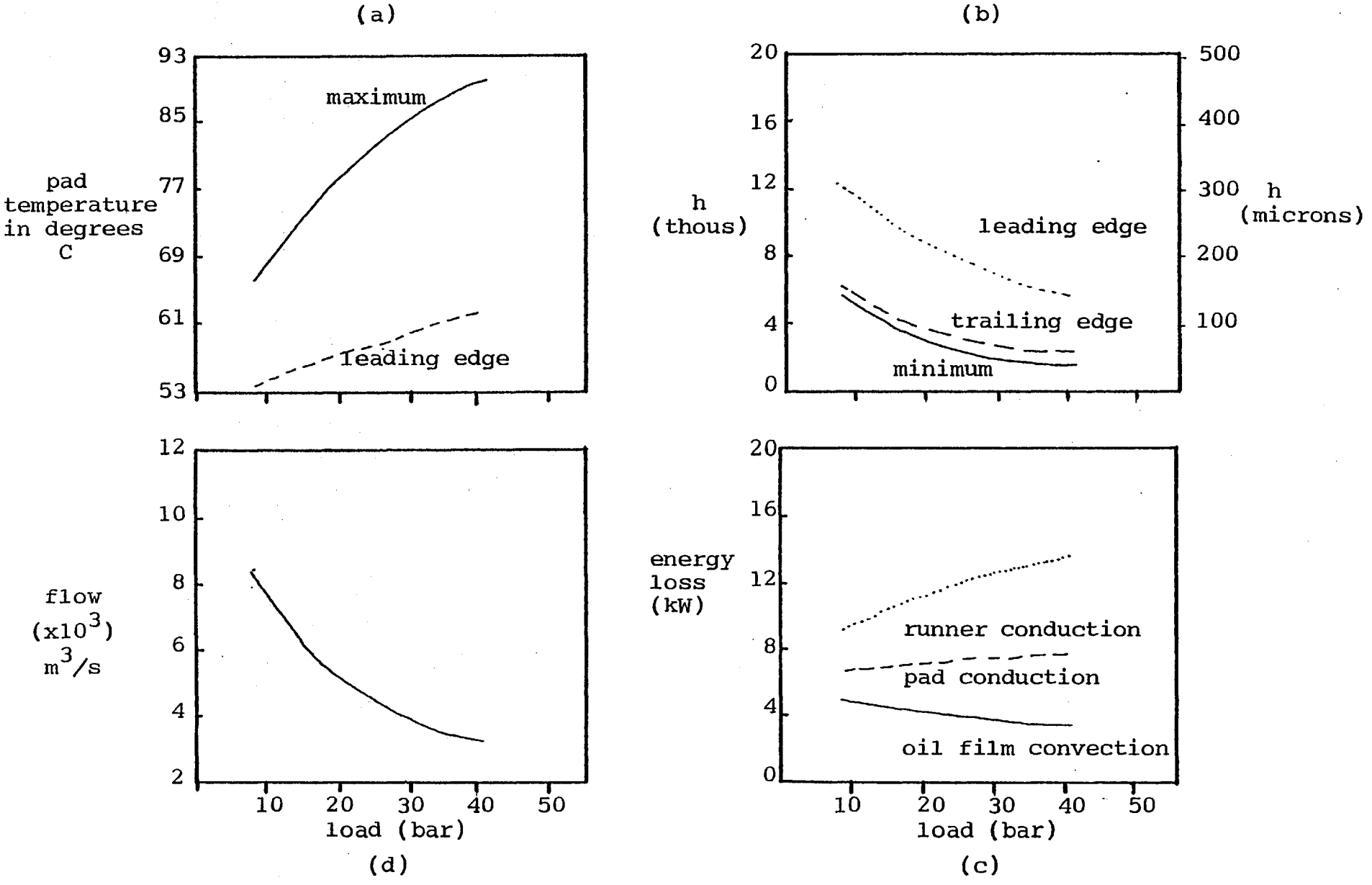

Figure 6F-6 Case 1 - Pad Theoretical Characteristics

in the oil film temperatures.

Fig 6F-7a shows a contour map of theoretical film thickness values, non-dimensionalised with respect to the undistorted pivot film thickness (h_{piv}). All values in Fig 6F-7 relate to the 40 bar load case. The pad deflected shape is shown in Fig 6F-7f with the support positions superimposed. Contours of pressure (6F-7b) show a small cavitated area at the trailing edge. The position of T_{max} closely corresponds with the position of minimum film thickness (Fig 6F-7a,c) both radially and circumferentially. The temperature distribution in the collar has a maximum value that falls directly above the maximum pad temperature (in the radial direction). The values of the maximum temperatures in the pad and collar are within 5 deg C. This suggests that the amount of conduction to the pad is very similar to that in the rotor. This is confirmed in Fig 6F-6c.

Fig 6F-8 shows three dimensional surface contours of temperature in the pad, oil film and the collar when viewed from the same relative position. The oil film thickness variation has been omitted, and the pad width used as a film thickness in order to illustrate the temperature variations in the z direction. Also shown is the deflected shape for the pad. The pad contours show a high intensity - reflecting a high temperature gradient - in the z direction compared with the lateral directions r, θ . This indicates that conduction across the pad accounts for most of the heat conducted via the pad. Fig 6F-9 shows radial sections of the

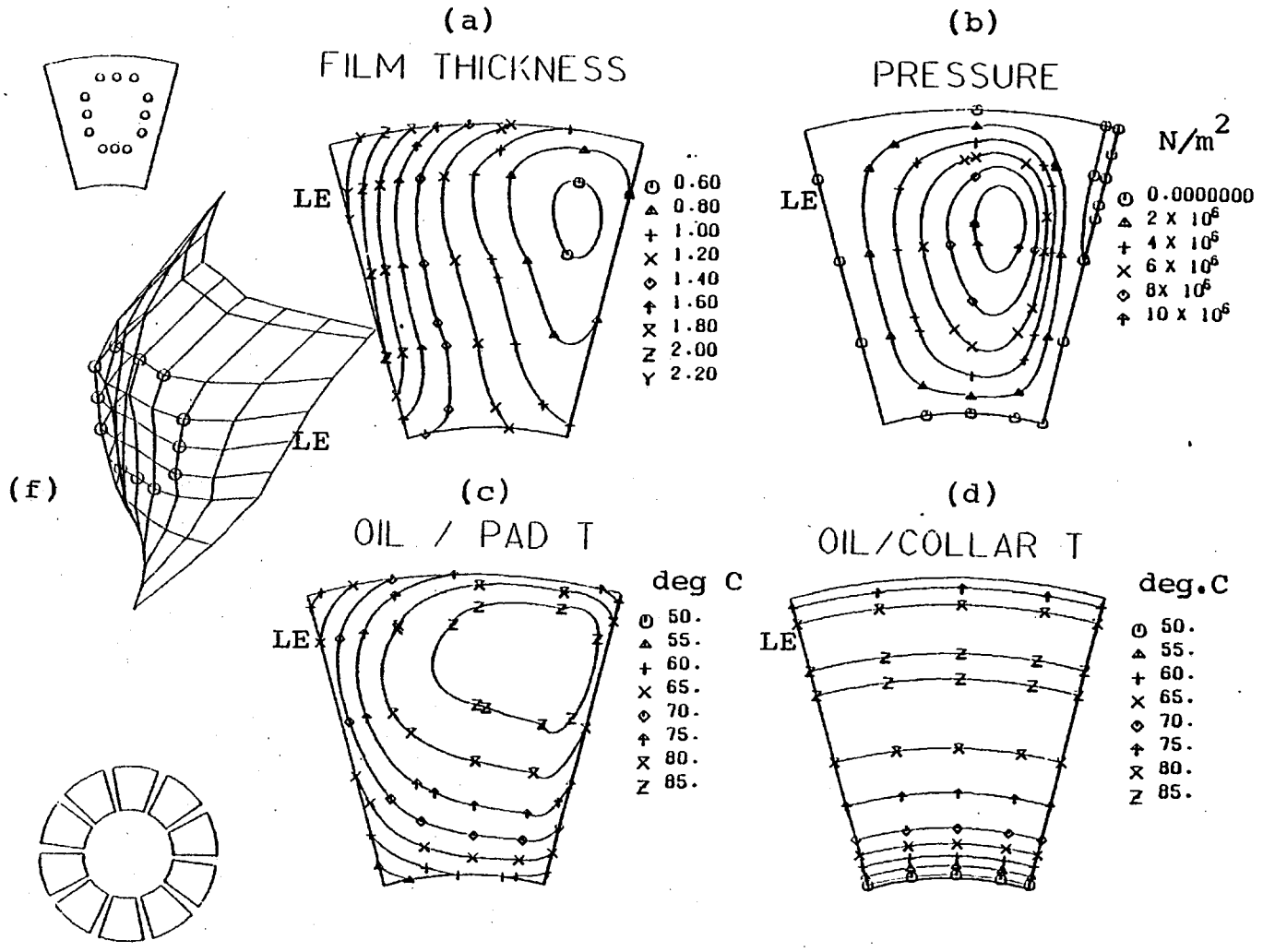

Figure 6F-7 Case 1 - p,T,h contours and Deflection Shape

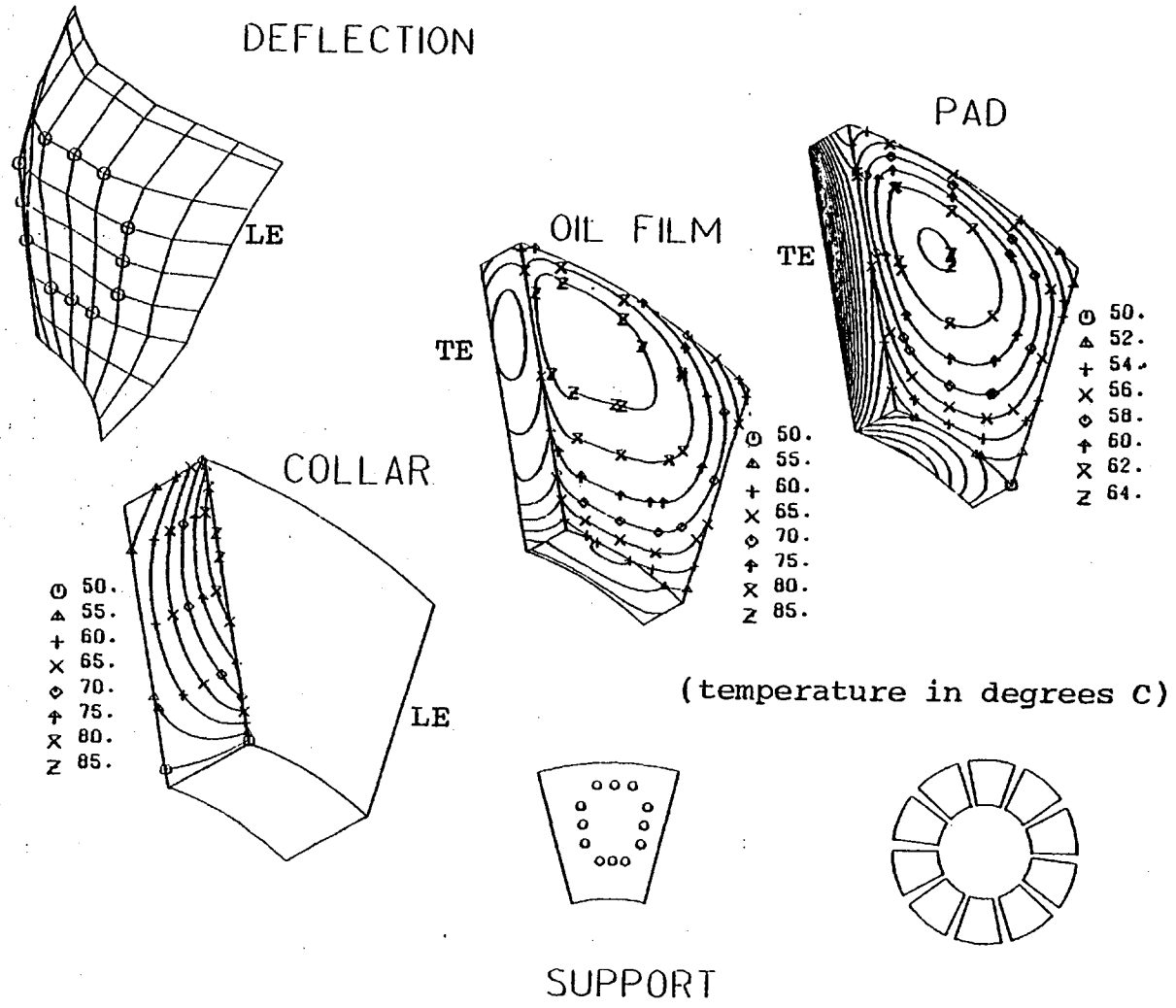

Figure 6F-8 Contours of Temperature in Pad, Runner and Oil Film (Case 1)

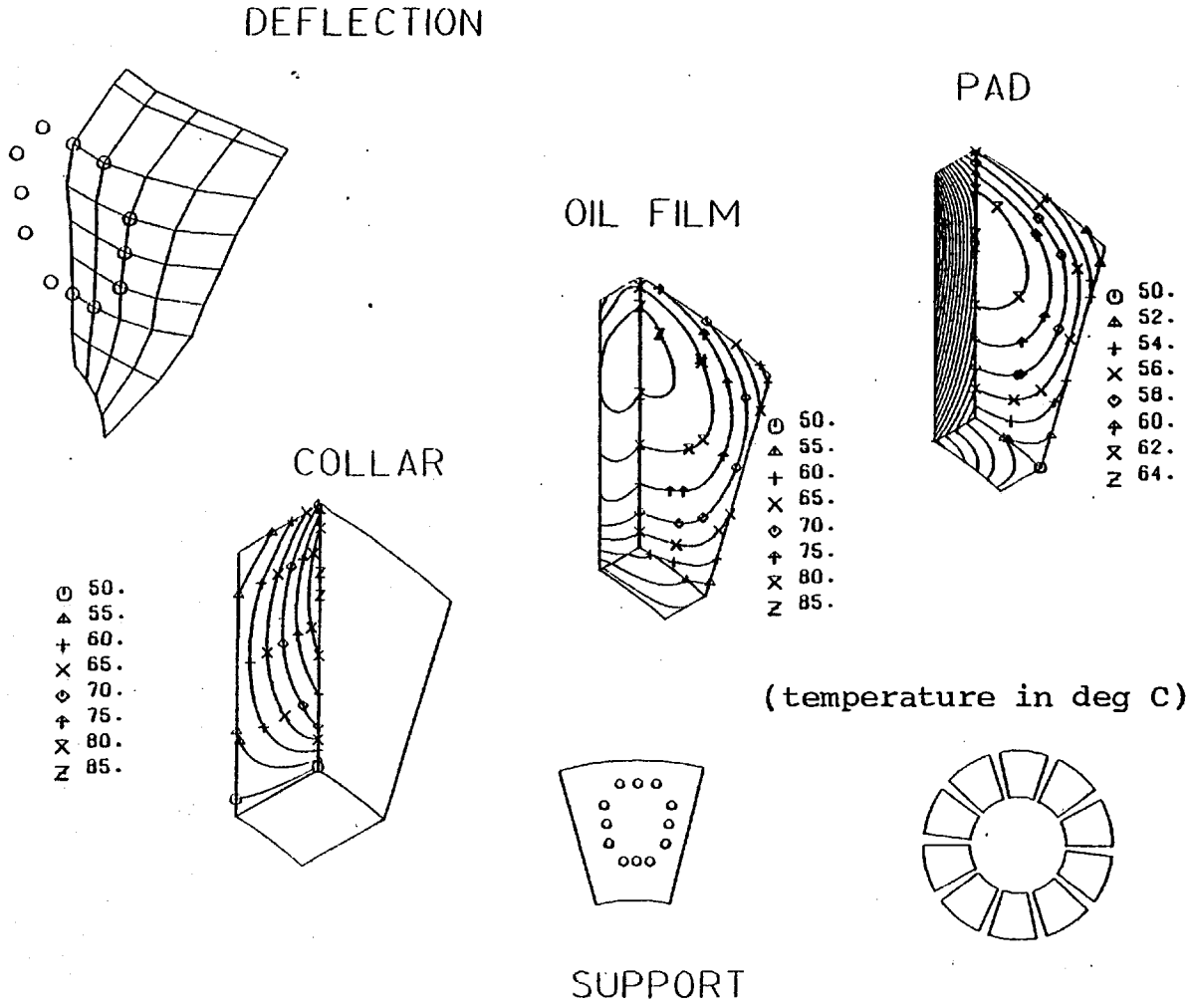

Figure 6F-9 Sectional View of Pad, Runner and Oil Film Showing Temperature Contours

pad, oil film and collar views in Fig 6F-8 (the section is taken at $\theta = \theta_{piv}$). The variation in pad contour density further supports the latter point.

The collar temperature contours remain the same for both views in Figs. 6F-8 and 6F-9 representing an axisymetrical distribution - an inherent feature of the present model. In Fig 6F-8, the oil film temperature distributions reveal a hot inner core, relatively symmetrical about the film mid-plane in the radial direction. The oil film thickness is 3 - 4 orders of magnitude smaller than other pad dimensions, and thus sharp temperature gradients result. In Fig 6F-10, temperature contours for vertical circumferential sections are shown at the inner, outer and mean radii. The oil film contours were plotted at 1 deg C intervals. Except for the inner radius section, the inlet oil temperature is lower than the collar temperature (for any circumferential position along a radial section). At inlet, the contours are equally spaced, confirming the linear inlet temperature profile assumption. The contours close to the rotor surface are straight and parallel to it. The differences in the shape of the temperature distribution at the inner radius, compared to the mean and outer radial sections, is a consequence of the boundary conditions imposed. At the inner radius the runner temperature is fixed equal to the oil bath temperature (see Chapter 3, section 3.3.3). At other radii the runner temperature is determined by the heat balance equations. Hence, a temperature increase at the collar inner radius is not allowed. The oil temperature at inlet cannot be lower than the bath

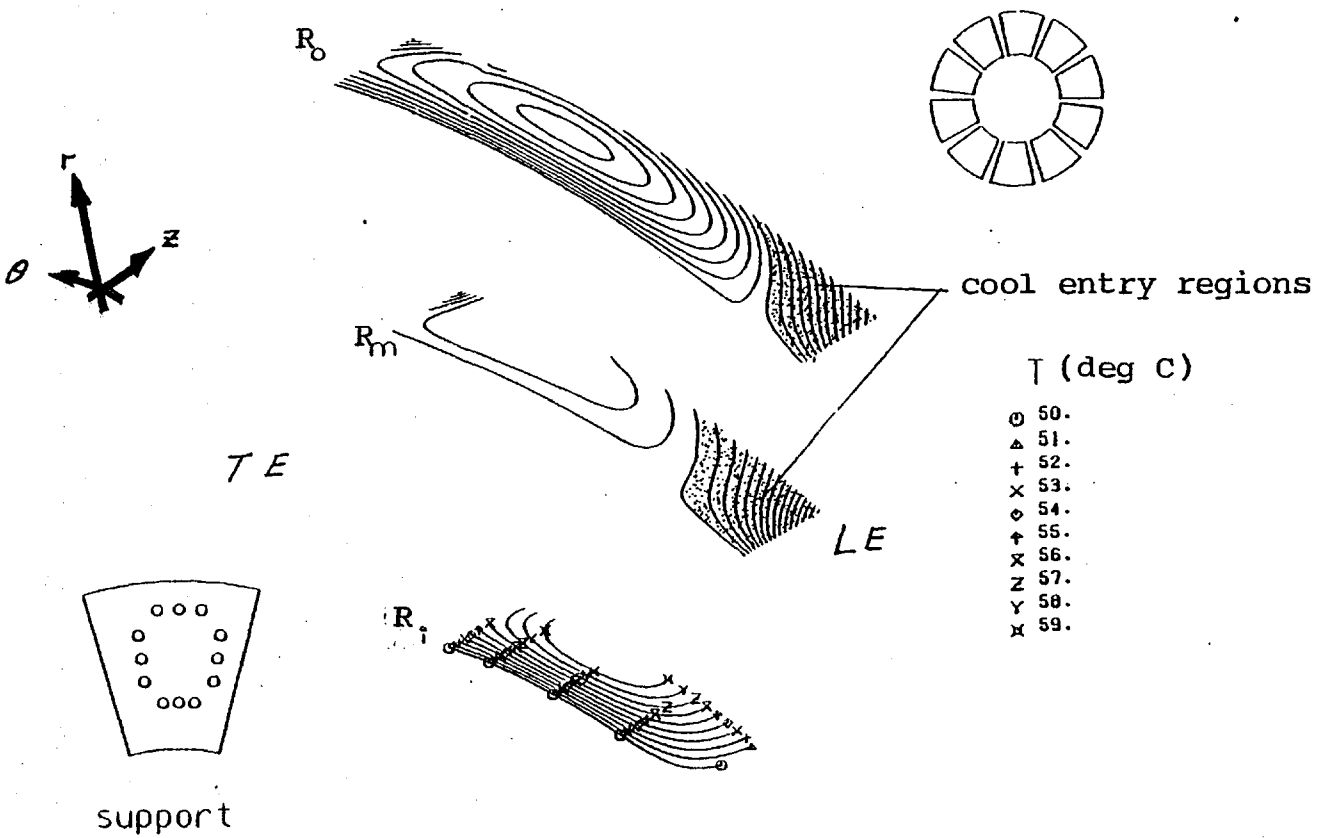

Figure 6F-10 Case 1 - Temperature Contours at Pad Inner, Outer, and Mean Radii

temperature, resulting in the absence of a cool entry region (relative to the collar). Ettles {R31} has shown the presence of 'a cool entry region' for the assumption of a linear temperature inlet profile (shown here for mean and outer radius). Others, who neglected temperature variations in the z-axis or assumed a constant inlet temperature {R25,R40,R10,R52,R82,R13,R14,R83} thereby neglected the 'cool inlet region' and all resulting temperatures are greater than the runner temperature. The effect of neglecting temperature variation (hence viscosity variation) at the inlet has been considered by Neal {R21}. Neal showed that variation of viscosity through the film thickness at inlet has a marked influence on the total quantity of lubricant drawn into the film and an even greater influence upon the pressure generated within the film. Most affected by the inlet temperature variation was the operating temperature. The relationship has been previously discussed above.

6.2.1 Case 2 - Medium Thrust Bearing

Tests conducted at the sea on the main propulsion thrust bearings of the destroyer USS Barry were reported by Elwell et al {R84}. The main bearing specifications are listed in Table 6T-2. The bearing consists of eight centrally pivoted pads. Temperature measurements were made at several locations in the pad including the pad centre. Measurements of oil groove temperatures were made using thermocouples of the same type as for the pad (copper - constantan). In addition film thickness measurements were carried out using two different systems - independant to each other. The

Table 6T-2 (Case 2)

Pad Angle	38.25 degrees
Inner Radius (R_i)	0.2096 m
Outer Radius (R_o)	0.3937 m
Number of Pads	8
Pad Thickness - min	0.023 m
- max	0.057 m
Pivot Position	centrally pivoted
Oil Viscosity	460 SUS at 100 deg F
	121 SUS at 150 deg F
	55.4 SUS at 210 deg F
Bath Temperature	38 deg C
Material	STEEL

Table 6T-3 (Case 2)

Load-Speed Relationship

Speed (rpm)	Unit Loading (psi)
100	50
200	205
300	495

first was a mutual inductance system which relies on the runner magnetic properties. The second is a capacitance system sensitive to the oil condition in the film. Overall accuracy of the film thickness measurements was estimated at + 5 microns. In the present work, comparison is made with steady runs in smooth-water trials of USS Barry (as inaccuracies have been reported in rough water measurements). Film thickness measurements were carried out for two shoes (pads). Comparison is limited to shoe number one {R84} with an initial maximum crown of 10 microns.

The speed load characteristic is given in Table 6T-3. The bath temperatures varied between 96 - 109 deg F (35.6 - 42.8 deg C). For simplicity a value of 100.4 deg F (38 deg C) is taken as the steady bath temperature.

6.2.2 Numerical Model

Since the pads are centrally pivoted, a regular grid has been used (see Fig 6F-11). For deflection the same boundary conditions apply as in Case 1.

The surface heat transfer coefficient values were obtained from thermocouple locations as described for Case 1. The values are expected to be more accurate since temperature measurements were made at the pad/oil interface using thermocouple leads machined flush with the working surface. Fig 6F-12 shows a correlation between the surface heat transfer coefficient and rotational speed (hence the load). It appears that at low speeds (less than 10

γ	$M_{r\theta} = 0$
$\vee$	$V_r = 0$
$\curvearrowright$	$M_r = 0$
$<$	$V_\theta = 0$
$\leq$	$M_\theta = 0$
$\times$	pressure node
$\circ$	$w = 0$

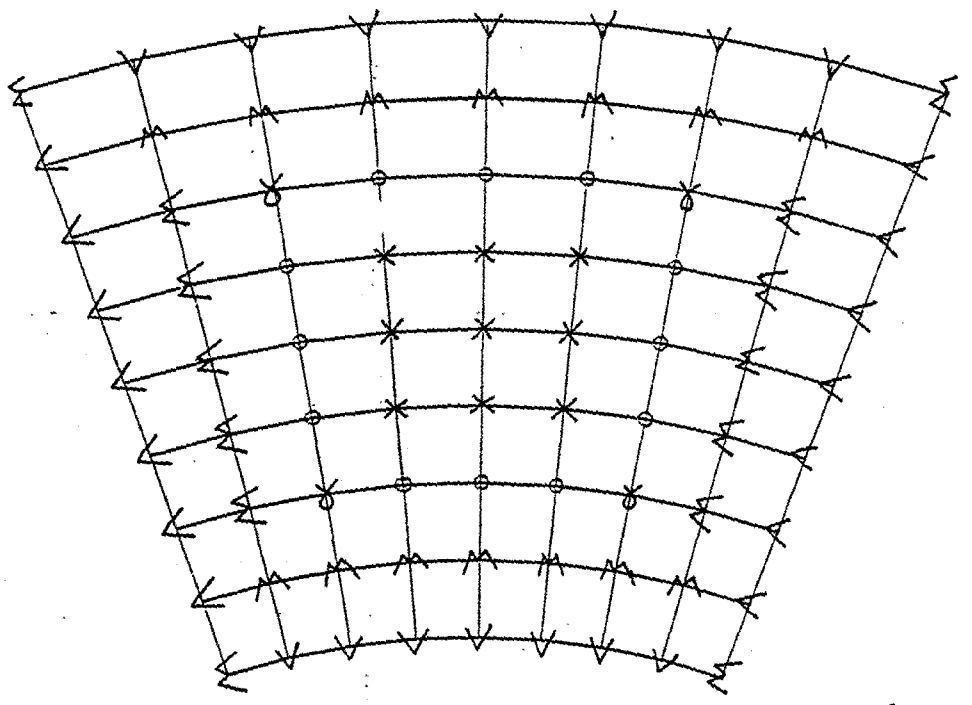

Figure 6F-11 Case 2 - The Grid and Deflection Boundary Conditions

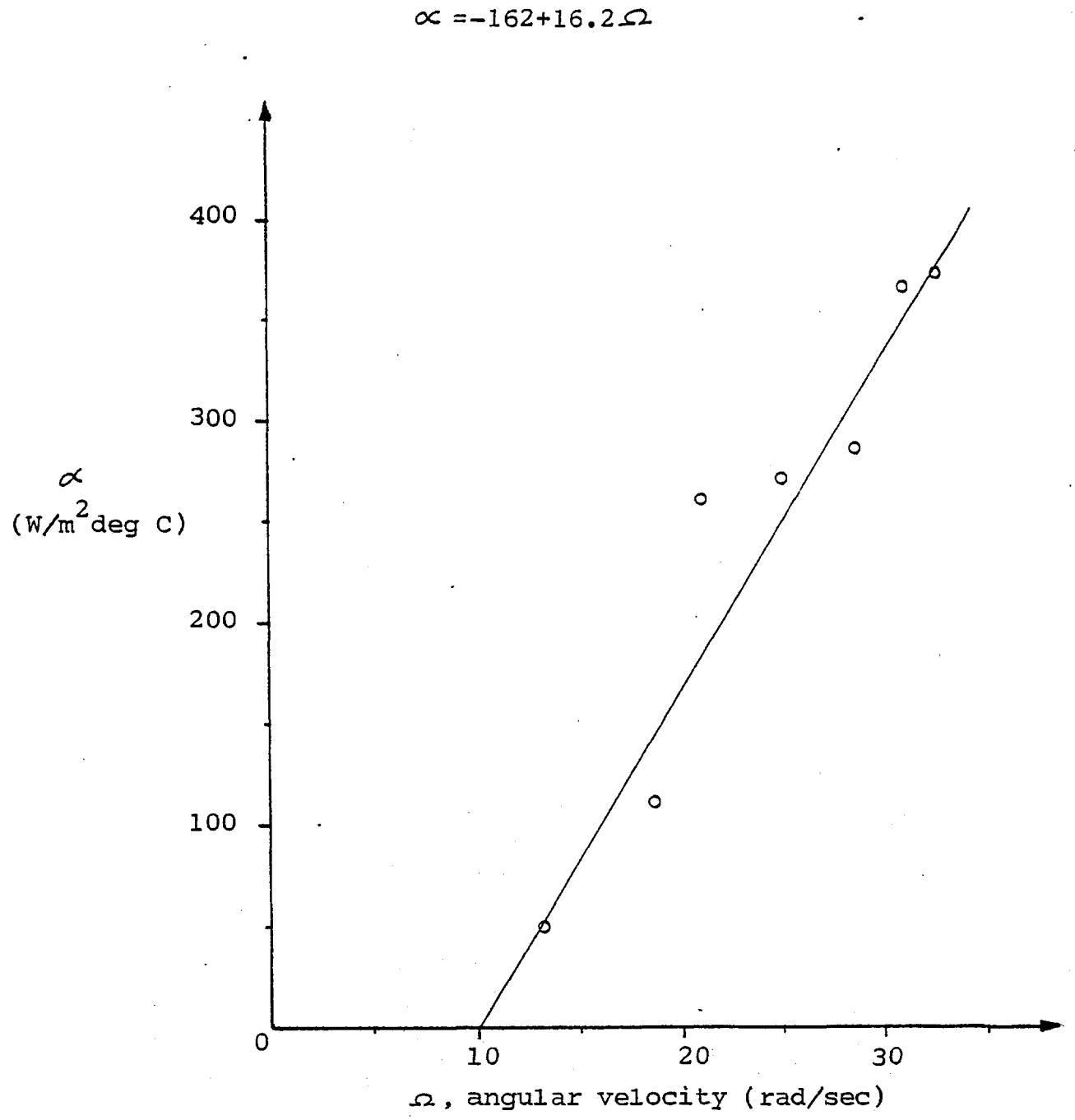

Figure 6F-12 The Variation of Suface Heat Transfer with Angular Velocity (Case2)

rad/sec) a negative surface heat transfer results. This is not possible and the coefficient values are expected to have a minimum positive value representing free convection. However since the region of interest lies above the speed of 10 rad/sec. This correlation yields

$$\alpha = -162 + 16.2\Omega \qquad \text{for } \Omega > 10 \text{ rad/sec}$$

The correlated values for α are obtained using the method outlined in Section 6.1.2.

Elwell et al {R84} gave details of the pad thickness variations. Again for a 9X9 grid it was not possible to include them (unless the changes were smooth). The maximum thickness was 2.25 inches (0.05715 m) and the minimum value was 0.775 inches (0.019685 m). The average value was 1.5 inches (0.0381 m), and was used as the pad thickness in the model. The collar thickness was assumed to be twice that of the pad.

6.2.3 Analysis of Results

Fig 6F-13 shows the film thickness variation with load at the pad centre. At 35 bars a difference of 5 microns (1/4 thou) exists between theory and measurement. As the load decreases, the gap widens to 15 microns. A difference of 5 microns is acceptable on the basis of the experimental errors reported. Thus a maximum film thickness error of 15% results for the low load. The temperature at pad centre is also plotted versus the load (Fig 6F-13 .) A consistent gap of 7 deg F (approx. 4 deg C) is

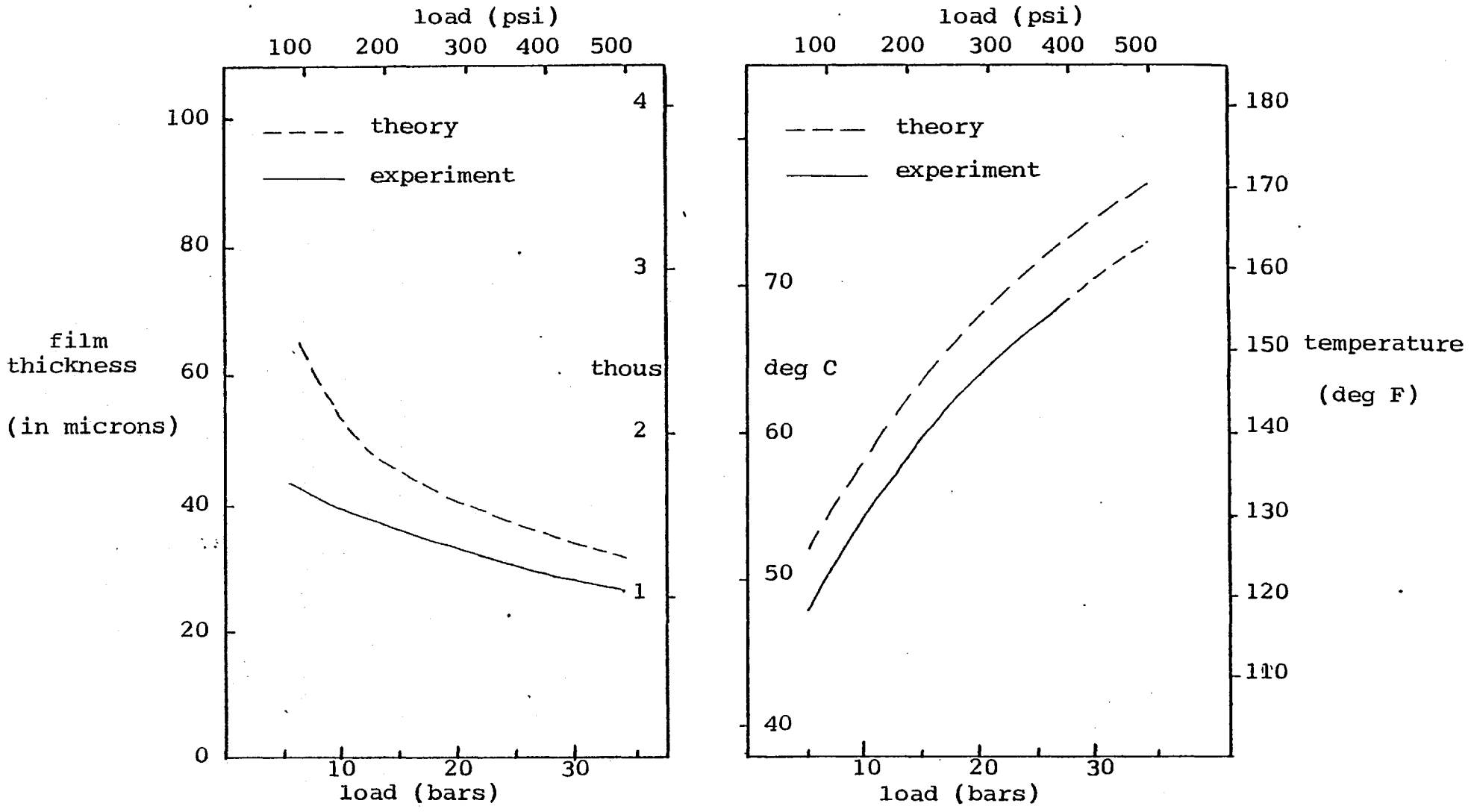

Figure 6F-13 Temperature and Film Thickness Versus Load - Case 2

shown for the entire load range. Fortunately, the analysis renders a higher temperature than measured and is therefore conservative.

Contours of predicted pressure predictions are shown in Fig 6F-14b. Film thickness contours are shown in Fig 6F-14a. The radial position of the minimum film thickness corresponds to the position of maximum temperature in both pad/oil and pad/runner interfaces (Fig 6F-14c, d). This is not the case when the circumferential position is considered. The hot core region on the pad surface (over 70 deg C) is circumferentially extended compared to the previous case. This may be partly due to the larger pad angle subtended. The film thickness pattern shows bending of the pad into a spherical shape, typical of a uniform plate with a constant temperature gradient across its thickness. Again this shows a marked contrast when compared to the film thickness pattern for the larger bearing in Case 1. The deflection pattern (Fig 6F-14f) confirms this (also refer to Fig 6F-7a, f). Fig 6F-15 shows three-dimensional surface temperature contours similar to those in Fig 6F-8. Two important differences may be observed. Firstly, the position of oil maximum temperature has moved radially outwards (that is nearer the outer radius). Secondly, that conduction along the pad (and runner) becomes as important as conduction through its thickness. This is reflected in a roughly equal spacing of contours along and across the pad. The vertical surface at the pad inner radius shows a hot spot at its centre. This is due to heat conducted along the pad from hotter regions (nearer the maximum temperature); the heat eventually

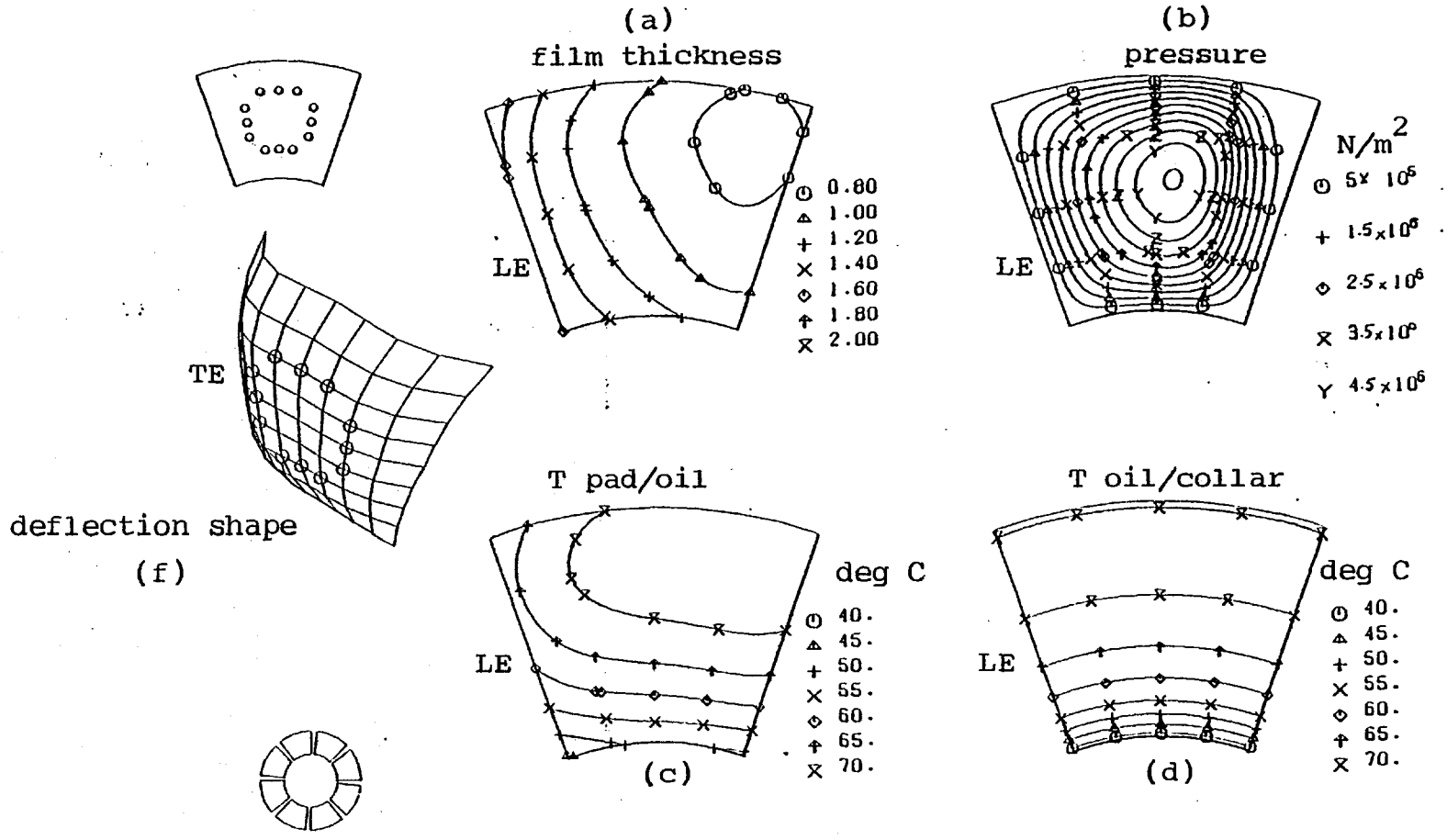

Figure 6F-14 p,T,h Contours and Deflection Shape (Case 2)

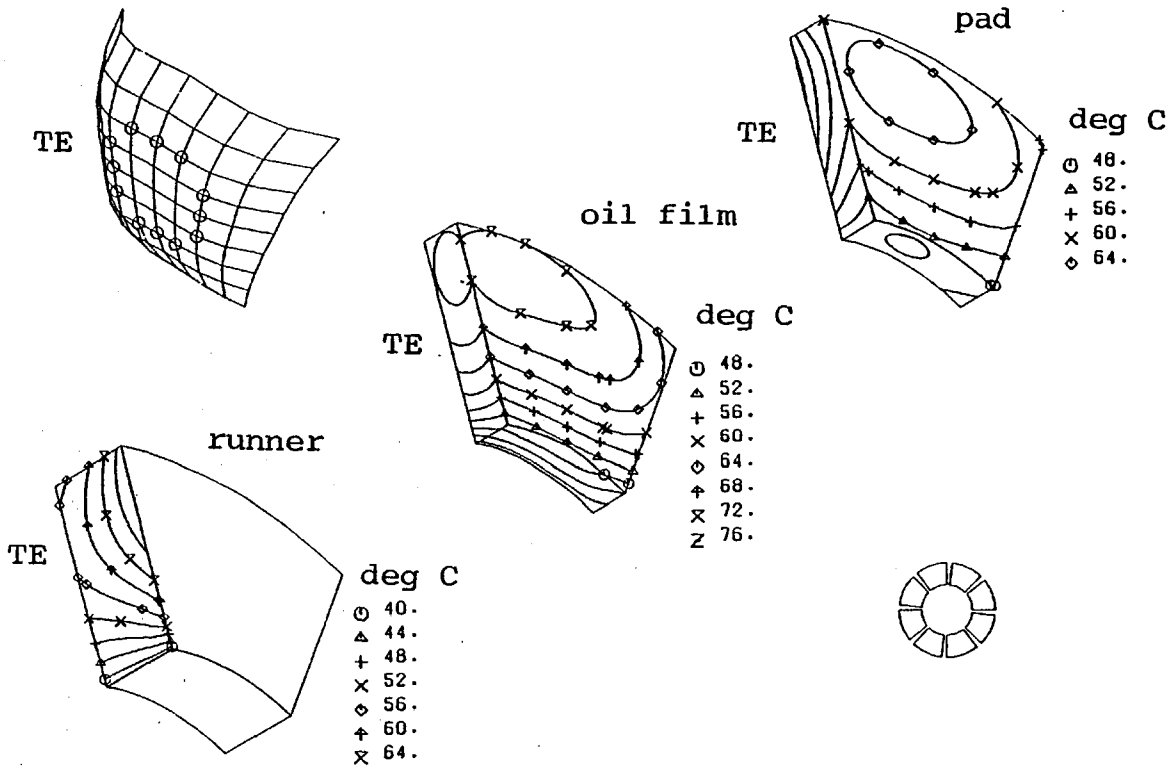

Figure 6F-15 Contours of Temperature in Pad, Oil Film and Runner - Case 2

given to the cooler oil film at the inner radius - as well as to the back of the pad. A sectional view (the section taken at the pivot angle position) is shown in Fig 6F-16. The contour density does not show an appreciable change.

6.3.1 Case 3 - Small Thrust Bearing

In 1979 Neal {R85} presented results of tests conducted on a 150 mm bearing. In 1981 {R33}, further results were presented for the same bearing. The main bearing specifications are given in Table 6T-4. Different pad arrangements were used: 3, 4, 6, and 8 (Fig 6F-17a).

The chamber oil temperature (T_{bath}) was measured at the positions indicated in Fig 6F-17a. The position of thermocouples within the pad are shown in Fig 6F-17b. The pads are assumed 'line' supported (as is the case for Glacier pads - {R86}). It should be noted that the pads are not exactly sector shaped and details in Table 6T-4 refer to the sector equivalent used for analysis. Temperature measurements were made at two positions in the collar using an air cooled slip ring. The thermocouples, 2.5 mm from the collar face, were located to correspond to the mid-radius of the bearing pads. The bearing operated in a flooded condition but the reverse face of the collar operated relatively free of oil by virtue of a radial seal at collar outer diameter. Pad to pad temperature variation was a maximum of 3 deg C - an indication of small random errors involved {R85}. The oil supply rate was fixed, hence the bath temperature varied with load and speed. Tests were conducted

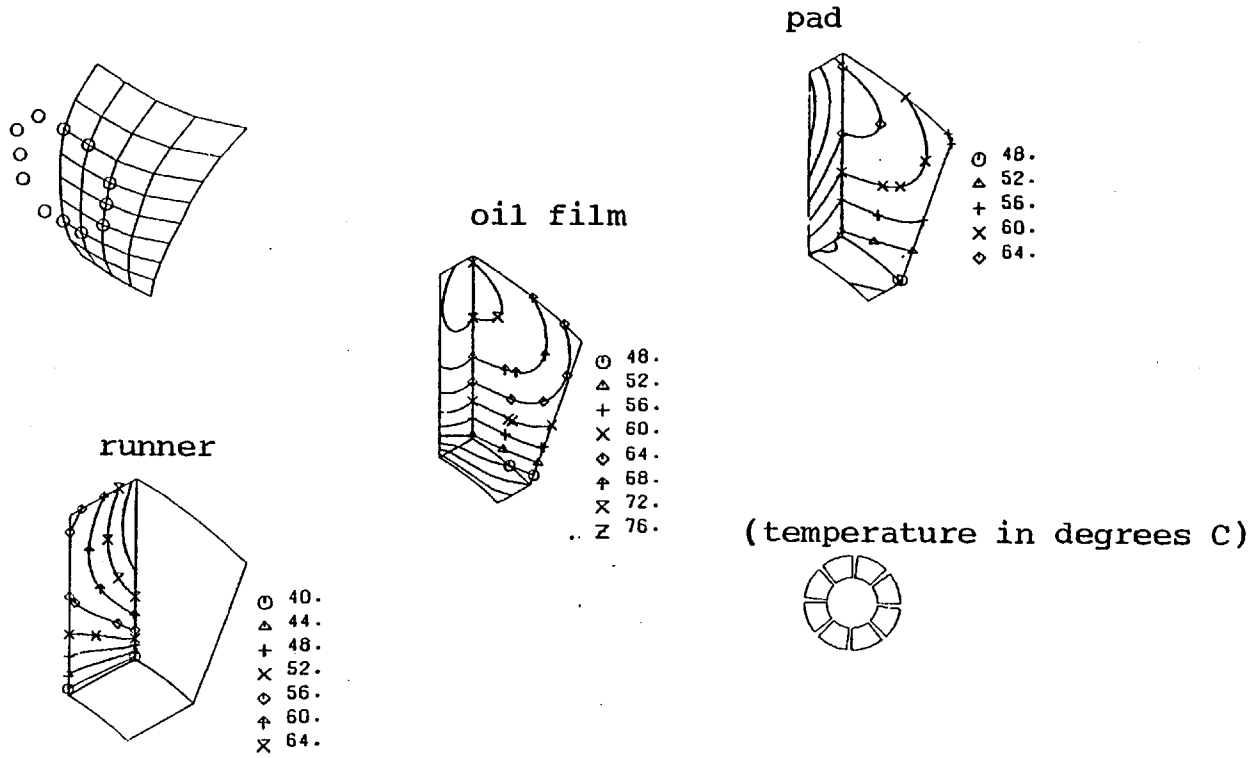

Figure 6F-16 Sectional View of Pad, Runner and Oil Film Showing Temperature Contours

Table 6T-4 (Case 3)

Pad Angle	32 degrees		
Inner Radius (R_i)	0.0395 m		
Outer Radius (R_o)	0.0745 m		
Number of Pads	3,4,6 and 8		
Pad Thickness	0.011 m		
Pivot Position	Line Support(central pivot)		
Angular Velocity	3000 rpm		
Oil Viscosity	0.018 kg/m s at 122 deg F		
	0.01 kg/m s at 158 deg F		
	0.0045 kg/m s at 212 deg F		
	Oil Bath Temperature (deg C)		
	3 pads	6 pads	8 pads
at 5 kN	59	61	63
10 kN	62	63	65
15 kN	63.5	65	66.5
20 kN	65	66.5	68
Pad material	STEEL		

(b)

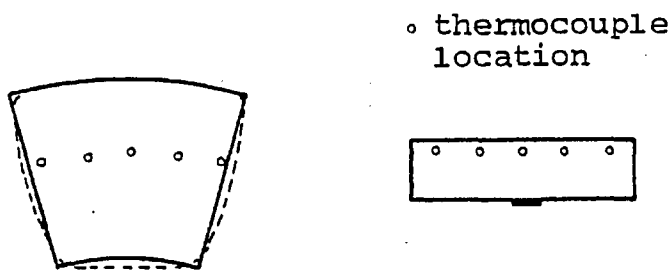

pad geometry

(a)

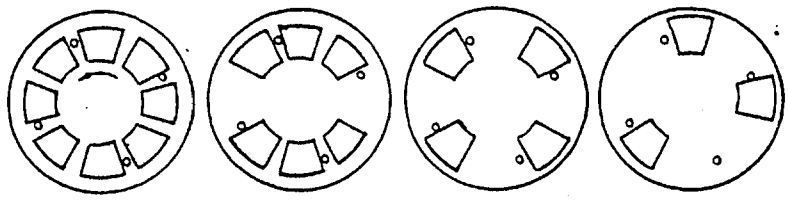

pad arrangements

Figure 6F-17 Pad Arrangements and Geometry (Case 3)

at four different speeds. The oil bath temperature variation with load was given for the 3000 rev/min case only. Thus, comparison will only be made at this speed.

6.3.2 Numerical Model

In order to model a 'line' support an assumption has to be made regarding the width of 'line'. Fig 6F-18 shows some alternative models. In Fig 6F-18a the support is shown as a series of fixed nodes along one line. Numerically this system is unstable since if the pressure forces are not exactly balanced a solution is not possible. This model cannot represent the true support since the 'line' is bound to have a finite width, however small. An alternative arrangement of support positions is shown in Fig 6F-18b. This leads to asymmetry, but has the advantage of stability for any pressure field distribution - not necessarily balanced about the line support. The complementary arrangement of nodes is shown in Fig 6F-18c. In Fig 6F-18d and e, two symmetrical arrangements are presented. Nodes 0_1 and 0_2 (and 0_3 and 0_4 in Fig 6F-18d) represent an increased stiffness in the tangential direction. Thus their position along the line support is important. In Fig 6F-18f a model is proposed which combines the virtues of all previous models. In essence two rows of nodes are chosen to represent the two edges of a line support of finite width. The width may be varied by varying the spacing between the nodes. On the other hand the circumferential stiffness due to the support spans the whole length of the support. Fig 6F-19 shows a plan of the pad with grid and

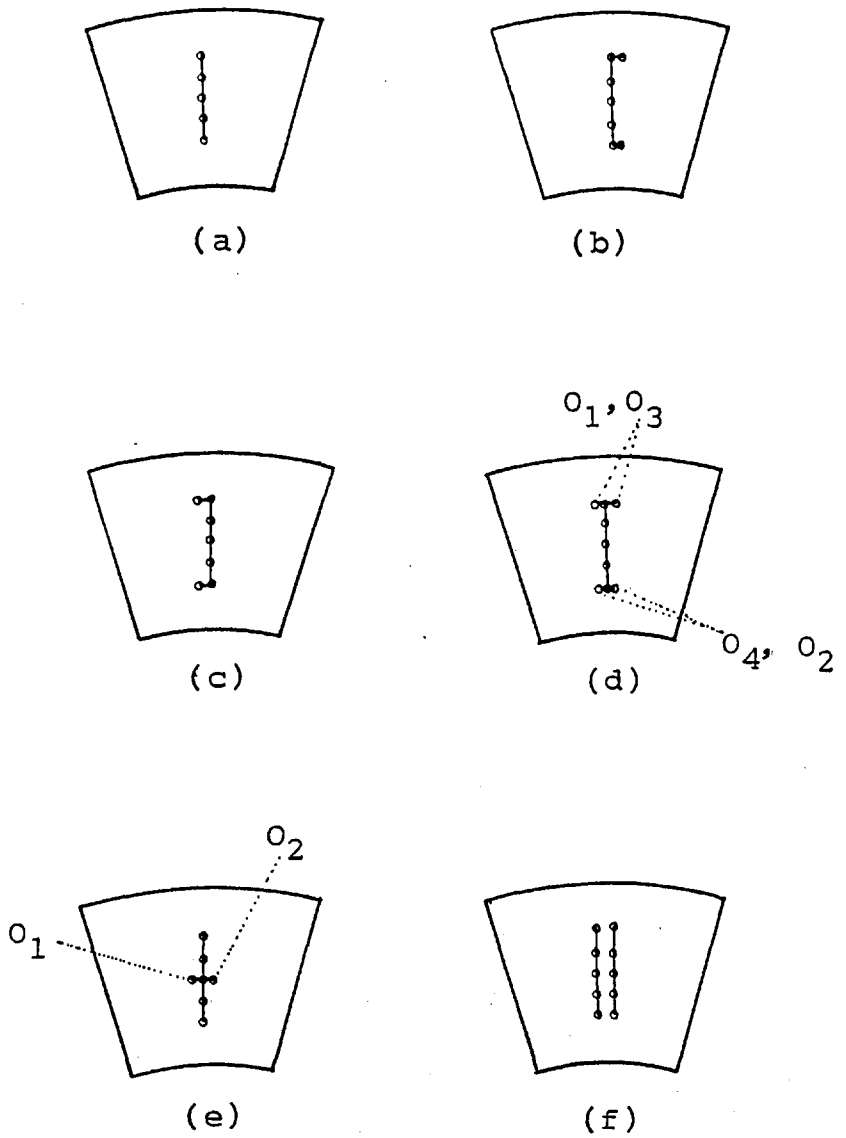

Figure 6F-18 Case 3 - Models for a Line Support

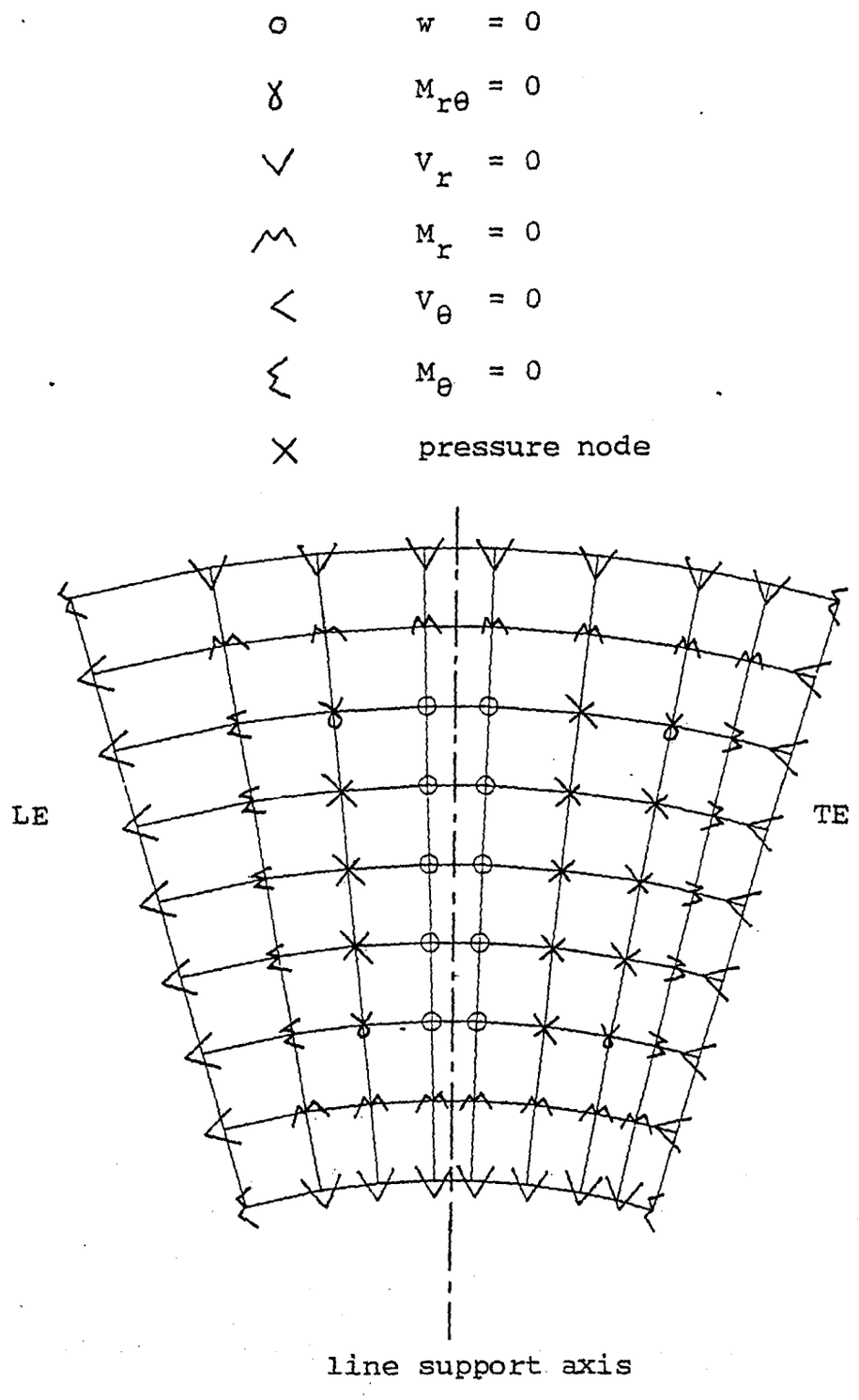

Figure 6F-19 Case 3 - The Grid and Deflection Boundary Conditions

node conditions shown.

The pivoting routine has also been adjusted to reflect a line support. Thus, tilting is carried out about the line support axis only (Fig 6F-19). The centre of pressure can lie at any point along the line support axis. The line support does not extend to the pad edges (as is the case with Glacier pads {R85}). The collar thickness is taken to be equal to three times the pad thickness (as given in specifications).

No details were given concerning the variation of temperature across the pad. A value of 1000 J/m^2 s C has been chosen to reflect good surface heat transfer coefficient (compared to approx. 200 or approx. 450 J/m^2 s C in previous cases) for the back faces of pad and collar side. The back of the collar has been described as relatively 'oil free'. Hence, a value of 10 J/m^2 s C - two orders of magnitude lower - has been chosen to represent the surface heat transfer coefficient for air.

6.3.3 Results and Analysis

Fig 6F-20 shows the maximum bearing temperature versus total bearing load for the 3, 6, and 8 pad arrangements. Since only five thermocouples were used at various tangential positions, along the same radius; the experimental values are expected to be equal to or lower than the actual maximum pad temperature. The difference between experimental temperature values for 8 pads and 3 pads increases as the load is increased. The difference at 20 kN is 4.5

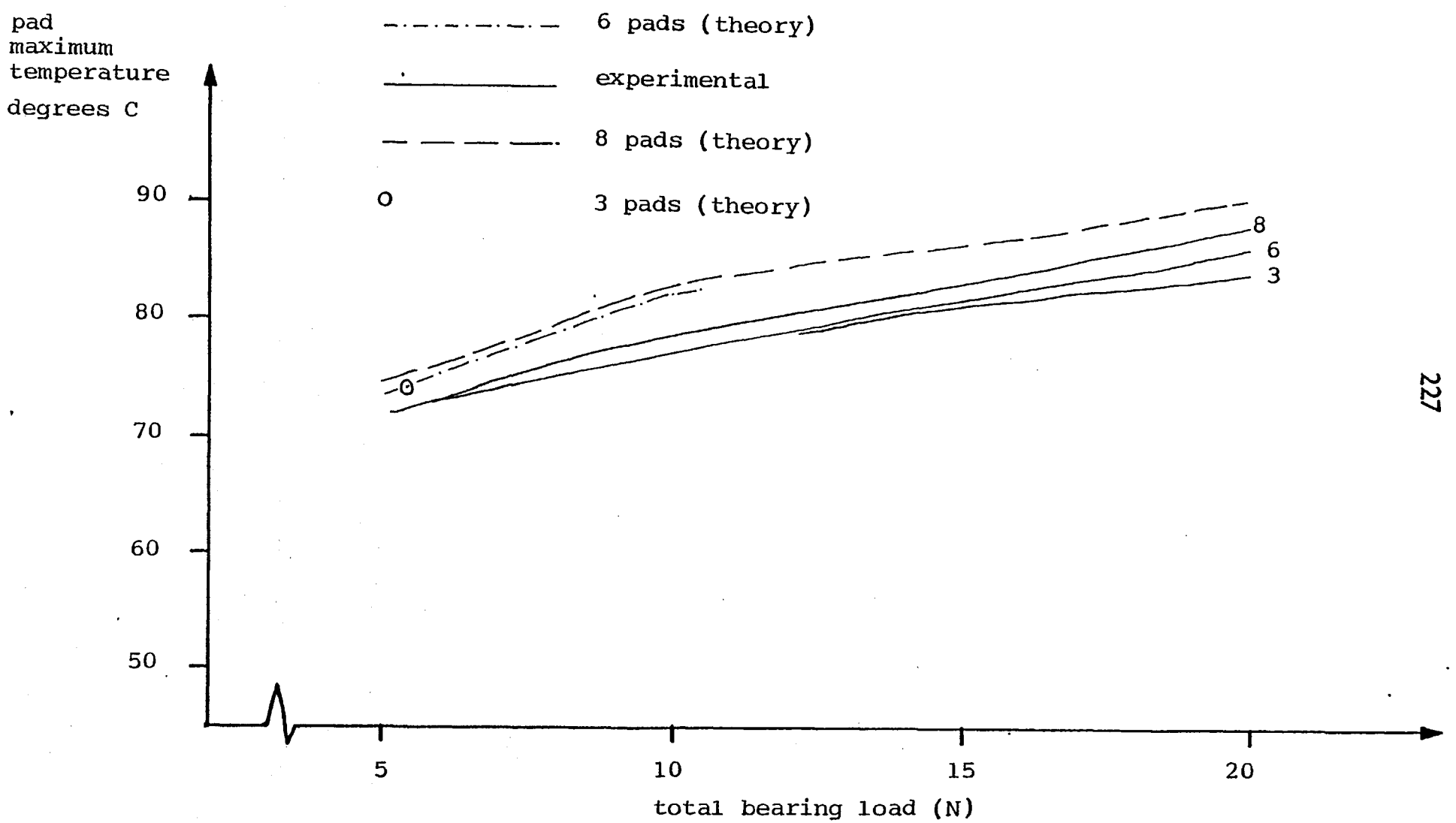

Figure 6F-20 Pad Maximum Temperature Versus Total Bearing Load - Case 3

deg C. The difference between the numerical model temperatures and measured values for the 8 pad case does not exceed 5 deg C; and narrows down to 2 deg C at 20 kN. Various numerical values for 3 and 6 pads are also shown.

Fig 6F-21 shows the circumferential temperature distribution for $r = 0.83r_0$. This corresponds to the radial position at I=6. A maximum variation of 2 deg C is found at pad outlet. The difference, for the maximum temperature, does not exceed 0.5 deg C. The temperature gradients at inlet and outlet (see Fig 6F-21) are steeper for the experimental values. This indicates that the heat transfer coefficients - at least for the side faces - are higher than the values used. Nevertheless the values used are satisfactory for prediction purposes and are thought to be close to the actual values.

In Fig 6F-22 the various energy components (conduction to rotor, conduction to pad, and convection) in the oil film are shown for the 3 and 8 pad cases versus total bearing load. The energy refers to that for a single pad oil film. Three observations can be made. First, the total energy generated per pad is higher for the three pad arrangement. This is expected since only three pads carry the same load carried by 8 pads in the second arrangement. The total energy generated for the whole bearing (for all pad oil films) is smaller in the 3 pad case, indicating a smaller power loss. The churning power loss in the inter pad cavities is not evaluated, but is expected to be larger for the 3 pad case -

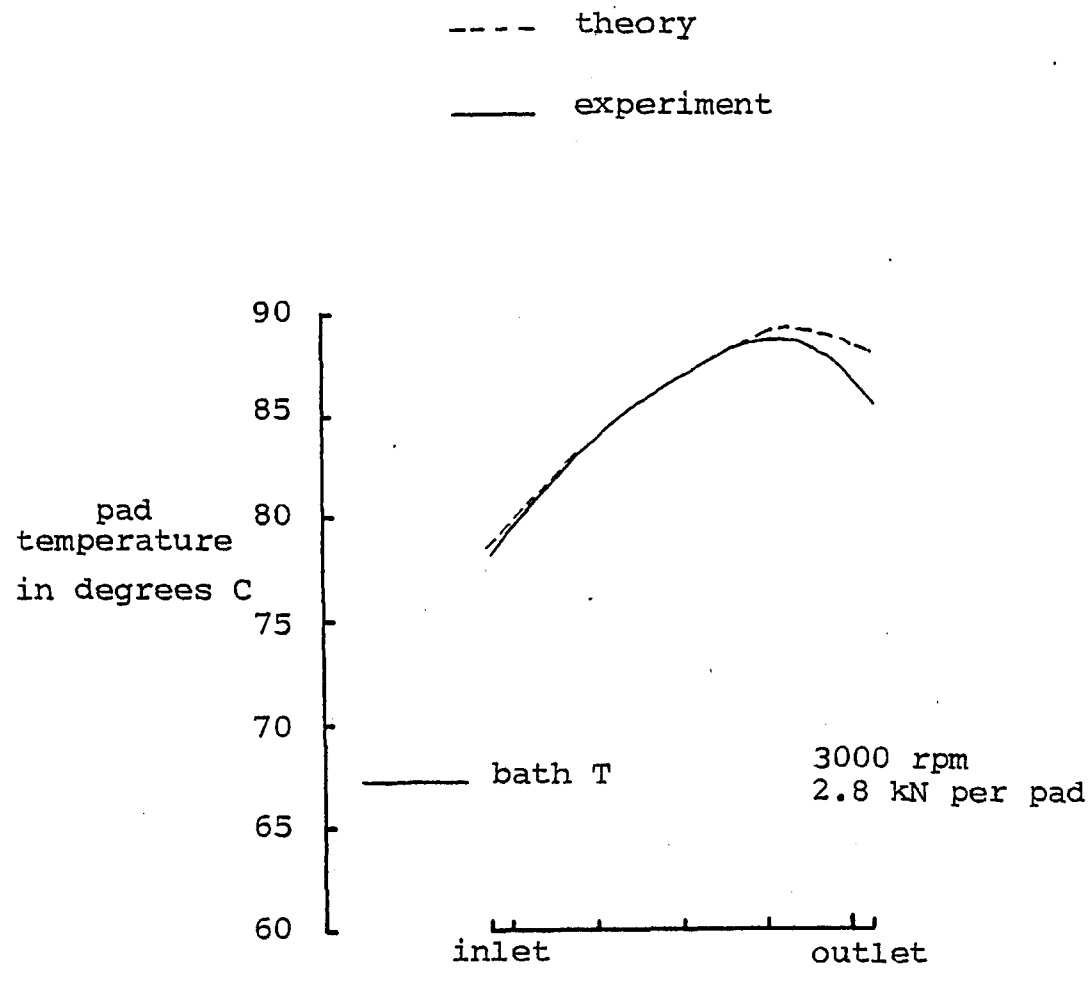

Figure 6F-21 Pad Circumferential Temperature Distribution

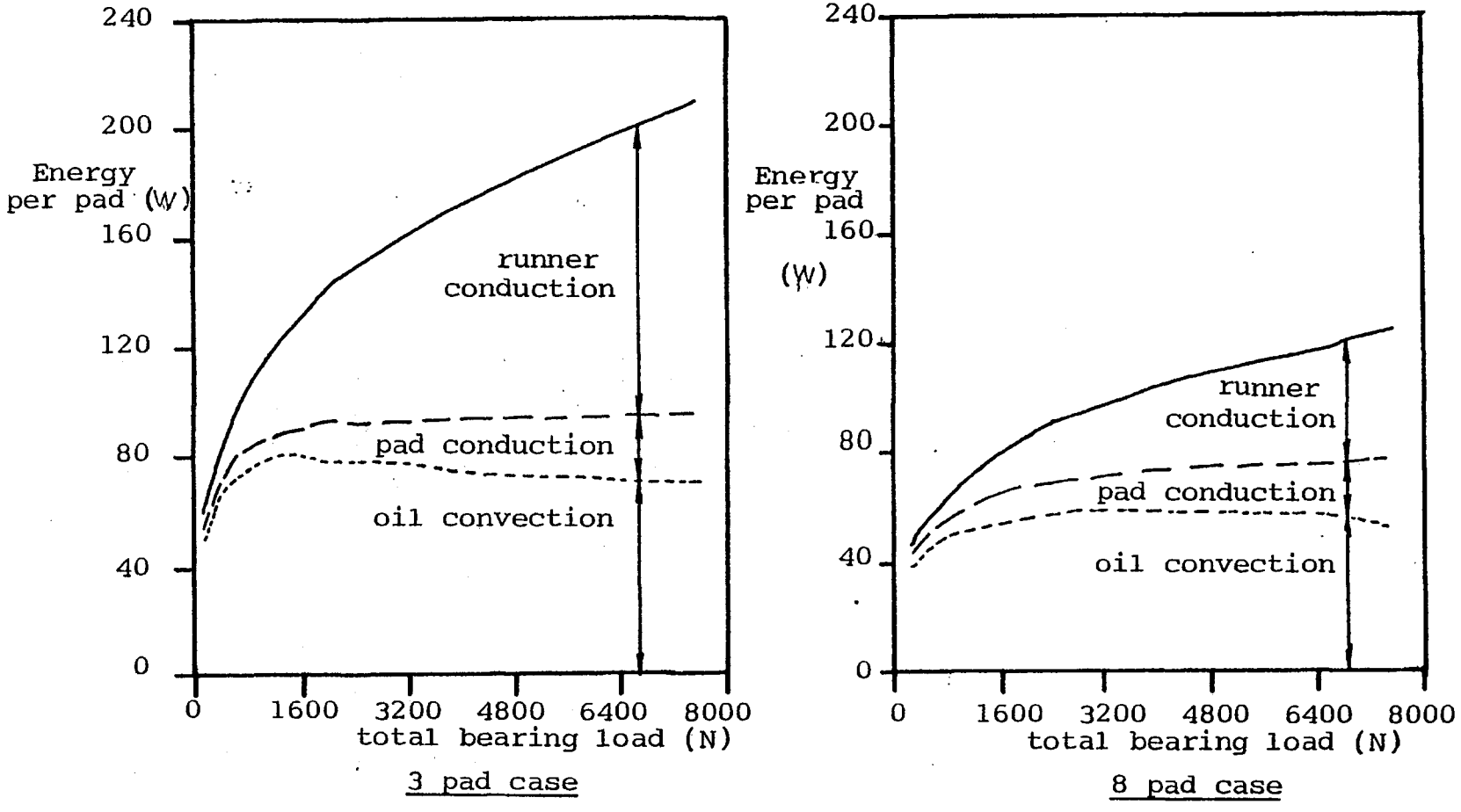

Figure 6F-22 Energy Conduction and Convection versus Total Bearing Load for the Oil Film - (THEORY)

diminishing the advantage of the 3 pad arrangement. A similar trend is verified experimentally {R33}. For the 8 pad arrangement, at a load of 20 kN, the total power loss per pad is found to be 232 W compared to a predicted value of 180 W. This represents a difference of 22%. The second observation concerns the proportion of total heat convected to total heat conducted. In both cases conduction plays a critical role; the proportion of heat convected to heat conducted being 1 and 0.5 for the 8 and 3 pad cases respectively. The third observation concerns the role of the runner in conducting away heat. The runner conduction for the 3 pad case is greater than both convection and pad conduction combined. This is due to the large inter pad cavities serving to absorb the energy conducted to the runner below the pads. This effect is diminished in the 8 pad arrangement, since less area is covered by the cavities compared to the area covered by oil film below the pads. All three observations are found in Neal's recent experimental investigation {R33}.

Fig 6F-23 shows results for the 8 pad arrangement at a load of 19 kN. The film thickness contours (Fig 6F-23a) show a predominantly cylindrical deflection pattern (rather than spherical as in the previous two). This is reflected in the deflected shape (Fig 6F-23f). The minimum film thickness position, as well as the maximum pad temperature positions have been shifted towards the outer radius compared to previous pad sizes. Fig 6F-24 shows three dimensional surface contouring results for temperature as well as the deflection shape. For the pad, the density of temperature

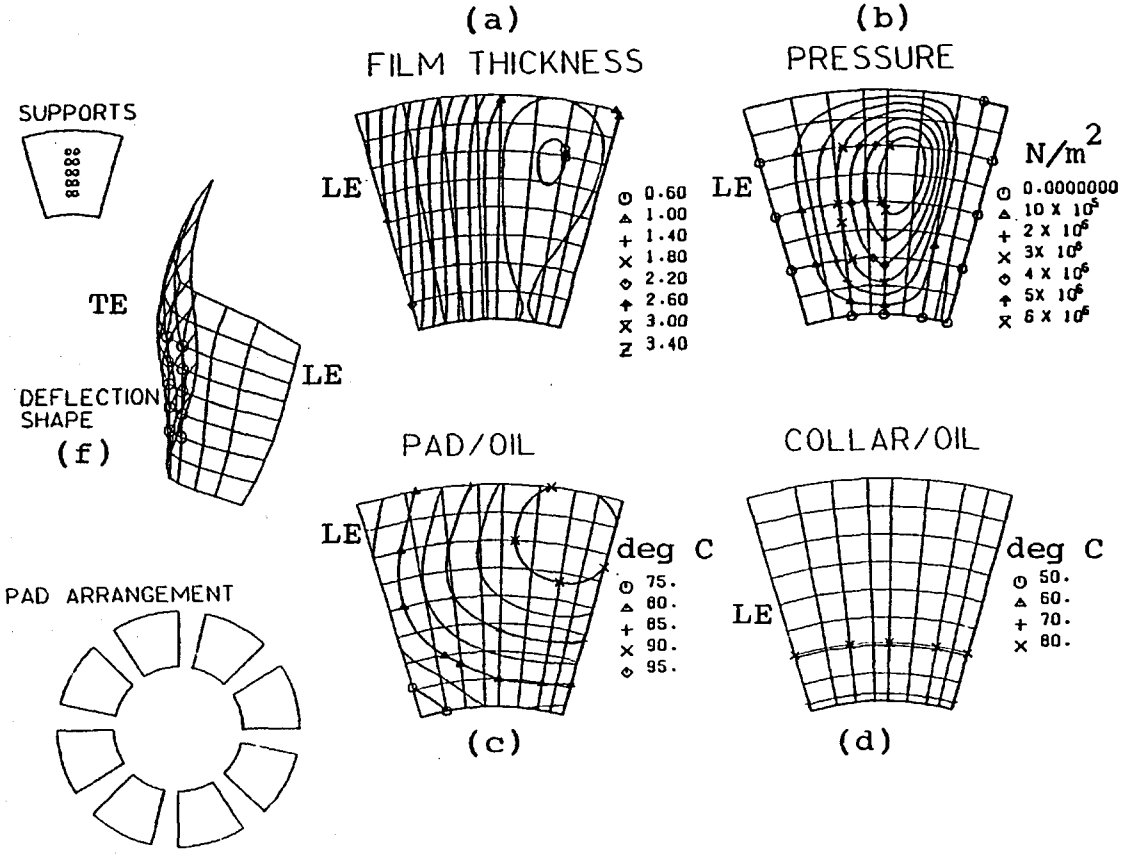

Figure 6F-23 p,T,h Contours and Deflection Shape - Case 3

(8 pad arrangement)

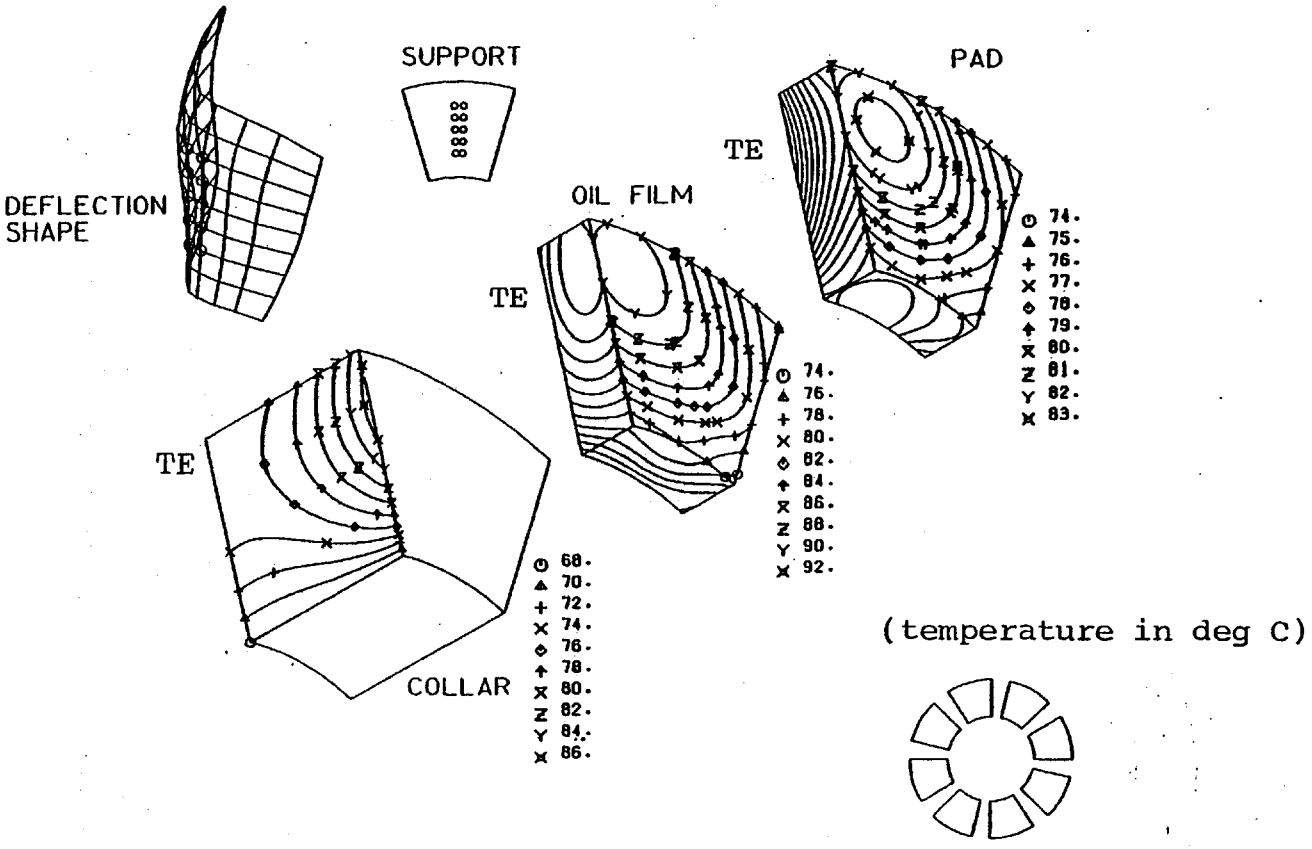

Figure 6F-24 Contours of Temperature in Pad, Runner and Oil Film - Case 3 (8 Pad Configuration)

contours in the rθ plane is similar to that in the rz plane. This shows that temperature gradients along and across the pad are similar. Fig 6F-25 shows a different viewpoint of the deflection shape. Fig 6F-26 shows three dimensional surface contours for the 3 pad arrangement at a load of 6.1 kN,which is approximately the same load per pad as for the 8 pad arrangement in Figs. 6F-23 to 6F-25. The trends are similar, but temperature values are approx. 10 - 15 deg C lower, reflecting the role of the inter pad cavities in cooling the bearing (due to the heat exchange via the runner {R33}.)

Kettleborough et al {R40} plotted experimental pad/oil temperature contours for a bearing of approximately the same size, load and speed as in the present case (Fig 6F-27 .) When compared to the present pad/oil temperature contours; a strong resemblance is found (6F-22,6F-24 .) It is interesting that the temperature drop beyond the maximum value circumferentially was attributed to conduction at the pad boundaries, reinforcing the importance of the conduction model in the solids

6.4 Concluding Remarks

The previous test cases have demonstrated the reliability of the proposed model for tilting pad bearing analysis. Good agreement was obtained for the entire size range regarding temperature values in the pads. In the first case (large bearing) the surface temperature distribution was successfully predicted at pad/oil interface. In the third case (small bearing) the pad

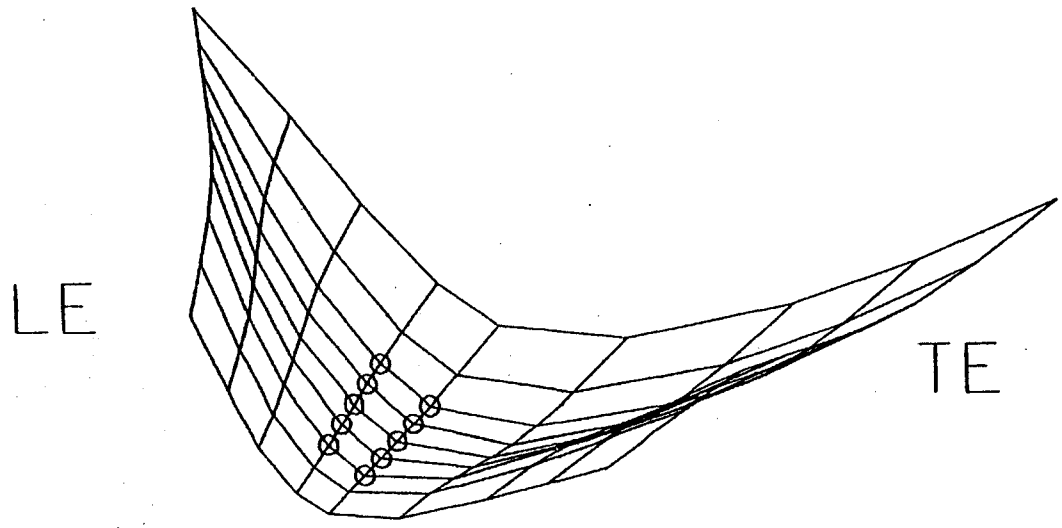

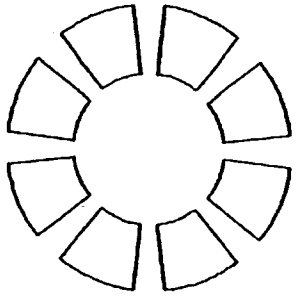

Figure 6F-25 Case 3 Deflection Shape

A Better View

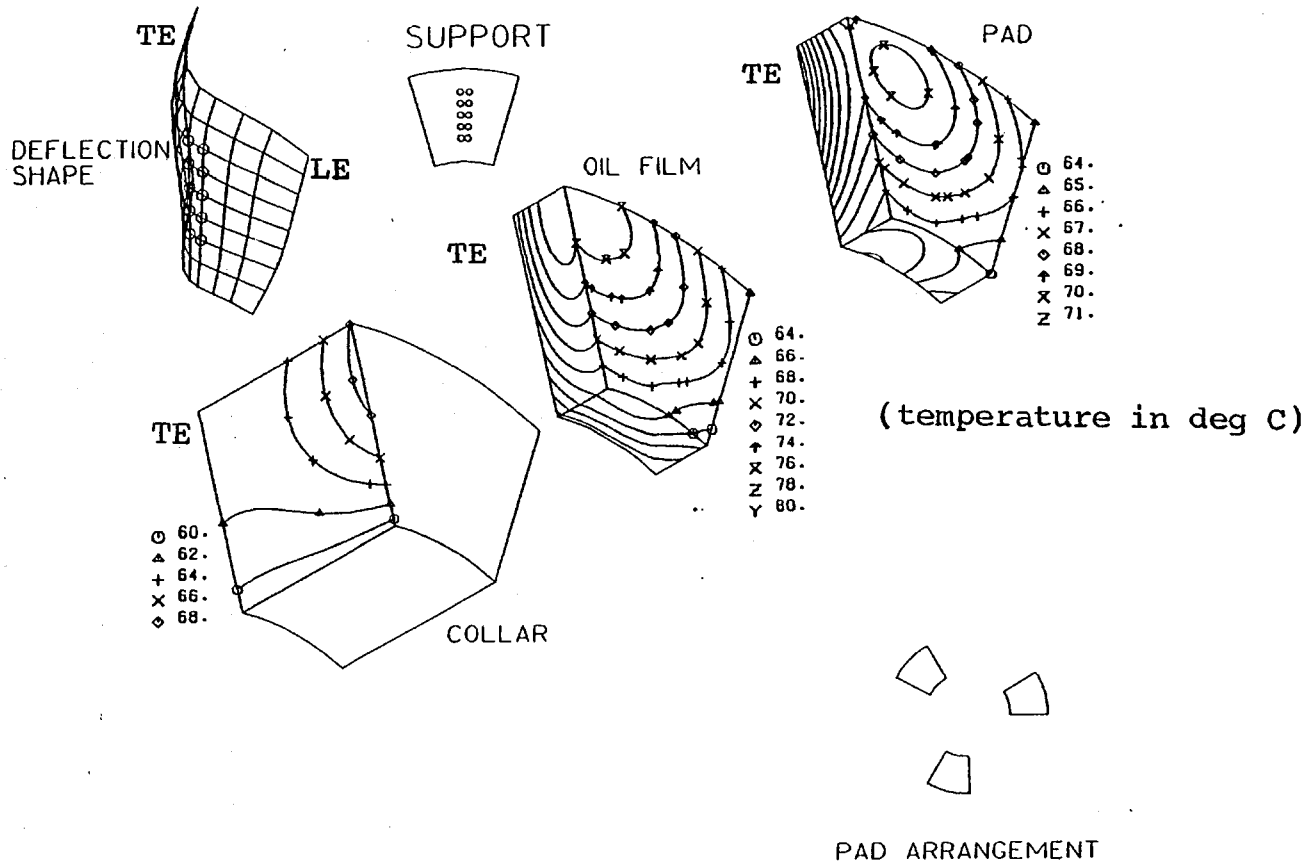

Figure 6F-26 Contours of Temperature in Pad, Oil Film and Runner - Case 3 (3 pad arrangement)

speed 2700 rpm
load 30 bar (approx)
pivot angle = 0.6 x pad angle

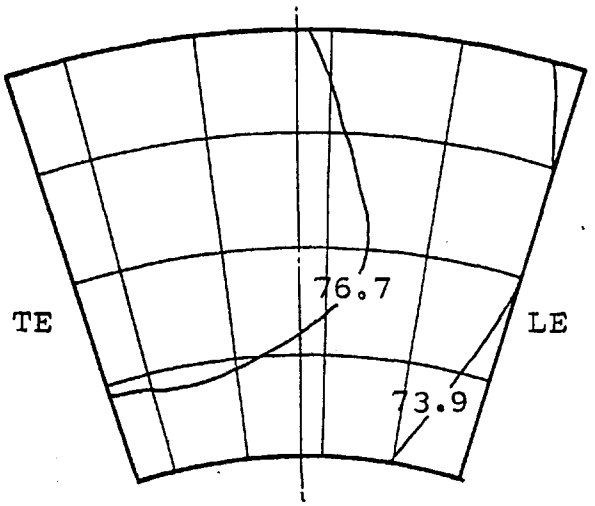

temperature in degrees C

Figure 6F-27 Experimental Temperature Distribution at Pad/Oil Interface - Kettleborough et al {R28}

circumferential temperature profile closely corresponded with the experimental measurements. In the second case (medium bearing) broad agreement was obtained for both temperature and film thickness measurements. Fair agreement was obtained for comparison between the experimentally deduced and numerically deduced energy losses in the oil film. The role of the runner was highlighted as an important heat exchanger transferring heat from the pad oil film to the inter-pad cavities.

In addition, the flexibility of the mesh system was demonstrated by accommodating the various support shapes (ring and line supports) for offset and centrally pivoted pads.

CHAPTER 7

SIZE EFFECTS AND DESIGN CONSIDERATIONS

Introduction

In vertical hydroelectric generators the thrust bearing is required to perform under increasingly heavier loads as the size and power of the installations continue to increase {R87}. The normally used, one-piece tilting pad bearing segment (which may vary in width, length and support) functions reliably up to a specific load of approximately 40 bars.

Ettles {R67} has shown that for a particular pad geometry the design may be scaled up if only elastic distortion is considered. He also showed that thermal distortion increases in proportion to size. Thus, it was concluded that thermal distortion was responsible for the problems associated with large bearings.

Several investigators {R41, R42, R88} have dealt with the problems of large thrust bearings and proposed methods of overcoming excessive thermal distortion. Baudry et al {R42} proposed a multiple support system in order to reduce maximum deflection by a factor of 3. Ettles and Cameron {R32} suggested cooling galleries in the pad as a method of reducing the temperature gradient causing the thermal deflection. They also suggested insulation as another alternative. Kawaike et al {R88} proposed a design (which was experimentally verified) in which several improvements were incorporated. A two piece shoe (thick backing supporting a thin face plate) was proposed by Bahr {R89} in 1959 in order to reduce

thermal distortion. This was adopted by Kawaike et al incorporating circumferential grooves at the upper surface of the backing plate (see Fig 7F-1). The lower edge of the upper layer (that is the thin face plate) was swept back to expose the grooves. This exposed part was designed to serve as an oil guide into the grooves within the pad - thus acting as circumferential 'cooling ducts'. In addition, small gaps were machined into the leading and trailing parts of the lower block to allow elastic deflection of the face plate. The gap depth was equivalent to half the expected minimum film thickness, thus providing an optimum longitudinal pad profile {R38} under loading.

In this chapter, a confirmation of the size effects is shown for a pad geometry similar to Case 1 in chapter 6, for two velocities: 10 m/s and 30 m/s. Various proposals are suggested to curb excessive thermal deformation. The effects of varying the pad thickness, pad insulation, rotor peripheral cooling, forced water cooling in pads, and the pivot circumferential position have been predicted, using the model presented in the previous chapters.

7.1 Geometry of Pad and Specifications

The pad geometry chosen is similar to that of Case 1 in chapter 6. A circular support is chosen for centrally pivoted pads. The pad materials and oil used are the same as for Case 1 (chapter 6). The pad scaling factors used are 0.05, 0.1, 0.2, 0.5, 1, and 2 of the basic size in Case 1. This spans a diameter range of 0.15 m to 6 m. The grid used is shown in Fig 7F-2 with the deflection

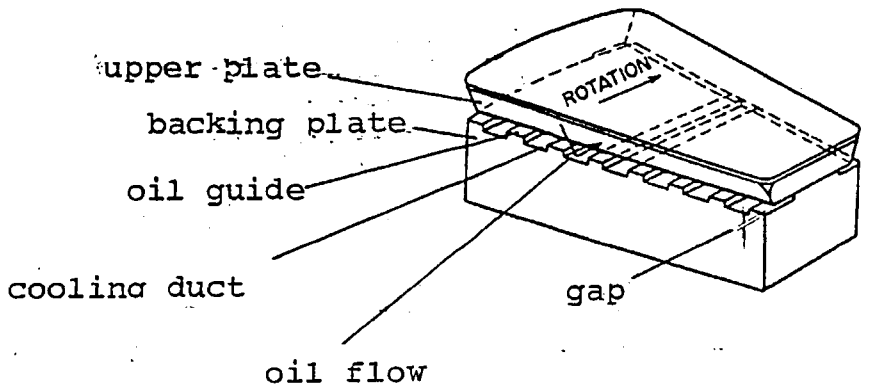

Figure 7F-1 Construction of Two-Piece Pad with Oil Cooling

$M_{r0} = 0$

$M_r = 0$

$w = 0$

pressure node

$V_r = 0$

$V_0 = 0$

$M_0 = 0$

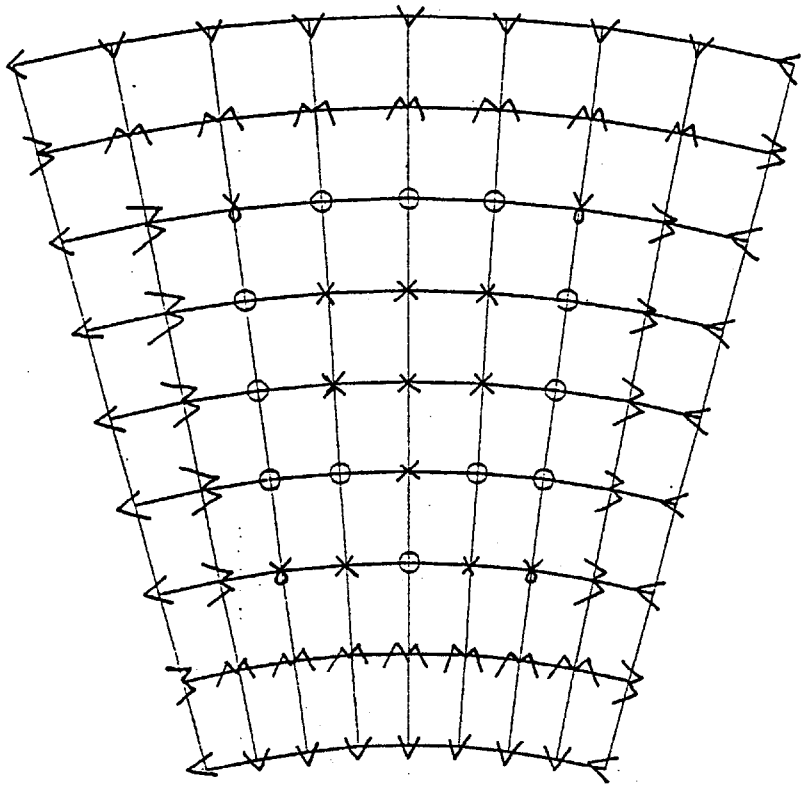

Figure 7F-2 Design Grid and Boundary Conditions

boundary conditions. The bearing set is composed of ten pads, the runner thickness being twice that of the pads throughout.

The oil inlet bath temperature (T_{bath}) is kept constant at 48 deg C. The surface heat transfer coefficient (at back faces of pad and runner) have been assigned a value of 450 J/m^2s deg C. In practice the value is dependant on surface velocity - and to a minor degree on other factors. Since the main purpose is to show size effects, the surface heat transfer coefficients have been kept constant for both values of surface velocity (see Section 7.2).

7.2 Size Effect Results

In Fig 7F-3 pad maximum temperature is plotted as a function of load versus pad scale factor for a mean surface velocity of 10 m/s. The scale factor is applied to the pad geometry of Case 1 in chapter 6. The mean radius is also shown corresponding to the scale factor axis. In order to raise the pad temperature from 81 deg C to 97 deg C (16 deg C rise) a load equivalent to 37 bars has to be added at a scale factor of 0.05. The load required at a scale factor of 0.2 is 41 bars; and for a scale factor of 2 it is 21 bars - for the same temperature rise. This implies that a scale factor of about 0.2 gives safest bearing performance (for the geometry chosen). This is represented graphically by the temperature contours having a maximum load capacity at a scale factor of 0.2.

Above a scale factor of 0.2, the curves dip steeply, whereas

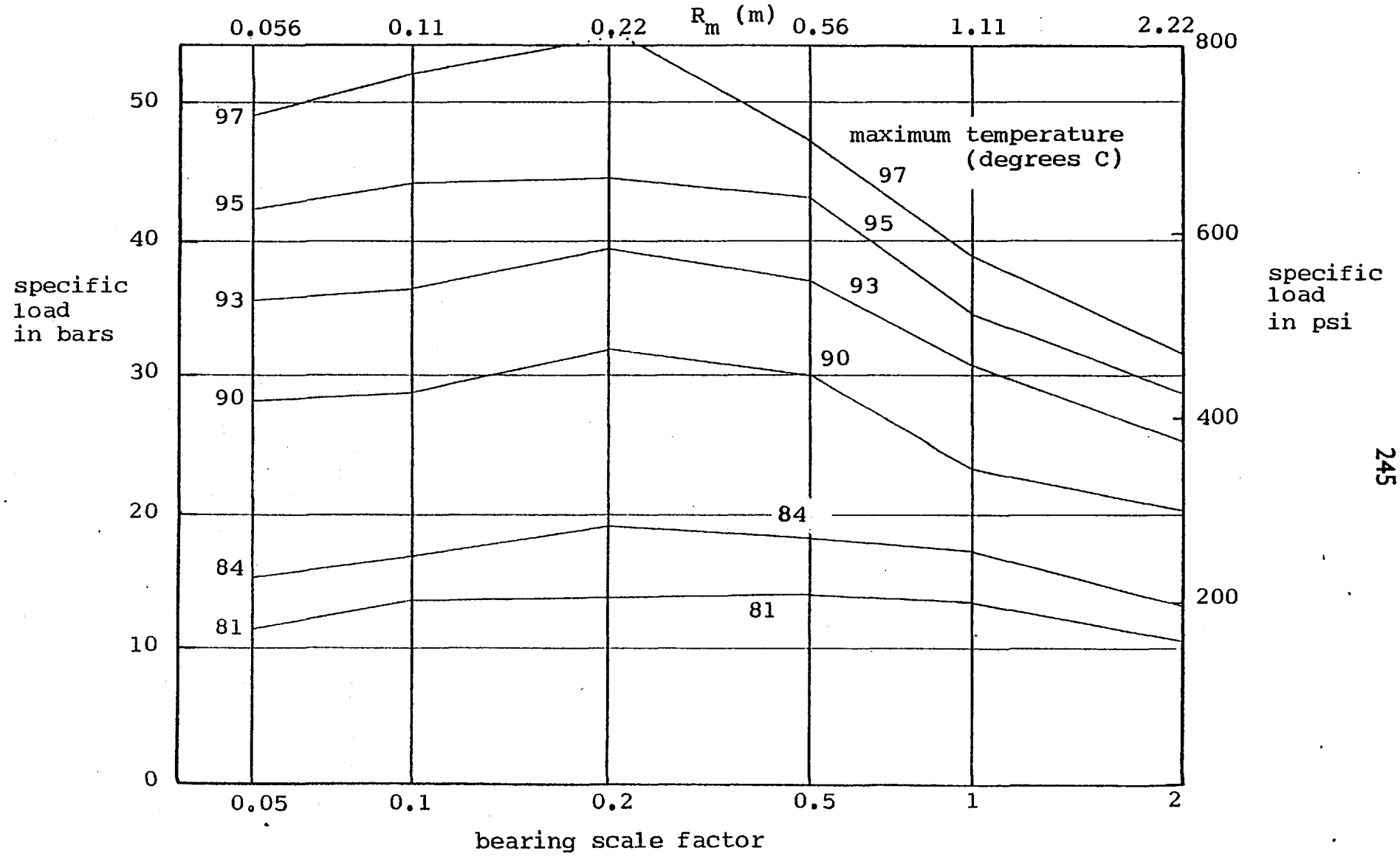

Figure 7F-3 Pad Maximum Temperature as a Function of Load and Pad Size - Speed 10 m/s

only a shallow dip is found below this value. The temperature contours become closer together for the larger bearing sizes. Thus, an increase in load for the large bearing sizes implies a steep increase in temperature. This in turn will cause more thermal distortion, yielding a less efficient oil film. Thus, more heat is generated causing further thermal distortion etc.. This process can rapidly lead to bearing failure as the film thickness eventually becomes of the order of magnitude of surface asperities. This process is known as thermal ratcheting.

For bearing sizes below a scale factor of 0.2, a much larger increase in load is required for the same process to take place. In other words, the factor of safety is drastically reduced for large bearings. Thus, in principle, much higher specific loads are obtainable with smaller bearings. In practice, the loads are limited by a minimum allowable film thickness or from mechanical considerations, such as crushing of the pivot {R67}. Raimondi {R44} has shown that a convex profile in the longitudinal direction (along the oil flow) is beneficial and improves bearing performance. The optimum crown was given as half the minimum oil film thickness. For very small pads, manufacturers supply pads with an initial crown. For large pads it is the elastic distortion that provides crowning during start up and at low loads {R42}.

The design of the ring support radius was subject to considerable research by Ettles {R17,R67}. In essence, a very small radius for the ring support will allow considerable edge

deflection - magnifying thermal distortion. A very large radius (edge support) is likely to give a concave rather than a convex profile (which is detrimental to bearing load capacity). Therefore, there exists an optimum ring size which allows a convex profile yet reduces the edge deflections to an acceptable level.

The temperature contour for 81 deg C is almost parallel to the scale factor axis over the range 0.1 to 1. Below 81 deg C the temperature contours are also almost parallel to the scale factor axis and size effects are eroded for this low load area.

Fig 7F-4 is a plot of temperature contours as a function of load versus size factor for a mean surface velocity of 30 m/s. The low load area - comparable to that in Fig 7F-3 below 81 deg C - becomes that below 95 deg C (for -approximately - a specific load of 10 bars). Again the contour density appreciably increases as the bearing size is increased, the contours showing a marked dip above a size factor of 0.2. For a large bearing (scale factor 2) operating at 10 bar specific load, an increase of 10 bars in specific load results in a 20 deg C temperature rise. For the 10 m/s case (Fig 7F-3) a similar increase in load yields a 10 deg C rise in temperature. Thus, it may be concluded that higher surface velocities accentuate size effects in thrust pads.

Fig 7F-5a shows the temperature contours in the pad and oil film at a circumferential section where $r = r_m$ (mean radius). The deflection profile for the same section is also shown. The pads (scale factor 1) are heavily loaded at a specific load of 65 bars

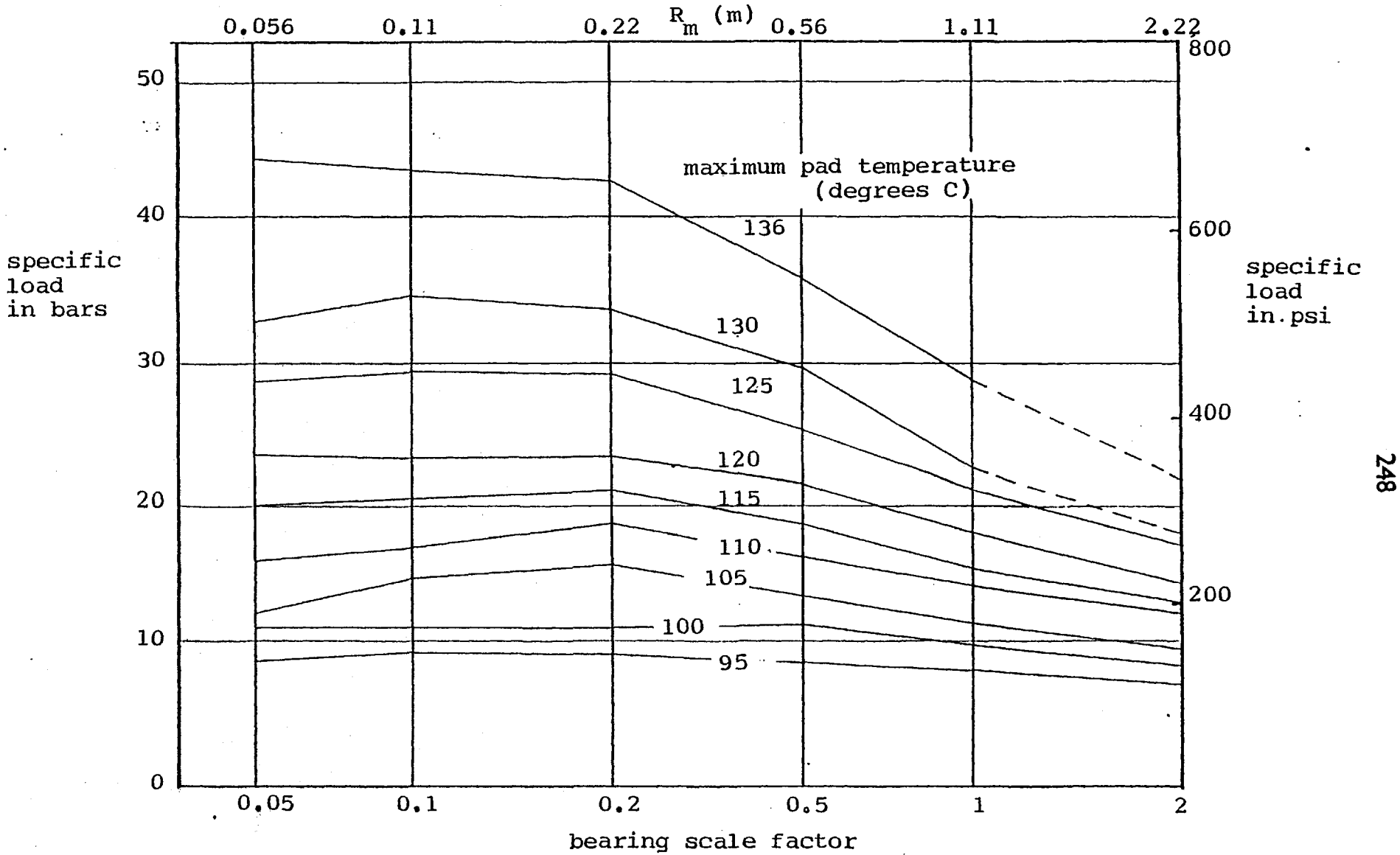

Figure 7F-4 Pad Maximum Temperature as a Function of Load and Pad Size - Speed 30 m/s

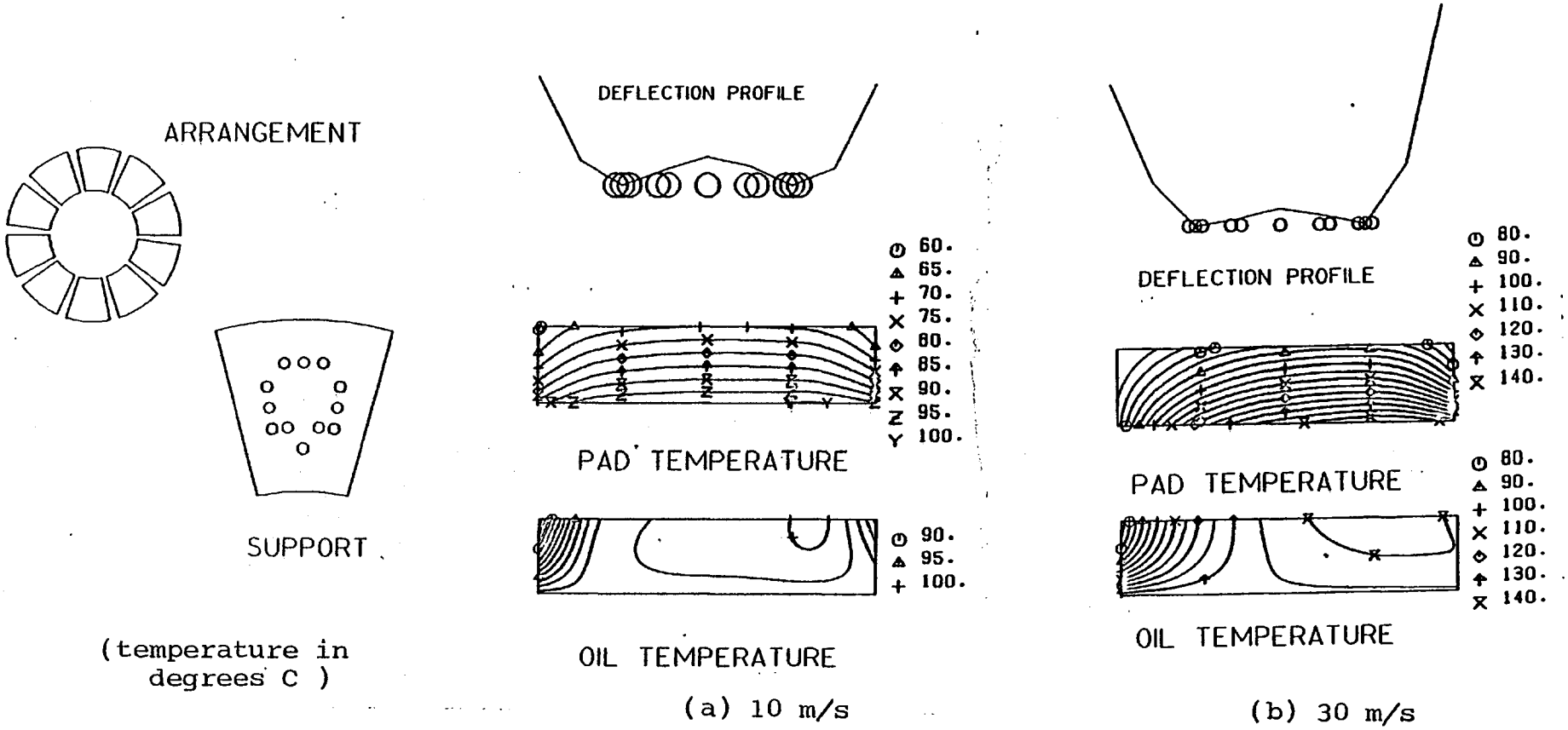

Figure 7F-5 Deflection Profile and Temperature Contours at the Mean Radius (R_m) Circumferential Section - Large Pad

at 10 m/s velocity. The temperature contours in the pad are parallel over most of the pad length. The temperature gradient is about 2.5 deg C/cm.

In the oil film, the 'cool entry region' spans about 15% of the pad length. In Fig 7F-5b contours for the same section as in Fig 7F-5a are shown for a velocity of 30m/s at a load of 63 bars (approximately the same as for Fig 7F-5a). The temperature gradient across the pad becomes 4 deg C/cm. In addition, the contour pattern shows asymmetry as the contour density is seen to increase towards the trailing edge. This asymmetry is reflected in the deflection profile, too. This is expected since the thermal moment generated at the trailing edge is larger than the moment at the leading edge, causing more deflection at the trailing edge.

In Fig 7F-5a, an approximately symmetrical temperature contour pattern yields similar trailing and leading edge deflections. A small concavity within the limits of the support ring is shown for both Fig 7F-5a and b deflection profiles. This is a result of the pressure forces (or elastic deflection.) The magnitude of elastic deflection to thermal deflection along the profile shown is about 0.25 for Fig 7F-5a and 0.1 for Fig 7F-5b. The pressure forces acting within the support ring area act in opposition to the thermal moment. Thus the deflection at the midpoint is expected to be larger in the absence of the thermal moments. Alternatively, in the absence of the pressure forces a larger deflection is expected at the edges.

Since a larger temperature gradient is found for the higher velocity, the thermal moments are increased. On the other hand the pressure (elastic) moments are expected to be similar for both cases (as the load is approximately the same). Thus, the ratio of thermal to elastic deflections is expected to increase as has been shown.

In Fig 7F-5b the extent of cool entry region is approximately double that in Fig 7F-5a. The temperature gradients across the oil film at entry are 10 and 40 deg C respectively for cases (a) and (b). This points to the necessity of considering temperature variations in the z-direction. It is also important to state the positions along the z axis at which temperature is determined in the oil film, particularly at the entry region. In the present model only a linear variation of temperature in the z-direction is allowed at any entry position (see chapter 3). A fully three dimensional model in the groove and entry region is required to determine the exact shape of the leading edge temperature profile.

Fig 7F-6a shows temperature contours for the same section as in Fig 7F-5 but for a pad of scale factor 0.05 at 10 m/s surface velocity and 30 bar specific load. Conduction along, as well as across, the pad is apparent. This is in contrast with very little conduction along the pads for the larger pad sizes (Fig 7F-5). This feature helps to reduce the bearing thermal deflection, as the thermal moment is a function of thermal gradients across the pad and independant of thermal gradients along the pad. The temperature

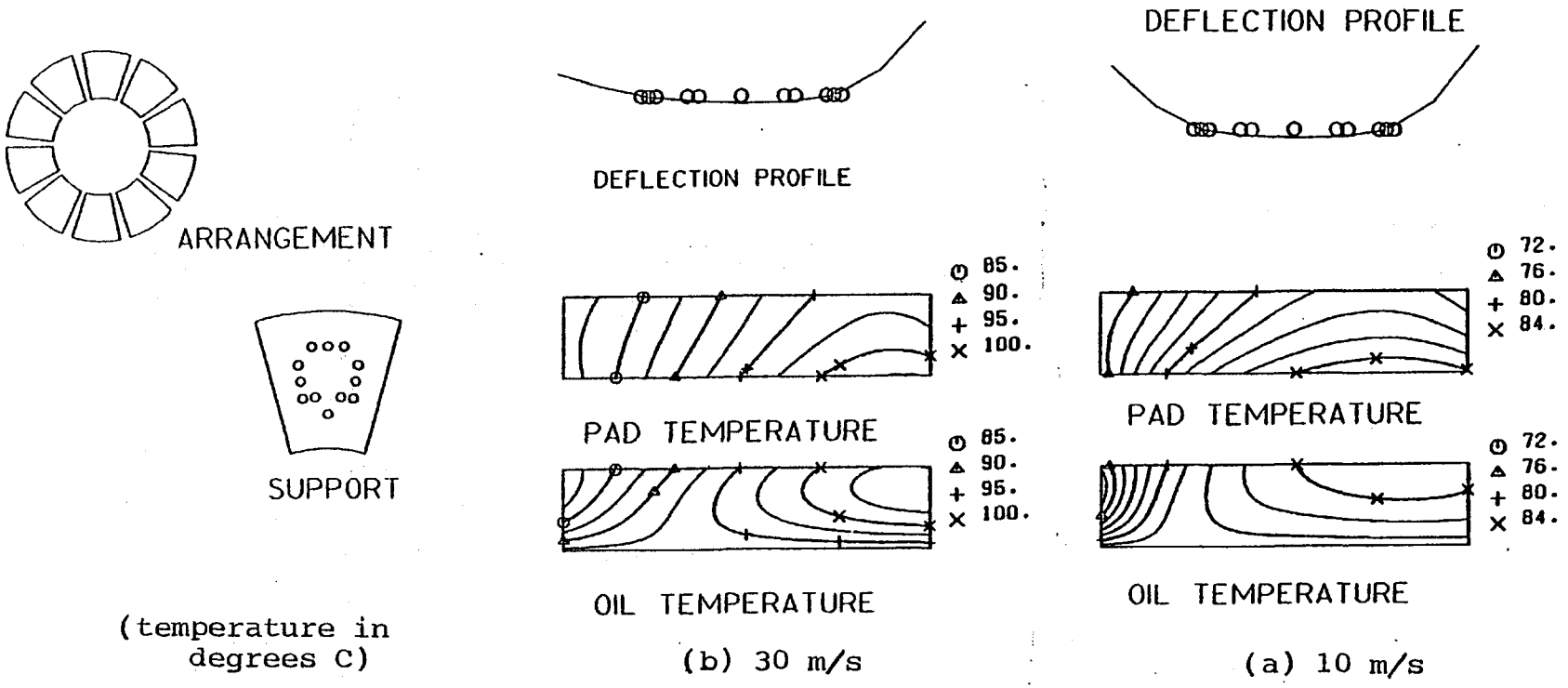

Figure 7F-6 Deflection Profile and Temperature Contours at the Mean Radius (R_m) Circumferential Section - Small Pad

gradient across the pad varies from approximately 2 deg C/cm at the leading edge to 5 deg C/cm near the trailing edge. In Fig 7F-6b the surface velocity is increased to 30m/s for the same bearing as in Fig 7F-6a, for a specific load of 21 bars. The 'cool entry region' is seen to increase. The temperature contours in the pad indicate an increasing amount of heat conducted along rather than across the pad (compared to Fig 7F-6a).

The deflection profile is marginally asymmetrical in Fig 7F-6a and becomes more so in Fig 7F-6b as the maximum thermal gradient shifts towards the trailing edge (this pattern has also been observed for the larger pad size - Fig 7F-5). It seems that a relationship exists between the length of the 'cool entry region' and the deflection profile. As the cool entry region is extended (for example by increasing the velocity from 10 to 30 m/s), the pad leading edge becomes cooler relative to the hot trailing edge - encouraging more heat conduction along the pad. This in turn produces larger deflections at the pad trailing edge leading to an asymmetrical deflection of the pad.

7.3 Possible Remedies

The problems associated with large bearings may be avoided by curbing excessive pad deflection. Regulation of the bath oil temperature, the materials used for the pad and collar, and the type of oil used will also influence the pad behaviour. In Section 7.2 the effect of surface velocity (on the runner) in relation to size effects has been shown. The factors involved in determining the pad

maximum temperature are interdependant (their relationship being complex and interrelated).

The model presented in chapters 2, 3, 4, and 5 cannot predict bearing performance in general, but can be applied to any specific case. This is a result of the detailed analysis for the energy and deflection equations and their interaction with the Reynolds equation, rendering solutions that are specific to the bearing geometry used, the oil specifications, the method of support, the number of pads, the materials, etc.. Thus, one bearing geometry is used as a starting point for further improvement. The pad geometry and configuration used for size effects (Section 7.1) has been chosen as it represents a typical industrial large thrust bearing. In order to limit the search for improvements the oil characteristics will be held the same throughout (oil used for Case 1, chapter 6), as well as the oil bath temperature. The pad materials will remain as steel throughout.

The ideas for improvements are classified as Passive and Active. Passive devices involve changes in bearing design only. Active devices require external devices to the bearing in order to maintain bearing operation. The ideas presented are not exhaustive. They were chosen in order to carry out the fewest changes to existing designs, in return for control of bearing pad deflection.

7.3.1 Passive Devices

i) Insulation of back sides of pad

It is thought that pad insulation will prevent most of the heat flux across its thickness. Thus, the temperature gradient across the pad is limited to an acceptable level, thereby controlling excessive distortion {R53}.

ii) Rotation induced oil cooling

The idea has been experimentally tried by Kawaike et al {R88}. The design has been described in the introduction to the present chapter. The principle is to make use of the rotor to induce oil into circumferential grooves within the pads. The grooves thus act as cooling ducts helping to reduce the thermal gradient across the pads (Fig 7F-1). The location of the grooves is close to the pad working face. The pad is composed of two pieces mechanically joined teogether. The backing block is relatively thick. Thus, a high thermal gradient may take place only across the thin face piece. Excessive deflection is prevented due to the rigidity of the backing block.

iii) Compensatory button

For a circular button (ring) support, the design can be modified in order to have a self regulating button radius. As edge deflection increases the button radius is caused to increase. Fig 7F-7 shows a typical button design modified for this purpose.

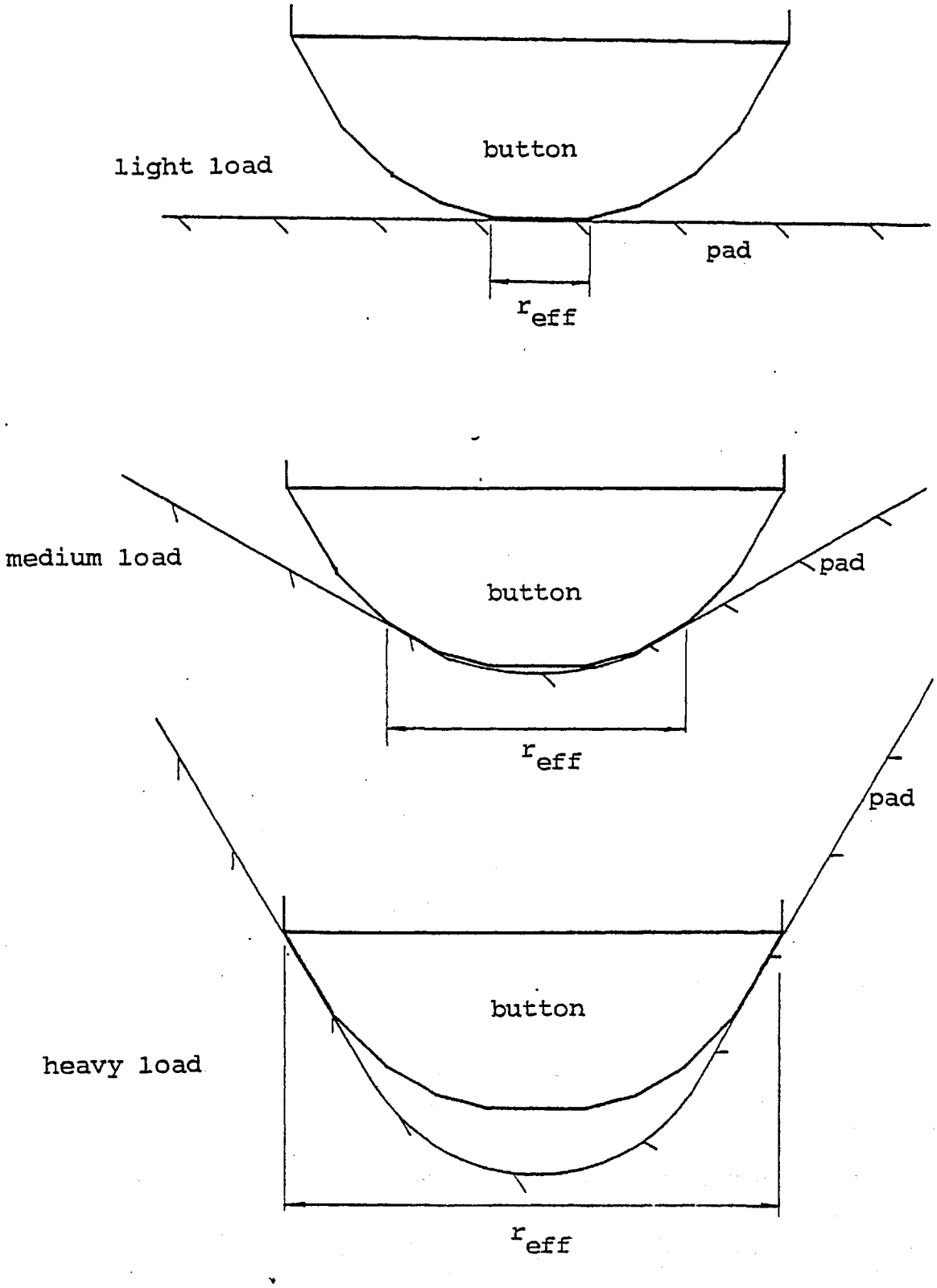

Figure 7F-7 Compensatory Button Support

iv) The method of pad support

a) Relieved Button: Fig 7F-8a shows a 'horse shoe' type of support. This is a simple modification of the usual button support. It involves relieving the usual circular button support at the dotted areas yielding a different type of support.

b) A multiple support may be simulated in a similar way as in iv(a). Fig 7F-8b shows a two part support which is again based on a relieved button as shown by the dotted areas.

c) A spring mattress: This type of support has been described by Vohr in a recent publication {R32}. A similar design was patented by Starcevic {R87}. The design can incorporate variable stiffness springs supported on a thick tilting block. The springs in turn support a relatively thin plate. Thus, resistance to deflection at the plate edges may be controlled by increasing the stiffness towards the plate edges (Fig 7F-9) providing a more efficient deflection profile.

v) Additional Cooling of Rotor Periphery

The design of the rotor radial periphery (normally immersed in the oil bath) can incorporate fins to enhance heat transfer (providing a greater heat transfer coefficient). This aids in rotor cooling, serving to cool the bearing as a whole. Hence the temperature gradient across the pads is lessened, helping to reduce thermal deflection.

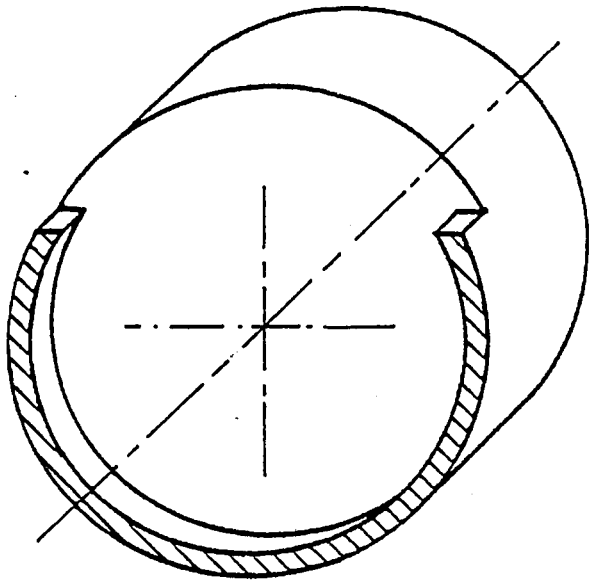

(a) horse-shoe support

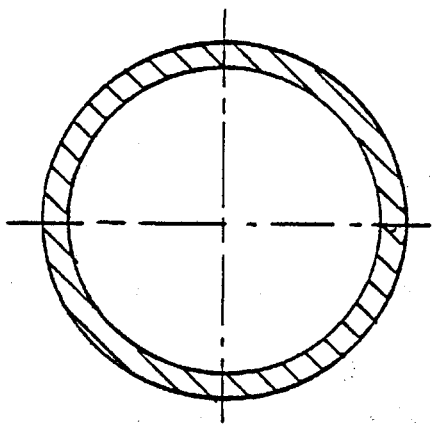

normal button

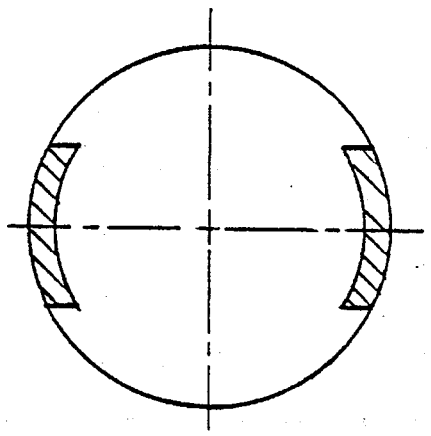

(b) multiple support

Figure 7F-8 Horse-shoe and Multiple Supports

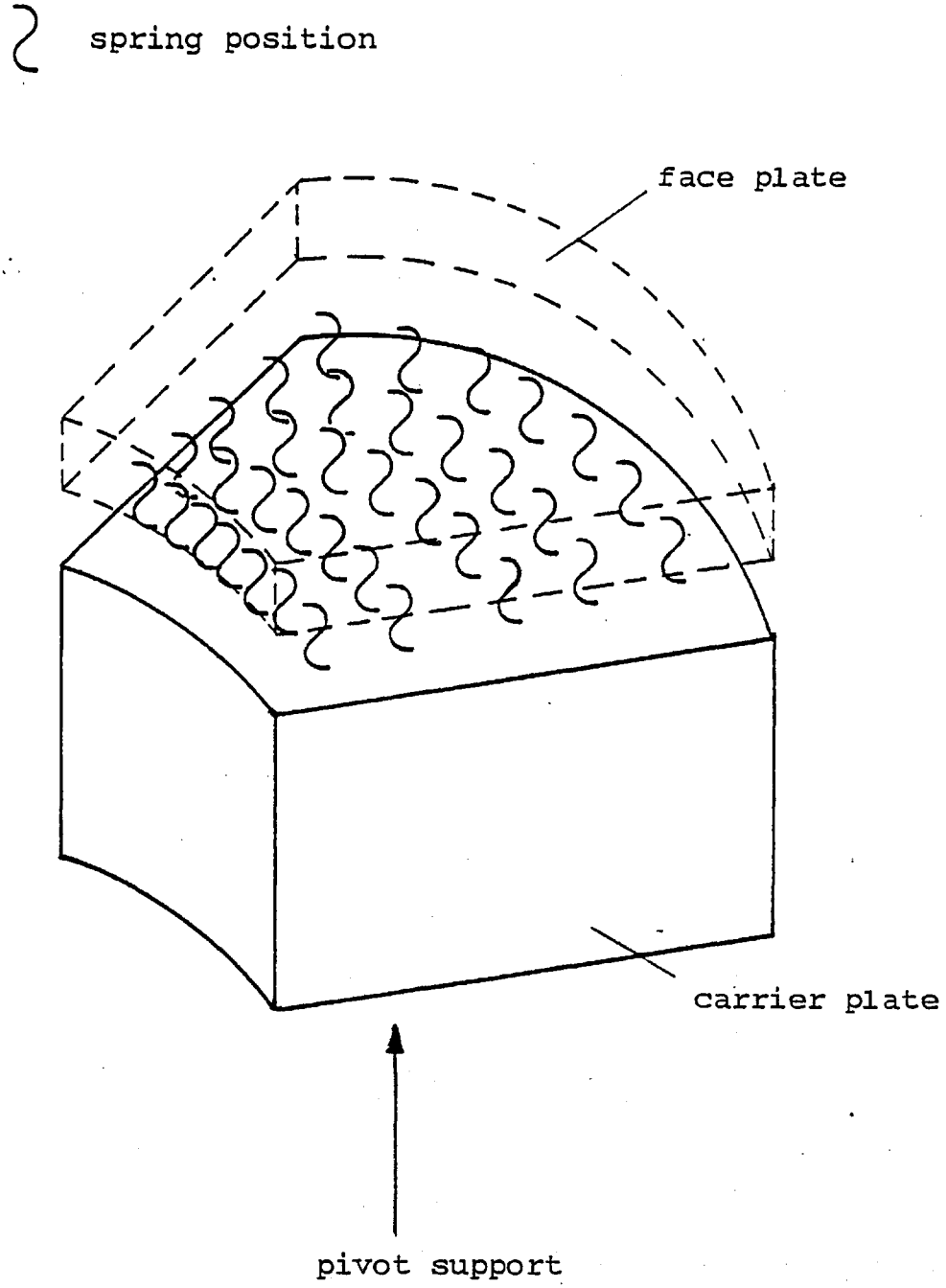

Figure 7F-9 Spring Mattress Design

7.3.2 Active Devices

i) High Pressure Jacking

Jacking is used to separate the pad and runner surfaces at start up in order to avoid surface damage (see Case 1, chapter 6). This is also used for large journal bearings for the same purpose. After a few revolutions, jacking is cut off and the oil hydrodynamic film carries the load. Jacking can be useful during bearing operation by injecting cold oil into the hot hydrodynamic film with the main purpose of regulating the oil film temperature down to an acceptable level. In addition the benefits of hybrid bearings (hydrostatic and hydrodynamic) are gained. This requires maintaining a secondary cool oil feed pumped at a high pressure. Failure during operation of the high pressure system is dangerous as it can lead to a rapid thermal ratcheting process resulting in seizure.

ii) Low Pressure Jacking

Low pressure jacking near the leading edge of the pads is possible since the maximum pressure usually falls between the pivot position and the trailing edge. Mikula {R90} reported that balancing can cause problems, unless similar jacking is applied close to the trailing edge. It is thought that a correct analysis of jacking close to the pad edges must be accompanied by analysis of the flow just outside the edge. In addition, a strong recirculation zone is thought to exist at the entry region {R91}. Thus, it is

likely that low pressure jacking may not be effective in blending cold jacked oil with the hot oil carried over by the runner, unless jacking is a suitable distance from the pad leading edge.

iii) Forced Water Cooling

The design of the pads allows the use of small radial cooling ducts as shown in Fig 7F-10. The coolant used is chosen to be a liquid with a large thermal capacity and good heat transfer coefficient in order to extract the maximum amount of energy - water. The velocity of the coolant can be regulated, too. This design is advantageous when compared to rotation induced oil cooling in several ways. The coolant used is better, its entry temperature can be regulated, and the velocity may be varied to produce the desired bearing temperature.

7.4 Variations of Pad Thickness

The bearing specifications for Case 1 (chapter 6) have been used to investigate the effects of pad thickness. The surface heat transfer coefficient used for the back faces of the pad is 180 J/m^2s deg C (as opposed to the maximum value of 450 used earlier). The pad thicknesses used are 7.62; 9.2; 12.7; and 20.32 cm. (The ratio of pad to collar thickness is kept constant).

Fig 7F-11 shows a graph of pad maximum temperature versus load. If a ceiling of 90 deg C is fixed for the pads, the maximum specific load allowed for a 7.62 cm thick pad is 10 bars. For the 9.2, 12.7, and 20.32 cm pads the loads are 15 bars, 25 bars, and 30

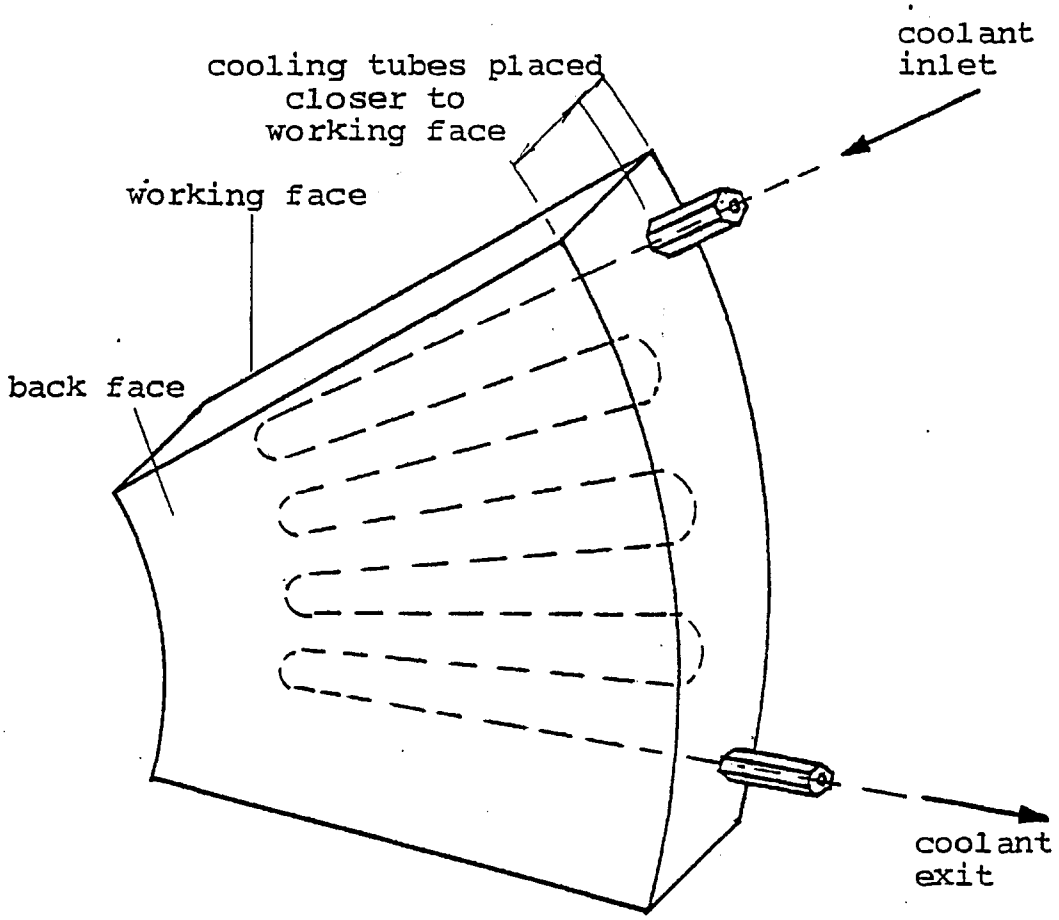

Figure 7F-10 Pad Water Cooling

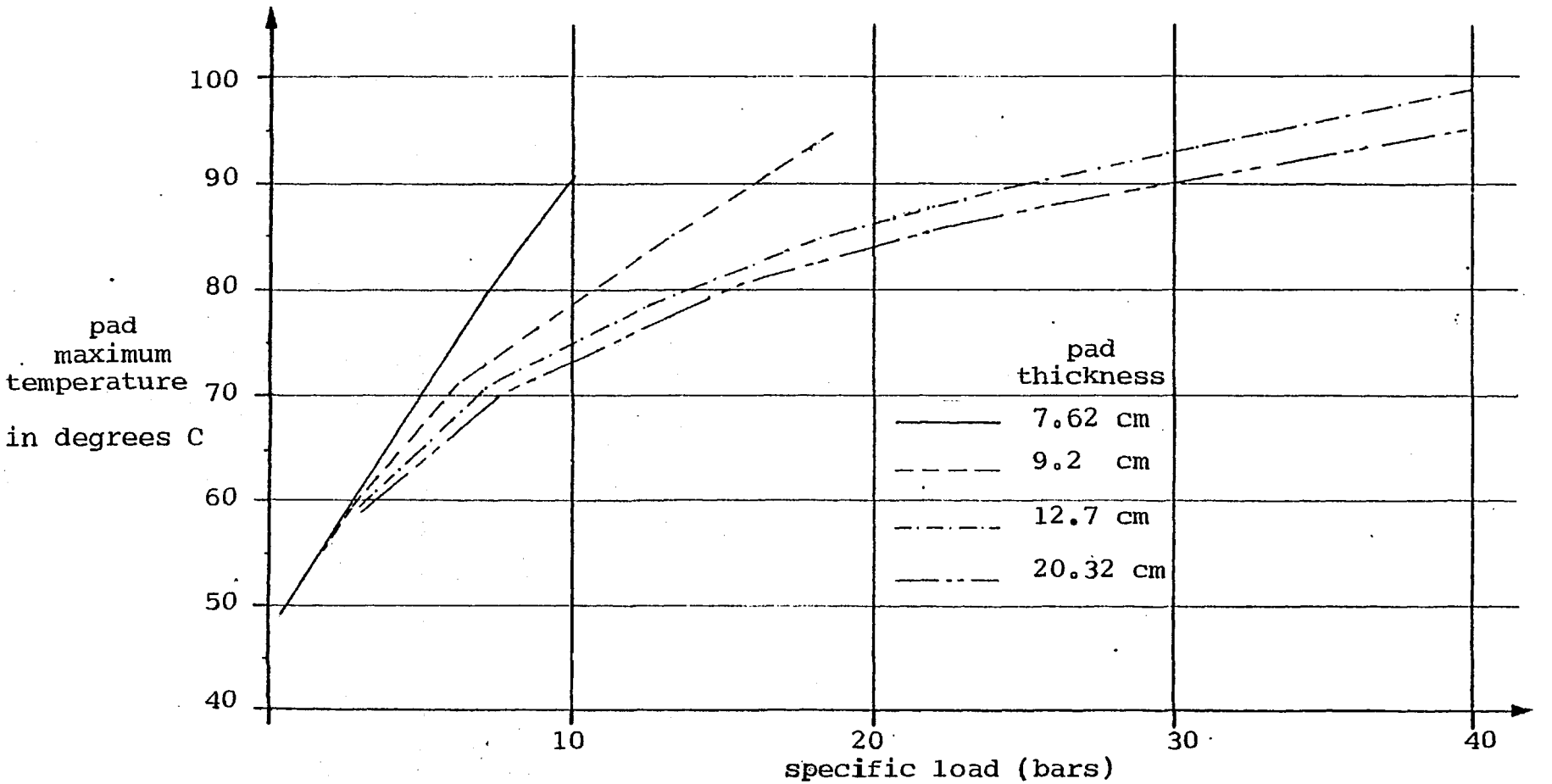

Figure 7F-11 Temperature Versus Load for Different Pad Thicknesses

bars respectively. Thus a thicker pad will reduce the maximum temperature at oil/pad interface. As the pad thickness increases the additional increment in load capacity gained decreases. On the other hand a very thick plate would be heavy, expensive, and unnecessary.

A pad thickness of 12.7 cm - the value used for the bearing in Case 1, chapter 6 - gives sufficient rigidity for pad operation up to 40 bars. A smaller pad thickness (9.2 cm curve) is likely to function satisfactorily up to only 20 bars.

7.5 Insulation, Cooling, Support Shape, and Pivot Position

The model developed and tested in previous chapters can be used to simulate insulation by decreasing the heat transfer coefficient at the back and side faces of the pad. Similarly, peripheral runner cooling can be simulated by increasing the surface heat transfer coefficient at the outer rim (not the back surface).

The bearing geometry used for size effect results (centrally pivoted) is used. A size factor of one has been chosen. The surface heat transfer coefficients at all pad surfaces - except the face in contact with the oil film - are set to three successive values 10; 50; and 100. This provides three levels of insulation, compared to a value of 450 J/m^2s deg C used initially. Similarly at the runner rim a value of 1000 J/m^2s deg C is used for the peripheral cooling model.

The deflection model developed in chapter 4 is amenable to

changes in geometry and support shape (as shown for Cases 1, 2, and 3 in chapter 6). Thus, a 'horse shoe' type of support (Fig 7F-8a) has been chosen to check the bearing characteristics, for the same pad geometry and bearing specifications used for the size effect results (size factor = 1).

The pivot position in Case 1 - chapter 6 - is offset (size factor = 1). All the above examples are modifications of the basic bearing geometry used for the size effect results - for the same oil conditions - at a size factor of 1. A surface velocity of 10 m/s is used throughout. Thus, for a particular specific load a direct comparison is possible on the basis of maximum pad temperature.

Fig 7F-12 shows a graph of maximum pad temperature versus specific load. Curve 'g' represents a centrally pivoted pad, size factor = 1, with the bearing specifications given in the size effects section. Curves 'a', 'b', and 'c' represent insulation surface heat transfer coefficients of 100; 50; and 10 respectively. It is apparent that, for any specific load, insulation causes an increase in pad maximum temperature (T_{max}). If a ceiling of 80 deg C is required for safe bearing operation, the maximum specific loads sustained are 1; 4; 6.5; and 12.5 bars for curves 'c', 'b', 'a', and 'g' respectively. One possible explanation is that insulation reduces heat conduction. The heat generated is transferred by the lubricant. Since the proportion of heat conducted is normally large, a sizeable increase in lubricant temperature is expected. Insulation may be beneficial in cases

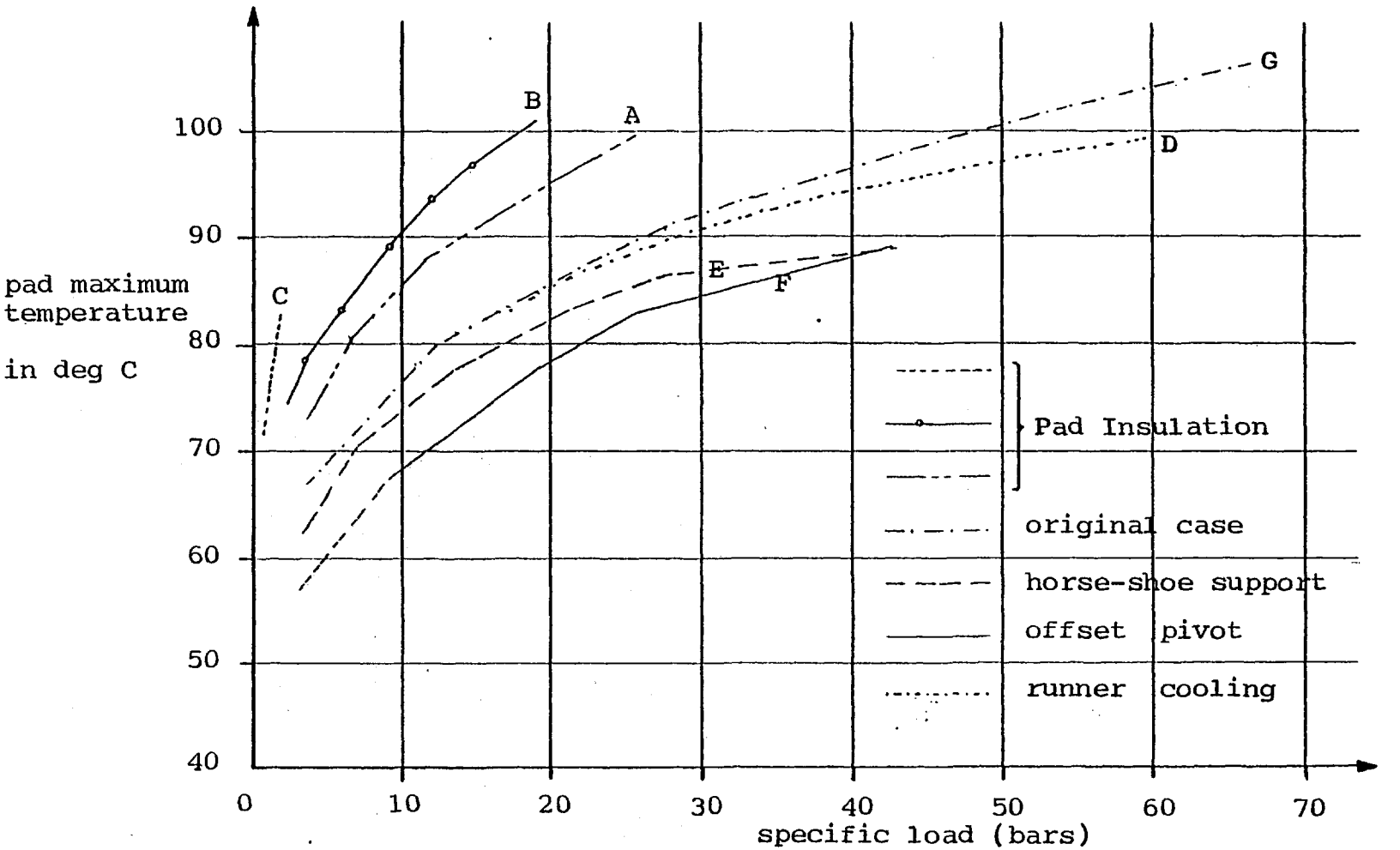

Figure 7F-12 Maximum Pad Temperature Versus Specific Load for Various Passive Design Modifications

where the proportion of heat conducted is small; as control of thermal deflection may be carried out at a small increase in lubricant temperature. In return a more efficient deflection profile prevents a large increase in temperature from taking place.

Curve 'd' represents a runner rim surface heat transfer coefficient equal to 1000 J/m^2s deg C - runner peripheral cooling. Physically better heat transfer is obtained using fins or an extended surface. A comparison between curves 'g' and 'd' shows a lower pad maximum temperature (T_{max}) for peripheral cooling. For a ceiling temperature of 95 deg C, the maximum loads sustained are 37 and 40 bars for curves 'g' and 'd' respectively.

A relieved button support is shown by curve 'e'. Beyond a specific load of 27 bars, the gap between curves 'g' and 'e' widens. At a load of 40 bars, a relieved button support cools the pads by 8 deg C compared to a conventional circular button. An advantage is obtained over the entire load range (0 - 40 bars) by using a relieved button.

An offset pivot position (θ_{piv} = 0.544×pad angle) has been used in Case 1 (chapter 6). The load temperature characteristic is shown as curve 'f'. Over the load range 0 - 40 bars an offset pivot bearing runs 10 deg C cooler than for a central pivot. If a ceiling temperature of 85 deg C is applied the maximum loads sustained are 20 and 32 bars for curves 'g' and 'f' respectively. Thus, an offset pivot pad bearing may support 50% more load than a central pivot bearing.

The above 'improvements' have shown that pad insulation is to be avoided for a geometry similar to the case tested. On the other hand, peripheral runner cooling provides a marginal improvement - and may be difficult to implement in practice. A relieved button and an offset pad show considerable improvements over the conventional design. These passive devices may be implemented with relative ease to existing designs of similar geometry. They can also be used to improve the performance of button supported pivoted pad bearings which are currently in use. An optimum pad thickness can be chosen by using the present model to give the theoretical bearing performance (load - temperature graph) as in Fig 7F-11.

7.6 Forced Water Cooling

In Section 7.3.2(iii) the use of small radial cooling ducts, within the pad, has been outlined. A large temperature gradient is expected between pad/oil interface and the cooling ducts. A relatively small gradient between the cooling ducts and the back face then results, as most of the heat conducted to the pad is convected away by the water within the ducts. Thus, the ducts are designed to be as close as is safely possible to the pad working surface. In addition, the pad thickness is extended to 0.254 m (double the original thickness) for added strength and rigidity. This ensures that the temperature gradient across most of the pad thickness is small (see Fig 7F-13). Thus, the effective thermal moment is controlled by the temperature, speed, and flow rate of

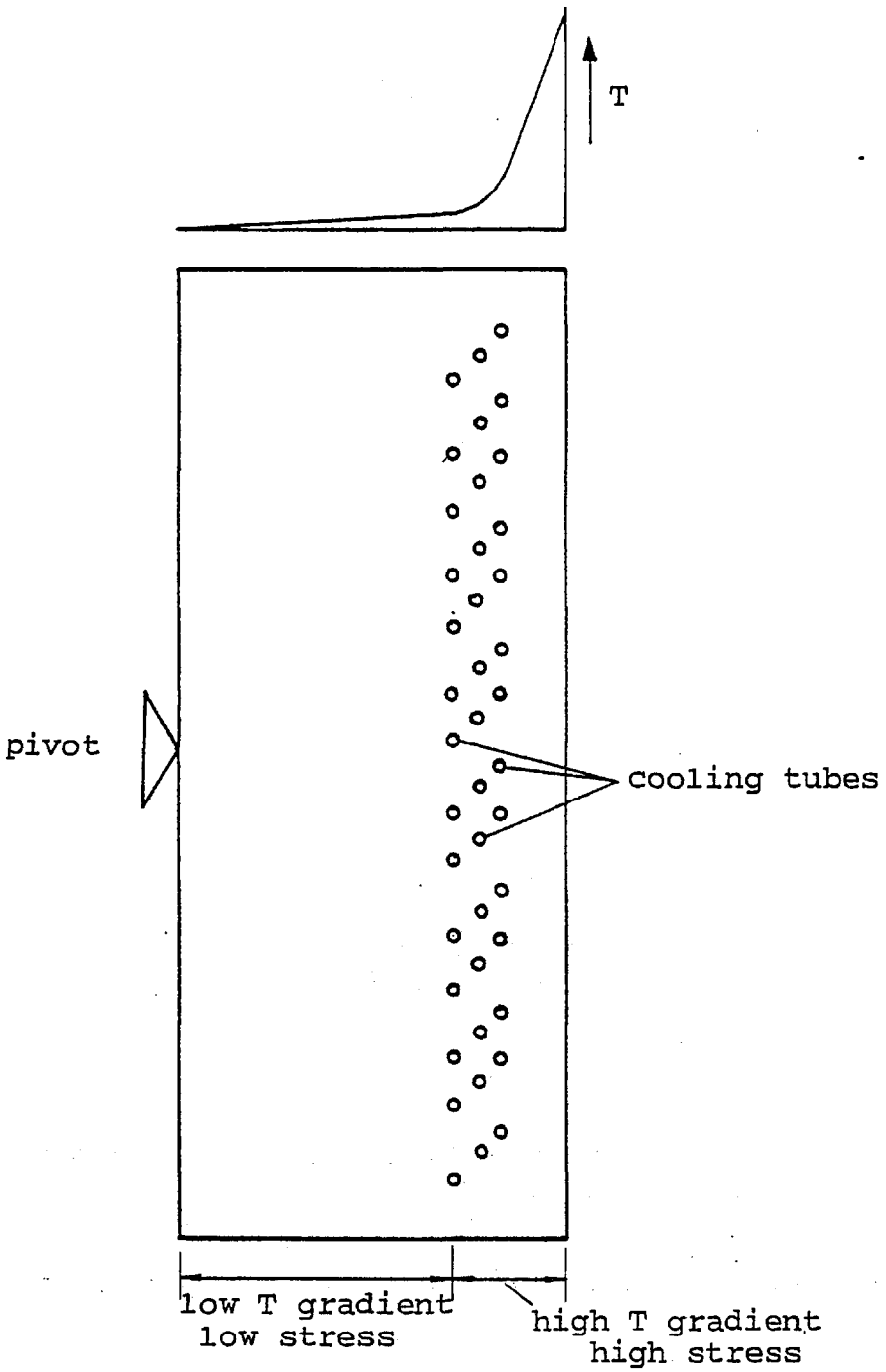

Figure 7F-13 Temperature Gradients Across Water-cooled Pad

coolant in the pad.

The grid used is shown in Fig 7F-14a. Five planes are used in the z-direction for the pad. Plane K = 2 is chosen to model the cooling ducts. A plan of the plane K = 2 is shown in Fig 7F-14b. The coolant enters at node (9,9) at temmperature T_{ci}. The path is zigzag shaped radially as shown. The coolant exits at node (1,1) at a hitherto unknown temperature T_{co}. The iteration process is adjusted to follow the path of the coolant for every iteration. At any node (I,J) in the plane K = 2 the heat transfer to the coolant is

$$Q = - \alpha_w (T_{CA} - T_{ij}) A_s n_t \qquad \text{E7-1}$$

where α_w is the heat transfer coefficient

n_t is the number of tubes

T_{CA} is the average coolant temperature within the control volume

T_{ij} is the temperature of the node within the control volume

A_s is the surface area of the coolant tube in the control volume

$$T_{CA} = 0.5 (T_{in} - T_{out}) \qquad \text{E7-2}$$

where T_{in} is the inlet temperature to the control volume (equal to exit temeperature of previous control volume)

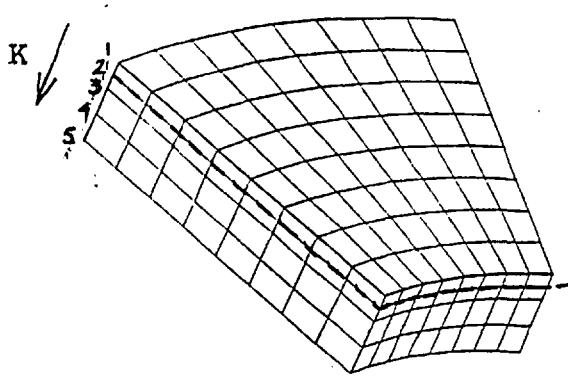

Pad Grid

cooling plane

(a)

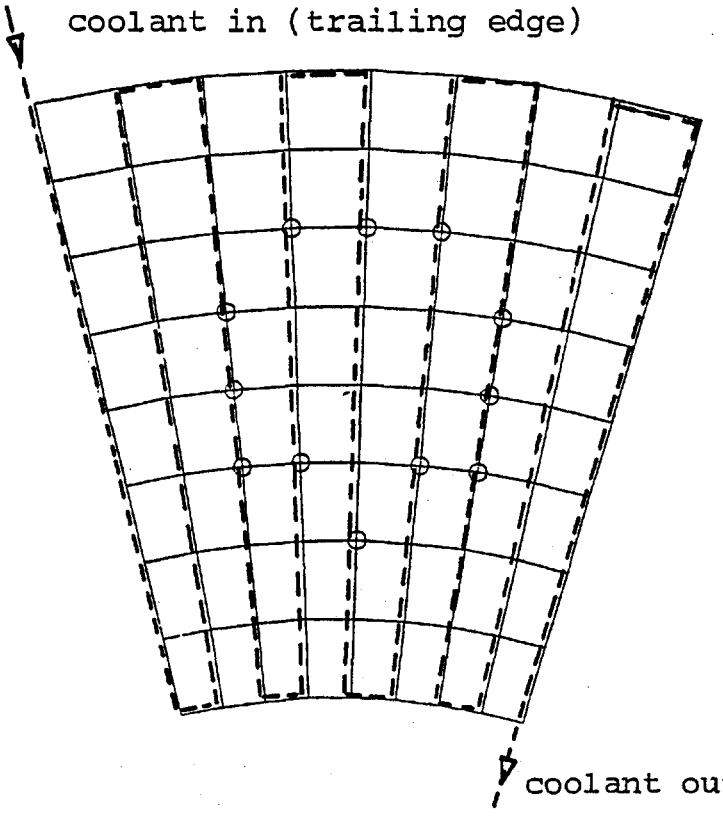

(b)

Coolant path in numerical grid (K=2 plane)

Figure 7F-14 Cooling Tube Representation in Thrust Pad

T_{out} is the exit coolant temperature from the control volume

The heat transfer may be expressed for the coolant water as (positive into coolant)

$$Q = \rho_w u_w A_c c_w (T_{out} - T_{in}) n_t \qquad \text{E7-3}$$

where ρ is the water density

u_w is the average water velocity

A_c is the surface area of the coolant tube cross-section

c_w is the specific heat capacity of the water

From E7-1, E7-2, and E7-3

$$T_{out} = T_{inlet} \frac{(2\ s - \delta r)}{(2\ s + \delta r)} + T_{ij} \frac{2\ \delta r}{(2\ s + \delta r)} \qquad \text{E7-4}$$

where $s = \rho_w u_w D_w^2 c / 17.456k$

δr = width of control volume

D_w = diameter of tubes

The energy convected by the coolant (equation E7-3) is used as a source term in the conduction equation within the pad (as for

energy input at the pad/oil interface). The mehtod of iteration in which the coolant path is numerically followed allows the coolant exit temperature at a node to be used as the coolant entry temperature in the following node. n_t, the number of tubes used, is an indication of the number of tubes per control volume that may be used. A larger value (integer) indicates more surface area available for cooling. The velocity of the coolant u_w, the area of the tubes A_c, and the coolant entry temperature are variables to be chosen by the designer.

The surface heat transfer coefficient for the coolant is evaluated assuming the constant heat transfer rate value for steady flow in tubes as 4.364k/D {R34}. A water inlet temperature of 30 deg C has been chosen (this value may be changed to vary the bearing performance). A tube diameter of 0.01 m (1 cm) is chosen. The heat transfer is improved as the tube diameter is decreased for two reasons. The first is that the heat transfer coefficient (α = 4.364k/D) is increased. The second is that the ratio of the exposed area per unit volume increases as the tube diameter is decreased. A drawback of decreasing the tube diameter is an increase in pressure drop between inlet and outlet.

Fig 7F-15 shows a graph of maximum pad temperature versus load. Curve 'a' represents a coolant velocity of 0.2 m/s (n_t = 1) for a circular central button support. Curve 'f' represents the size effects geometry and specification, at a size factor of 1, for comparison purposes (Curve 'g' in Fig 7F-12). At 40 bars specific

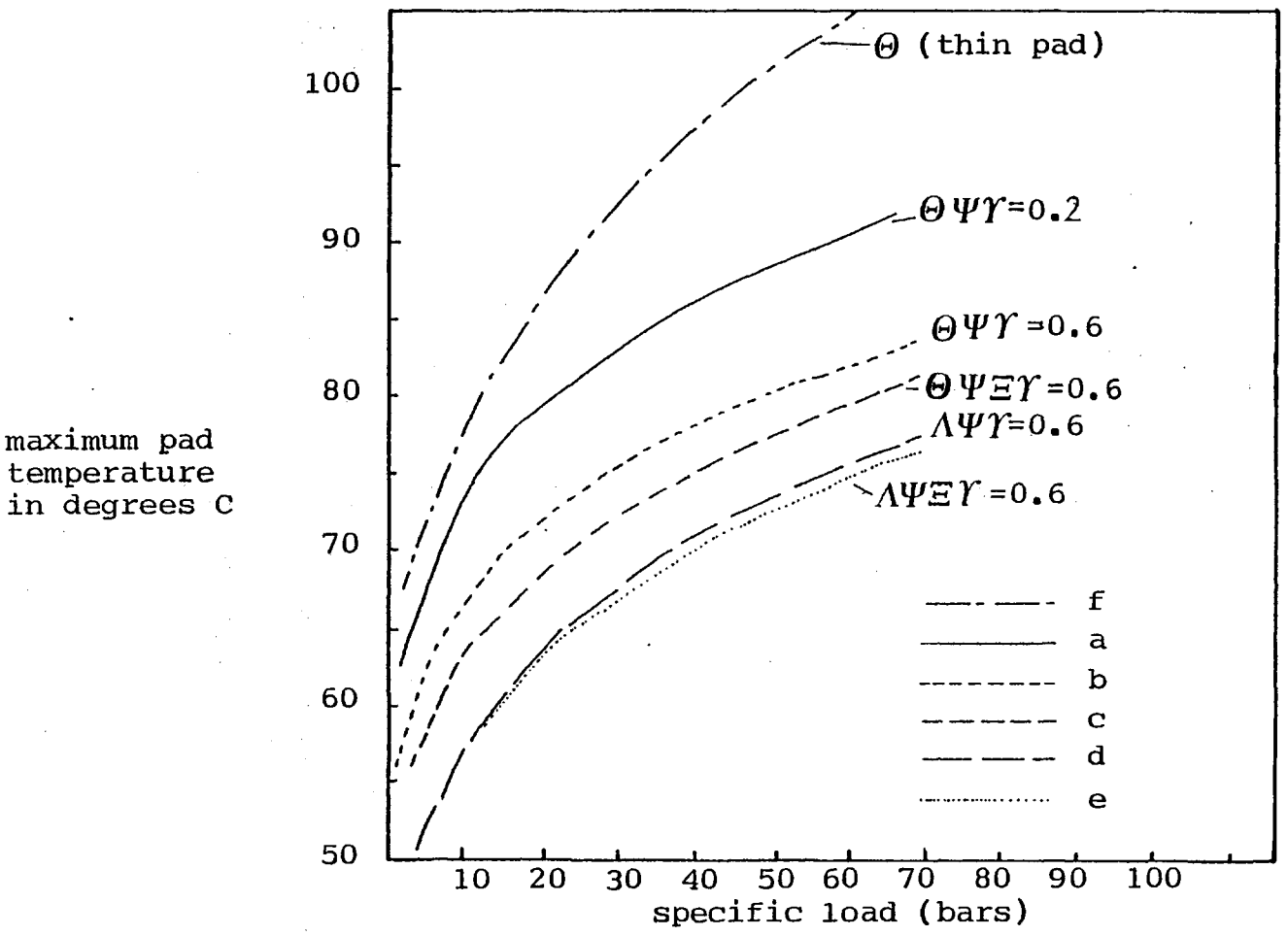

Figure 7F-15 Maximum Pad Temperature Versus Specific Load for Various Designs

load, a reduction of 12 deg C is obtained for the water cooled design in curve 'a' relative to 'f'. The gap widens to more than 14 deg C at 70 bars - maximum pad temperature of 92 deg C for the water cooled pads. Curve 'b' represents the same bearing as in 'a' but at a coolant velocity of 0.6 m/s and $n_t = 5$. A significant decrease (8 deg C) in T_{max} accompanies the increased coolant velocity; yielding T_{max} = 84 deg C at 70 bars. Compared to the modifications for pad support and peripheral cooling, water cooling (in thicker pads) provides a substantial decrease in pad maximum temperature.

A combination of water cooled thick pads and a relieved button (coolant velocity of 0.6 m/s, $n_t = 5$) produces curve 'c'. If in addition to water cooling an offset pivot (for a circular button) is used, curve 'd' results. If a relieved button is used for the case in curve 'd'; curve 'e' results. A combination of improvements to the pad design yields cumulative benefits. Curve 'e' (representing a relieved button, offset support, thick, water cooled pads) shows T_{max} of 76 deg C at 70 bars, compared to 107.5 deg C for the initial case. Thus, the improved bearing design runs 32.5 deg C cooler than the conventional one at 70 bars specific load, and 27 deg C cooler at a specific load of 40 bars.

Fig 7F-16 shows the temperature distribution for the pad, oil film, and runner for the case represented by curve 'a' at 70 bars specific load. A sharp temperature gradient is shown in the pad close to the oil film surface. This represents the heat transfer from the oil film to the coolant. The temperature gradient rapidly

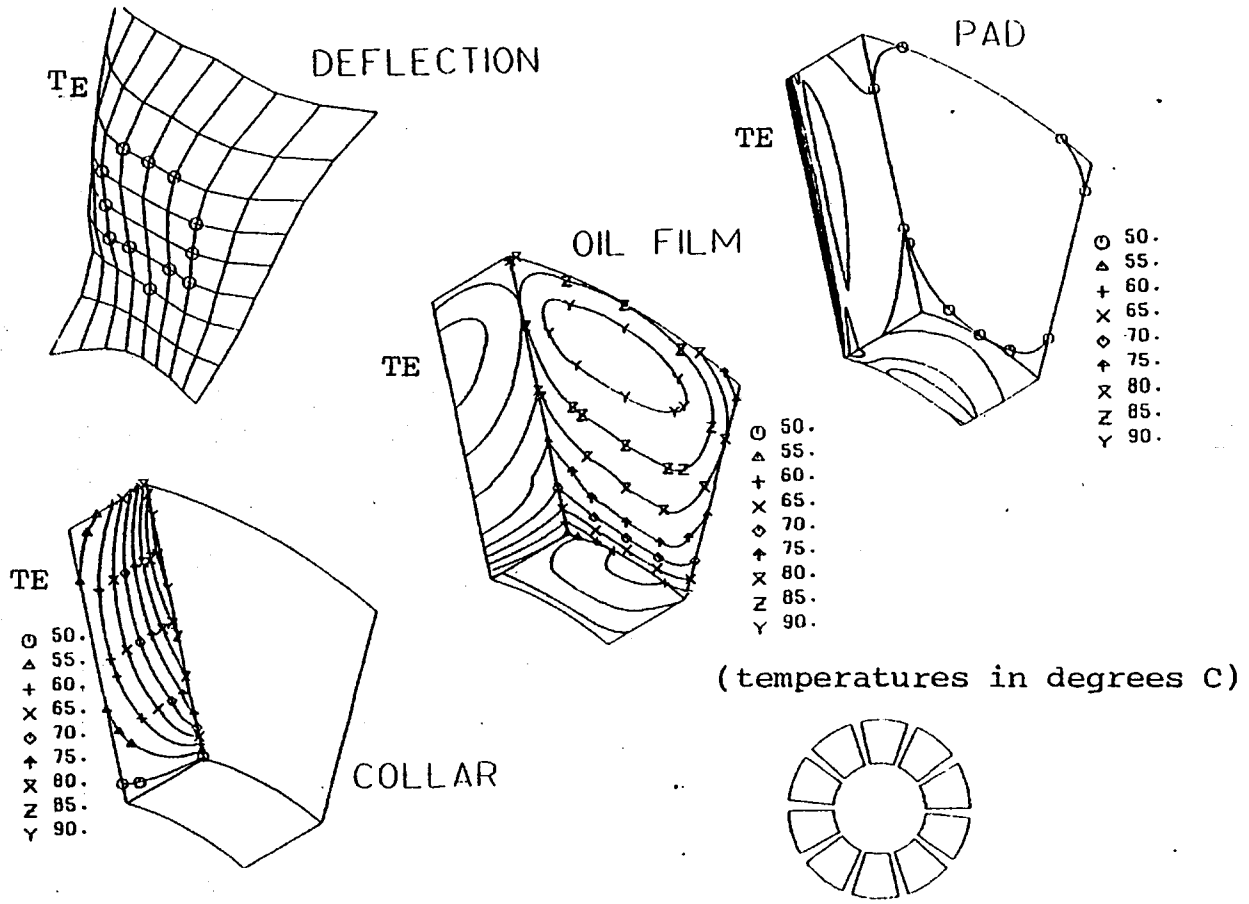

Figure 7F-16 Temperature Distribution in Pad, Oil Film and Runner - including water cooling

decreases for the remainder of the pad thickness. The deflection shape is also shown.

Fig 7F-17 shows a radial section at the pivot circumferential position. The temperature gradient in the pad, close to the pad/oil interface, shows a similar trend as in Fig 7F-16. The distribution of temperature, pressure, and film thickness are shown in Fig 7F-18. The maximum to minimum film thickness ratio is approximately 2.5. Thus, it appears that thermal deflection has been controlled. The maximum pad temperature is approximately equal to the maximum collar temperature - 90 deg C - and takes place at the same radial position. The temperature distribution is fairly symmetrical about the axis A-A in the pad. Since the coolant enters at the pad trailing edge at 30 deg C and leaves at the leading edge (with respect to the oil film) at 73 deg C, a larger amount of cooling takes place near the pad trailing edge - where the largest temperature gradients take place in conventional designs. This serves to explain the relative symmetry about axis A-A.

In Fig 7F-19 the film temperature, pressure, and film thickness distributions are shown for case 'b' at 70 bars specific load. The coolant exit temperature is 36.4 deg C - an increase of 6.4 deg C. This reflects the larger coolant velocity. All temperatures show a decline compared to case 'a' (Fig 7F-18). Deflection is also reduced - giving evidence of the control of excessive thermal deflection. Case 'c' is represented in Fig 7F-20a at a specific load of 70 bars. The pressure distribution reveals

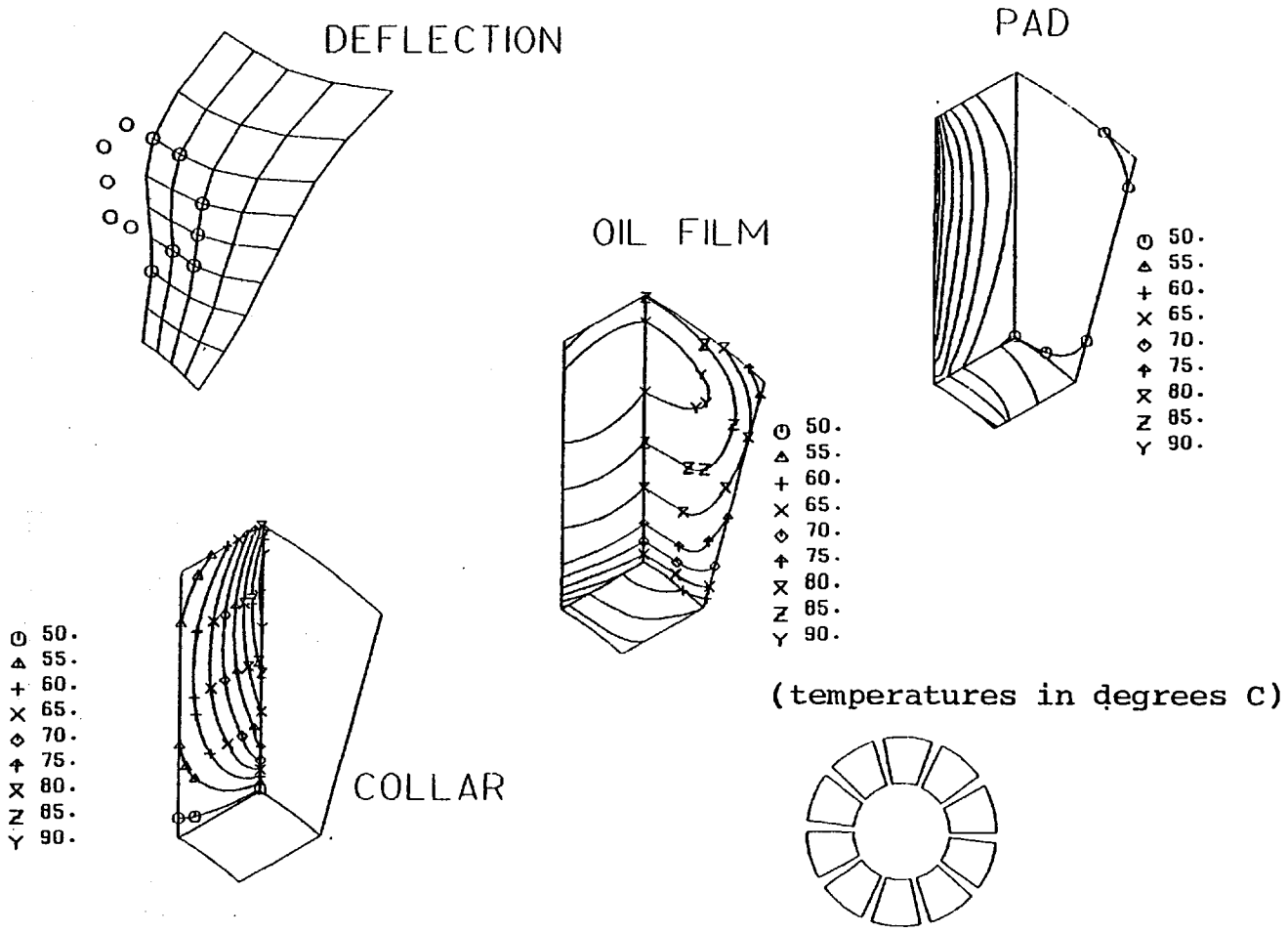

Figure 7F-17 Sectional View of Pad, Oil Film and Runner Showing Temperature Contours – Water Cooled Case

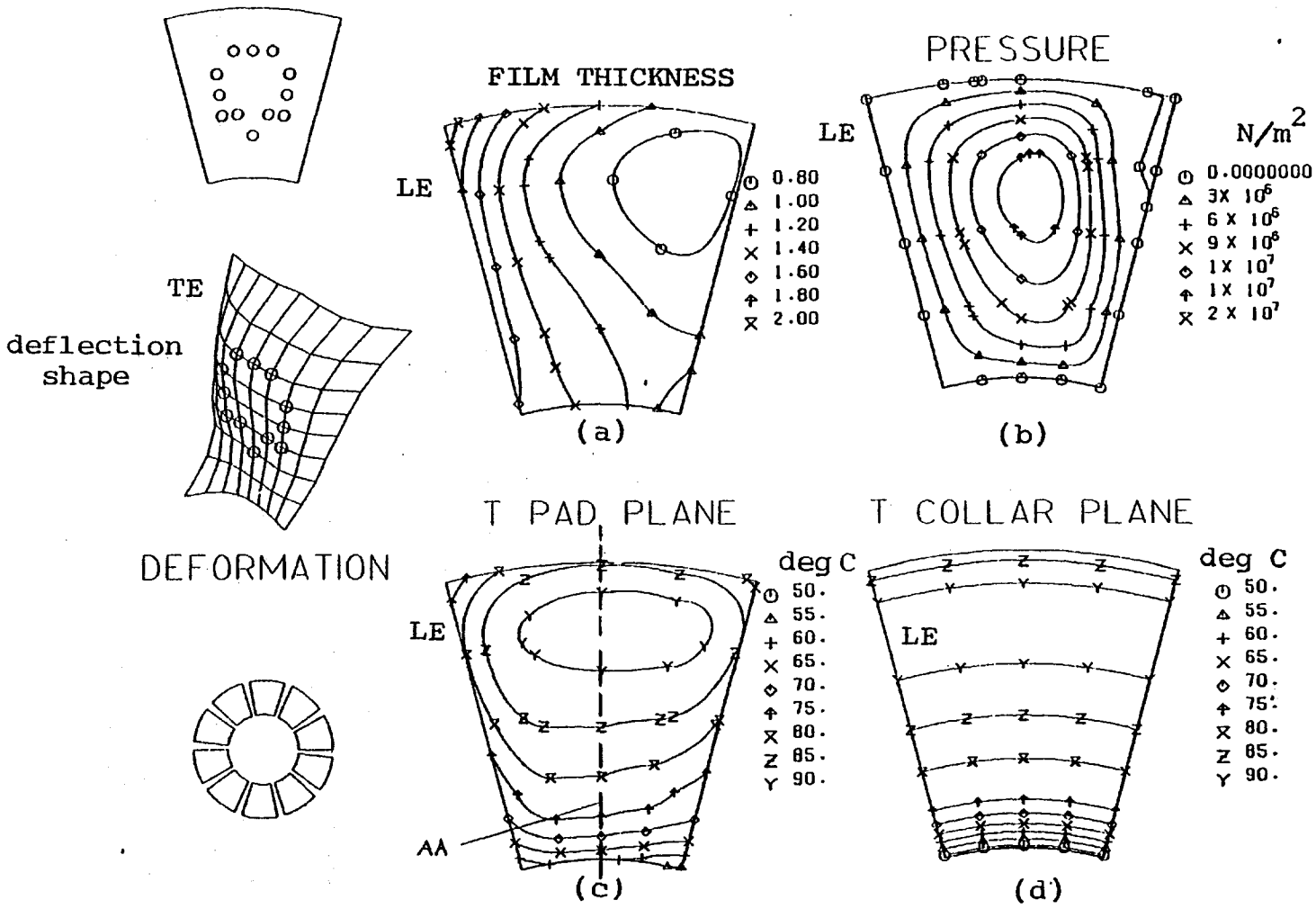

Figure 7F-18 p,T,h Contours and Deflection Shape for Design Case a

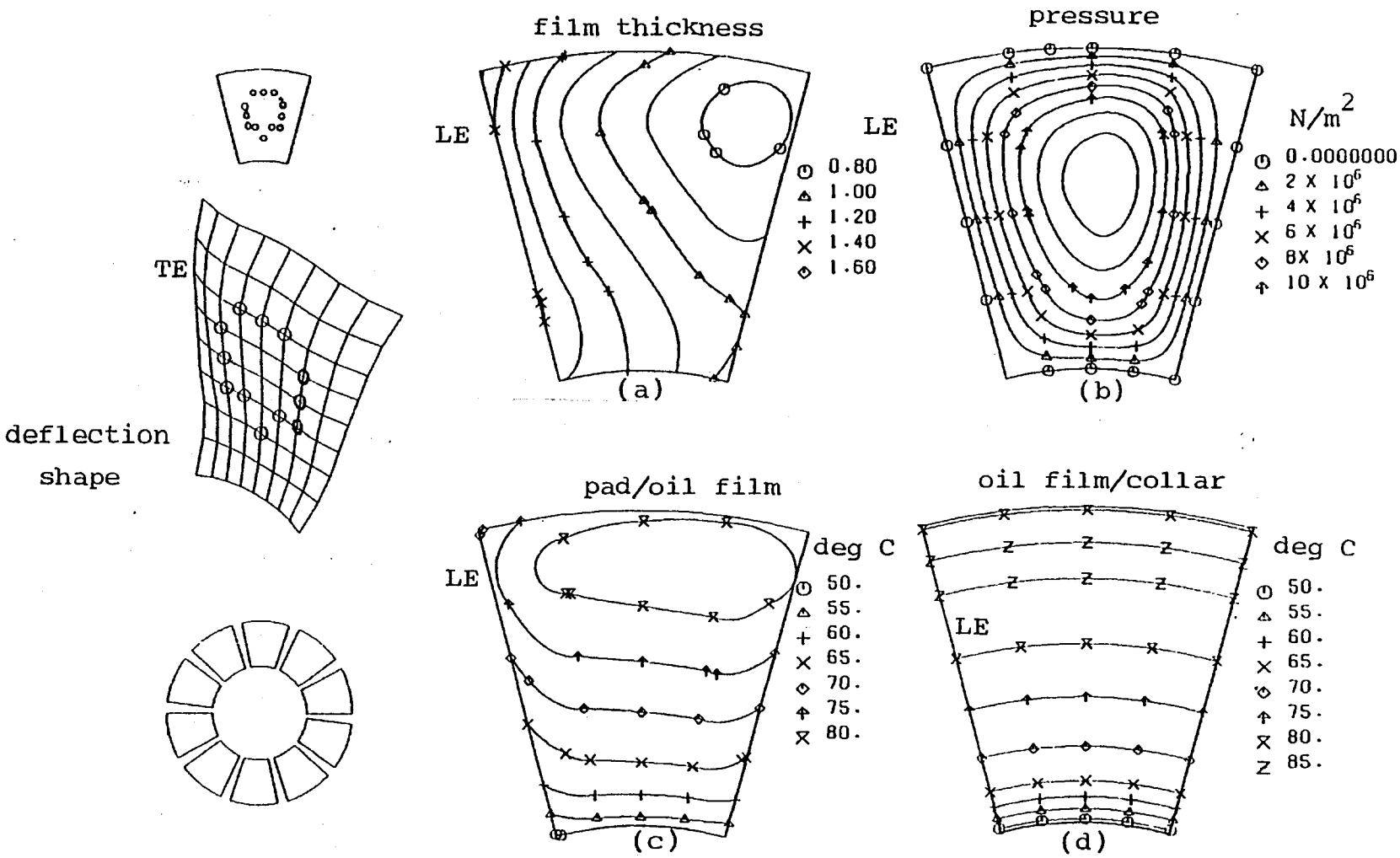

Figure 7F-19 p,T,h Contours and Deflection Shape for Design Case b

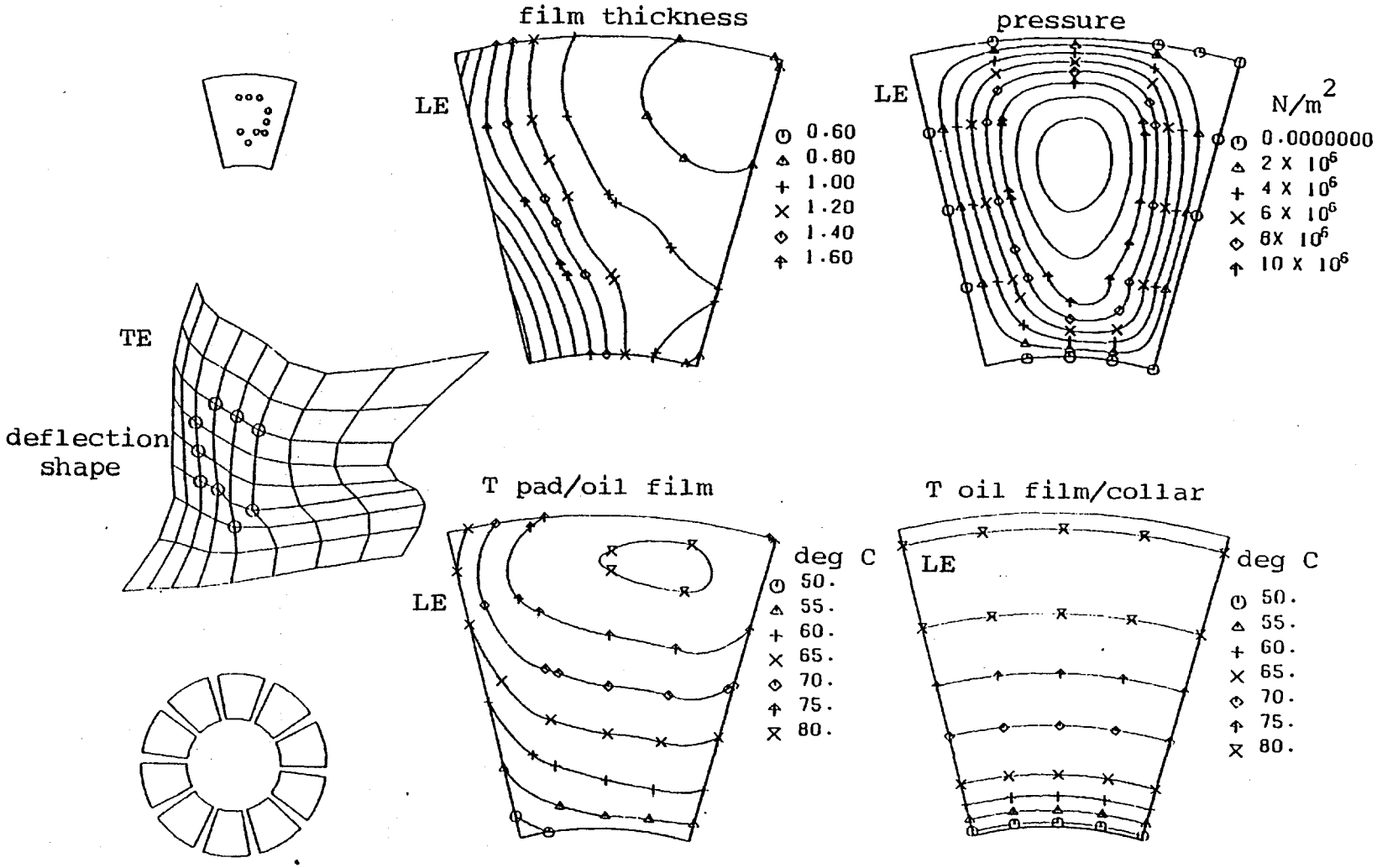

Figure 7F-20a p,T,h Contours and Deflection Shape for Design Case c

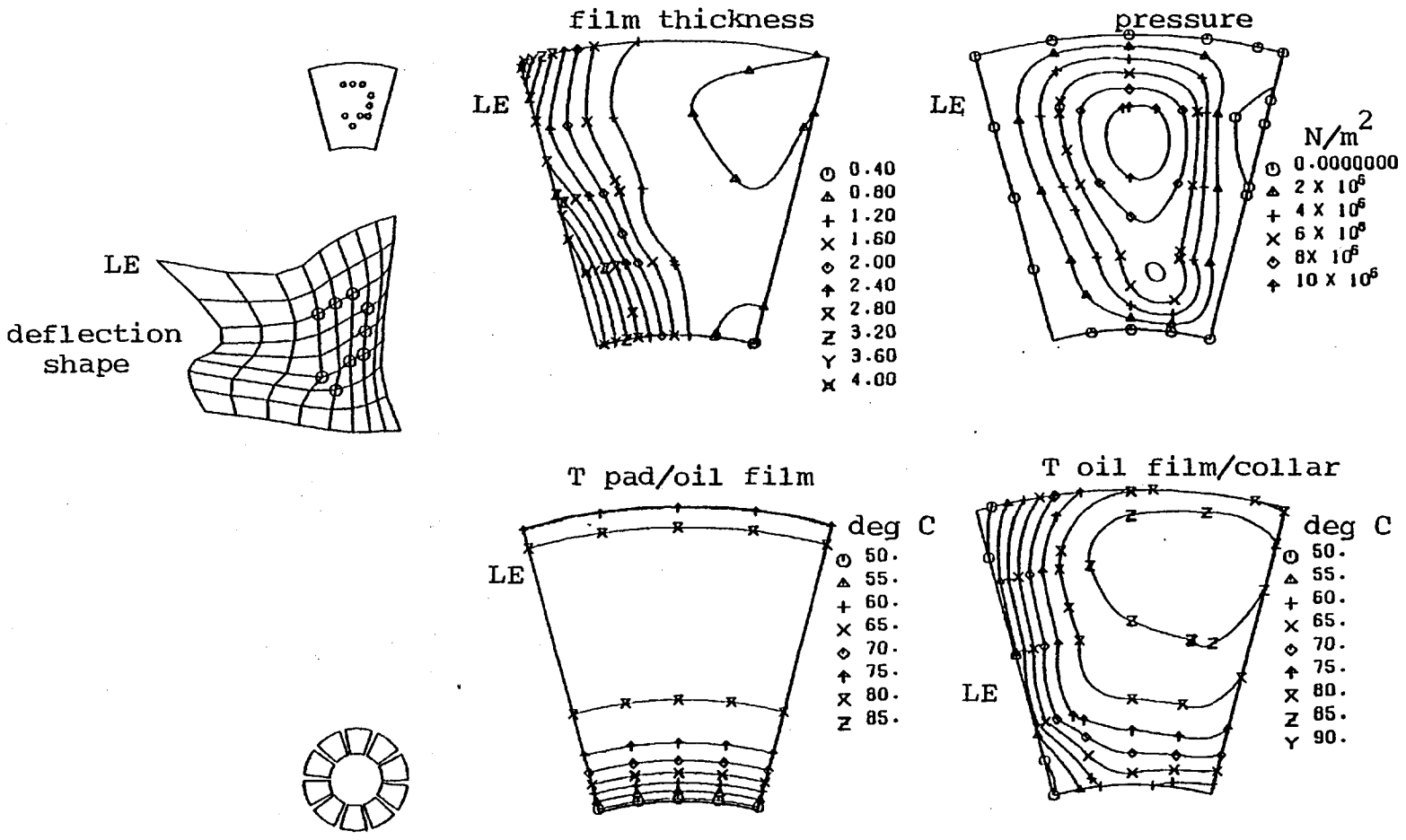

Figure 7F-20b p,T,h Contours and Deflection Shape for relieved button, thin pad case

the existance of two peaks (maxima). This is reflected in the film thickness distribution by the formation of two minima; one close to the outer radius trailing edge and the other near the inner radius trailing edge. The deflection shape resembles the tapered land bearing shape which is reflected in the density of the film thickness contours. Fig 7F-20b shows contours for the releived button case in Section 7.5 (no cooling, thin pad). The presence of two pressure peaks is demonstrated. The deflection shape is very similar to Case 'c'. Case 'd' is shown in Fig 7F-21 for a specific load of 70 bars. The offset pivot position results in the asymmetric pressure contour distribution. Pad deflection is minimal as shown by the film thickness contours. A comparison of minimum film thickness variations with specific load for Cases 'a', 'b', 'c', 'd', and 'e' is shown in Fig 7F-22. Curves 'a' and 'b' are very close and show that the variation in coolant velocity and number of tubes does not greatly affect the minimum film thickness. It has been shown earlier that deflection is curbed by cooling. Thus, for the same minimum film thickness a greatly improved film shape takes place in Case 'b'. A relieved button, Case 'c', shows a larger minimum film thickness (h_{min}) than for pure cooling. An offset pad position increases h_{min} - as for 'd' and 'e' - especially at low loads.

7.7 Discussion

For the bearing geometry and specifications chosen, various modifications have been made in an effort to reduce thermal

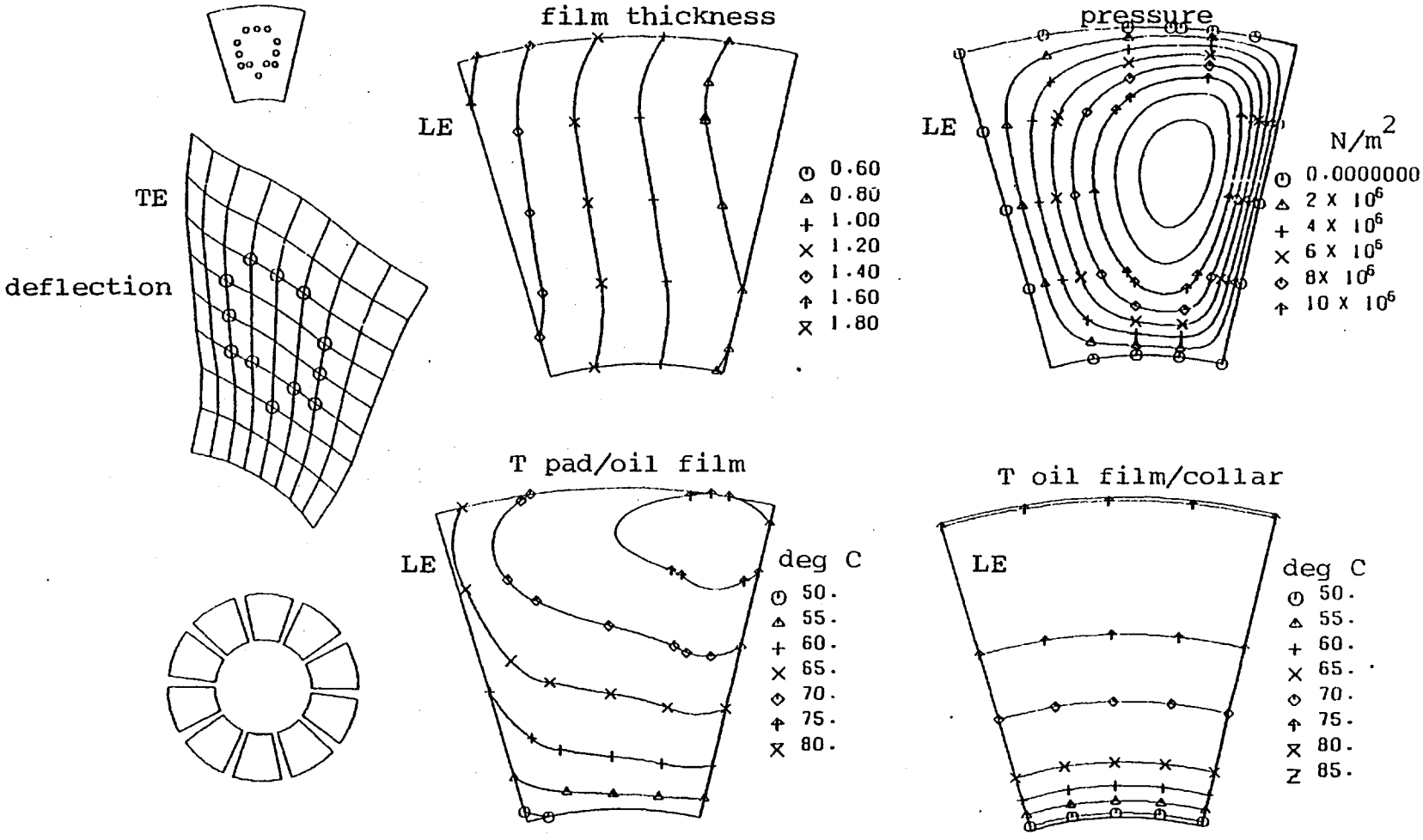

Figure 7F-21 p,T,h Contours and Deflection Shape for Design Case d

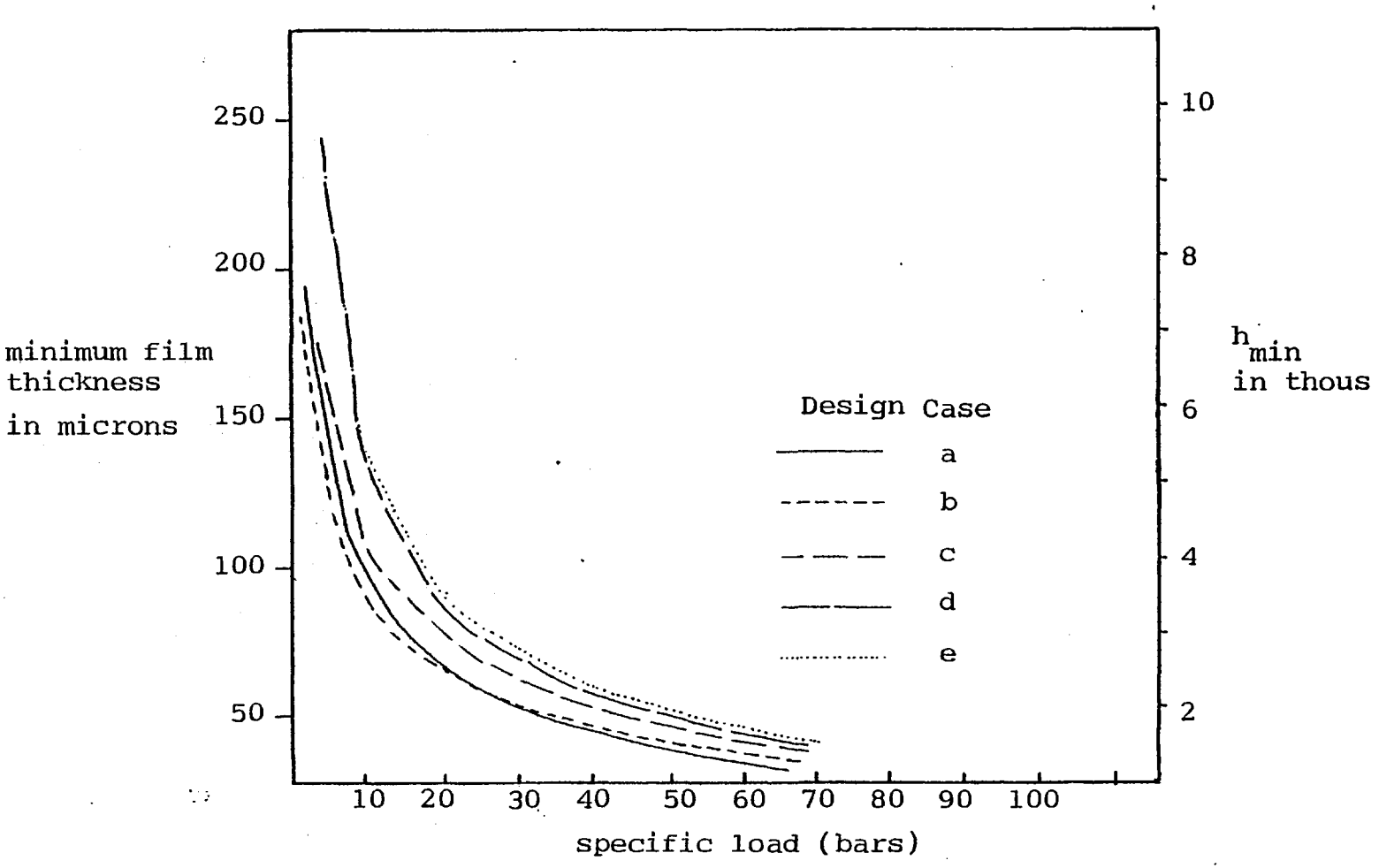

Figure 7F-22 Minimum Film Thickness Versus Specific Load for Various Design Cases

deflection. Pad peripheral cooling has been shown to produce a small positive contribution (Section 7.5). A relieved button is very useful, especially at higher loads, in reducing pad thermal deflection; whilst an offset pivot position reduces bearing maximum temperature (T_{max}) over the whole load range. Forced water cooling can be used to obtain a significant improvement in bearing load range (reducing T_{max} by over 20 deg C). A disadvantage of the latter method is its dependance on an active external system to supply the coolant at the required temperature (30 deg C in this case). In view of the extension in load range such a system is justified. In addition, control of individual pad temperatures can be achieved so that problems of uneven pad levelling can be more easily dealt with. 'Fine tuning' of the bearing operating temperature can be done by regulating the coolant flow. In contrast, the two-piece pad suggested by Kawaike et al relies on oil cooling 'circumferentially' in ducts (see introduction, where the oil velocity cannot be controlled. In addition, the oil specific heat is inferior to that of water. The 'cold' bath oil enters the ducts at the leading edge (rather than trailing edge as in water cooling - Section 7.6). Thus, the problem of increasing thermal moment close to the trailing edge is likely to remain. The Kawaike design is a passive design - hence much simpler to operate.

Active devices involving oil jacking will require a more elaborate external system than that used for water cooling. Since water cooling provides an effective method of curbing distortion, it is thought that oil jacking is unnecessary, except during start up

to prevent damage to the bearing surfaces.

Other methods of solving excessive distortion may involve use of smaller pads arranged in two concentric rings of equal area to a conventional pad arrangement. Use of more pads (20 or more) may help to reduce circumferential distortion of the pads as the pad angle is reduced. In the latter case, special care for the support method is required to prevent radial distortion. The method of oil supply is also important and has been amply covered by Mikula et al [R90].

CHAPTER 8

OVERALL CONCLUSIONS

8.1 Model

8.2 Comparison Between Model and Experiment

8.3 Size Effects

8.4 Modifications in Large Pad Design

8.1 Model

a) It is possible to set up a three-dimensional analysis of titlting thrust pad bearings to accurately model the fluid flow, heat transfer and pad deflection, and to obtain solutions that are both qualitative and quantitative.

b) A simplified groove mixing model is able to furnish good resluts provided the runner is modelled comprehensively.

c) The quadratic approximation for the temperature profile through the oil film is useful in reducing the complexity of the problem.

d) The 'Polynomial Difference Method' is effective in handling the various boundary conditions for the solution of the biharmonic equation for variable rigidity thin plates.

8.2 Comparison between Model and Experimental Results

a) Good agreement was obtained for pad temperatures for three pad sizes spanning the thrust bearing size range. The agreement for maximum pad temperature improved for the higher specific loads. This may be primarily due to neglect of elastic shear deformation in the model. This is supported by the result that thermal deflections

share a greater proportion of the total distortion at the higher loads - diminshing the effect of elastic deformations (including shear deflections).

b) The predicted pad maximum temperatures were slightly greater than measured values. This may be due to two possibilities. Firstly, the actual pad maximum temperature does not necessarily have to be at the exact location of a measurement thermocouple. Thus, a lower temperature is recorded. Secondly, even if thermocouples are positioned flush with the working pad surface, a slight contact resistance at the thermocouple/oil interface will cause a drop in the recorded temperature.

c) Measurements of oil film thickness were in good agreement with the predicted values (Case 2 - chapter 6).

d) Good agreement was obtained for the temperature distribution at the pad/oil interface (Cases 1 and 3 - chapter 6).

e) The energy losses in the oil film due to conduction to the runner, conduction to the pad, and oil film convection were given for the small pad bearings. Agreement with experimental estimates was relatively good for different pad configurations (3, 6 and 8 pads).

8.3 Size Effects

a) For the same bearing geometry and running conditions, large bearings are shown to exhibit a large increase in temperature for a small increase in specific load when compared to smaller bearings. Thus, the margin of safety is considerably reduced.

b) The size effects are accentuated at higher runner velocities.

c) For small pads, thermal deformation as a means of generating a small crown can be beneficial. Beyond a certain pad size, thermal deformation becomes detrimental.

8.4 Modifications in Large Pad Design

a) Pad insulation was found to be detrimental. In the absence of insulation, a large proportion of the heat generated is conducted via the pad. For an insulated pad, less heat is allowed to escape via the pad. This is reflected in a much higher oil film temperature.

b) A relieved button (horse-shoe support) is found to be a useful modification in lowering the pad maximum temperature.

c) Forced water cooling (in the pad) is shown to be an excellent method of regulating the bearing temperature and curbing excessive thermal deflection. The coolant (water) velocity, and/or coolant inlet temperature,

may be varied to obtain optimum performance.

d) An offset pivot reduces pad maximum temperature.

e) Peripheral runner cooling is beneficial. When compared to (b), (c) and (d); its benefits seem negligible in lowering the pad maximum temperature.

f) A combination of (b), (c) and (d) can lower the maximum pad temperature of a typical large bearing by 30 deg C or more. Thus, the specific load capacity is approximately doubled when compared to conventional designs, whilst maintaining a safe bearing operating temperature.

APPENDIX A

REYNOLDS EQUATION DERIVATION

Figure P-1 shows a typical control volume. The various stresses acting in the circumferential direction are shown. A balance of tangential forces is as follows:

$$p\,\delta r\delta z - \left(p + \frac{\partial p}{\partial \theta}\,\delta\theta\right)\,\delta r\delta z + \tau_{\theta r}\, r\delta r\delta z$$

$$- \left(\tau_{\theta r} + \frac{\partial \tau_{\theta r}}{\partial r}\,\delta r\right)\,(r + \delta r)\,\delta\theta\delta z + \tau_{\theta z}\, r\delta\theta\delta r$$

$$- \left(\tau_{\theta z} + \frac{\partial \tau_{\theta z}}{\partial z}\,\delta z\right)\,(r\delta\theta\delta r) = 0 \qquad \text{(AA-1)}$$

Similarly in the radial direction,

$$p\left(r - \frac{\delta r}{2}\right)\,\delta\theta\delta z - \left(p + \frac{\partial p}{\partial r}\,\delta r\right)\,\left(r + \frac{\delta r}{2}\right)\,\delta\theta\delta z + \tau_{r\theta}\,\delta r\delta z$$

$$- \left(\tau_{r\theta} + \frac{\partial \tau_{r\theta}}{\partial \theta}\,\delta\theta\right)\delta r\delta z + \tau_{rz}\, r\delta\theta\delta r - \left(\tau_{rz} + \frac{\partial \tau_{rz}}{\partial z}\,\delta z\right) r\delta\theta\delta r$$

$$+ p\,\delta r\delta z\,\frac{\delta\theta}{2} + \left(p + \frac{\partial p}{\partial \theta}\,\delta\theta\right)\,\delta r\delta z\,\frac{\delta\theta}{2} = 0 \qquad \text{(AA-2)}$$

Equations AA-1 and AA-2 may be reduced - using the assumptions in Chapter 2 as follows:

$$\frac{\partial p}{\partial \theta} + r\,\frac{\partial \tau_{\theta z}}{\partial z} = 0 \qquad \text{(AA-3)}$$

$$\frac{\partial p}{\partial r} + \frac{\partial \tau_{rz}}{\partial z} = 0 \qquad \text{(AA-4)}$$

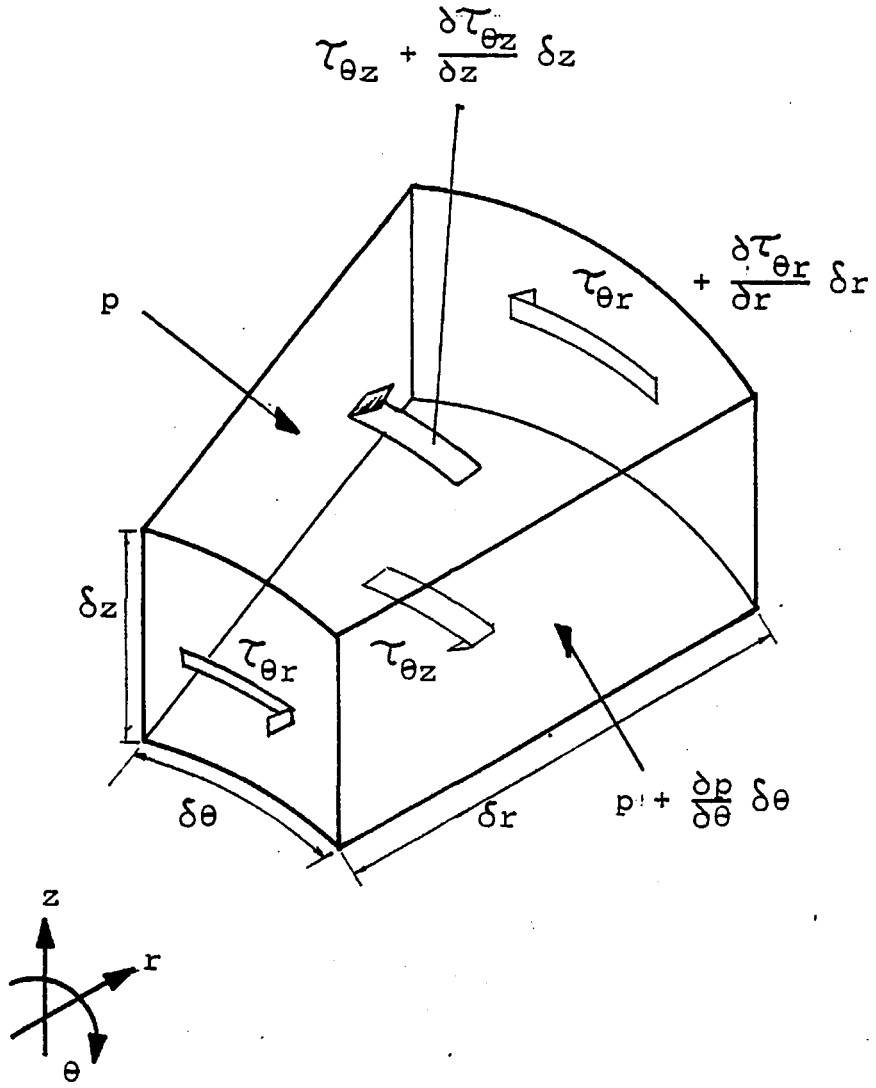

Figure P-1 A typical Control Volume

Now $$\tau_{\theta z} = -\mu \frac{\partial u}{\partial z} \qquad \text{(AA-5)}$$

$$\tau_{rz} = -\mu \frac{\partial v}{\partial z} \qquad \text{(AA-6)}$$

Using the above equations and integrating

$$u = C_1 \int \frac{dz}{\mu} + \frac{1}{r} \frac{\partial p}{\partial \theta} \int \frac{z}{\mu} dz + C_2 \qquad \text{(AA-7)}$$

$$v = B_1 \int \frac{dz}{\mu} + \frac{\partial p}{\partial r} \int \frac{z}{\mu} dz + B_2 \qquad \text{(AA-8)}$$

where C_1, C_2, B_1, B_2 are functions of r,θ.

The boundary conditions are

$$\text{at } z = 0 \text{ (runner surface)}; \; u = r\Omega; \; v = 0 \qquad \text{(AA-9)}$$

$$\text{at } z = h \text{ (pad surface)}; \quad u = 0 \; ; \; v = 0 \qquad \text{(AA-10)}$$

This yields,

$$u = \frac{1}{r} \frac{\partial p}{\partial \theta} F_1 + r\Omega F_2 \qquad \text{(AA-11)}$$

$$v = \frac{\partial p}{\partial r} F_1 \qquad \text{(AA-12)}$$

$$\text{where } F_1 = \int_o^z \frac{z}{\mu} dz - \frac{I_2}{I_1} \int_o^z \frac{dz}{\mu} \qquad \text{(AA-13)}$$

$$F_2 = \frac{\int_z^h \frac{dz}{\mu}}{I_1} \qquad \text{(AA-14)}$$

$$I_1 = \int_o^h \frac{dz}{\mu} \qquad \text{(AA-15)}$$

$$I_2 = \int_o^h \frac{z}{\mu} dz \qquad \text{(AA-16)}$$

The continuity equation may be written (Figure P-2)

$$q_\theta + q_r - (q_\theta + \frac{\partial q_\theta}{\partial \theta}\delta\theta) - (q_r + \frac{\partial q_r}{\partial r}\delta r) = 0 \qquad \text{(AA-17)}$$

where

$$q_\theta = \int_o^h u dz \delta r \qquad \text{(AA-18)}$$

$$q_r = \int_o^h v dz r \delta\theta \qquad \text{(AA-19)}$$

Equations AA-11 to AA-19 yield:

$$\frac{1}{r}\frac{\partial}{\partial\theta}\left(\frac{\partial p}{\partial\theta}\Gamma_1\right) + \frac{\partial}{\partial r}\left(r\frac{\partial p}{\partial r}\Gamma_1\right) = -r\Omega\frac{\partial}{\partial\theta}\Gamma_2 \qquad \text{(AA-20)}$$

where

$$\Gamma_1 = \int_o^h F_1 dz \quad ; \quad \Gamma_2 = \int_o^h F_2 dz$$

The above equation was deduced for laminar flow. Factors k_x, k_z and $\bar{\tau}_c$ are used to modify the equations based on a model by Ng, Pan and Elrod (see Chapter 5, section 5.3) to introduce turbulence effects:

$$\frac{1}{r}\frac{\partial}{\partial\theta}\left(\frac{\partial p}{\partial\theta}\frac{\Gamma_1}{k_x}\right) + \frac{\partial}{\partial r}\left(r\frac{\partial p}{\partial r}\frac{\Gamma_1}{k_z}\right) = -r\Omega\frac{\partial\Gamma_2}{\partial\theta}$$

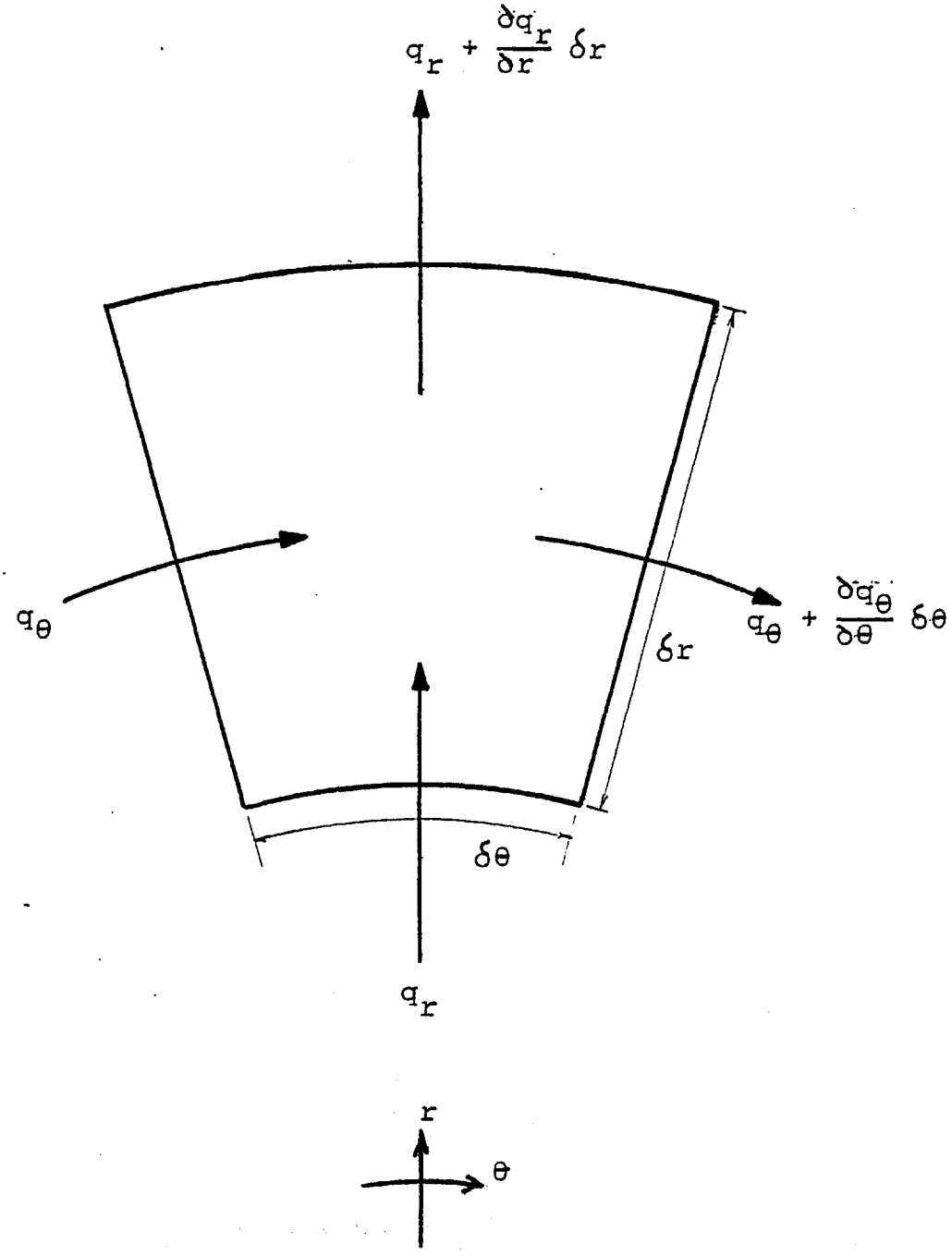

Figure P-2 The Flow in a Control Volume

APPENDIX B

FINITE DIEFERENCE APPROXIMATION OF THE REYNOLDS EQUATION

For a set of three consecutive nodes (Figure P-3) along the m axis

$$\left.\frac{\partial f}{\partial m}\right|_n = f_{n-1}\left(\frac{-\alpha}{(\alpha+1)\Delta}\right) + f_n\left(\frac{\alpha-1}{\alpha\Delta}\right) + f_{n+1}\left(\frac{1}{(\alpha+1)\alpha\Delta}\right) \tag{AB-1}$$

Applied to the radial and tangential directions:

$$\Delta_r \left.\frac{\partial f}{\partial r}\right|_i = e_1 f_i + e_2 f_{i-1} + e_3 f_{i+1} \tag{AB-2}$$

where

$$e_1 = \frac{\alpha-1}{\alpha}\ ;\quad e_2 = \frac{-\alpha}{\alpha+1}\ ;\quad e_3 = \frac{1}{\alpha(\alpha+1)} \tag{AB-3}$$

$$\Delta_\theta \left.\frac{\partial f}{\partial \theta}\right|_j = \zeta_1 f_j + \zeta_2 f_{j-1} + \zeta_3 f_{j+1} \tag{AB-4}$$

where

$$\zeta_1 = \frac{\beta-1}{\beta}\ ;\quad \zeta_2 = \frac{-\beta}{\beta+1}\ ;\quad \zeta_3 = \frac{1}{\beta(\beta+1)} \tag{AB-5}$$

Define,

$$S_i = \Gamma_1 \frac{r}{k_r}\quad ;\quad S_j = \Gamma_1 \frac{1}{k_\theta} \tag{AB-6}$$

The first term in the Reynolds equation is

$$\frac{1}{r}\frac{\partial}{\partial\theta}\left(\frac{\partial p}{\partial\theta}\,\Gamma_1\,\frac{1}{k_\theta}\right) \tag{AB-7}$$

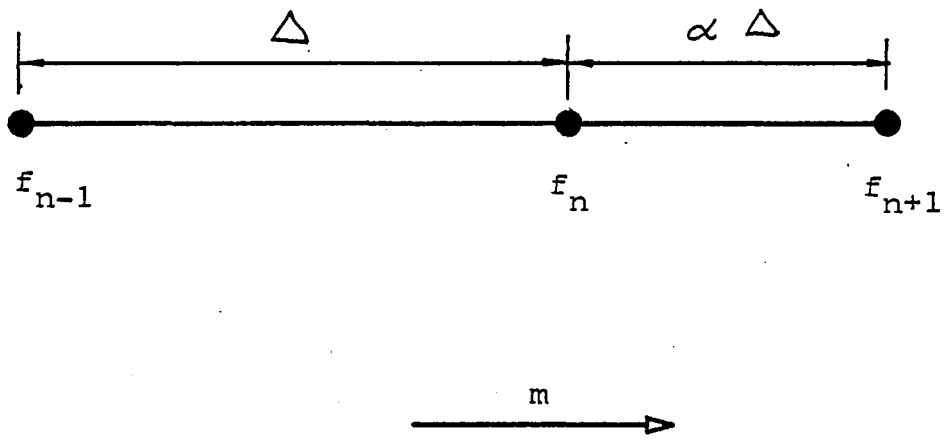

Figure P-3 Nodes along a Grid Axis

Define

$$a = \frac{\partial p}{\partial \theta} \Gamma_1 \frac{1}{k_\theta} = \frac{\partial p}{\partial \theta} S_j \qquad \text{(AB-8)}$$

The term in AB-7 may be written

$$\frac{1}{r} \frac{\partial a}{\partial \theta} \qquad \text{(AB-9)}$$

Hence,

$$r \Delta_\theta \left(\frac{1}{r} \frac{\partial a}{\partial \theta}\right) = \zeta_1 a_j + \zeta_2 a_{j-1} + \zeta_3 a_{j+1} \qquad \text{(AB-10)}$$

or

$$r \frac{\Delta_\theta}{2} \left(\frac{1}{r} \frac{\partial a}{\partial \theta}\right) = \zeta_1 a_J + \zeta_2 a_{j-\frac{1}{2}} + \zeta_3 a_{j+\frac{1}{2}} \qquad \text{(AB-11)}$$

Now

$$\frac{\Delta\theta}{S_j} a_j = \zeta_1 p_j + \zeta_2 p_{j-1} + \zeta_3 p_{j+1} \qquad \text{(AB-12)}$$

$$\frac{\Delta\theta}{S_{j-\frac{1}{2}}} a_{j-\frac{1}{2}} = p_j - p_{j-1} \qquad \text{(AB-13)}$$

$$\frac{\Delta\theta}{S_{j+\frac{1}{2}}} a_{j+\frac{1}{2}} = \frac{p_{j+1} - p_j}{\beta} \qquad \text{(AB-14)}$$

Thus, AB-7 to AB-14 yield:

$$\frac{1}{r} \frac{\partial}{\partial \theta} \left(\frac{\partial p}{\partial \theta} \frac{\Gamma_1}{k\theta}\right) = p_j \,(\text{CON1.DIVT}) + p_{j-1}(\text{CON2.DIVT}) + p_{j+1}(\text{CON3.DIVT}) \qquad \text{(AB-15)}$$

where

$$\text{CON1} = S_j (\zeta_1)^2 + S_{j-\frac{1}{2}} \zeta_2 - S_{j+\frac{1}{2}} \frac{\zeta_3}{\beta} \qquad \text{(AB-16)}$$

$$CON2 = S_j\ \zeta_1\ \zeta_2 - S_{j-\frac{1}{2}}\ \zeta_2 \qquad \text{(AB-17)}$$

$$CON3 = S_j\ \zeta_1\ \zeta_3 - S_{j+\frac{1}{2}}\ \frac{\zeta_3}{\beta} \qquad \text{(AB-18)}$$

$$DIVT = \frac{2}{r(\Delta\theta)^2} \qquad \text{(AB-19)}$$

A similar procedure is applied to the remaining two terms yielding for the Reynolds equation,

$$p_{ij} = p_{i,j-1}\ CW + p_{i,j+1}\ CE + p_{i-1,j}\ CS + p_{i+1,j}\ CN + CA \qquad \text{(AB-20)}$$

where

$$CN = -COE3\ .\ DIVR/CP \qquad \text{(AB-21)}$$

$$CS = -COE2\ .\ DIVR/CP \qquad \text{(AB-22)}$$

$$CW = -CON2\ .\ DIVT/CP \qquad \text{(AB-23)}$$

$$CE = -CON3\ .\ DIVT/CP \qquad \text{(AB-24)}$$

$$CA = (\zeta_1\ \Gamma_{2j} + \zeta_2\ \Gamma_{2j-1} + \zeta_3\ \Gamma_{2j+1})DIVZ/CP \qquad \text{(AB-25)}$$

$$DIVZ = -r_j\Omega/\Delta\theta \qquad \text{(AB-26)}$$

$$CP = CON1.DIVT + COE1.DIVR \qquad \text{(AB-27)}$$

and

$$COE1 = S_i\ e_1^2 + S_{i-\frac{1}{2}}\ e_2 - S_{i+\frac{1}{2}}\ \frac{e_3}{\alpha} \qquad \text{(AB-28)}$$

$$COE2 = S_i\ e_1\ e_2 - S_{i-\frac{1}{2}}\ e_2 \qquad \text{(AB-29)}$$

$$COE3 = S_i\ e_1\ e_3 + S_{i+\frac{1}{2}}\ \frac{e_3}{\alpha} \qquad \text{(AB-30)}$$

$$DIVR = \frac{2}{(\Delta r)^2} \qquad \text{(AB-31)}$$

APPENDIX C

ENERGY EQUATION DERIVATION

The energy equation may be written (see Figure P-4):

$$Q_N + Q_S + Q_E + Q_W + Q_G + Q_K - S = 0 \qquad \text{(AC-1)}$$

where the source term is

$$S = q_\theta \frac{1}{r}\frac{\partial p}{\partial \theta} r\delta\theta + q_r \frac{\partial p}{\partial r}\delta r + r\Omega\tau_o \, r\delta\theta\delta r \qquad \text{(AC-2)}$$

flow work shear work

where τ_o is the shear stress at $z = 0$

Hence, (using previous results in Appendices A and B),

$$S = \left(\frac{1}{r^2}\left(\frac{\partial p}{\partial \theta}\right)^2 \Gamma_1 + \Omega\,\Gamma_2 \frac{\partial p}{\partial \theta}\right) r\delta r\delta\theta + r\left(\frac{\partial p}{\partial r}\right)^2 \Gamma_1 \, \delta\theta\delta r$$

$$- r\,\Omega\,\delta\theta\delta r \frac{\partial p}{\partial \theta}\left(\frac{I_2}{I_1} - \frac{r^3\Omega^2}{I_1}\right)\delta\theta\delta r \qquad \text{(AC-3)}$$

Now $$Q_S = \rho c r\delta\theta \int_o^h \frac{\partial p}{\partial r} F_1 \, T \, dz \qquad \text{(AC-4)}$$

The inverse vicosity is assumed quadratic through the film,

$$\frac{1}{\mu} = az^2 + bz + c \qquad \text{(AC-5)}$$

Now $$I_1 = \int_o^h \frac{1}{\mu} dz = \frac{a}{3}h^3 + \frac{b}{2}h^2 + ch \qquad \text{(AC-6)}$$

$$I_2 = \int_o^h \frac{z}{\mu} dz = \frac{ah^4}{4} + \frac{bh^3}{3} + \frac{ch^2}{2} \qquad \text{(AC-7)}$$

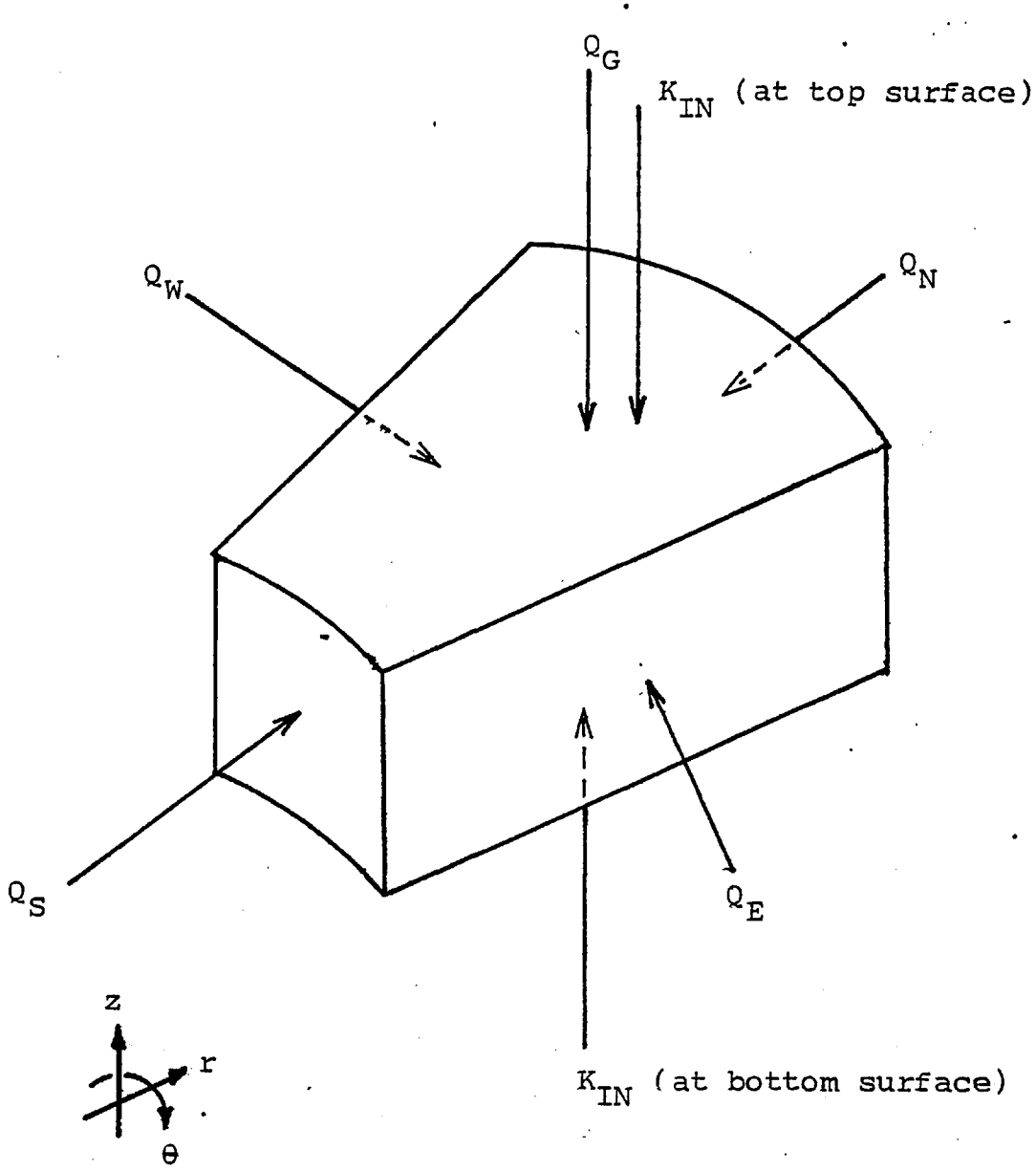

Figure P-4 The Heat Flux into a Control Volume

$$F_1 = \int_o^z \frac{z}{\mu}\, dz - \frac{I_2}{I_1} \int_o^z \frac{dz}{\mu} \qquad \text{(AC-8)}$$

$$F_1 = \frac{a}{4} z^4 + \frac{b}{3} z^3 + \frac{c}{z} z^2 - \frac{I_2}{I_1} \left(\frac{a}{3} z^3 + \frac{b}{2} z^2 + cz\right) \qquad \text{(AC-9)}$$

$$\Gamma_1 = \int_o^h F_1\, dz$$

$$\Gamma_1 = \frac{a}{20} h^5 + \frac{b}{12} h^4 + \frac{c}{6} h^3 - \frac{I_2}{I_1} \left(\frac{a}{12} h^4 + \frac{b}{6} h^3 + \frac{c}{2} h^2\right) \qquad \text{(AC-11)}$$

$$F_2 = \frac{1}{I_1} \left[\left(\frac{a}{3} h^3 + \frac{b}{2} h^2 + ch\right) - \left(\frac{az^3}{3} + \frac{bz^2}{2} + cz\right)\right] \qquad \text{(AC-12)}$$

$$\Gamma_2 = \frac{1}{I_1} \left[\frac{a}{4} h^4 + \frac{b}{3} h^3 + \frac{c}{2} h^2\right] \qquad \text{(AC-13)}$$

Therefore equation EC-4 may be rewritten

$$Q_S = \rho c r \delta\theta \frac{\partial p}{\partial r} \int_o^h \left[\frac{a}{4} z^4 + \frac{b}{3} z^3 + \frac{c}{2} z^2 - \frac{I_2}{I_1} \left(\frac{az^3}{3} + \frac{b}{2} z^2 + cz\right)\right]$$

$$[dz^2 + ez + f]dz \qquad \text{(AC-14)}$$

where $T = dz^2 + ez + f$ (AC-15)

Therefore

$$Q_S = \rho c r \delta\theta \frac{\partial p}{\partial r} (d\, V_1 + e\, V_2 + f\, V_3) \qquad \text{(AC-16)}$$

where

$$V_1 = \frac{ah^7}{28} + \frac{bh^6}{18} + \frac{ch^5}{10} - \frac{I_2}{I_1} \left(\frac{ah^6}{18} + \frac{bh^5}{10} + \frac{ch^4}{4}\right) \qquad \text{(AC-17)}$$

$$V_2 = \frac{ah^6}{24} + \frac{bh^5}{15} + \frac{ch^4}{8} - \frac{I_2}{I_1} \left(\frac{ah^5}{15} + \frac{bh^4}{8} + \frac{ch^3}{3}\right) \qquad \text{(AC-18)}$$

$$V_3 = \frac{ah^5}{20} + \frac{bh^4}{12} + \frac{ch^3}{6} - \frac{I_2}{I_1} \left(\frac{ah^4}{12} + \frac{bh^3}{6} + \frac{ch^2}{2}\right) \qquad \text{(AC-19)}$$

$$Q_N = -\rho c r d\theta \frac{\partial p}{\partial r} (dV_1 + eV_2 + fV_3) \qquad \text{(AC-20)}$$

(The negative sign is used to maintain that all flows into the control volume are positive).

Similarly,

$$Q_N = \frac{\rho c}{r} \frac{\partial p}{\partial \theta} \delta r \, (dV_1 + eV_2 + fV_3) + \frac{\rho c r \Omega \delta r}{I_1} (dV_4 + eV_5 + fV_6) \qquad \text{(AC-21)}$$

$$Q_E = -\frac{\rho c}{r} \frac{\partial p}{\partial \theta} \delta r \, (dV_1 + eV_2 + fV_3) + \frac{\rho c r \Omega \delta r}{I_1} (dV_4 + eV_5 + fV_6) \qquad \text{(AC-22)}$$

$$Q_G = q_G \, \rho c \, T \qquad \text{(AC-23)}$$

The temperature is assumed constant for flow into or out of a groove, sparing the need for integration.

Q_K represents the heat conducted to the oil film at the top and bottom surfaces and is of the form

$$Q_{K,top} = K \left.\frac{\partial T}{\partial Z}\right|_{top} r\delta\theta\delta r \qquad \text{(AC-24)}$$

$$Q_{K,bot} = -K \left.\frac{\partial T}{\partial Z}\right|_{z=0} r\delta\theta\delta r \qquad \text{(AC-25)}$$

a,b,c,d,e,f may be evaluated as

$$a = \frac{2}{h^2} \left(\frac{1}{\mu_3} - \frac{2}{\mu_2} + \frac{1}{\mu_1}\right) \qquad \text{(AC-26)}$$

$$b = \frac{1}{h} \left(-\frac{3}{\mu_1} + \frac{4}{\mu_2} - \frac{1}{\mu_3}\right) \qquad \text{(AC-27)}$$

$$c = \frac{1}{\mu_1} \qquad \text{(AC-28)}$$

$$d = \frac{2}{h^2} (T_3 - 2T_2 + T_1) \qquad \text{(AC-29)}$$

$$e = \frac{1}{h} (-3T_1 + 4T_2 - T_3) \qquad \text{(AC-30)}$$

$$f = T_1 \qquad \text{(AC-31)}$$

(1,2,3 refer to through film positions: runner, midpoint, pad).

Hence, a convection flux (energy) at one face is expressed:

$$Q = T_1 g_1 + T_2 g_2 + T_3 g_3 \qquad \text{(AC-32)}$$

Equation AC-1 may be written

$$\sum Q_{IN} - \sum Q_{OUT} + Q_K - S = 0 \qquad \text{(AC-33)}$$

or $$\sum Q_{IN} + Q_K - S = \sum Q_{OUT} \qquad \text{(AC-34)}$$

but $$\sum Q_{OUT} = \sum (T_1 g_1 + T_2 g_2 + T_3 g_3) \qquad \text{(AC-35)}$$

or $$\sum Q_{OUT} = T_1 \sum g_1 + T_2 \sum g_2 + T_3 \sum g_3 \qquad \text{(AC-36)}$$

Hence AC-34 may be written

$$\sum Q_{IN} + Q_K - S = T_1 \sum g_1 + T_2 \sum g_2 + T_3 \sum g_3 \qquad \text{(AC-37)}$$

or $$T_2 = \frac{\sum Q_{IN} + Q_K - S - (T_1 \sum g_1 + T_3 \sum g_3)}{\sum g_2} \qquad \text{(AC-38)}$$

where T_2 is the middle node temperature to be found

APPENDIX D

MEAN ABSOLUTE WEIGHTED RESIDUAL

The mean absolute weighted residual (MAWR) is defined to compare two fields of values (new field and old field in an iteration - or two fields representing an interface for example the oil pad interface). For a field of values a_i and another field b_i the MAWR is defined:

$$\text{MAWR} = \frac{\sum_i \{|b_i||1 - a_i/b_i|\}}{\sum_i |b_i|}$$

APPENDIX E

FINITE DIFFERENCE MODEL FOR PAD

The Laplace equation applies to a node within the solid pad. A more general approach allows for both the Laplace governing equation as well as the various boundary conditions. Consider the control volume shown in Figure P-5. Six surfaces are considered U,D,N,S,E,W. These have areas $A_V, A_D, A_N, A_S, A_E, A_W$ consecutively. For any particular surface S_i (Figure P-6), the heat transfer into the control volum due to conduction is:

$$Q_{i,s} = -k\, A_i \frac{(T_{IN} - T_{OUT})_i}{\Delta_i} \qquad \text{(EE-1)}$$

Now define

$$c_i = -\frac{k\, A_i}{\Delta} \qquad \text{(EE-2)}$$

The total heat transfer due to conduction at all surfaces where conduction takes place is:

$$\sum Q_i = \sum c_i\, (T_{IN} - T_{OUT_i}) \qquad \text{(EE-3)}$$

Similarly at a surface where convection takes place

$$Q_i = -\alpha_i A_i\, (T_{IN} - T_{OUT})_i \qquad \text{(EE-4)}$$

Define $d_i = -\alpha A_i$ (EE-5)

The heat transfer due to convection at all surfaces where convection takes place is:

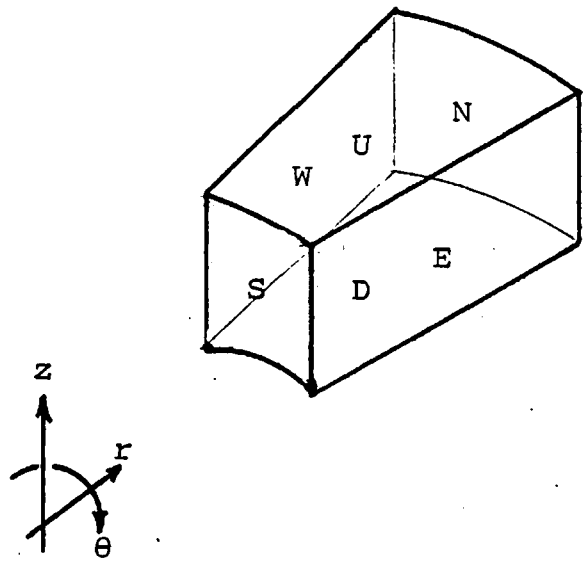

Figure P-5 The Six Faces of the Control Volume

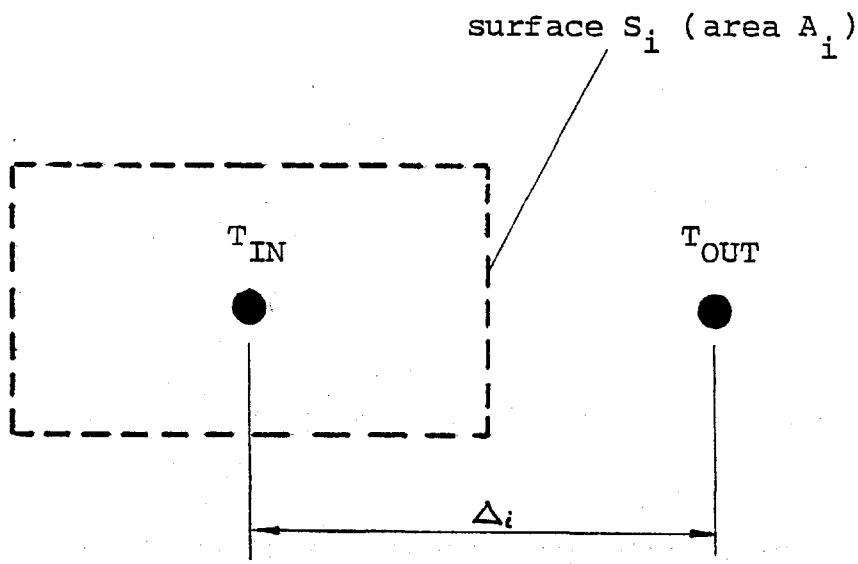

Figure P-6 The Heat Flux at a Control Volume Face

$$\sum Q_i = \sum d_i \ (T_{IN} - T_{OUT_i}) \qquad \text{(EE-6)}$$

The final boundary conditon concerns a specific heat flux into the control volume at a particular surface:

$$Q_i = Q_{Fi} A_i = e_i \ Q_{Fi} \qquad \text{(EE-7)}$$

Assembling the various types of flux at all surfaces of the control volume:

$$\sum c_i \ (T_{IN} - T_{OUT_i}) + \sum d_i \ (T_{IN} - T_{OUT_i}) + \sum e_i \ Q_{Fi} = 0 \qquad \text{(EE-8)}$$

in the absence of heat sources or sinks within the control volume.

The subject of the equation is to be T_{IN}, hence,

$$\sum c_i T_{IN} - \sum c_i T_{OUT_i} + \sum d_i T_{IN} - \sum d_i T_{OUT_i} + \sum e_i Q_{Fi} = 0 \qquad \text{(EE-9)}$$

or

$$T_{IN} = \frac{\sum c_i T_{OUT_i} + \sum d_i T_{OUT_i} - \sum e_i Q_{Fi}}{\sum c_i + \sum d_i} \qquad \text{(EE-10)}$$

APPENDIX F

The governing equation for the bending of sector shaped plates of varying rigidity is

$$\frac{\partial^3 w}{\partial r \partial \theta^2}\left(-\frac{2}{r^2}\frac{\partial D}{\partial r}+\frac{2D}{r^3}\right)+\frac{\partial^2 w}{\partial r \partial \theta}\left(-\frac{2}{r^2}\frac{\partial^2 D}{\partial r \partial \theta}-\frac{2\nu}{r^3}\frac{\partial D}{\partial \theta}+\frac{2\nu}{r^2}\frac{\partial^2 D}{\partial r \partial \theta}\right)$$

$$+\frac{\partial^2 w}{\partial \theta^2}\left(-\frac{1}{r^4}\frac{\partial^2 D}{\partial \theta^2}+\frac{3}{r^3}\frac{\partial D}{\partial r}-\frac{4D}{r^4}-\frac{\nu}{r^2}\frac{\partial^2 D}{\partial r^2}\right)+\frac{\partial^3 w}{\partial \theta^3}\left(-\frac{2}{r^4}\frac{\partial D}{\partial \theta}\right)$$

$$+\frac{\partial^4 w}{\partial r^4}(-D)+\frac{\partial w}{\partial \theta}\left(\frac{2}{r^3}\frac{\partial^2 D}{\partial \theta \partial r}+\frac{2\nu}{r^4}\frac{\partial D}{\partial \theta}-\frac{2\nu}{r^3}\frac{\partial^2 D}{\partial r \partial \theta}-\frac{2}{r^4}\frac{\partial D}{\partial \theta}\right) \qquad \text{(AF-1)}$$

$$+\frac{\partial^3 w}{\partial \theta \partial r^2}\left(-\frac{2}{r^2}\frac{\partial D}{\partial \theta}\right)+\frac{\partial^4 w}{\partial \theta^4}\left(-\frac{D}{r^4}\right)+\frac{\partial w}{\partial r}\left(-\frac{1}{r^3}\frac{\partial^2 D}{\partial \theta^2}-\frac{\nu}{r}\frac{\partial^2 D}{\partial r^2}+\frac{1}{r^2}\frac{\partial D}{\partial r}-\frac{D}{r^3}\right)$$

$$+\frac{\partial^4 w}{\partial \theta^2 \partial r^2}\left(-\frac{2D}{r^2}\right)+\frac{\partial^2 w}{\partial r^2}\left(-\frac{\nu}{r^2}\frac{\partial^2 D}{\partial \theta^2}-\frac{\partial^2 D}{\partial r^2}-\frac{2}{r}\frac{\partial D}{\partial r}+\frac{D}{r^2}-\frac{\nu}{r}\frac{\partial D}{\partial r}\right)$$

$$+\frac{\partial^3 w}{\partial r^3}\left(-\frac{2\partial D}{\partial r}-\frac{2D}{r}\right)=-p$$

For Thermal Deflection:

$$M^T=\frac{E\alpha}{1-\nu}\int_{-h/2}^{h/2} Tz\,dz \qquad \text{(AF-2)}$$

if T is a linear function, then

$$M^T=D(1+\nu)\alpha\frac{\partial T}{\partial z} \qquad \text{(AF-3)}$$

Now $$M_r^T=M_r-M^T \qquad \text{(AF-4)}$$

$$M_\theta^T=M_\theta-M^T \qquad \text{(AF-5)}$$

$$V_r^T=V_r-\frac{\partial}{\partial r}(M^T) \qquad \text{(AF-6)}$$

$$V_\theta^T=V_\theta-\frac{1}{r}\frac{\partial}{\partial \theta}(M^T) \qquad \text{(AF-7)}$$

If including temperature deflection, the right-hand side of equation (AF-1) becomes:

$$= - p + \frac{1}{r^2} \frac{\partial^2 M^T}{\partial \theta^2} + \frac{\partial^2 M^T}{\partial r^2} + \frac{1}{r} \frac{\partial M^T}{\partial r}$$

The following relationships are needed for the application of boundary conditions.

$$M_r = - D \{\frac{\partial^2 w}{\partial r^2} + \nu[\frac{1}{r} \frac{\partial w}{\partial r} + \frac{1}{r^2} \frac{\partial^2 w}{\partial \theta^2}]\} \quad \text{(AF-8)}$$

$$M_\theta = - D \{\frac{1}{r} \frac{\partial w}{\partial r} + \frac{1}{r^2} \frac{\partial^2 w}{\partial \theta^2} + \nu \frac{\partial^2 w}{\partial r^2}\} \quad \text{(AF-9)}$$

$$M_{r\theta} = - M_{\theta r} = (1 - \nu) D \{\frac{1}{r} \frac{\partial^2 w}{\partial r \partial \theta} - \frac{1}{r^2} \frac{\partial w}{\partial \theta}\} \quad \text{(AF-10)}$$

$$V_r = Q_r - \frac{\partial M_{r\theta}}{r \partial \theta} \quad \text{(AF-11)}$$

$$V_r = \frac{\partial^3 w}{\partial r \partial \theta^2} (- \frac{2D}{r^2} + \frac{\nu D}{r^2}) + \frac{\partial^3 w}{\partial r^3} (-D) + \frac{\partial^2 w}{\partial r \partial \theta} (\frac{2\nu}{r^2} \frac{\partial D}{\partial \theta} - \frac{2}{r^2} \frac{\partial D}{\partial \theta})$$
$$+ \frac{\partial w}{\partial \theta} (- \frac{2\nu}{r^3} \frac{\partial D}{\partial \theta} + \frac{2}{r^3} \frac{\partial D}{\partial \theta}) + \frac{\partial^2 w}{\partial \theta^2} (\frac{3D}{r^3} - \frac{\nu}{r^2} \frac{\partial D}{\partial r} - \frac{\nu D}{r^3})$$
$$+ \frac{\partial^2 w}{\partial r^2} (- \frac{\partial D}{\partial r} - \frac{D}{r}) + \frac{\partial w}{\partial r} (- \frac{\nu}{r} \frac{\partial D}{r} + \frac{D}{r^2}) \quad \text{(AF-12)}$$

$$V_\theta = Q_\theta - \frac{\partial M_{r\theta}}{\partial r} \quad \text{(AF-13)}$$

$$V_\theta = \frac{\partial^3 w}{\partial r^2 \partial \theta} (\frac{\nu D}{r} - \frac{2D}{r}) + \frac{\partial^3 w}{\partial \theta^3} (- \frac{D}{r^3}) + \frac{\partial^2 w}{\partial r \partial \theta} (\frac{2\nu}{r} \frac{\partial D}{\partial r} - \frac{2}{r} \frac{\partial D}{\partial r} - \frac{2\nu D}{r^2})$$
$$+ \frac{\partial w}{\partial \theta} (- \frac{2\nu}{r^2} \frac{\partial D}{\partial r} + \frac{2}{r^2} \frac{\partial D}{\partial r} + \frac{2\nu D}{r^3} - \frac{2D}{r^3}) + \frac{\partial w}{\partial r} (- \frac{1}{r^2} \frac{\partial D}{\partial \theta})$$
$$+ \frac{\partial^2 w}{\partial \theta^2} (- \frac{1}{r^3} \frac{\partial D}{\partial \theta}) + \frac{\partial^2 w}{\partial r^2} (- \frac{\nu}{r} \frac{\partial D}{\partial \theta}) \quad \text{(AF-14)}$$

References

1. Martin, F. A., 'Rapid Design Aids', Tribology Convention, Paper 16, I.Mech.E., 1970.
2. Pinkus, O., and Sternlicht, B., 'Theory of Hydrodynamic Lubrication', McGraw Hill, New York, 1961.
3. Cameron, A., 'The Principles of Lubrication', Longmans, London, 1966.
4. Capitao, J. W., Gregory, R. S., Whitford, R. P., 'Effects of High Operating Speeds On Tilting Pad Thrust Bearing Performance', J.Lub.Tech., 98 , 73-80, 1976.
5. Taylor, C.M., Dowson, D., 'Turbulent Lubrication Theory, Application to Design', Trans. ASME, Paper No.73-LubS-10, 1973.
6. Brazier, P. H., 'An Optimum SOR Procedure for the Solution of Elliptic Partial Differential Equations with any Domain or Coefficient Set', Computer Methods in Appl. Mech. and Eng., 3 , 335-347, 1974.
7. Fogg, A., 'Fluid Film Lubrication of Parallel Thrust Surfaces', Proc. of I.Mech.E., 155 , 49, 1946.
8. Christopherson, D. G., 'A New Mathematical Method for the Solution of Film Lubrication Problems', Proc. I.Mech.E., 146 , 126-135, 1942.
9. Hahn, E. J., and Kettleborough, C. F., 'Thermal Effects in Slider Bearings', Proc. I.Mech.E., 183 , Pt.1, 631, 1968-69.

10. Hahn, E. J., and Kettleborough, C. F., 'The Effects of Thermal Expansion in Infinitely Wide Slider Bearings - Free Thermal Expansion', Trans. ASME, J.Lub.Tech., 90 , 233, 1968.

11. Charnes, A., Osterle, F., and Saibel, E., 'On the Energy Equation for Fluid Film Lubrication', Proc. Roy. Soc., 214 , 133, 1952.

12. Osterle, F., Cahrnes, A., and Saibel, E., 'Effect of Temperature on the Viscosity', Trans. ASME, 75 , 1117, 1953.

13. Hahn, E. J., and Kettleborough, C. F., 'Solution for the Pressure and Temperature in an Infinite Slider Bearing of Arbitrary Profile', J.Lub.Tech., 89 , 445, 1967.

14. Dowson, D., and Hudson, J. D., 'Thermohydrodynamic Analysis of the Infinite Slider Bearing: Part I - The Plane Inclined Slider Bearing, Lub. and Wear Conference, 1963.

15. Neal, P. B., 'Analysis of the Taper-Land Bearing Pad', J.Mech.Eng.Sci., 12 , 73-84, 1970.

16. Castelli, V., and Malanoski, S. B., 'Method for the Solution of Lubrication Problems with Temperature and Elasticity Effects: Application to Sector, Tilting Pad Bearings', J.Lub.Tech., 91 , 634-640, 1969.

17. Ettles, C., 'Development of a Generalised Computer Analysis for Sector Shaped Tilting Pad Thrust Bearings', Trans. ASLE, 19 , 2, 152, 1975.

18. Sternlicht, B., 'Energy and Reynolds Considerations in Thrust-Bearing Analysis', Proc. I.Mech.E., Lubrication Conference, 21, 28-38, 1957.

19. Ettles, C., 'Hydrodynamic Thrust Bearing Study', Ph.D. Thesis, Imperial College, London, 1965.

20. Advani, S., 'A Study of Tapered Land Thrust Bearings', Ph.D. Thesis, Imperial College, London, 1969.

21. Neal, P. B., 'Influence of Film Inlet Conditions on the Performance of Fluid Film Bearings', J.Mech.Eng.Sci., 12 , 153, 1970.

22. Seireg, A., and Ezzat, H., 'Thermohydrodynamic Phenomena in Fluid Film Lubrication', ASME Paper No. 72-Lub-25, 1972.

23. Stokes, M. J., 'Thermohydrodynamic Journal Bearing Study', Ph.D. Thesis, Imperial College, 1972.

24. Ezzat, H. A., and Rohde, S. M., 'A Study of the Thermohydrodynamic Performance of Finite Slider Bearings', Trans. ASME, Series F, 95 , 298-307, 1973.

25. Rohde, S. M., and Oh, K. P., 'A Thermoelastohydrodynamic Analysis of a Finite Slider Bearing', J.Lub.Tech., 97 , 450-460, 1975.

26. Huebner, K. H., 'A Three-Dimensional Thermohydrodynamic Analysis of Sector Shaped Thrust Bearings', ASLE Trans., 17 , 1, 62-73, 1974.

27. Ettels, C., and Cameron, A., 'Considerations of Flow Across a Bearing Groove', Trans. ASME, J.Lub.Tech., Series F, 90 , 312, 1968.

28. Ettles, C., 'Solutions for Flow in a Bearing Groove', Proc. I.Mech.E., 182 , 3N, 122, 1968.

29. Ettels, C., 'Hot Oil Carry-Over in Thrust Bearings', Proc.

I.Mech.E., 184 , 3L, 75, 1975.

30. Ettles, C., and Advani, S., 'The Control of Thermal and Elastic Effects in Thrust Bearings', Proc. 6th Leeds-Lyon Conf., 105-116, Mech.Eng. Press, London, 1979.

31. Ettles, C., 'Transient Thermo-Elastic Effects in Fluid Film Bearings', Wear, Scheduled to appear May/June 1982.

32. Vohr, J. H., 'Prediction of the Operating Temperature of Thrust Bearings', Trans. ASME, J.Lub.Tech., 103 , 1, 97, 1981.

33. Neal, P. B., 'Heat Transfer in Pad Thrust Bearings', To Be Published.

34. Kays, W. M., 'Convection Heat and Mass Transfer', McGraw Hill, N.Y., 1966.

35. Fogg, A., 'Fluid Film Lubrication of Parallel Thrust Surfaces', Proc. I.Mech.E., 155 , 49, 1946.

36. Charnes, A., Saibel, E., and Ying, A. S., 'Effect of Transverse Curvature', Trans. ASME, 75 , 507, 1953.

37. Raimondi in Discussion of R36.

38. Raimondi, A. A., and Boyd, J., 'The Influence of Surface Profile on the Load Capacity of Thrust Bearings with Centrally Pivoted Pads', Trans. ASME, 77 , 321, 1955.

39. Baudry in Discussion of R38.

40. Ketleborough, C. F., Dudley, B. R., and Baildon, E., 'Michell Bearing Lubrication', Proc. I.Mech.E., 169 , 746, 1955.

41. Ettles, C., and Cameron, A., 'Thermal and Elastic Distortion in Thrust-Bearings', Conference on Lubrication and Wear, Paper 21, Oct. 1957.

42. Baudry, R. A., Kuhn, E. C., and Wise, W. W., ' Influence of Load and Thermal Distortion on the Design of Large Thrust Bearings', Trans. ASME, 80 , 807-818, 1958.

43. Sternlicht, B., Carter, G. K., and Arwas, E. B., 'Adaibatic Analysis of Elastic Centrally-Pivoted, Sector, Thrust Bearing Pads', J.Appl.Mech., 28 , 179-187, 1961.

44. Raimondi, A. A., 'The Influence of Longitudinal and Transverse Profile on the Load Capacity of Pivoted Pad Bearings', ASLE Trans., 3 , 2, 265, 1960.

45. Sternlicht, B., Reid, J. C., and Arwas, E. B., ' Performance of Elastic Centrally Pivoted, Sector, Thrust Bearing Pads - Part I', Trans. ASME, J.Basic Eng., 83 , 169, 1961.

46. Neal, P. B., Wallis, J. F., and Duncan, J. P., ' A University Research for Industry', Eng., 191 , 434, 1961.

47. Hemingway, E. W., 'The Measurement of Oil Film Thickness in Thrust Bearings and the Deflected Shape of Parallel Surface Thrust Pads', Proc. I.Mech.E., 180 , 1025, 1965.

48. Bennet, A. H., ' The Parallel-Surface Self-Acting Thrust Bearing', M.Sc. Thesis, Imperial College, 1967.

49. Hemingway, E. W., 'A Performance Investigation into the Elastically Stepped and Shrouded Thrust Bearing', Proc. I.Mech.E., 182 , 38, 769, 1967-68.

50. Shawcross, E., and Dudley, B. R., 'The Performance of Tilting Pad Thrust Bearings', Ind.Lub.Tri., 23 (6), 211, 1971.

51. Dayson, C., 'Flexible Stepped Thrust Bearings', ASLE Trans., 16 , 1, 32-41, 1972.

52. Robinson, C. L., and Cameron, A., 'Studies in Hydrodynamic Thrust Bearings', Phil. Trans. Roy. Soc., 278 , 351-395, 1975.

53. Gardner, W. W., 'Performance Tests on Six Inch Tilting Pad Thrust Bearings', Trans. ASME, Paper No. 74-Lub-13, 1974.

54. Robinson, E. L., 'Strength of Steam Turbine Diaphragms', GEC Report No. 16380, 43pp, 1923.

55. Wahl, A. M., 'Strength of Semicircular Plates and Rings Under Uniform External Pressure', Trans. ASME, 54 , 311-320, 1932.

56. Taylor, V. C., ' Stress and Deflection Test of Steam Turbine Diaphragms', Trans. ASME, 73 , 877, 1961.

57. Carrier, G. F., and Ithaca, N. Y., 'The Bending of the Clamped Sectorial Plate', J.Appl.Mech., 11 , A-134, 1944.

58. Deverall, L. I., and Thorne, C. J., 'Bending of Thin Ring Sector Plates', J.Appl.Mech., 18 , 359, 1951.

59. Conway, H. D., Huang, M. K., and Ithaca, N. Y., 'The Bending of Uniformly Loaded Sectorial Plates with Clamped Edges', J.Appl.Mech., 19 , 5, 1952.

60. Muster, D. F., and Sadowsky, M. A., 'Bending of a Uniformly Loaded Semicircular Plate, Simply Supported around the Curved Edge and Free along the Diameter', J.Appl.Mech., 23 , 329, 1956.

61. Chen, S. H., and Pickett, G., 'Bending of Plates of Any Shape and with any Variation in Boundary Conditions', J.Appl.Mech., 34 , 217, 1967.

62. Bhattacharya, A. P., 'Bending of Sectorial Plate Having Clamped Straight Edges', J.Appl.Mech., 42 , 229, 1975.

63. Rubin, C., 'Bending of Ring and Pie-Shaped Sectors', J.Appl.Mech., 42 , 492, 1975.

64. Lo, K.H., Christensen, R. M., and Wu, E. M., 'A High Order Theory of Plate Deformation', J.Appl.Mech., 44 , 663, 1977.

65. Goodier, J. N., 'Thermal Stress and Deformation', J.Appl.Mech., 24 , 417, 1957.

66. Szilard, R., 'Theory and Analysis of Plates - Classical and Numerical Methods', Prentice Hall, New Jersey, 1974.

67. Ettles, C., 'Size Effects in Tilting Pad Thrust Bearings', Wear, 59 , 231-245, 1980.

68. Mathematics Lecture Notes, 2nd Year Undergraduate Studies, Imperial College, 1977.

69. Abramovitz, S., 'Turbulence in a Tilting Pad Thrust Bearing', ASME/ASLE Conference, Oct.1954.

70. Taylor, C. M., 'Turbulent Lubrication Theory Applied to Fluid Film Bearing Design', Proc. I.Mech.E., 184 , 3L, 1970.

71. Constantinescu, V. N., 'Basic Relationships in Turbulent Lubrication and Their Extention to Include Thermal Effects', J.Lub.Tech., 95 , 147, 1973.

72. Hirs, G. G., ' A Bulk-Flow Theory for Turbulence in Lubricant Films', J.Lub.Tech., 95 , 137, 1973.

73. Taylor and Dowson, 'Turbulence Lubrication Theory - Application to Design', ASME Paper No. 73-LubS-10, 1973.

74. Van Driest, E. R., 'On Turbulent Flow Near a Wall', J.Aero.Sci., 23 , 1007, 1956.

75. Venkateswarlu, and Rodkiewicz, G.M., 'On the Thrust Bearing

Characterisitcs in Turbulent Flow', J.Lub.Tech., 103 , 453, 1981.

76. Burton, R. A., 'An Experimental Study and Analysis of Turbulent Film Tilted-Pad Bearings', Trans. ASME, Paper No. 73-LubS-20, 1974.

77. Pinkus, O., and Lund, J. W., 'Centrifugal Effects in Thrust Bearings and Seals Under Laminar Conditions', J.Lub.Tech., 103 , 126, 1981.

78

79. Classified Co. Report,

80. Timoshenko, and Woinowsky-Krieger, 'Theory of Plates and Shells', McGraw Hill, N.Y., 1959.

81. Cameron, A., 'The Surface Roughness of Bearing Surfaces and Its Relation to Oil Film Thickness at Breakdown', Proc. I.Mech.E., 161 , 73, 1949.

82. Hunter, W. B., and Zienkiewicz, O. C., 'Effect of Temperature Variations Across the Lubricant Films in the Theory of Hydrodynamic Lubrication', J.Mech.Eng.Sci., 2 , 52, 1960.

83. Dowson, D., and Hudson, J. D., 'Thermohydrodynamic Analysis of the Infinite Slider Bearing : Part II - The Parallel Surface Bearing', Lub. and Wear Convention, 1963.

84. Elwell, R. C., Gustafson, R. E., and Reid Jr, J. C., 'Performance of Centrally Pivoted, Sector, Thrust Bearing Pad in Sea Trials Aboard U.S.S. Barry', ASME Paper No. 63-WA-124, 1963.

85. Neal, P. B., 'Some Factors Influencing the Operating

Temperature of Pad Thrust Bearings', 6th Leeds-Lyon Conference, MEP Ltd, Sept. 1979.

86. Glacier Metal Co., 'Designer's Handbook No.5'.

87. Starcevic, and Mez, F., 'The Development of Large Thrust Bearings for Vertical Hydro-Electric Generators', Brown Boveri Rev. 2 , Switzerland, 1980.

88. Kawaike, K., Okano, and Furukawa, Y., 'Performance of a Large Thrust Bearing with Minimised Thermal Distortion', ASLE Paper No. 77-LC-1A-2, 1977.

89. Bahr, H. C., 'Recent Improvements in Load Capacity of Large Steam Turbine Thrust Bearings', ASME Paper No. 59-A-139, 1959.

90. Mikula, A. M., 'A Comparison of Tilting Pad Thrust Bearing Lubricant Supply Methods', Trans. ASME, Paper No. 81-Lub-8, 1981.

91. Ettels, C., 'Transient Thermo-Elatic Effects in Fluid Film Bearings', Wear, Scheduled to appear May/June 1982.

92. Kuno, R., 'Strength of a Semicircular Plate', J.S.M.E., 37 , 101, 1934.

93. Hasse, H. R., 'The Bending of a Uniformly Loaded Clamped Plate in the Form of a Circular Sector', Q.J. Mech. and App.Math., 3 , 271, 1950.